ENERGY LEVEL STRUCTURE
OF THE
RARE EARTH IRON GARNETS

A THESIS

Presented to

The Faculty of the Graduate Division

by

Fred Leland Grismore, Jr.

In Partial Fulfillment

of the Requirements for the Degree

Doctor of Philosophy

in the

School of Electrical Engineering

Georgia Institute of Technology

June 1970

In presenting the dissertation as a partial fulfillment of the requirements for an advanced degree from the Georgia Institute of Technology, I agree that the Library of the Institute shall make it available for inspection and circulation in accordance with its regulations governing materials of this type. I agree that permission to copy from, or to publish from, this dissertation may be granted by the professor under whose direction it was written, or, in his absence, by the Dean of the Graduate Division when such copying or publication is solely for scholarly purposes and does not involve potential financial gain. It is understood that any copying from, or publication of, this dissertation which involves potential financial gain will not be allowed without written permission.

7/25/68

ACKNOWLEDGMENTS

It is impossible to acknowledge all one's teachers and fellow workers who have contributed to his abilities and professional being. Ideas and concepts are acquired from a diversity of sources many from the remote past. Always I find myself thankful to God for what innate abilities have been afforded me and for an environment in which to develop them. Such an environment existed for me at Georgia Tech and I will always be indebted to several specific people there for their guidance and support.

Dr. D. C. Ray, my thesis advisor, was a constant source of encouragement, moral support, and technical direction. It was through him as my teacher that my interest in the atomic structure of matter was stimulated. I will always be grateful for his help in this work.

Dr. E. J. Scheibner too contributed immeasurably to my development at Georgia Tech. It was through his leadership as Head of the Physical Sciences Division of the Engineering Experiment Station that I was able to acquire funds and equipment to carry out this research. But in addition to that I have, under his direction, absorbed a great deal of insight into the overall concepts of materials research. Dr. Scheibner possesses the unusual combination of theoretical competence and practical insight. I have learned much by studying his

ENERGY LEVEL STRUCTURE
OF THE
RARE EARTH IRON GARNETS

Approved:

Chairman

Date approved by Chairman: 6/4/70

approach to the solution of difficult research problems.

Dr. J. Elmer Rhodes stands out for me as the one person who has most directly influenced my approach to the solution of technical problems. During this research program he has been not only my associate but a teacher and friend. Although I have never taken a formal course from him I studied under him constantly. Dr. Rhodes has the ability to strip a complex problem of its superfluous detail and concentrate only on its key features; a characteristic I am trying to model in my own work. His diversity of interests and congenial manner have considerably broadened my own interests and insights. His influence is present on nearly every page of this manuscript.

I am indebted to Ruth Ann my wife. She has suffered not only from lack of a "normal" husband but in addition performed all the typing of this thesis. Therefore her influence too is entrained throughout it. I suspect her greatest reward, however, is not the appearance of her name on this page but the fact that it is the last one to be typed.

Finally I owe a debt of thanks to the other members of my reading committee Dr. G. P. Rodrigue and Dr. J. W. Hooper. Their comments and corrections of the original draft were valuable in compiling this final copy.

TABLE OF CONTENTS

TABLE OF CONTENTS (Continued)

LIST OF TABLES

LIST OF TABLES (Continued)

LIST OF ILLUSTRATIONS

LIST OF ILLUSTRATIONS (Continued)

LIST OF ILLUSTRATIONS (Continued)

SUMMARY

This research has undertaken the study of the valence electron energy level structure of the heavy rare earth iron garnets. Explicit data are presented for gadolinium iron garnet and terbium iron garnet. The work includes a combination of experimental and theoretical efforts.

Experimentally the optical spectra of single crystal bulk garnets was measured over the 2 eV to 5 eV energy range using reflectivity techniques. From the reflectivity data the complex refractive index was determined as well as the optical absorption coefficient. Oscillator strengths, f, of the major transitions have also been computed. Values of f in the range of 10^{-2} to 10^{-1} are typical, indicating strong electric dipole "charge transfer" transitions.

LCAO (linear combination of atomic orbitals) molecular orbital theory has been used to explain the atomic origin of the experimentally observed structure. This approach was motivated by the lack of agreement between experimental data and previous crystal field model calculations. A complete chapter of this thesis, Chapter III, explains the details of the LCAO theoretical model used. Computer programs are included in the Appendices. In the technique applied here diagonal matrix elements of the secular equation are determined

from atomic ionization potentials. Off-diagonal elements are found using a modified Wolfsberg-Helmholz approximation.

The LCAO theory was applied to the iron atom octahedral and tetrahedral sites. Adjustable parameters in the computation were first determined by applying the technique to orthoferrite data which contains only octahedral iron sites. The energy level spectra predicted by the molecular orbital calculations agrees very well with the observed spectra. Average error between computed and observed transition energies is less than 0.2 eV and all but two experimentally observed lines are accounted for in a natural way. One of these lines appears at 3.9 eV in the GdIG and is believed to be a rare earth 4f electronic transition. The other line appears at 4.35 eV in both samples and is believed to be a lead impurity transition.

The results indicate that LCAO techniques are capable of providing an understanding of the atomic origin of optical transitions in solids. In addition to the energy levels computed, the resulting orbital wave functions should make it possible to compute Faraday rotation associated with the charge transfer transitions. This may ultimately provide an insight into the most desirable atomic properties necessary to obtain high (rotation/absorption) ratios. Such information is very desirable for magneto-optical device applications.

Finally, using data relating to the transition probability associated with a rare earth ion transition, such as

the 3.9 eV Gd line, the feasibility of a new optical memory is evaluated. In this approach, optical excitation of the rare earth ions is employed to change their net moment and hence the coercive field of the material. The results indicate that an optical pumping power of less than 4 milliwatts should be required. It is believed that exploitation of this phenomena would permit the development of high density magneto optic memories unhampered by the problems associated with thermo magnetic techniques now being used.

CHAPTER I

INTRODUCTION

An area of major concern in the development of digital computing hardware is the lack of a technology capable of providing high density random access memory. Thin magnetic films are currently used for memories of approximately 10^6 bits and cycle times of 500 nanoseconds. This technology however is limited by energy loss constraints as the input and output transmission lines become extremely small at higher bit densities. Cryogenic memories are potentially capable of overcoming this difficulty because of the negligible losses in superconducting paths. Work in this field has however not been successful after ten years of development.

An alternative to the cryogenic approach is one exploiting the magneto optical properties of certain materials. One proposal of this type[1] makes use of laser induced heating of a magnetic material to change the coercive force at one small spot in a ferrimagnet. In this approach storage density and switching times are limited by the thermal characteristics of the material.

A more promising approach is to exploit photon-electron interactions rather than photon-phonon interactions. Recently Forlani and Minnaja[2] proposed that population of the first excited state in rare earth ions by optically induced

electronic transitions involving the 4f electrons should cause a significant change in their magnetic moment. This is referred to as optical pumping. They proposed that an excitation of this type should manifest itself as a reduction in magnetic coercivity in materials such as the rare earth garnets. The existence of this phenomena would provide the potential of a memory technology with bit density being constrained primarily by the resolution limits of the incident light. Ultimate resolution would of course depend on the minimum size of a stable reverse magnetic domain. Time constants for such an excitation would be governed by the lifetimes of the excited states, typically 10^{-6} to 10^{-7} seconds. A 10^{8} bit memory might be fabricated on a single plane of material three inches square.

Concept of Optically Pumped Memory

It seems possible that materials like the rare earth iron garnets might be suitable for such a memory application. Crystallographic and magnetic structure[3,4] of these materials have been well studied. A unit cell consists of eight chemical formula units of the type $RE_3Fe_5O_{12}$. Each rare earth ion occupies a dodecahedral or (c) site, and iron atoms occupy either a tetrahedral (d) site or octahedral (a) site. The unit cell contains rare earth atoms in 24 (c) sites, and iron atoms in 16 (a) sites and 24 (d) sites. Oxygen atoms occupy 96 (b) positions.

Magnetization in the rare earth iron garnets occurs because of superexchange forces between magnetic atoms through intermediate oxygen atoms. It has been found that a Neél ferrimagnetic effective field model[5] provides a very satisfactory description using effective field constants of $n_{aa} = -352$, $n_{cc} \approx 0$, $n_{dd} = -211$, $n_{ad} = 742$, $n_{cd} = 35$. The subscripts denote the associated crystallographic sites. Thus the iron (a) sites are parallel coupled together to form one sublattice. The iron (d) sites are also strongly parallel coupled. The effect of the large positive n_{ad} coefficient is to couple these two iron sublattices in an antiparallel fashion resulting in a net iron moment of approximately $5\mu_B$ per formula unit in the direction of the tetrahedral, i.e., (d) site iron moment. The small n_{cd} coefficient couples the rare earth ions antiparallel to the (d) sites and hence antiparallel to the net iron moment.

At very low temperatures the rare earth atoms' magnetic moment will be uniformly aligned antiparallel to the net iron moment. Because of the large rare earth atom spin moment, e.g., $18\mu_B$ per formula unit with terbium, the net garnet magnetic moment is in the direction of the rare earth. However, because of the very small magnitude of n_{cd} the net rare earth moment falls rapidly as temperature increases. Since the interiron lattice effective field coefficients are so large the iron sublattice magnetization stays approximately constant up to about $400^{\circ}K$ and hence the rare earth moment can be

written approximately as

$$M_{RE} = \frac{H_{eff}\, C}{T-T_c}$$

where $H_{eff} = -(n_{cd})(M_{Fe})$ = effective field

C = Curie Constant

T_c = effective Curie temperature of rare earth sublattice, $T_c \approx 0$.

Thus as temperature is raised, the iron moment remains sensibly constant while the terbium moment varies inversely with temperature. At one temperature, approximately 246° K for TbIG, the two sublattice magnetizations are equal and opposite. This temperature is called the compensation point. At this point there is no net magnetization of the material and hence no couple between the spin system and an external field since

$$\bar{M}_{net} \times \bar{H}_{ext} = 0.$$

As a result the coercive field becomes very high at this point. In a rotational switching model the coercivity, given as $H_c = 2K_u/M_{net}$, where K_u is the first order magneto-anisotropy constant, approaches infinity. In actual practice crystal nonuniformities guarantee that a large but finite coercive field exists. Around this compensation point the coercive field is a very sensitive function of sublattice

magnetization.[1,6] For example a change of five per cent in the terbium magnetization can reduce the coercive field by a factor of nearly five.

A memory exploiting this effect would be accessed in the following manner: Assume a single crystal slab of terbium iron garnet is magnetically saturated to a single domain configuration with the iron sublattice moment pointing left and the terbium sublattice pointing right. The temperature of the sample is held constant at the compensation temperature. If a magnetic field directed from left to right is applied to the entire sample no switching will occur if the field strength is less than the coercive field. Assume the applied field has an amplitude of $H_c'/2$ where H_c' is the coercive field at the compensation point. Application of a focused laser beam to a predetermined spot would then, through the optical pumping process described by Forlani and Minnaja, reduce the terbium magnetization. This in turn would uncompensate the net spin system, and hence reduce the coercive field at that spot. As a result there would be a local switching with the net moment pointing from left to right. Removal of the laser beam and magnetic field would then leave a stable reversed magnetic domain with the iron moment right directed and the terbium moment left directed. Such a configuration might be designated as binary "1" while the oppositely directed configuration would be called logical "0".

The sense of a particular spot could be read out using

the Faraday effect: This phenomena is caused by a difference in the refractive index for right hand and left hand circularly polarized radiation. The dispersion associated with a transition is the source of the strong Faraday effect. Dillon[1] has shown that by employing radiation with frequency appropriate to iron atom transitions, the resulting Faraday rotation is due primarily to the iron sublattice alone. This provides a way to monitor the direction of the iron sublattice even when the net magnetization is zero.

The feasibility of such a scheme depends heavily on an understanding of the basic atomic energy level structure of the garnet material. The process of pumping the terbium or other rare earth ions depends on a knowledge of the appropriate transition energy. In addition, the transition probability and excited state lifetime are required. A knowledge of the transitions associated with the iron atoms is desirable to optimize the Faraday effect used to monitor the iron sublattice direction.

Previous Material Research

There has been to date little success in the detailed study of the atomic energy level structure of these materials. The crystallographic structure however has been evaluated in detail[3] and the net magnetic effects experimentally measured.[4,6] The first attempts at explaining the optical spectra was due to Clogston[7] in 1959. In this paper a crystal field theory

model was applied to only the octahedral iron site. The paper attempted to show the source of the optical absorption lines and Faraday rotation observed experimentally by Dillon.[8] At best Clogston could only hope to explain the low level absorption at 16,000 cm^{-1}, i.e., 2 eV observed by Dillon. In fact he noted that, "It is possible that this model is over simplified and that a better theory must consider charge transfer states involving electrons associated with the oxygen ligands."

Dillon's data, was taken by light transmission through thin slabs of garnet cut from single crystals. Because of strong absorption setting in at about 18,000 cm^{-1}, i.e., 2.25 eV, no information could be obtained beyond that energy. Similar data by Bailey[9] taken later for a variety of rare earth iron garnets suffered the same limitation. The first data providing any information at energies above 2.2 eV was reflectivity of YGaG and YIG by Grant in 1967.[10] However, for lack of a technique, such as a Kramers-Kronig analysis, he could report only the location of reflectivity peaks. Hence no concrete information on transition probability could be obtained. Grant did compare his reflectivity peaks with an extended crystal field model calculation of Wood and Remeika[11] involving both octahedral and tetrahedral sites. The correlation was very poor indicating a serious limitation existed with the crystal field model.

The only absorption data available at high energies was reported by MacDonald et al.[12] taken by transmission through a thin film prepared by R.F. sputtering. Only relatively broad structure was detectable in this data. No significant detail could be extracted to determine any fine structure transitions. In addition there was no a´priori reason to believe the film structure would duplicate bulk material characteristics to any great extent.

Scope of Present Research

There has been, therefore, a significant gap in our knowledge concerning the optical properties of these materials. First, absorption data is needed over the entire visible range and should be taken on bulk single crystal samples. Secondly, a theoretical model is needed to explain the resulting optical spectra in terms of fundamental atomic levels. This is particularly important if we are to determine the location of the rare earth transitions amidst the many transitions associated with iron atoms. This information is necessary if any reasonable estimate is to be made of the feasibility of an optically pumped memory. The research undertaken and reported here has been directed to filling in this gap.

To that end a two phase program was undertaken. The first was directed towards fabricating GdIG and TbIG single crystal samples and determining the absorption spectra over the 2 eV to 5 eV energy range. The optical data was obtained

by very detailed reflectivity measurements. From this data the complex index of refraction was obtained and a decomposition of the loss component provided information on oscillator strength and half width of the significant transitions.

The second phase consisted of carrying out a molecular orbital analysis of the iron atom sites. It was found that the linear combination of atomic orbital (LCAO) approach provides a very satisfactory theoretical description of the observed structure. This technique appears to be far superior to the crystal field approach previously used, and promises to facilitate analysis of many other solid state materials in the future.

Finally, the last chapter of this thesis studies the details of an optically pumped memory scheme using the garnets. Feasibility estimates are obtained using the data acquired during the experimental and theoretical phases.

CHAPTER II

OPTICAL ABSORPTION SPECTRA OF GADOLINIUM AND TERBIUM IRON GARNETS

Introduction

Gadolinium and terbium iron garnets were selected for study. With the long range view of an optically pumped memory an initial consideration is the long lifetime associated with the rare earth spin flip 4f electronic transitions. This is desirable if a significant population of excited ions is to be obtained with minimum pumping power. Dieke and Hall[13] have shown that gadolinium and terbium ions displayed by far the longest excited state lifetimes of a number of rare earth ions studied in chlorides and sulphates. They found lifetimes of about 5 m sec for Gd^{3+} and 0.5 m sec for Tb^{3+} while dysprosium for example showed a lifetime of less than 10 μ sec. In addition the compensation temperatures of GdIG and TbIG are the closest of all REIG to room temperature. This again is a desirable characteristic for practical memory system considerations.

The overall goal of this phase of the research was to obtain data on the energy and transition probability of all significant electronic transitions from 2 eV to 5 eV of the bulk garnet materials. Because of the high absorption

coefficient over most of the visible energy range, reflectivity techniques were therefore indicated. Recent work by Hunter[14] had shown that the technique of double angle reflectivity measurements could provide accurate calculations of the complex index of refraction. The desired energies and transition probabilities can be obtained directly from the complex index. Hence this general approach was chosen. The following sections outline the theory of the computation techniques, the experimental apparatus and measurements, and the computed results leading to the overall absorption spectra.

Theory of Reflectivity Technique

Reflectivity at an air-material interface is a function of the real and imaginary components of the refractive index, $N = n - jk$, the polarization, and the angle of incidence. It is described analytically by the well known Fresnel equations. For radiation polarized in the plane of incidence Fresnel's equation is

$$R_p = R_s \cdot [(a-\sin\theta\tan\theta)^2+b^2]/[(a+\sin\theta\tan\theta)^2+b^2] \qquad (1)$$

where θ = angle of incidence

$$R_s = [(a-\cos\theta)^2+b^2]/[(a+\cos\theta)^2+b^2]$$

$$a = 1/2\{[(n^2-k^2-\sin^2\theta)^2+4n^2k^2]^{1/2}+(n^2-k^2-\sin^2\theta)\}$$

$$b = 1/2\{[(n^2-k^2-\sin^2\theta)^2+4n^2k^2]^{1/2}-(n^2-k^2-\sin^2\theta)\}.$$

By using light linearly polarized in the plane of incidence and measuring reflectivity at two different angles of incidence, sufficient information is provided to uniquely determine n and k. The transcendental nature of the equations, however, prevents a closed form solution. To overcome this problem a modification of a computer algorithm proposed by Hunter[14] has been used.

Given initially assumed values of n and k the computer solves the Fresnel equations at the two angles of incidence used in the experiment and computes and error between the calculated and actually measured reflectivities. The error expression used is

$$E = [(R_m(\theta_1)-R_c(\theta_1))/R_m(\theta_1)]^2+[(R_m(\theta_2)-R_c(\theta_2))/R_m(\theta_2)]^2 \quad (2)$$

where $R_m(\theta)$ is the measured reflectivity and $R_c(\theta)$ is the computed reflectivity at the same angle for the assumed n and k. A systematic search over the n-k plane is then carried out to find the point resulting in minimum error E. The reported results were obtained with an increment of n and k of 0.002. This technique overcomes many of the problems associated with carrying out a Kramers-Kronig integral analysis. The actual ALGOL program carrying out this algorithm is given in Appendix A.

From the values of n and k, several other parameters describing the interaction of light and atomic structure can

be computed. For example the complex dielectric constant $\varepsilon = \varepsilon_1 - j\varepsilon_2$ is given as

$$\begin{aligned} \varepsilon_1 &= n^2 - k^2 \\ \varepsilon_2 &= 2\,nk. \end{aligned} \tag{3}$$

The loss term ε_2 is often written in terms of the conductivity σ of the material as $\varepsilon_2 = \sigma/\omega$ so one can also compute the optical conductivity as

$$\sigma = 2\,\omega nk. \tag{4}$$

In the work carried out here, however, the absorption constant K has been used to describe the strength of a given transition. K is defined by the equation

$$I(x) = I_o\, e^{-Kx} \tag{5}$$

where I is the radiation intensity in ergs/(sec·cm^2) at some point x from the surface of the material and I_o is the intensity at the air-material interface. The variable x is zero at the interface and is positive along the direction of propagation. The units of K are cm^{-1} and it can be shown to be given in terms of k as[15]

$$K = \frac{2\omega k}{c} = \frac{4\pi k}{\lambda}\ . \tag{6}$$

Here ω is the radian frequency associated with the transition energy, i.e., $E_2 - E_1 = \hbar\omega$, and c is velocity of light in free space.

The absorption coefficient may be related to the rate of atomic transitions as follows. Consider the case of a single transition line. From the definition of K in equation (5) we see

$$\frac{dI}{dx} = -KI \quad \text{or} \quad K = -\frac{1}{I}\frac{dI}{dx} . \tag{7}$$

But $-\frac{dI}{dx}$ is simply the energy lost per second per cm^3 of material. Thus if w is the number of atomic transitions per sec per cm^3, each of energy $\hbar\omega$, we can write

$$-\frac{dI}{dx} = \hbar\omega w$$

and

$$K = \frac{\hbar\omega w}{I} . \tag{8}$$

Hence a measurement of the absorption coefficient allows us to calculate directly the transition rate to excited states for a given input intensity.

In the data to be presented, the absorption spectrum over a wide energy range is given. At any energy the total absorption is due to the combined effect of several individual transition energies. In order to determine the characteristics of the individual lines the overall spectrum is approximated by a series of Lorentzian shaped lines. The series employed for this fitting is

$$K(E) = K_o + \sum_i \frac{K_i}{(E-E_i)^2 + (\Gamma_i/2)^2} \qquad (9)$$

Here K_o is a constant absorption level chosen arbitrarily as a base absorption on which the variations appear. E_i is the energy around which the individual line is centered and Γ_i is the line half width. The process used to actually determine the coefficients of equation (9) was one of trial and error. A computer program was written which computed K(E) for any given set of K_o, K_i's, E_i's, and Γ_i's. The values of the E_i's were chosen initially to agree with the peaks of the absorption spectra which were in turn computed from the index of refraction. The resulting output plot of K(E) was then compared with the actual experimental characteristic, and coefficients were manually adjusted until the two curves agreed to within less than three per cent over the entire energy range. There is of course no guarantee of a unique solution of eq. (9). However, from a practical point of view one can place reasonable confidence in the general results obtained because the

absorption spectra has a great deal of detailed structure on which to base the assumed coefficient values.

A final parameter which provides valuable insight into the nature of an optical transition is the oscillator strength. The concept of oscillator strength is based on the relationship between optical polarizability as derived quantum mechanically and classically.

It can be shown[16] that the polarizability associated with a single ground state i and a range of excited states j is given quantum mechanically as

$$\alpha_i = \frac{e^2}{m} \sum_j \frac{f_{ij}}{(\omega_{ij}^2 - \omega^2)} \tag{10}$$

where

$$f_{ij} = \frac{2\omega_{ij}\, m |M_{ij}|^2}{he^2} \tag{11}$$

Here the energy difference between states is $\hbar\omega_{ij}$ and $|M_{ij}|$ is the dipole moment matrix element

$$|M_{ij}| = \int \phi_i^* \, \bar{r} \, \phi_j \, d\tau.$$

The quantity f_{ij} is called the oscillator strength and has the physical significance that if only a single excited state is considered, then a value of f = 1 results in equation (10) being identical to the expression for the polarizability of a classical harmonic oscillator.

The oscillator strength can be related to the absorption coefficient because the transition rate w is also directly related to the dipole moment matrix element. This relationship is derived in Appendix B under the assumption of a single ground state, monochromatic radiation and a density of excited states N(E) states/erg cm^3. The result is that the transition rate to the excited density of states at E_j is

$$w = \frac{4\pi^2}{c\hbar} I N(E_j) \quad |M_{ij}|^2 . \tag{12}$$

Now assume we consider the oscillator strength associated with transitions between the ground state and excited states between E_j and $E_j + dE$. If there are N atoms/cm^3 and each atom contributes one excited state over this range, the density of excited states is

$$N(E_j) = N/dE.$$

Then combining equations (11) and (12) gives

$$f_{ij} = \frac{2\ \omega_{ij} m}{\hbar e^2} \cdot \frac{c\hbar w}{4\pi^2\ I\ N}\, dE = \frac{1}{2\hbar} \frac{mc}{\pi^2 e^2} \frac{E_{ij} w}{I\ N}\, dE \tag{13}$$

Combining equation (13) with the definition of w in terms of the absorption coefficient K, eq. (8), gives

$$f_{ij} = \frac{mc}{\hbar \pi e^2} \frac{K(E_j)}{N} dE \ . \qquad (14)$$

Integrating over the entire excited density of states results in a definition for line oxcillator strength in terms of absorption coefficient:

$$f = \frac{mc}{N\hbar \pi e^2} \int K(E)\, dE \ . \qquad (15)$$

To the first order this may be approximated, assuming the absorption coefficient constant over the half width and zero elsewhere, as

$$f_j = \frac{mc}{N\hbar \pi e^2} K(E_j)\ \Delta E_j = \frac{4\ mc}{N\hbar \pi e^2} \frac{K_j}{\Gamma_j} \qquad (16)$$

where $K(E_j) = K_j/(\Gamma_j/2)^2$ and $\Delta E_j = \Gamma_j$ as defined from equation (9).

Experimental Apparatus

Crystal Growing

The samples of TbIG and GdIG were grown by the molten flux method described by Nielson.[17] This technique uses a combination of PbF_2 and PbO as solvents for the rare earth and iron oxides. The desired crystals are formed as a molten solution at about 1200°C is slowly cooled through a range of crystallization temperatures. Growth of good crystals dictates a cooling rate of between 1/2 to 2°C per hour from

1200°C to about 850°C. Very accurate temperature control with long term stability is therefore required.

A vertical tube furnace was designed which is capable of ultimate temperatures of 1300°C. The heating element with its associated alumina and fittings can be purchased as a complete set from Kenthal Corporation. The unit used in this furnace is Kenthal Type No. REH-7-30 rated at 1350 watts. Figure 1 shows a cross sectional drawing of the unit and Figure 2 is a photograph of the complete oven and power supply. During operation it was found that gases which evolved from the molten flux reacted with the Kenthal heating element causing failure after about 800 hours. To overcome this problem it is necessary to insert a protective alumina tube inside the heater. The oven requires 24 volts at approximately 60 amps. A silicon controlled rectifier power controller feeds power to the oven through a 115 volt to 24 volt step down transformer. The circuit diagram is shown in Figure 3. The SCR network is a zero cross-over firing network providing one complete cycle of power each time a logic signal is received. Using this approach there is no large dI/dt during turn on and hence a minimum of R.F.I. Large transients can cause serious interference with the logic of the controller and therefore are to be avoided.

The temperature controller and rate generator are designed to provide a uniform temperature rate with respect to time of 0.5°C/hour. The sensitivity of the circuit provides

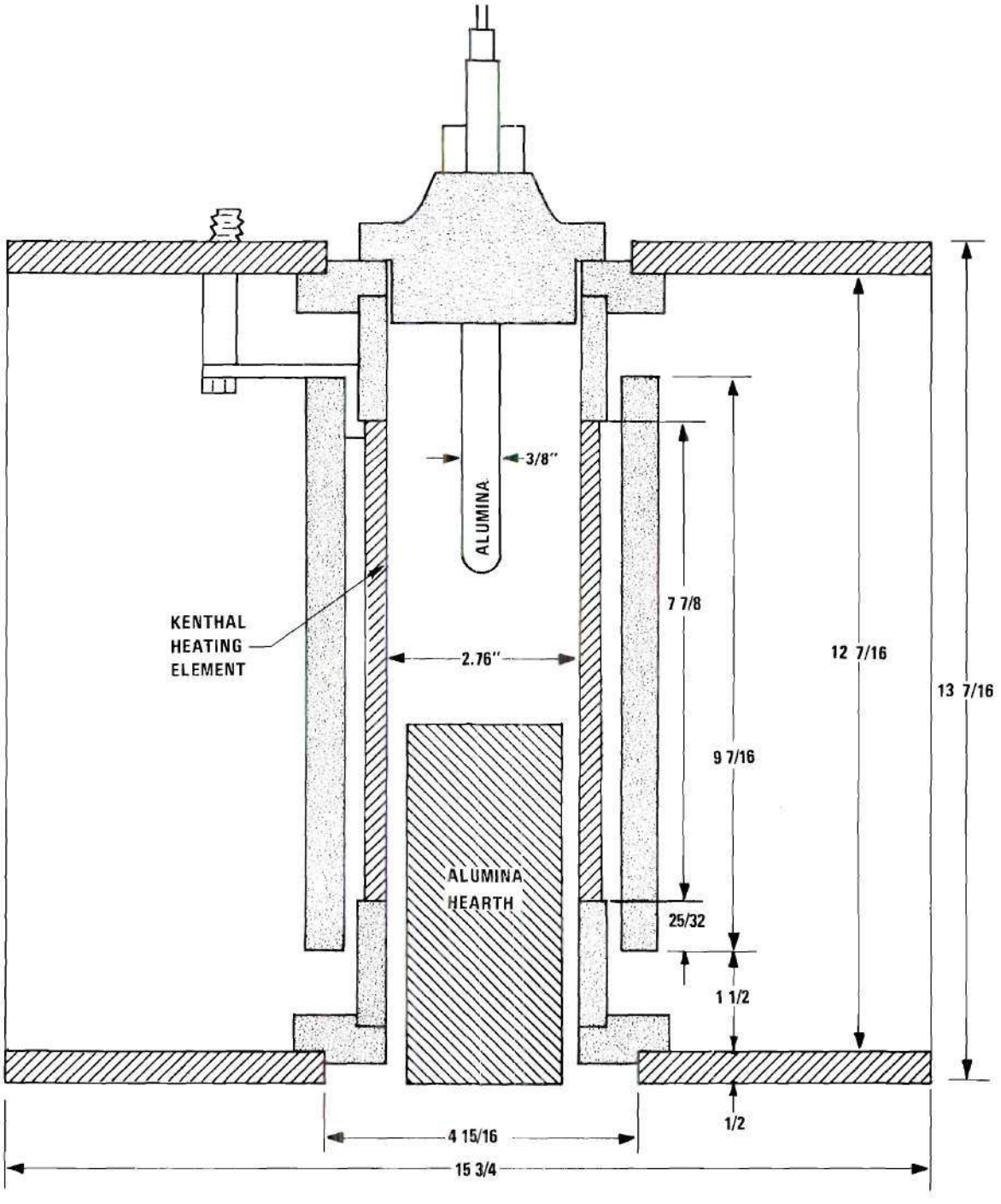

Figure 1. Cross Sectional View of Crystal Growing Furnace

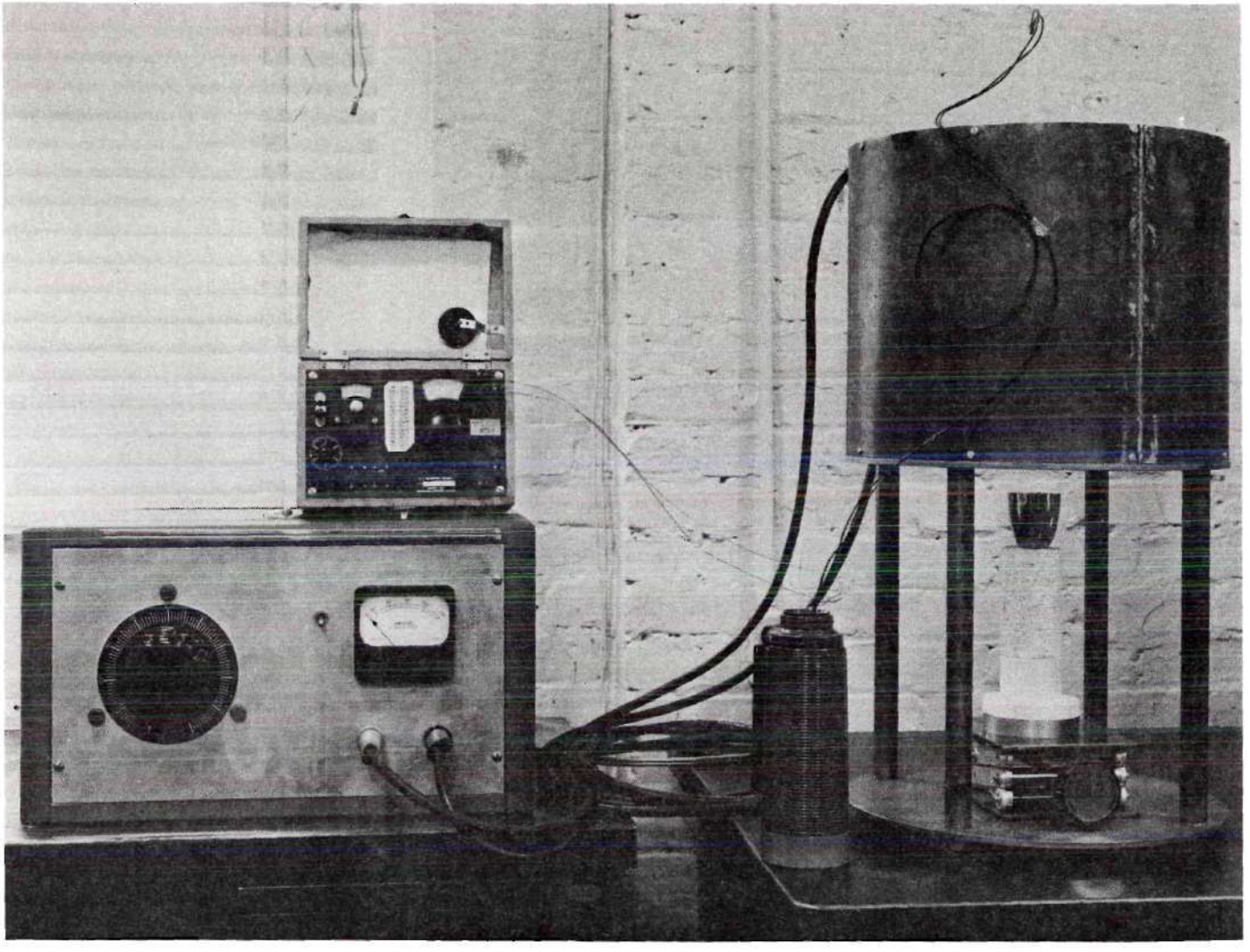

Figure 2. Photograph of Complete Furnace and Power Supply

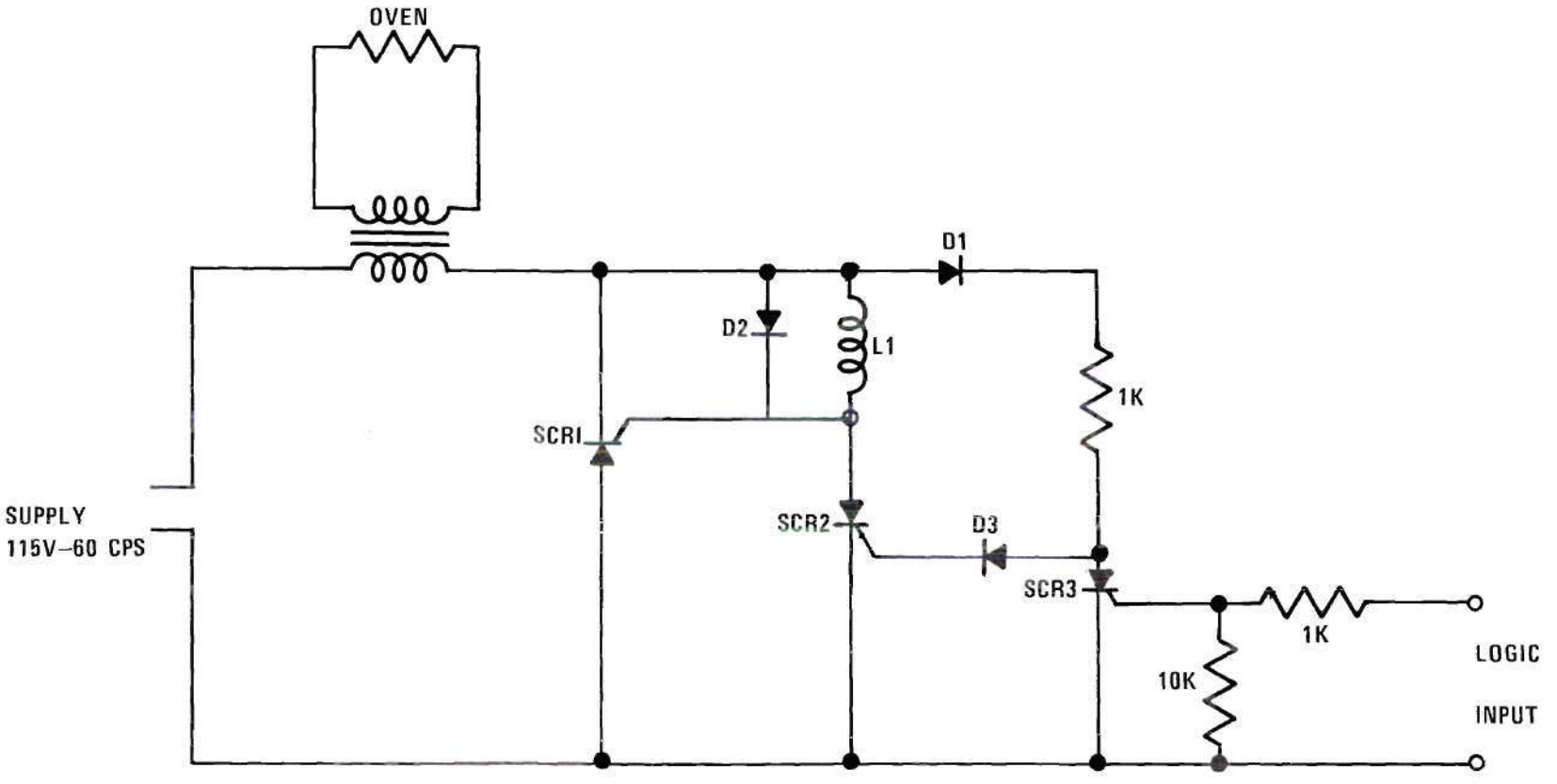

Figure 3. Silicon Controlled Rectifier Power Switch

for a temperature swing of no more than ± 0.2°C around the programmed temperature profile. A circuit diagram of the controller is shown in Figure 4.

Reflectivity Apparatus

It was desired to be able to make accurate reflectivity measurements over the range from 2 eV to 5 eV. Measurements were made on polished natural crystal faces at room temperature. In order to obtain sufficient illumination at high energies a high pressure mercury arc lamp was mounted in a specially designed air-cooled assembly. Design of the optical system itself required a great deal of care to assure accurate and repeatable angles of incidence and reflectance. Control over these angles as well as the convergence angle of incident light is necessary if accuracy is to be obtained from the double angle analysis technique.

A diagram of the reflectivity apparatus is shown in Figure 5. The light source, a high pressure type B-H6 air-cooled mercury vapor lamp, is focused on the monochrometer entrance slit with a metallic spherical mirror. Slit height is restricted to approximately 0.5 mm to reduce the solid angle subtended by illumination at the crystal surface. The monochrometer is a standard quartz prism instrument. Exit slit width was maintained at 0.3 mm yielding an effective bandwidth of 0.04 to 0.12 eV over the range of the measurements. A quartz lens images the exit slit on the sample and is apertured so that the included angle of the light incident

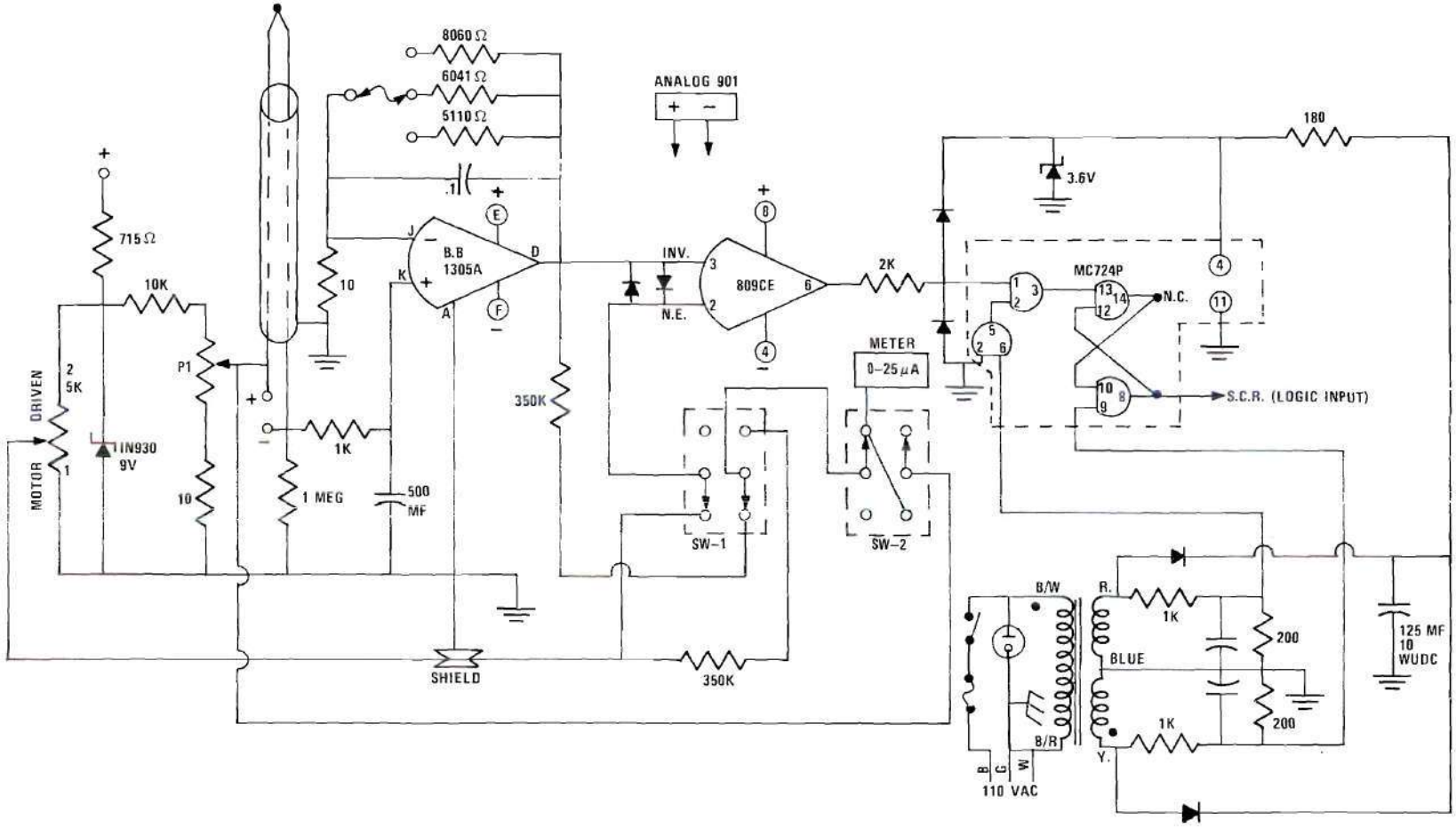

Figure 4. Circuit Diagram of Programmed Temperature Controller

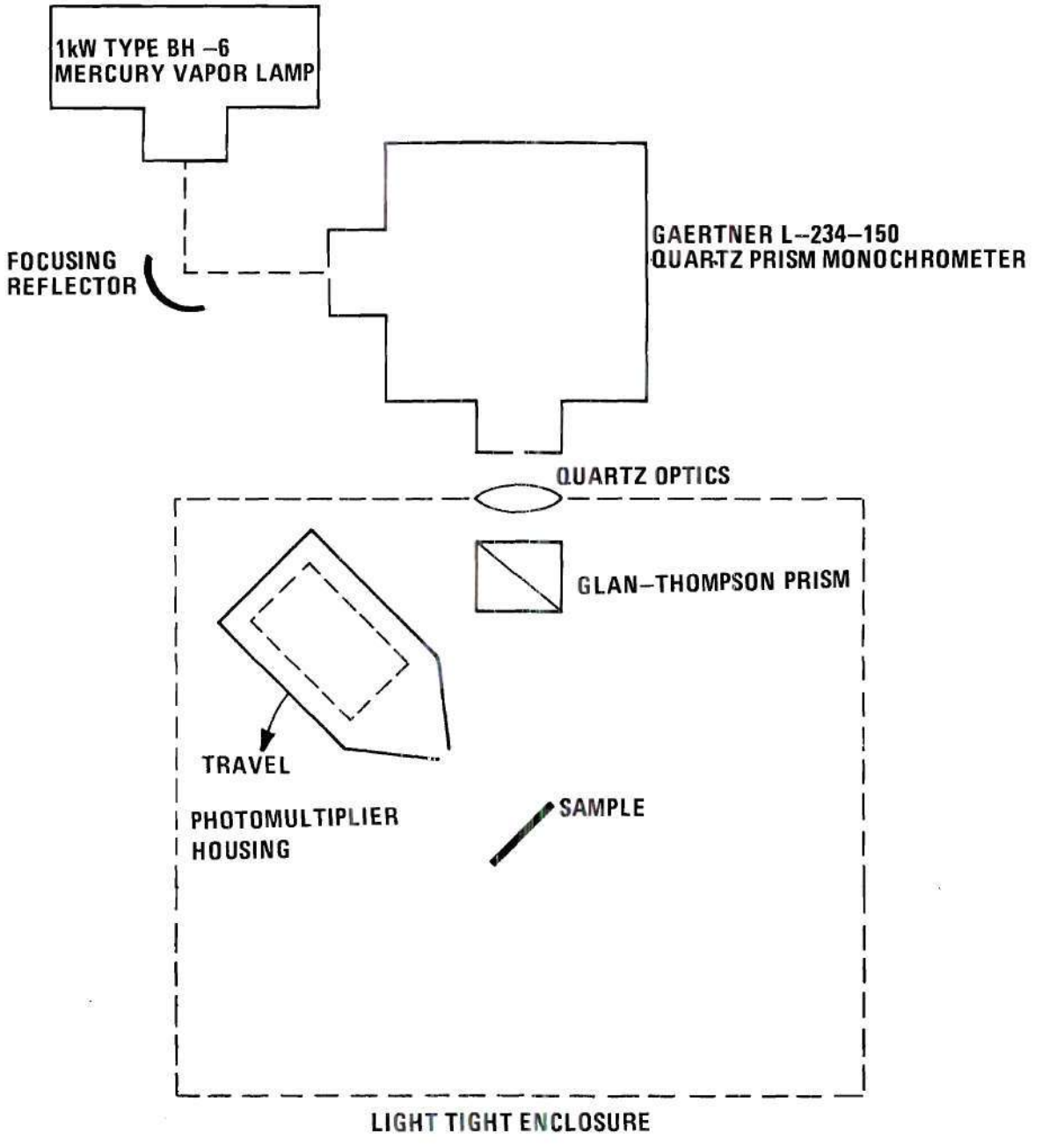

Figure 5. Reflectivity Apparatus

on the crystal surface is less than 1°. As mentioned before, this angle must be kept small as the analysis of the reflectivity data is sensitive to variations in angle of incidence at the sample. A Glan-Thompson prism is used to polarize the light parallel to the plane of incidence.

The photomultiplier tube and sample are mounted on concentric vertical shafts which allow independent angular positioning around a common center. A series of accurately machined indexing stops permits reliable angular settings. In addition, the sample may be lowered completely out of the beam for measurement of incident intensity. The EMI 960B photomultiplier is rotated around its longitudinal axis to a position where its gain is insensitive to variations in the earth's magnetic field which it experiences as the assembly is rotated in a horizontal plane during the measurement process. This tube has a special blown envelope window which permits measurements to at least 5.5 eV without the need of conversion phosphors.

The crystal sample itself is mounted on a special holder which permits accurate "forward-backward" motion as well as complete angular pitch adjustment. Accurate measurements require the sample to be located very precisely on its rotation axis so the beam position does not change with angle of incidence.

In order for the reflectivity measurements and resulting computed optical constants to be meaningful it is

necessary to assure that the errors in the data and reduction technique are negligible. To this end the potential sources of error have been evaluated in some detail and their cumulative effect on the observed absorption spectra estimated.

The basic measurements, the reflectivities, were especially subject to uncertainties when the reflectivity was low; and it was low (typically 0.01) for all measurements at 70 degree angle of incidence. Imperfections on the crystal surface scatter the incident radiation and the fraction of this entering the photomultiplier add to that truly reflected from the extended crystal surface. The scattered light becomes a smaller fraction of the reflected light at shorter wavelengths where the reflectivity at 70° is greater. For incidence angle of 20 degrees this scattered radiation added negligibly to the measured reflection.

This scattered radiation should not change rapidly with the direction of observation. It was estimated by making measurements of the angular distribution of reflected intensity in the vicinity of the angle of specular reflection. A narrow slit was used over the photomultiplier to obtain this data. Based on the amplitude of the intensity in the wings of this distribution a spatial filter was designed in front of the photomultiplier to assure that scattered radiation accounted for no more than five parts per hundred of the total observed intensity.

The measured reflectivity depended on the quotient of two measured intensities, both measured with the same photomultiplier tube, and associated circuits. The photomultiplier whose axis was horizontal, was rotated about a vertical axis to successively measure the direct beam intensity, the reflected beam intensity for 70° incidence and the reflected beam intensity for 20° incidence. The gain of the photomultiplier is sensitive to the direction of the earth's magnetic field through the tube. For the rotation about a vertical axis just described it was found that the gain could vary up to 0.04 of its magnitude. However, this change varied for different orientations of the tube about its horizontal axis. By trial and error a position was found for which the variation in gain for the positions at which measurements were made was approximately 0.005. This small systematic error is negligible in comparison with those introduced by fluctuations in the light source and impurity scattering.

The high pressure mercury arc fluctuated in intensity over time intervals of the order of a second. Fluctuations sometimes amounted to 0.1 of the average reading. This was true at all wavelengths through the monochrometer. Direct and reflected beam intensities were measured by observing the photomultiplier current with an electrometer (Kiethley 600 A) over several seconds and the average needle position was estimated by the observer. Typically, three readings at each of the three angles were made and averaged. A particular

observation was repeated only after observation of the other two angles had been measured. This would bring in any drift of period larger than the fluctuations. Usually there was no drift and a typical fractional standard deviation of several observations had a value of about 0.01.

The electrometer specifications indicate that the measured current should be within 0.03 of the indicated current. Consistency of readings when the scale was switched suggest that the relative consistency may be better than this, possibly as good as 0.01.

The dark current of the photomultiplier was subtracted from each reading. Usually this correction was a small fraction of the reading itself and should not have contributed significantly to the uncertainty of the reading of relative intensity. At short wavelengths (four electron volts and more) and for 70 degree reflection the dark current was an appreciable fraction (up to about one third) of the total current. In these cases fluctuations in the dark current and the consequent uncertainty in selecting an average value increased the uncertainty of the relative intensity measurement by a small amount.

These uncertainties in reflectivity measurements are summarized in Table 1. They amount to a net total uncertainty in the measured reflectivity of about two per cent.

The effects of these uncertainties on the absorption constant computed through the Fresnel equations has been

Table 1. Summary of Uncertainties in Reflectivity at a Given Angle

	Source of Uncertainty	Estimated Fractional Magnitude
Systematic	Photomultiplier Orientation	±.005
	Relative Calibration of Electrometer	±.01
	Scattering Off Crystal Imperfections	0-.05
Random	Fluctuations of Light Intensity, Direct Beam	±.01
	Fluctuations of Light Intensity, Reflected Beam	±.01
Resulting Uncertainty in Intensity of Direct Beam		±.015
Resulting Uncertainty in Intensity of Reflected Beam (not including scattering)		±.015
Resulting Uncertainty in Reflectivity (not including scattering and effect of angular spread)		±.022
Resulting Uncertainty in Absorptivity		±.004
Resulting Uncertainty in Absorptivity due to Scattering		0-.01
Resulting Uncertainty in Absorptivity due to Beam Spread		.05 (from Hunter's plots)
Resulting Uncertainty in absorptivity due to Imperfect Polarization		negligible

estimated from the examination of the equations presented by Hunter[14] as well as sensitivity calculations using the reflectivity program, Appendix A. From these evaluations it was found that the complex index of refraction of the garnets falls in a region where the absorptivity is not extremely sensitive to uncertainties in the observed reflectivities. The region is that around n = 2 (real part of index), k = .25-1.0 (imaginary part of index). Figure 8 of Hunter's paper indicates that this should be theoretically true. From the sensitivity studies of the computer program the ratios of change in K to the change in reflectivity were determined to be

$$\frac{\Delta K}{\Delta R_{20°}} \sim .07$$

and

$$\frac{\Delta K}{\Delta R_{70°}} \sim .18$$

This would indicate that the absorptivities computed should be correct within one part in a hundred.

The wavelength at the center of the monochrometer slit was correct to 10 or 20 Å, as close as could be read on the scale. This was indicated by a calibration with a low pressure mercury source.

The aperture was chosen to keep the beam divergence within one degree each side of the specified direction and

one degree each side of the plane of incidence. A detailed experimental analysis of the effect of this angular convergence was not carried out but Hunter's computations (his Figure 7) indicate the effect is small.

The intensity of the incident beam was controlled by a pair of Glan-Thompson prisms (not shown in Figure 5) which were set to deliver plane polarization approximately at 45° to the slit of the monochrometer.

Another Glan-Thompson prism (the one shown in Figure 5) selected the component in the plane of incidence at the crystal. This prism was adjusted to give minimum reflected signal at 70°. This adjustment was very sensitive and it is felt that the setting was certainly within one half degree of the true minimum. One half degree would give about 0.01 for the amplitude of the wrong polarization. This amount of improper polarization would produce no effect on the reflectivity at 70° or any other angle, and hence would not cause uncertainty in K.

The uncertainties in K are also included in Table 1, the overall result being that a very high degree of confidence may be placed in the data and resulting optical parameters.

Experimental Results

Figure 6 shows plots of measured reflectivity as a function of energy for samples of GdIG and TbIG. The measurements were made on mechanically polished faces of the grown

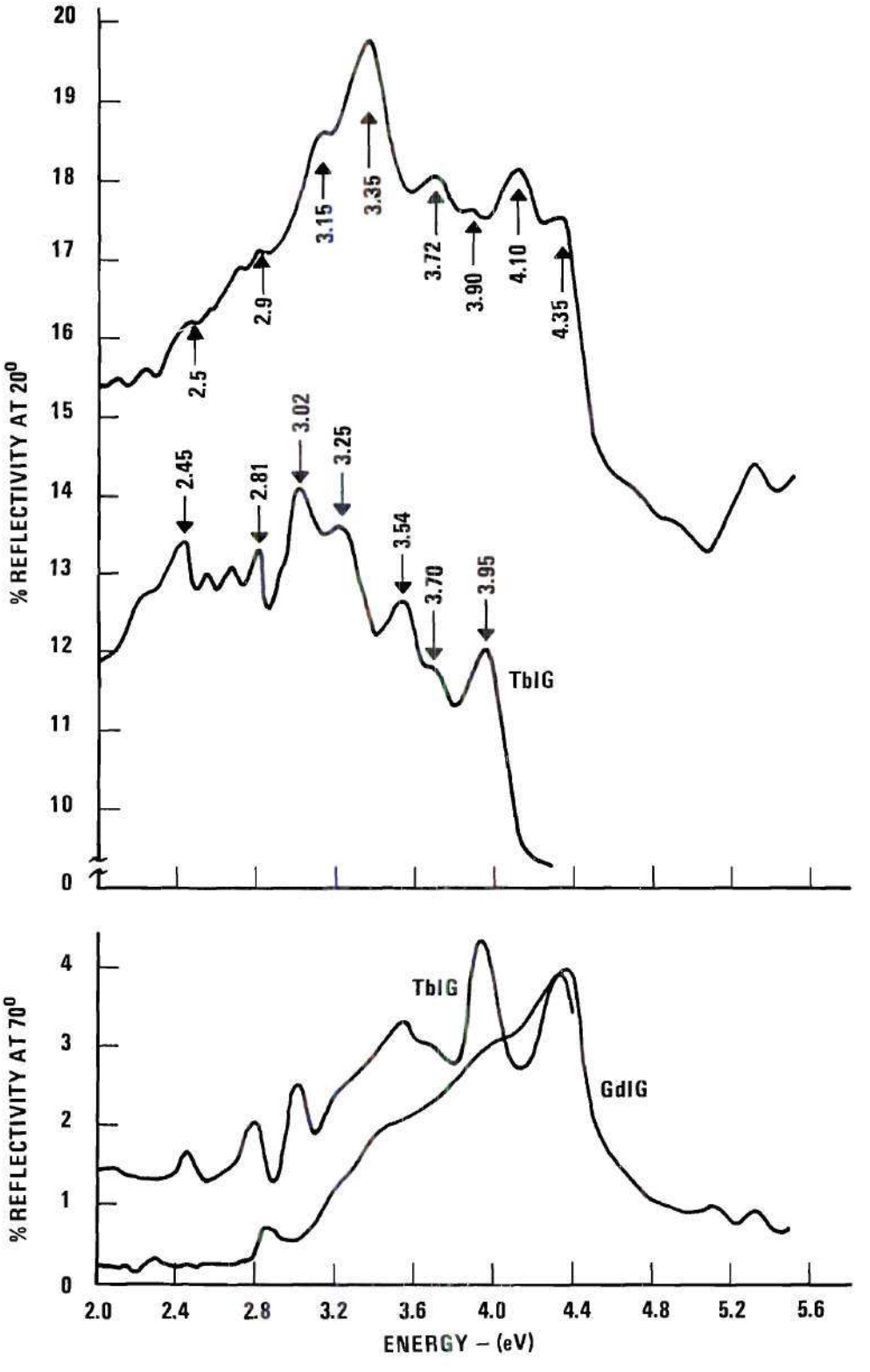

Figure 6. Plots of Measured Reflectivity

crystals. X-ray diffraction was used to select (111) planes. These planes are perpendicular to the magnetic easy axis in the rare earth iron garnets.

It is interesting to note the similarity of the fine structure in the GdIG data above 3 eV with that obtained by Grant[10] for YIG. Our data shows reflectivity peaks at 3.15, 3.35, 3.72, 3.90, 4.10, and 4.35 eV. Grant reports peaks in YIG at 3.14, 3.35, 3.74, 4.04, and 4.35 eV. One would therefore tend to conclude that most of these lines probably are transitions associated with the iron sites since these are common to both YIG and GdIG. Note however that the 3.9 eV line does not correlate with the YIG data and might well be associated with the first excited state transition for gadolinium which occurs at 3.85 eV in gadolinium chloride. It will be shown in Chapter IV that this agrees with the theoretical LCAO calculations. The strong peak at 4.35 eV is probably a charge transfer transition, masking the second gadolinium transition which should appear somewhere around 4.32 eV.

There is reasonable but not exact correlation with the "charge transfer" lines in the TbIG data. Here the prominent peaks above 3 eV are at 3.02, 3.23, 3.54, 3.70, 3.95, and 4.35 eV. These appear in general to be about 0.1 to 0.15 eV lower in energy than for the GdIG; however, the relative spacing and amplitudes seem to indicate they are probably due to the same transitions.

Note however that below 3 eV the terbium data contains some rather prominent structure which is not duplicated in the GdIG. This extra structure might be anticipated in TbIG if the rare earth electronic transitions are observable, for it is known that terbium has a number of excited states in the visible range while Gd does not. Of particular interest is the line at 2.45 eV. It is known from data on hydrated terbium chloride[13] that there is a terbium absorption line at about 20,600 cm^{-1}, i.e., 2.54 eV and Keller and Pettit[18] have observed this transition in fluorescence in terbium doped YGG. The 0.1 eV difference in this sample is consistent with the other data and thus leads to the possibility that the line could be due at least in part to terbium absorption.

Figures 7 and 8 show plots of the real and imaginary components of the refractive index, n and k, for GdIG and TbIG. In general they reflect the structure apparent in the reflectivity data. Comparing k in Figures 7 and 8, we see that TbIG exhibits a broader spectrum in the 3.2 eV to 3.6 eV range and much more pronounced lines at 3.9 eV and 4.1 eV. This effect might be associated with Tb ion transitions and would be consistent with the Tb^{3+} ion spectra reported by Dieke and Hall.[13] Their line data has been included in Figure 8 for reference.

Figure 9 shows the absorption coefficient for GdIG computed from the values of k from Figure 7 using the computer program of Appendix A. The graph shows an apparent

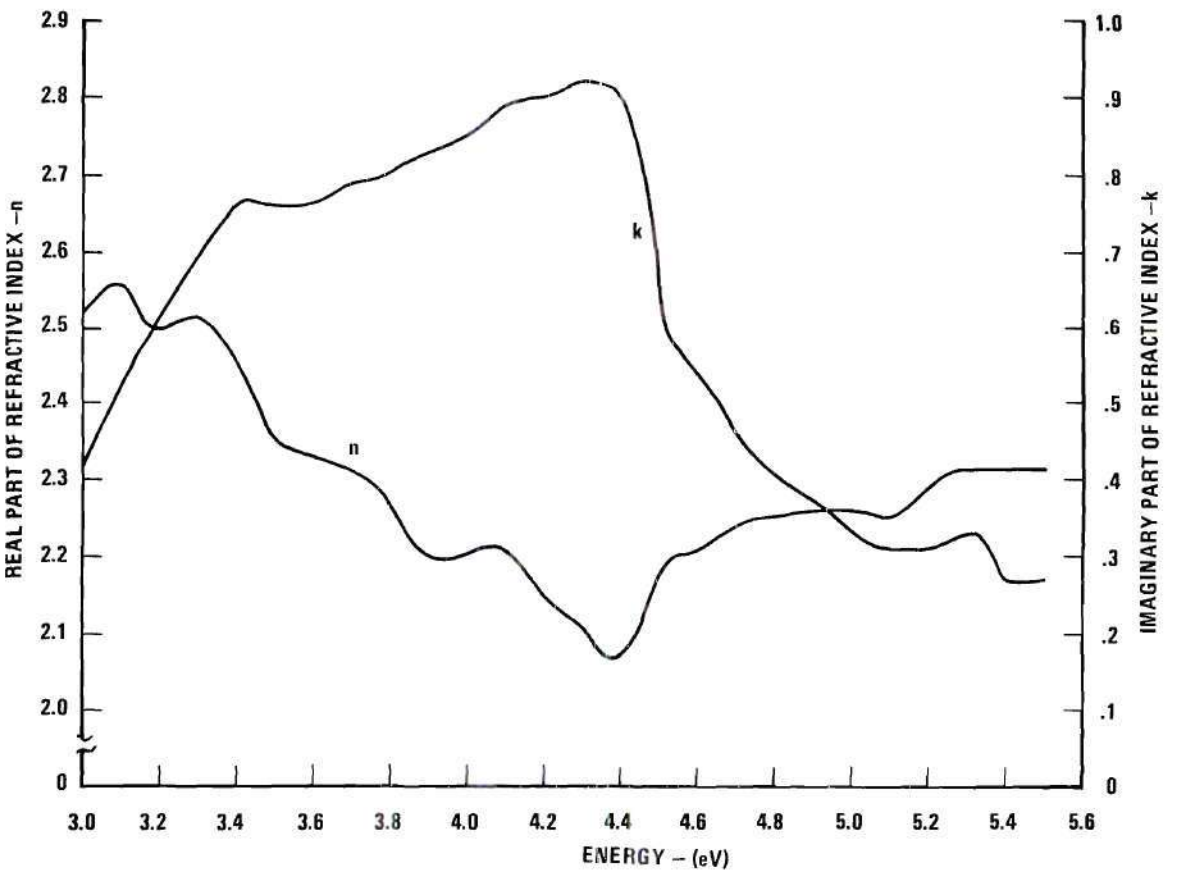

Figure 7. Calculated Components of Refractive Index N=n-jk of GdIG

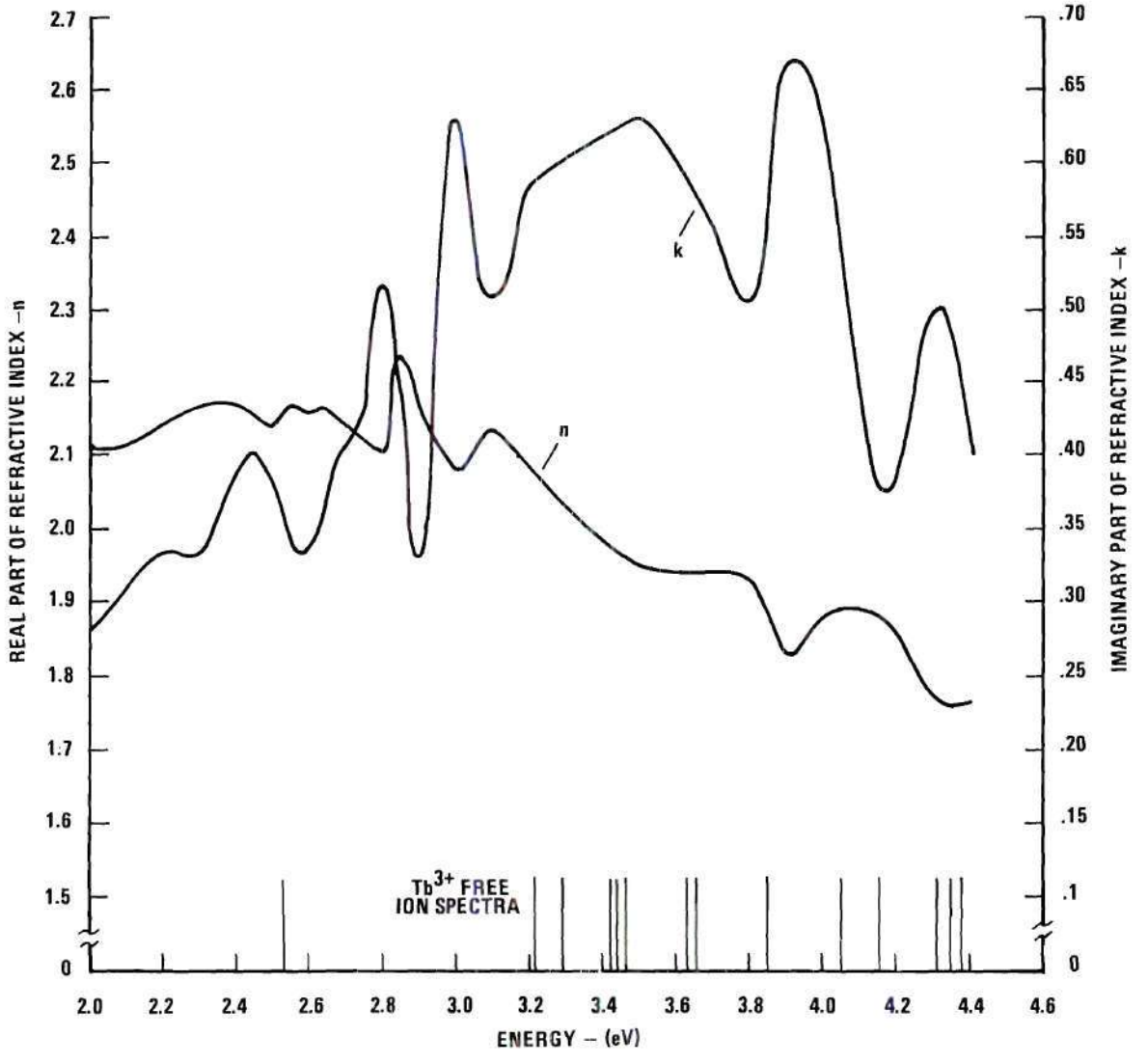

Figure 8. Calculated Components of Refractive Index N=n-jk of TbIG

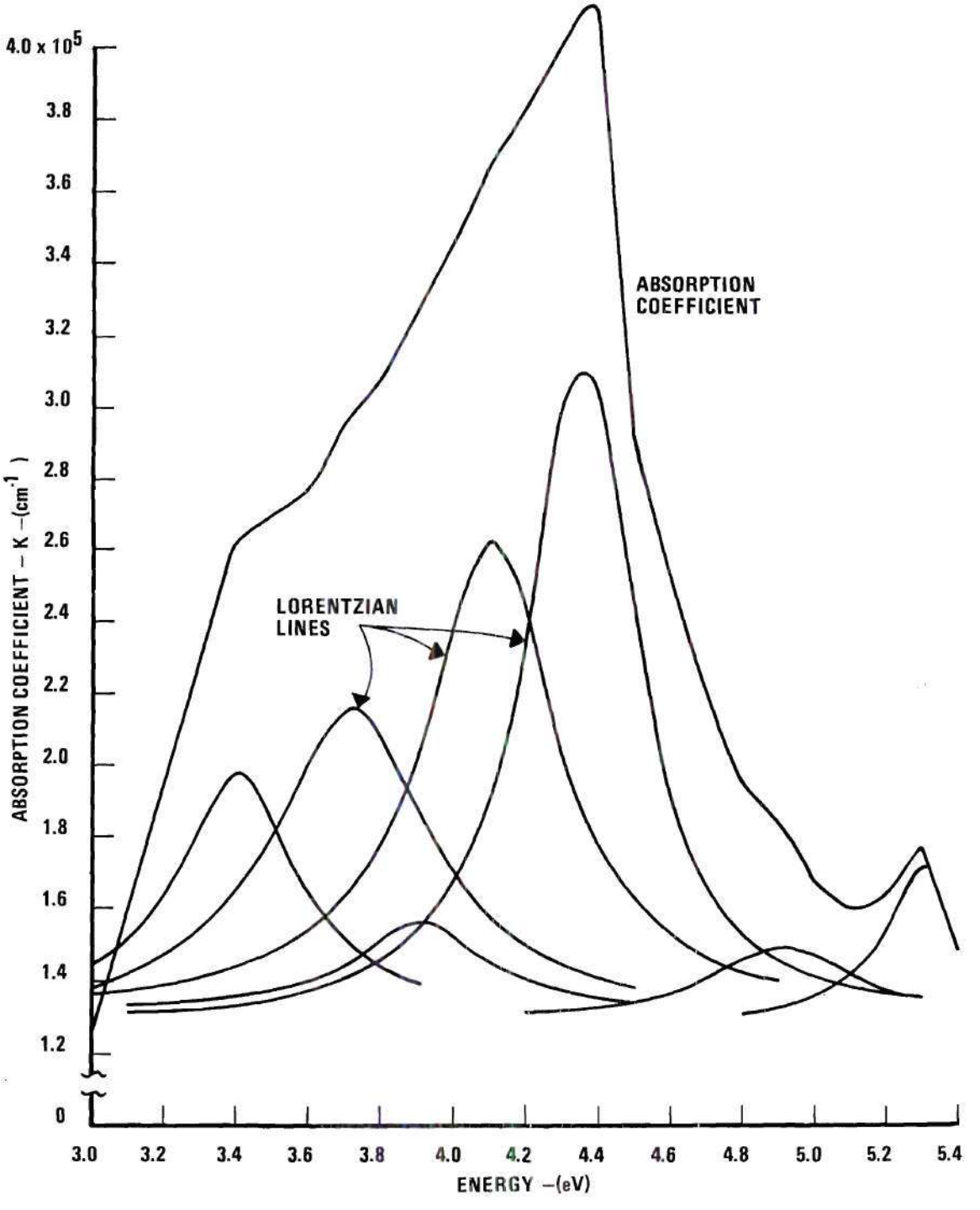

Figure 9. Absorption Spectrum for GdIG Single Crystal

base in the absorption constant at about 1 x 10^5 to 2 x 10^5 cm^{-1} with some additive fine structure between 3 and 5 eV. MacDonald et al.[12] have measured an absorption coefficient of about 3 x $10^5 cm^{-1}$ on 0.1μ thick films, their data also showing a relatively constant absorption in this energy range. The agreement is therefore considered to be satisfactory. By assuming a constant absorption of 1.3 x 10^5 cm^{-1} over the energy range between 3 eV and 5 eV the GdIG fine structure has been approximated with a series of Lorentzian shaped lines according to equation (9). These individual lines are also shown in Figure 9. Error between the series approximation and actual absorption curve is less than three per cent except at the lower energy end.

In general, the half widths of the individual lines appear to be around 0.4 eV or 0.5 eV. Peak values of K are between 0.2 x 10^5 cm^{-1} and 3 x $10^5 cm^{-1}$. Table 2 gives the coefficient for the Lorentzian series according to equation (9), and corresponding oscillator strengths from equation (16). Oscillator strengths of this size ($.01 \leq f \leq .08$) are typical of strong electric dipole type transitons. If the 3.9 eV line is in fact a forbidden Gd^{3+} transition, it must be materially strengthened by the allowed lines in close energy proximity. Such effects have been experimentally verified in other materials.[10]

Figure 10 shows similar type data as Figure 9 except for TbIG. The lines of the Lorentzian series used to fit

Table 2. Lorentz Series Coefficients for GdIG Absorption

Line Energy (eV)	3.40	3.72	3.90	4.10	4.35	4.90	5.30
$K_i \times 10^2 (cm^{-1}eV^2)$	2.70	6.00	1.50	7.00	5.40	1.00	0.60
Γ_i (eV)	0.40	0.53	0.48	0.46	0.34	0.46	0.24
$f_i \times 10^2$	4.10	6.60	1.60	8.30	8.00	1.20	1.40

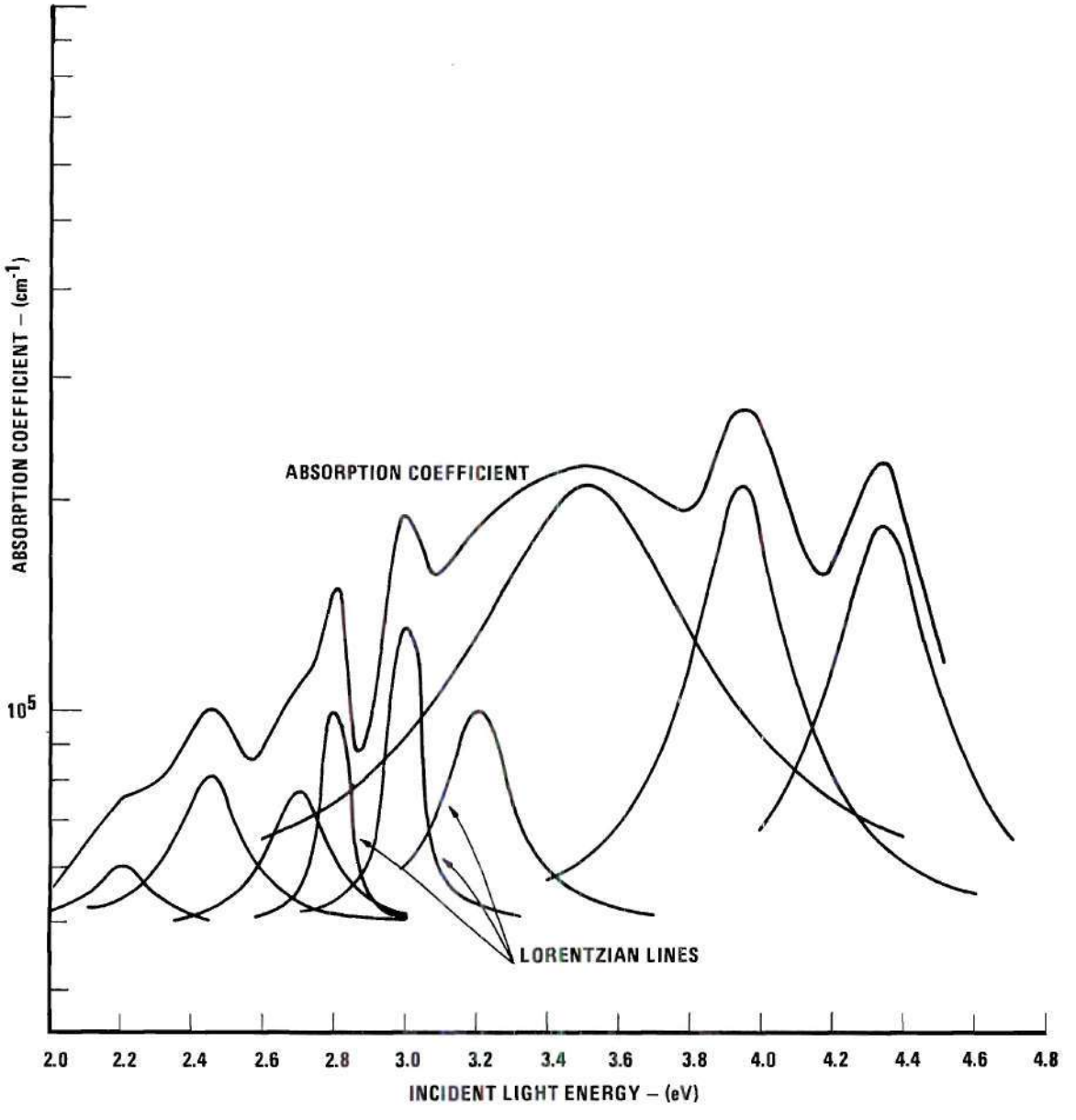

Figure 10. Absorption Spectrum for TbIG Single Crystal

the absorption coefficient curve are also shown. The large wide line used at 3.5 eV may result from the combined effect of the collection of Tb^{3+} lines in that vicinity, broadened by exchange coupling. Table 3 lists the appropriate coefficients for the lines of the TbIG fine structure. The TbIG spectra contains lines which appear stronger and narrower than in GdIG. The total absorption coefficient above 3 eV is nearly the same as GdIG; however, a constant base line for the structure somewhat lower than in the GdIG calculations has been assumed. A base absorption which increases from 0.5×10^5 cm^{-1} at 2 eV to about 1.0×10^5 cm^{-1} at 3 eV and remains constant at that value to higher energies leads to oscillator strengths of the TbIG lines which fall into the same range as the GdIG spectra.

Summary of Optical Spectra

These measurements, with the resulting analysis, provide the first complete absorption and index of refraction data on bulk rare earth iron garnets. The location and oscillator strengths and half widths of individual measurements have been estimated. These data are necessary for nearly any estimates of optical effects when the garnets are considered for practical device applications.

We are interested, from a pumped memory point of view, as to the possibility of some of the observed lines being due to rare earth ion transitions. Little can be said about this without some way of separating out the iron atom lines.

Table 3. Lorentz Series Coefficients for TbIG Absorption

Line Energy (eV)	2.20	2.45	2.73	2.80	3.02	3.25	3.54	3.95	4.34
$K_i \times 10^2 (cm^{-1}eV^2)$	1.00	3.00	2.20	0.60	1.30	5.00	144	25	25
Γ_i (eV)		0.20	0.20	0.18	0.07	0.08	0.20	0.60	0.25	0.27

This is the purpose of the molecular orbital analysis described in Chapters III and IV. There it will be shown that the 3.9 eV line might indeed be due to Gd^{3+}. However the 2.45 eV line which is near a known Tb^{3+} transition can be accounted for by a tetrahedral iron molecular orbital excitation. As a result, the fine structure experimentally observed is probably due primarily to iron atoms. This will be discussed in more detail later in Chapter V.

There remains the possibility that some of the observed lines may be due to impurity atoms in the crystal structure. An analysis of the samples grown was performed by emission spectroscopy. The results are shown in Table 4. It is noted that the only major impurity is lead, but it exists in both samples at a concentration in excess of three per cent. The only other impurity of any significance was about .3 per cent of erbium in the TbIG sample. It is not believed that this causes any noticable modification of the spectra.

The lead, however, could be the source of observed transitions. It is believed for example that the line at 4.34 eV could be due to lead. A line at this energy shows up on Grant's reflectivity data on lead flux grown YIG, but does not appear on recent sputtered thin film GdIG samples measured by Levenson and Sawatzky.[19]

The overall line location of the rare earth iron garnets in the 2 eV to 5 eV range as indicated by the combination of TbIG and GdIG data is shown in Figure 11.

Table 4. Impurities Detected in Rare Earth Iron Garnet Crystals

Impurity	TbIG	GdIG
Lead	3%	3%
Cadmium	0.002-0.02%	--
Boron	0.01-0.1%	--
Silicon	0.02-0.2%	--
Iron	Strong	Strong
Manganese	0.001-0.01%	--
Magnesium	--	0.0005-0.005%
Bismuth	0.002-0.02%	--
Gadolinium	--	Strong
Copper	--	0.0005-0.005%
Calcium	0.002-0.02%	0.02-0.2%
Aluminum	--	0.0002-0.002%
Terbium	Strong	0.001%
Erbium	0.1-0.5%	--

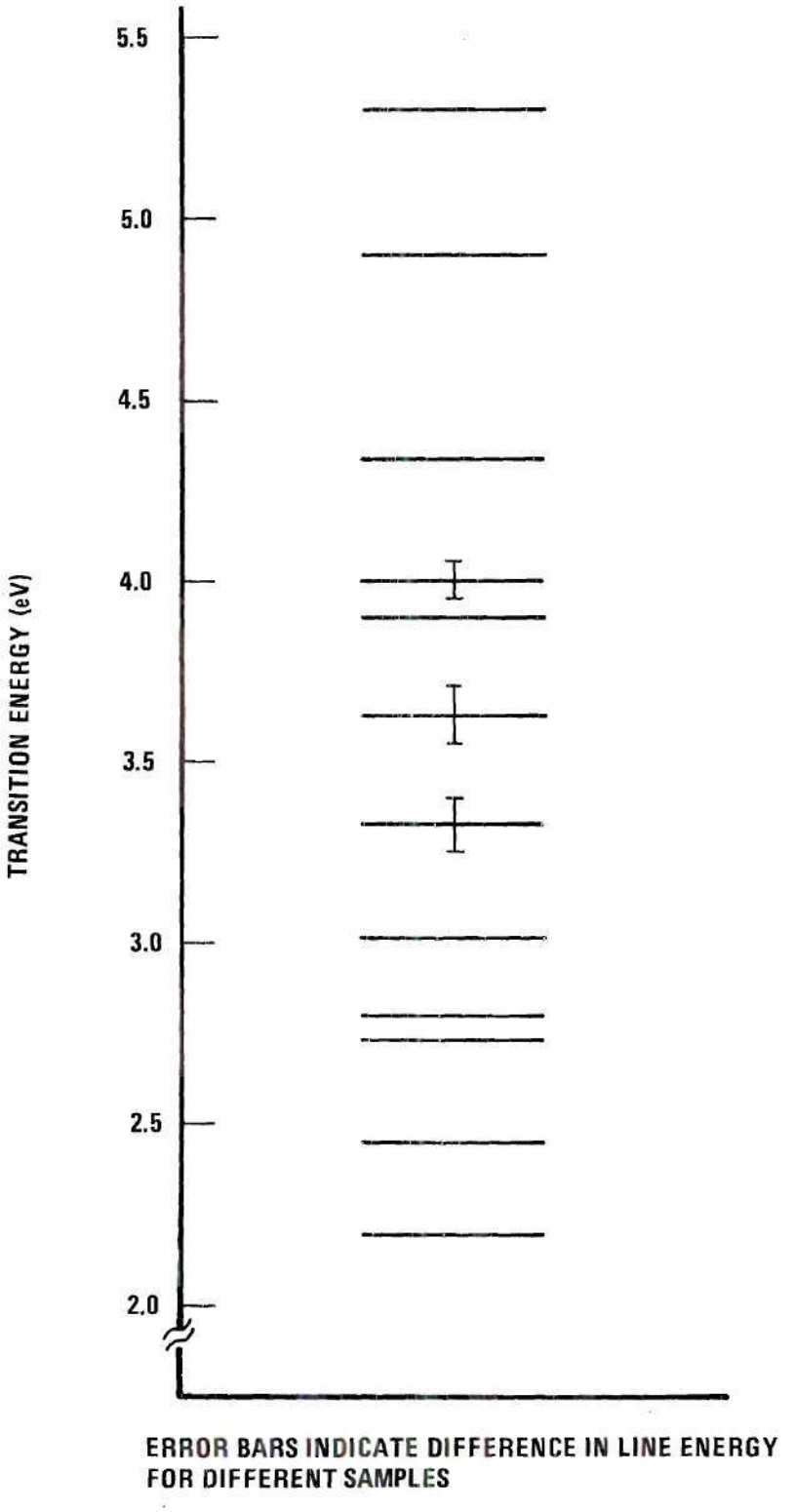

Figure 11. Location of Observed Absorption Lines in TbIG and GdIG

CHAPTER III

THEORY OF THE LCAO MOLECULAR ORBITAL APPROACH

Introduction

As discussed in Chapter I recent studies of the optical characteristics of magnetic oxides have indicated that many of the observed phenomena cannot be explained by considering only the transition series ions. While apparent success was achieved in accounting for the low level, i.e., 1 eV and 2 eV absorptions in αFe_2O_3 and the rare earth iron garnets, the large absorption coefficients and Faraday rotation reversal at higher energies could not be explained. Clogston[7] pointed out that these effects could be explained on the basis of "charge transfer" type of transitions but until now there have been no attempts to predict the location of such transitions.

The reason for this previous lack of theoretical development is that these materials exist in a kind of no-man's-land. They are too complicated to be handled rigorously with a band structure calculation because of the large and complicated crystallographic unit cell. On the other hand they are not ionic enough to be treated from a purely crystal field point of view. This is apparent from the previously mentioned differences in observed and predicted optical

spectra. The problem therefore is to find an analytical approach which will permit inclusion of the oxygen electrons in an explicit way but will not be so complicated as to preclude a complete solution.

A review of the various possible approaches to this problem led to the concept of employing the molecular orbital theory approach, using a linear combination of atomic orbitals as the basis set. McClure[20] had proposed the application of this approach to solids in 1959. However, at that time there apparently were no solutions carried out for solids. Wolfsberg and Helmholz[21] had presented their semi-empirical technique and applied it to the complexes MnO_4^- and CrO_4^- but these were chemically stable molecular complexes existing in liquid or solid solution. To date the technique has still been used primarily only by the chemists studying bonding properties of molecular complexes. There appears to be no reason the techniques should not be equally applicable to molecular-like structures in solids and especially in the oxides where one often finds a unit cell being composed of a combination of octahedral, or tetrahedral molecular-like sites.

It is therefore one of the main purposes of this research to investigate the applicability of the LCAO molecular orbital approach in explaining the optical spectra measured for the rare earth iron garnets. A simplified semi-empirical form of the theory will be applied as originally

proposed by Wolfsberg and Helmholz[21] and recently extended by Ballhausen and Gray[22]. Additional improvements have been incorporated in the work herein reported, and it will be shown that this technique is indeed capable of explaining the observed optical spectra. The following paragraphs in this chapter outline the basic theory of the approach and the details of the calculations.

Basic LCAO Approximation

The basic premise of the LCAO molecular orbital approach is that the wave functions of the molecule can be expanded as a linear combination of atomic wave functions derived from its constituent atoms. (In the broad sense used here, we consider a molecule as any arrangement of atoms describable by a crystallographic symmetry point group.) This assumption cannot be proven rigorously because there is no way to verify that the set of atomic wave functions spans the function space of the molecular orbitals. However, it is physically reasonable to assume that an electron in an orbital extending over the entire molecule would behave as if it were in an atomic orbital when in the near vicinity of a particular atom. Hence when all atoms are considered as a group it is not unreasonable to assume that a linear combination of atomic wave functions could be used to provide a reasonably accurate description of the states of an electron.

By describing the molecular orbitals as a linear combination of atomic orbitals it is easy to show that "charge transfer" like transitions are explicitly included. For example let two molecular orbital wave functions Φ_A and Φ_B be written in a generalized LCAO (linear combination of atomic orbitals) as:

$$\Phi_A = c_{M1}\Psi_{M1} + c_{L1}\Psi_{L1}$$
$$\Phi_B = c_{M2}\Psi_{M2} + c_{L2}\Psi_{L2}$$

In general

$$\Psi_{M1} = \sum_i c_i\psi_{Mi} = \text{linear combination of metal atomic orbitals}$$

$$\Psi_{L1} = \sum_i c_i\psi_{Li} = \text{linear combination of ligand, (oxygen), atomic orbitals}$$

and Ψ_{M2}, Ψ_{L2} are similarly constituted. Assume in addition that Ψ_{M1}, Ψ_{M2}, Ψ_{L1} and Ψ_{L2} are individually normalized, but not necessarily orthogonal to each other. Now consider the effect of an applied perturbation to the molecular orbitals. In particular if the application of an incident radiation field is considered, the electric dipole perturbation operator would be given as $H = e\bar{A}$ where $\bar{A}$ is the vector potential of the field. The matrix element describing the interaction between Φ_A and Φ_B is then given as

$$\langle \Phi_A | H | \Phi_B \rangle = c^*_{M1} c_{M2} \langle \Psi_{M1} | H | \Psi_{M2} \rangle + c^*_{M1} c_{L2} \langle \Psi_{M1} | H | \Psi_{L2} \rangle + c^*_{L1} c_{M2} \langle \Psi_{L1} | H | \Psi_{M2} \rangle + c^*_{L1} c_{L2} \langle \Psi_{L1} | H | \Psi_{L2} \rangle .$$

Here we use the standard Dirac notation where

$$\langle \Phi_A | H | \Phi_B \rangle = \int \Phi^*_A H \Phi_B d\tau .$$

Note that the first term accounts for a transition probability between two metal wave functions. This is the only type of transition which can be accounted for in a crystal field theory model. In the molecular orbital description, however, we see the occurrence of three other types of transitions. The second term corresponds to a transition from a metal orbital to a ligand, eg., oxygen orbital. The third term describes the reverse transition. These are the so called "charge transfer" transitions and are very prominent in the magnetic oxides above 2 eV. Finally, there is the possibility of a transition taking place between oxygen orbitals and this is accounted for by the last term. It is seen therefore that the LCAO molecular orbital approach provides the basic formulation required to study the complex optical spectra of the magnetic oxides. It is true that a number of simplifying assumptions will be necessary to make a numerical solution feasible. However, the same is true for crystal field calculations and the resulting description is very incomplete. It will be shown that the LCAO molecular orbital approach,

proposed by Wolfsberg and Helmholz, is capable of explaining the optical transition spectra of the rare earth orthoferrites and garnets.

The LCAO Secular Equation

Making the basic LCAO assumption we proceed to develop the technique required to explicitly calculate the eigenfunctions of the molecular system. Assume there are m atomic functions available with which we are to approximate the molecular functions. Thus the molecular orbital function Φ_n is written in terms of the atomic functions ψ_k as

$$\Phi_n = c_{n1}\psi_1 + c_{n2}\psi_2 + \cdots c_{nk}\psi_k + \cdots c_{nm}\psi_m \qquad (17)$$

The coefficients are to be chosen so as to minimize the expected energy $\langle\Phi_n|H|\Phi_n\rangle$ of the molecular orbital, while maintaining normalization, i.e., $\langle\Phi_n|\Phi_n\rangle = 1$. This then becomes a max-min problem of a function of several variables, the c_{nk}'s, and a subsidiary condition. The standard method of solution is the application of Lagrangian multipliers.[23] This method requires that the function

$$F_n = \langle\Phi_n|H|\Phi_n\rangle + \lambda_n\langle\Phi_n|\Phi_n\rangle \qquad (18)$$

be made stationary. If the molecular functions Φ are written in expanded form, in terms of the atomic functions ψ_j the

result is

$$F_n = \sum_{i=1}^{m} \sum_{j=1}^{m} c^*_{ni} c_{nj} \left[\langle \psi_i | H | \psi_j \rangle + \lambda_n \langle \psi_i | \psi_j \rangle \right]. \tag{19}$$

F_n is thus a function of the 2m variables c_{n1}, c_{n2} $\cdots$ c_{nm}, c^*_{n1}, c^*_{n2}, $\cdots$ c^*_{nm}, and may be made stationary by setting the differential dF_n equal to zero. Thus the c's must satisfy the relation

$$dF_n = \frac{\partial F_n}{\partial c^*_{n1}} dc^*_{n1} + \frac{\partial F_n}{\partial c^*_{n2}} dc^*_{n2} + \cdots + \frac{\partial F_n}{\partial c^*_{nm}} dc^*_{nm} \tag{20}$$

$$+ \frac{\partial F_n}{\partial c_{n1}} dc_{n1} + \frac{\partial F_n}{\partial c_{n2}} dc_{n2} + \cdots + \frac{\partial F_n}{\partial c_{nm}} dc_{nm} = 0$$

Carrying out the required operations gives

$$dF_n = \sum_i \sum_j c_{nj} \left[\langle \psi_i | H | \psi_j \rangle + \lambda_n \langle \psi_i | \psi_j \rangle \right] dc^*_{ni} \tag{21}$$

$$+ \sum_i \sum_j c^*_{nj} \left[\langle \psi_j | H | \psi_i \rangle + \lambda_n \langle \psi_j | \psi_i \rangle \right] dc_{ni} = 0.$$

The Hermetian character of the Hamiltonian operator allows some simplification of the above equation since

$$\langle \psi_j | H | \psi_i \rangle = \langle \psi^*_i | \overset{*}{H} | \psi^*_j \rangle = \text{conjugate } \langle \psi_i | H | \psi_j \rangle .$$

Thus the second double summation is simply the conjugate of the first, essentially reducing the number of variables by a factor of two. In order for eq. (21) to hold for arbitrary dc^*_{ni} it is necessary to require the coefficient of each dc^*_{ni} to independently go to zero. This gives the final result that for every n, i.e., for each molecular orbital, we must satisfy the set of simultaneous equations:

$$\sum_i \sum_j c_{nj} \left[\langle \psi_i | H | \psi_j \rangle + \lambda_n \langle \psi_i | \psi_j \rangle \right] = 0. \qquad (22)$$

It can be shown from first order perturbation theory[24] that the value of λ turns out to be the negative of the one electron energy of state Φ. If we therefore write $\lambda_n = -E_n$ and express the matrix elements by the notation

$$\langle \psi_i | H | \psi_j \rangle = H_{ij}$$

and

$$\langle \psi_i | \psi_j \rangle = S_{ij}$$

equation (22), written out explicitly becomes

$$c_{n1}(H_{11}-E_nS_{12}) + c_{n2}(H_{12}-E_nS_{12}) + \cdots + c_{nm}(H_{1m}-E_nS_{1m}) = 0 \quad (23)$$

$$c_{n1}(H_{21}-E_nS_{21}) + c_{n2}(H_{22}-E_n) + \cdots + c_{nm}(H_{2m}-E_nS_{2m}) = 0$$

$$c_{n1}(H_{31}-E_nS_{31}) + c_{n2}(H_{32}-E_nS_{32}) + \cdots + c_{nm}(H_{3m}-E_nS_{3m}) = 0$$

$$\vdots$$

$$c_{n1}(H_{m1}-E_nS_{m1}) + c_{n2}(H_{m2}-E_nS_{m2}) + \cdots + c_{nm}(H_{mm}-E_n) = 0.$$

This set of equations is somewhat different than the set which generally appears in descriptions of atomic systems because of the overlap integral terms S_{ij}. They are present in the equations because in general the atomic orbitals on different atoms, i.e., the functions we are using for a basis, are not orthogonal. In simple atomic systems where wave functions are made up of an orthonormal basis on the same atom these terms reduce simply to the delta function. In the case of a molecule, however, these terms, the overlaps, play a critical role in the derivation of the molecular orbitals.

The final step in applying eq. (23) to find the appropriate c_n's is to note that in order to obtain non-trivial values for the c's, i.e., $c \neq 0$, we must demand that the determinant of their coefficients vanish. Thus we arrive at a form of the well known secular equation

$$\det|H_{ij}-E_nS_{ij}| = 0 \quad ; \quad S_{ij} = 1 \text{ for } i = j \quad (24)$$

or explicitly:

$$\begin{vmatrix} (H_{11}-E_n) & (H_{12}-E_nS_{12}) & (H_{13}-E_nS_{13}) & \cdots & (H_{1m}-E_nS_{1m}) \\ (H_{21}-E_nS_{21}) & (H_{22}-E_n) & (H_{23}-E_nS_{23}) & \cdots & \vdots \\ & & & & \vdots \\ & & & & (H_{mm}-E_n) \end{vmatrix} = 0 \qquad (25)$$

The secular equation is obviously an m^{th} order polynomial in E_n. There are therefore m values of E_n satisfying the requirements of the secular equation, each one representing an eigenstate of the molecular orbital Φ_n. Substituting each value of E_n back into eq. (23) permits the evaluation of a set of c_n's which in turn define the eigenfunction $\Phi_n = \sum_i c_{ni}\psi_i$ corresponding to that energy level.

It is apparent from eq. (23) that all the c_n's cannot be determined independently since there are only m equations but m + 1 unknowns, i.e., m unknown c_n's and E_n. We can however solve for the ratios of coefficients. Assuming $c_{n1} \neq 0$ the ratios

$$c_{n2}/c_{n1},\ c_{n3}/c_{n1},\ c_{n4}/c_{n1},\ \cdots\ c_{nm}/c_{n1}$$

can be completely determined.

Finally the normalization criteria may be used to completely define the total eigenfunction,

$$\Phi_n = N[\psi_1 + (c_{n2}/c_{n1})\psi_2 + \cdots + (c_{nm}/c_{n1})\psi_m]. \qquad (26)$$

Equations (23), (24), and (26) form the basic background of the calculations to be performed. There are of course many details to consider in order to actually carry out the solution of the secular equation. The first of these details is applying the symmetry properties of the molecule in such a way as to reduce the size of the secular equation. In doing this we also gain a great deal of physical insight into the structure of the resulting molecular orbitals in terms of their atomic origin. Further details will be concerned with maintaining proper normalization and finally the problem of actually calculating the matrix elements for substitution into the secular equation. These problems will be considered in the following sections.

Symmetry Factorization of Secular Equation

Geometry of Atomic Orbitals

Before discussing the application of symmetry to factor the secular equation, it is desirable to consider the geometrical properties of the atomic orbitals. The atomic orbital functions to be used in this work will be of the self-consistent-field type. Since this type of calculation makes use of a spherically symmetric effective field, the Schrödinger equation is separable, becoming a typical central field problem. The result of this is that self-consistent atomic functions have the same general form as the hydrogenic

orbitals and can be written as:

$$\psi_{n,\ell,m} = R_{n,\ell}(r)\ Y_{\ell}^{m}(\theta,\phi). \tag{27}$$

The term $Y_{\ell}^{m}(\theta,\phi)$ is the spherical harmonic function. Thus these atomic orbitals have the same angular dependence as the hydrogenic wave functions.

The radial term is however different from the hydrogenic function because of the electron-electron electrostatic interactions. A great deal of effort has been extended in calculating the radial functions since Hartree's original proposal in 1928.[25] The most significant work has, however, occurred rather recently as a result of a technique proposed by Roothaan.[26] Roothaan's method determines the radial functions as a series of Slater type orbitals, having the form

$$R_{n,\ell}(r) = \sum_{k=\ell+1}^{n} c_{k\ell,n}\ [(2\zeta_{k\ell})^{2k+1}/(2k)!]^{1/2}\ r^{k-1}\ \exp(-\zeta_{k\ell}r).$$

The functions are therefore analytically described rather than being presented simply numerically as in the old Hartree-Fock scheme. There is a rather complete catalog of atomic wave functions presently available, one of the best being that of Clementi.[27]

The angular part of the orbital wave function determines its directional properties, i.e., it provides information about the angular distribution of charge with respect to

a fixed set of coordinates. It is shown in many text books[28] that the spherical harmonics have the form

$$Y_{\ell}^{m}(\theta,\phi) = N(m,\ell)P_{\ell}^{m}(\cos\theta)\ \exp(im\phi) \tag{28}$$

where P_{ℓ}^{m} is one of the set of associated Legendre polynomials and $N(m,\ell)$ is a normalizing factor to provide

$$\int Y_{\ell}^{m*}(\theta,\phi)\ Y_{\ell'}^{m'}(\theta,\phi)\ \sin\theta d\theta d\phi = \delta_{\ell\ell'}\delta_{mm'}. \tag{29}$$

For bounded solutions it is necessary for ℓ to be a positive integer and m may take the values $-\ell$, $-\ell+1$, $\cdots 0$, $+1$, $+2$, $\cdots$, $+\ell$. Thus for each value of ℓ there are $2\ell+1$ independent angular distributions which are solutions of the Schrodinger equation.

By forming linear combinations of the complex spherical harmonic solutions it is possible to form real solutions. Functions of this type are easier to manipulate in the calculations to be performed and are easier to "picture" geometrically. The manipulation to produce such real functions is straightforward[24] and results in the equations of Table 5. These functions are normalized according to eq. (29).

The directional properties of these functions can be ascertained from their form. The s function is spherically symmetric. The three p functions p_x, p_y, and p_z all have the same general form but are each directed along a specific axis.

Table 5. Real Normalized Angular Wave Functions for s, p, and d Functions

Type	ℓ	$\lvert m \rvert$	Function
s	0	0	$s = 1/\sqrt{4\pi}$
p	1	0	$p_z = \sqrt{3/4\pi}\ (z/r)$
		1	$p_x = \sqrt{3/4\pi}\ (x/r)$; $p_y = \sqrt{3/4\pi}\ (y/r)$
d	2	0	$d_{z^2} = \sqrt{5/4\pi}\ [z^2 - 1/2(x^2+y^2)]/r^2$
		1	$d_{yz} = \sqrt{15/4\pi}\ (yz/r^2)$
		1	$d_{xz} = \sqrt{15/4\pi}\ (xz/r^2)$
		2	$d_{xy} = \sqrt{15/4\pi}\ (xy/r^2)$
		2	$d_{x^2-y^2} = \sqrt{15/16\pi}\ (x^2-y^2)/r^2$

The d functions are not quite so easy to visualize but again are directed in symmetrical fashion with respect to the coordinate axes. An aid in visualizing the geometry of these orbitals is provided by boundary surface diagrams. These are figures representing the three dimensional outlines of a large fraction of $|\psi|^2$, i.e., orbital charge, with signs included to indicate the sign of the lobes of ψ. Figures 12, 13, and 14 show the boundary surface figures of s, p, and d orbitals respectively. We will make explicit use of the geometrical characteristics of the atomic orbitals in the subsequent discussion of symmetry.

Group Theoretical Considerations

Solution of the n^{th} secular equation would in general result in m different eigenvalues according to the formulation of eq. (25). However, in a real molecular structure there will in fact be some degeneracy because of the inherent symmetry. It is possible to take advantage of this symmetry in advance and, as a result, reduce the large high order single secular equation to a number of simple lower order ones. The development of the formalism necessary to accomplish this requires application of group theoretical concepts. It is not appropriate here to detail these concepts and in the following, we will use several theorems without proof. Proofs and expanded details can be found in the literature.[29]

The significant result of group theory to the molecular orbital problem is that for every site symmetry type

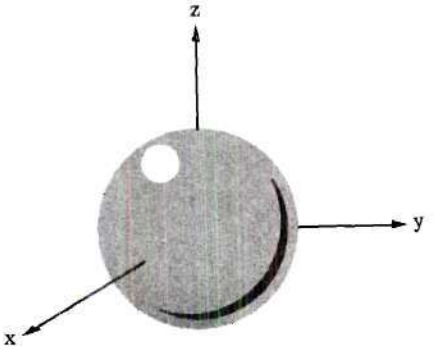

Figure 12. The Boundary Surface of an s Orbital

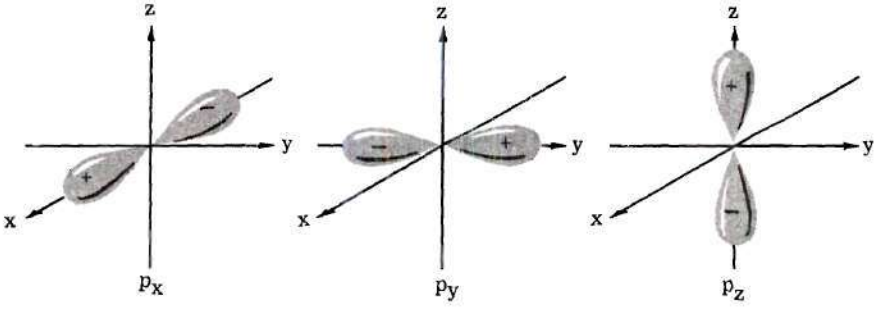

Figure 13. Boundary Surfaces of the p Orbitals

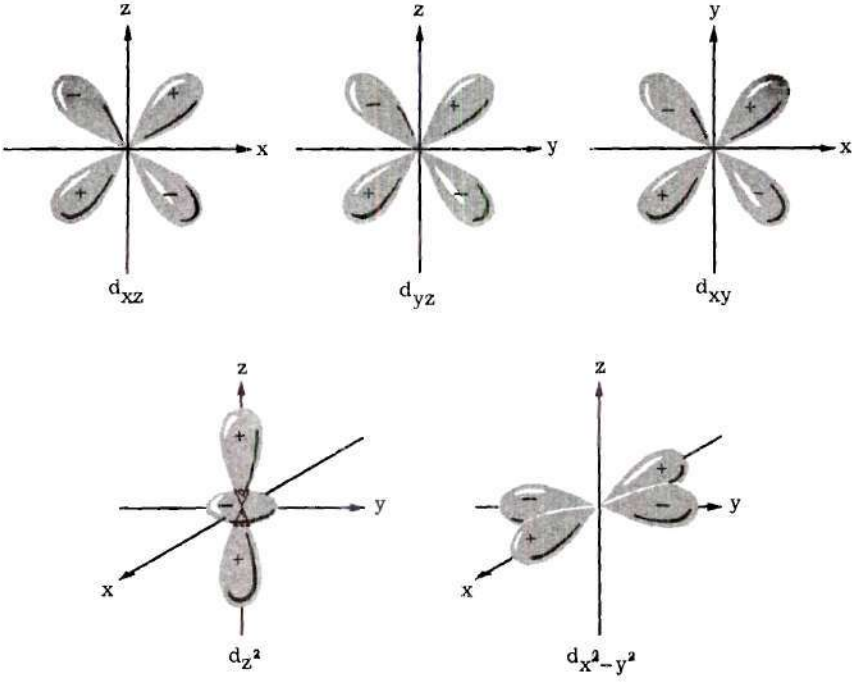

Figure 14. Boundary Surfaces of the d Orbitals

it is possible to catalog once and for all the physically allowable orbitals in terms of their geometry and degeneracy. This is easy to understand physically. For example, consider a molecular orbital which has the same geometrical properties as the atomic p_x function. Assume additionally that the molecular structure, i.e., the geometrical arrangement of the nuclei making up the molecule, is cubic. It is apparent in this case that a molecular orbital with the geometry of p_y or p_z would not be energetically distinguishable from that of geometry p_x because rotating the molecular structure 90° around the x, y, and z axes would leave the molecule unchanged but transform p_x into p_y etc. Since the molecule is unchanged after such a transformation the energy is unchanged, and orbitals of p_x, p_y and p_z type symmetry are energetically degenerate. It is apparent from this qualitative argument that the formalization of the symmetry properties involves the application of linear operators causing rotations, reflections, and inversions of the nuclear sites of a molecular structure. The operators which perform these transformations, so as to interchange one nucleus with another of the same molecule are the symmetry operators of the molecule. The set of operators which transform a molecule into itself are defined as follows.

Rotation: For an axis of n-fold rotational symmetry, the operation of rotation by $\frac{2\pi k}{n}$ degrees is denoted by C_n^k. Note that k may be positive or negative.

Reflection: The operation of reflecting a molecule in a plane of symmetry is denoted by σ.

Inversion: This operation is only applicable to structures possessing a center of symmetry. In this case, if 0 is the center of symmetry, then the inversion operator has the effect of transferring a point A to a point A' along the line A-0-A'. The segment 0A' is equal to A0. This operator is denoted by the symbol i.

Identity: The identity operator E applied to a molecule leaves all nuclei unchanged.

Improper Rotation: This is a combination operation consisting of a rotation followed by a reflection in a symmetry plane. It is denoted as S_n^k where k and n have the same meaning as in simple rotation. The reflection is implied by the symbol S.

The product of two operators is defined to imply successive application of the individual operators. Thus the product operation

$$\sigma_a C_n^k$$

causes the successive transformations of a rotation of $\frac{2\pi k}{n}$ degrees followed by reflection in the a^{th} plane of symmetry. In general, symmetry operators do not commute.

The inverse of a symmetry operator is defined to mean the operation which, when applied after a given operator,

returns the molecule to its original position. Thus if R is any general symmetry operator the inverse R^{-1} is such that

$$R^{-1}R = RR^{-1} = E.$$

Defined in this way it can be shown that the set of symmetry operators form a group, i.e., they satisfy the following requirements.

(1) The product QP of two elements P and Q of the set is itself an element of the set.

(2) The product is associative.

(3) The identity operation is an element of the set.

(4) Each element of the set has an inverse which is also an element of the set.

One of the basic results of group theory applied to the symmetry point group is the partitioning of it into classes of conjugate elements. Formally, two elements P and Q are said to be conjugate to each other if there exists some element R of the group such that

$$P = R^{-1}QR. \tag{30}$$

Physically this simply implies that the operator Q can be transformed into P by a symmetry operator of the same group. An example of the results of division into classes of

conjugate elements is given below for the ammonia molecule. This molecule has the symmetry C_{3V} as denoted by Schoenflies notation. The set of operators applicable to this molecule, i.e., its point group, are E, C_3^1, C_3^2, σ_a, σ_b, σ_c. The molecule has an axis of three fold rotational symmetry, and three planes of reflection symmetry as can be seen from the point group. It can be shown using the definition that this point group can be divided into three classes of conjugate elements. They are (E), (σ_a, σ_b, σ_c), and (C_3^1, C_3^2). It is apparent that the classes could be determined geometrically and in fact there are theorems to do so,[29] however, the generality of the group theory derivation provides the formal base on which these theorems are built. It should be noted from the above example that E is in a class by itself. This is true for any symmetry because E commutes with all symmetry operators. Thus if R is any operator

$$R^{-1}ER = R^{-1}RE = E, \tag{31}$$

i.e., E is conjugate only to itself.

The symmetry point group, i.e., the set of operators transforming a molecule into itself, and its separation into classes is based only on the geometry of the molecule. We now need to show that this particular set of operators may be used to reduce the large molecular orbital secular

equation into several small ones. To accomplish this it is necessary to make use of the concepts and terminology of representation theory.

Appendix C derives the basic characteristics of an operator representation. It is shown there that a symmetry operator may be described, or represented, by a square matrix. This matrix representation is defined as follows. Let ψ_1, $\psi_2 \cdots \psi_n$ form an n-dimensional basis set covering a given function space, for example the space of all 3d atomic orbitals. Then the symmetry operator O_R applied to some function

$$\phi = \alpha_1\psi_1 + \alpha_2\psi_2 + \cdots + \alpha_n\psi_n = \sum_k \alpha_k\psi_k \tag{32}$$

is computed as

$$O_R\phi = \phi' = [\psi_1\psi_2 \cdots \psi_n] \begin{bmatrix} & & \\ & T_R & \\ & & \end{bmatrix} \begin{bmatrix} \alpha_1 \\ \alpha_2 \\ \cdot \\ \cdot \\ \cdot \\ \alpha_n \end{bmatrix} \tag{33}$$

This can also be written as

$$O_R\phi = \sum_j \alpha'_j\psi_j \qquad \text{where } \alpha'_j = \sum_k \left[T_r \right]_{jk} \alpha_k. \tag{34}$$

The matrix $[T_R]$ is the representation of the operator O_R with respect to the basis $(\psi_1, \psi_2, \cdots \psi_n)$. Appendix C proves that $[T_R]$ is the transpose of the transformation matrix describing the application of O_R to the basis functions.

As a simple example let O_R be C_4^1 operating on a basis set composed of the atomic p_x, p_y, p_z functions. Assume the two-fold axis of symmetry to be the z axis. Applying C_4^1 to this basis set produces a new set of functions p_x', p_y', p_z' which can be written as

$$\begin{bmatrix} p_x' \\ p_y' \\ p_z' \end{bmatrix} = \begin{bmatrix} 0 & 1 & 0 \\ -1 & 0 & 0 \\ 0 & 0 & 1 \end{bmatrix} \begin{bmatrix} p_x \\ p_y \\ p_z \end{bmatrix} .$$

The representation matrix of C_4^1 with respect to the basis p_x, p_y, p_z is the transpose of the above 3 x 3 matrix. Thus

$$\left[T_{C_4^1}\right] = \begin{bmatrix} 0 & -1 & 0 \\ 1 & 0 & 0 \\ 0 & 0 & 1 \end{bmatrix} .$$

The two key characteristics of representation theory which are of direct application in factoring the secular equation are the "character" and "irreducible components"

of a representation. The concept of the "character" of a representation stems from the desirability of having a single quantity which characterizes a representation matrix irrespective of the particular basis set chosen. This is necessary since the elements of the representation matrix change if the basis set initially chosen is linearly transformed into another set. It turns out that the trace of the representation matrices possesses this property. The following theorem can be shown to be true.[29]

Theorem I: Two n x n representations $\left[T_R^{(f)}\right]$ and $\left[T_R^{(g)}\right]$ are equivalent, i.e., have the same trace, if a matrix A exists such that

$$\left[T_R^{(g)}\right] = \left[A\right]\left[T_R^{(f)}\right]\left[A\right]^{-1} \tag{35}$$

for every operation of the group.

Given any n-dimensional vector space covered by a basis set $f_1, f_2, \cdots f_n$ it can be shown that $[A]^{-1}$ is simply the transformation matrix describing a new basis $g_1, g_2, \cdots g_n$ as

$$\bar{g} = [A]^{-1} \bar{f} \quad . \tag{36}$$

It can also be shown that the character of matrices for operators in the same class are always identical. Hence a

point group can be characterized by classes rather than individual operators.

Reducibility of a representation into irreducible representations, (IR's), is the touch stone with the final goal of reducing the molecular equation. In general, for an arbitrarily selected basis set the representation matrices of a point group will have finite values of all ij locations, (row i, column j). However it is found that for some bases, obtained by a transformation as eq. (36), the representations take on a block diagonal form as shown diagrammatically in eq. (37).

$$T_R = \begin{bmatrix} T_R^{(1)} & 0 & 0 & 0 & 0 \\ 0 & T_R^{(2)} & 0 & 0 & 0 \\ 0 & 0 & T_R^{(3)} & 0 & 0 \\ 0 & 0 & 0 & \ddots & 0 \\ 0 & 0 & 0 & 0 & T_R^{(p)} \end{bmatrix} \qquad (37)$$

According to the previous concept of equivalence, the representation of eq. (37) is equivalent to the most general representations since the bases are related by eq. (36). The trace of the representation eq. (37), which is the sum of the traces of submatrices $\left[T_R^{(1)}\right]$ through $\left[T_R^{(p)}\right]$, is identical to that of all other representations obtained via eq. (36). A basis which produces a representation of matrices similar to eq. (37) is therefore composed of subsets which transform under the symmetry operations completely

independent of the remainder of the basis. These subsets are called irreducible representations. The significant feature here is that since the Hamiltonian operator commutes with the operators of the symmetry point group the molecular orbital secular equation factors into a similar form. This will be discussed in detail later.

There are two key theorems from group theory which generalize the previous discussion of "reducibility" and "character". The first is:

> Theorem II: Given a group G which contains g elements (including the identity operation) and possesses k different classes of conjugate elements then:
>
> The group possesses exactly k different IR's T_1, T_2, $\cdots$, T_k whose dimensions n_1, n_2, $\cdots$, n_k satisfy the equation $n_1^2 + n_2^2 + \cdots n_k^2 = g$.

This theorem yields the number of IR's for each symmetry point group independent of the basis set employed for any representation. The number of IR's is a function only of the geometry of the molecule. The individual IR's are denoted by a symbolism which indicates the dimension of the submatrix. The nomenclature is:

A----1 dimensional IR

E----2 dimensional IR

T----3 dimensional IR.

Subscripts are used to distinguish between several equi-dimensional IR's of the same point group. Tables can thus be

constructed which display the character of each IR under the transformation of each class in the point group. In the research of this thesis direct application is made of the character tables for octahedrally and tetrahedrally coordinated molecules. These are classified as O_h and T_d symmetries respectively. The character tables for these two molecular symmetries are listed in Tables 6 and 7.

The second theorem of importance in utilizing the symmetry properties of the point group is:

> Theorem III: The set of characters $\chi_i^{(u)}$, i = 1, 2, $\cdots$ k belonging to the u^{th} IR is unique within the group.

This is graphically illustrated in Tables 6 and 7 where it is observed that each IR has a unique set of characters. This feature is used in associating the various elements of an arbitrary basis with a given IR. For example consider a basis set consisting of the 3d, 4s, and 4p atomic functions. It is immediately apparent that only the 4s function transforms as A_1 since it is left unaltered by all symmetry operations.

In the preceding paragraphs the basic concepts of formalizing and cataloging the symmetry properties of a molecule have been reviewed. The final step in utilizing this data is to show the equivalence between degenerate eigenfunctions of the molecular Hamiltonian operator H and the basis functions of an IR of the symmetry point group.

Table 6. Character Table for Octahedral (Oh) Symmetries

Oh	E	$8C_3$	$6C_2$	$6C_4$	$3C'_2$	i	$6S_4$	$8S_6$	$3\sigma_h$	$6\sigma_d$	$f^{(j)}$
A_{1g}	1	1	1	1	1	1	1	1	1	1	$x^2+y^2+z^2$
A_{2g}	1	1	-1	-1	1	1	-1	1	1	-1	
A_{1u}	1	1	1	1	1	-1	-1	-1	-1	-1	
A_{2u}	1	1	-1	-1	1	-1	1	-1	-1	1	
E_g	2	-1	0	0	2	2	0	-1	2	0	$3z^2-r^2, x^2-y^2$
E_u	2	-1	0	0	2	-2	0	1	-2	0	
T_{1g}	3	0	-1	1	-1	3	1	0	-1	-1	R_x, R_y, R_z
T_{2g}	3	0	1	-1	-1	3	-1	0	-1	1	xy, xz, zy
T_{1u}	3	0	-1	1	-1	-3	-1	0	1	1	x, y, z
T_{2u}	3	0	1	-1	-1	-3	1	0	1	-1	

Table 7. Character Table for Tetrahedral (Td) Symmetries

Td	E	$8C_3$	$3C_2$	$6S_4$	$6\sigma_d$	$f^{(j)}$
A_1	1	1	1	1	1	$x^2+y^2+z^2$
A_2	1	1	1	-1	-1	
E	2	-1	2	0	0	$3z^2-r^2, x^2-y^2$
T_1	3	0	-1	1	-1	R_x, R_y, R_z
T_2	3	0	-1	-1	1	$x, y, z; xy, xz, yz$

To do this assume that E_r, a particular eigenvalue of the equation

$$H\phi_r = E_r\phi_r, \tag{38}$$

is n-fold degenerate. Hence there exist n independent eigenfunctions $\phi_1, \phi_2, \cdots \phi_n$ which satisfy eq. (38) and span the space of all solutions with eigenvalue E_r. This space consists of all functions which are linear combinations of ϕ_1 through ϕ_n. A general member of the set of all such solutions is

$$\phi_{ru} = \sum_{i=1}^{n} a_i\phi_i = [\phi_1\phi_2 \cdots\phi_n] \begin{bmatrix} a_i \\ a_2 \\ \cdot \\ \cdot \\ a_n \end{bmatrix} . \tag{39}$$

Now assume a general function like ϕ_{ru} is operated on by a symmetry operator O_R which commutes with H. Application of such an operator O_R to ϕ_{ru} then transforms it to some new function. But since O_R commutes with H this new vector is also a solution of eq. (38) and can be written as a linear combination of $\phi_1, \phi_2, \cdots \phi_n$. In general then

$$O_R\phi_{ru} = [\phi_1\phi_2\cdots\phi_n]\begin{bmatrix} & T_{OR} & \end{bmatrix}\begin{bmatrix} a_1 \\ a_2 \\ \cdot \\ \cdot \\ a_n \end{bmatrix} \tag{40}$$

where $[T_{OR}]$ is a matrix representing the operator.

Consider the case where the operator is applied to one of the basis functions, for example ϕ_k. In this case the resulting function is also a combination of the ϕ's and can easily be shown (see Appendix C) to be given explicitly as

$$O_R\phi_k = \sum_{i=1}^{n} r_{ik}\phi_i, \tag{41}$$

where r_{ik} are elements of the k^{th} column from the matrix T_{OR}. Thus application of a symmetry operator which commutes with H to one of the degenerate functions of E_r produces another function which is a linear combination of the degenerate set. This is one of the properties required of a matrix if it is a representation of a symmetry operator.

It can now be shown that the consecutive application of two such symmetry operators is represented by a matrix which is simply the product of the individual matrices representing each operator. This in turn verifies that these matrices form a representation of such operators as defined by group theory.

If O_R of eq. (41) is a member of a group which commutes with H, and O_S is another member of the same group,

$$O_S\phi_k = \sum_{j=1}^{m} s_{jk}\phi_j \ . \tag{42}$$

Successive application of R and S must be equivalent to another operator of the group T, i.e., let SR = T. If T is applied to ϕ_k we have, in a similar fashion to equations (41) and (42),

$$O_T\phi_k = \sum_{j=1}^{n} t_{jk}\phi_j \ . \tag{43}$$

We also have

$$O_T\phi_k = (O_S O_R)\phi_k = O_S(O_R\phi_k) = \sum_{i=1}^{n} r_{ik} O_S\phi_i \tag{44}$$

where we have used the property that O_S commutes with a constant. Applying equation (42) to (44)

$$O_S O_R\phi_k = \sum_{i=1}^{n} r_{ik} \sum_{j=1}^{n} s_{ji}\phi_j = \sum_{i=1}^{n}\sum_{j=1}^{n} r_{ik}s_{ji}\phi_j \ . \tag{45}$$

Comparing eq. (45) with (43) we have

$$t_{jk} = \sum_{i=1}^{n} s_{ji}\, r_{ik} \tag{46}$$

which is the multiplication rule for the product of two matrices.

This proves that the matrices representing the individual operators commuting with H do in fact form a representation of the entire group as required by group theory. The basis, under which this representation has been proven valid, consists of the degenerate eigenfunctions corresponding to a common eigenvalue E_r.

It can be shown[29] that the operators of the point group for a molecule commute with H. This is true because all such operators transform the molecule into itself and hence the energy after the transformation must be identical to the original energy. We have previously shown that the point group is represented with matrices obeying eq. (46). It can therefore be concluded that the n independent eigenfunctions of an n-fold degenerate eigenvalue E_r form a basis for a representation of the symmetry point group. In addition it can be shown[30] that the representation is irreducible. These concepts then lead to the very important theorem:

> Theorem IV: Eigenfunctions belonging to the same eigenvalue form a basis for an irreducible representation of the symmetry point group. The dimension of this representation is equal to the degree of degeneracy.

Now, assume that the molecular orbitals for any given molecule problem are a set of functions $\Phi_1, \Phi_2, \cdots \Phi_n$. These

are the eigenfunctions of the Hamiltonian operator. According to Theorem IV this set forms a basis for a representation of the operators of the molecular point group so as to yield matrices of block diagonal form. Thus in general, any function

$$f = a_1\Phi_1 + a_2\Phi_2 + \cdots a_n\Phi_n$$

would transform under an operator of the point group according to the matrix equation:

$$O_R f = [\Phi_1\Phi_2\cdots\Phi_k\cdots\Phi_n]\begin{bmatrix} r_{11} & r_{12} & \cdots & r_{1k} & & \\ r_{21} & r_{22} & \cdots & r_{2k} & 0 & 0 \\ \vdots & & & & & \\ r_{k1} & r_{k2} & \cdots & r_{kk} & & \\ & & & & \ddots & \\ & 0 & & & & 0 \\ & & & & & \\ & 0 & & & 0 & \end{bmatrix}\begin{bmatrix} a_1 \\ a_2 \\ \vdots \\ \\ \\ \\ a_n \end{bmatrix} \quad (47)$$

This is the block diagonal form previously discussed as eq. (37). The first k functions $\Phi_1, \Phi_2, \cdots \Phi_k$ form a basis for the first irreducible representation. Succeeding subsets similarly form bases for each of the submatrices along the diagonal. Each of these subsets of molecular orbitals consists of eigenfunctions degenerate with respect to the molecular Hamiltonian.

In addition, the dimension of the submatrices, i.e., the irreducible representations, is equal to the degree of degeneracy.

Of special interest is the transformation of the eigenfunctions or basis vectors themselves under the point group operators. It is apparent from eq. (47) that

$$
\begin{aligned}
O_R\Phi_1 &= r_{11}\Phi_1 + r_{21}\Phi_2 + \cdots r_{k1}\Phi_k \\
O_R\Phi_2 &= r_{12}\Phi_1 + r_{22}\Phi_2 + \cdots r_{k2}\Phi_k \\
&\vdots \\
O_R\Phi_k &= r_{1k}\Phi_1 + r_{2k}\Phi_2 + \cdots r_{kk}\Phi_k \,.
\end{aligned}
\tag{48}
$$

In other words the symmetry operations mix functions belonging to the basis of a given IR but do not mix functions belonging to different IR's. It is possible therefore to consider the individual IR's separately rather than the large general representation. Accordingly we say an eigenfunction Φ_u^j belongs to the u^{th} row of the j^{th} IR of dimension j if

$$
O_R\Phi_u^j = \sum_{i=1}^{kj} r_{iu}\Phi_i^j \,. \tag{49}
$$

This is simply a generalization of eq. (48).

The symmetry of the molecule determines completely the number of IR's and their individual dimension, as specified by Theorem II. Thus from symmetry alone we know the

total number of eigenfunctions possible and the symmetry property of each. The symmetry properties of the eigenfunctions, i.e., the way they transform under the operations of the symmetry point group, are the key to reducing the order of the secular equation.

Symmetry Adapted Atomic Orbitals

The atomic orbitals used to construct an LCAO molecular orbital Φ should be chosen so as to transform under the symmetry operators according to the same IR as Φ. Assume we are to construct the u^{th} molecular orbital belonging to the j^{th} IR of the point group. This orbital function will satisfy an eigenvalue equation of the form

$$H_{op}\ \Phi_u^j = E_i\ \Phi_u^j\ .$$

Since the symmetry operators of the point group commute with the Hamiltonian

$$H(O_R\Phi_u^j) = E_i(O_R\Phi_u^j) \tag{50}$$

i.e., the transformed molecular orbital must also have the eigenvalue E_i. Then according to Theorem IV $O_R\Phi_u^j$ must also belong to the j^{th} IR.

If Φ is expressed as a linear combination of atomic functions as

$$\Phi_u^j = c_1\psi_1 + c_1\psi_1 + \cdots\ ,$$

then the set (ψ_1, ψ_2, $\cdots$) must also form a basis for the j^{th} IR. If they did not, the symmetry operations on an arbitrary function $a_1\psi_1 + a_2\psi_2 + \cdots$ would result in a new function having a different eigenvalue.

Thus the number of atomic orbitals associated with a given molecular orbital is much smaller than the total set of all atomic orbitals. The functions ψ_1, ψ_2, $\cdots$ may be individual atomic orbitals or combinations of atomic orbitals. They are called symmetry adapted functions and provide for a significantly simplified secular equation.

The symmetry properties are now used to reformulate the secular equation problem. For a particular molecular geometry, we can determine the number of irreducible representations and the dimension of each. For each IR of dimension n there are n degenerate molecular orbitals with the symmetry properties defined by the IR. For each IR the appropriate symmetry adapted atomic functions are found by systematically checking the transformation properties of atomic functions and matching them to the particular point groups via the character table. These symmetry adapted functions are then used as a basis for the secular equation formulation rather than the complete set of individual atomic functions.

The detailed development of selecting the proper symmetry adapted orbitals may be found in the literature.[22] It

is appropriate here only to discuss the conventional nomenclature appropriate to the literature and perhaps illustrate the general technique with a simple example.

Consider an octahedrally coordinated site where a metal atom is surrounded by six ligand atoms. Figure 15 illustrates this situation. The ligand atoms are numbered one through six and the x-y-z coordinates associated with each ligand position indicate reference orientation for designating each ligand atomic orbital. Note that the z-axis at each ligand site is directed towards the central metal atom M. The coordinate system for the central atom is right handed while that for each ligand is left handed. This convention appears to have been originally adopted by Mulliken[31] and has been universally used since that time.

Ligand atomic orbitals are classified as σ or π functions depending upon their symmetry with respect to the interatomic axis, i.e., the ligand z-axis. An orbital symmetric with respect to rotation around the z-axis is of the σ type. This includes s, p_z, and d_{z^2} orbitals. Those which exhibit two nodes in a plane perpendicular to the z-axis are π type and include p_x, p_y, d_{xz}, d_{yz} and d_{xy} orbitals.

In general atomic functions of the central metal atom can be easily associated with a given IR of the point group. If the metal atom is of the first transition series, then we are interested only in the 3d, 4s and 4p orbitals since all others are completely filled. There is only one s orbital

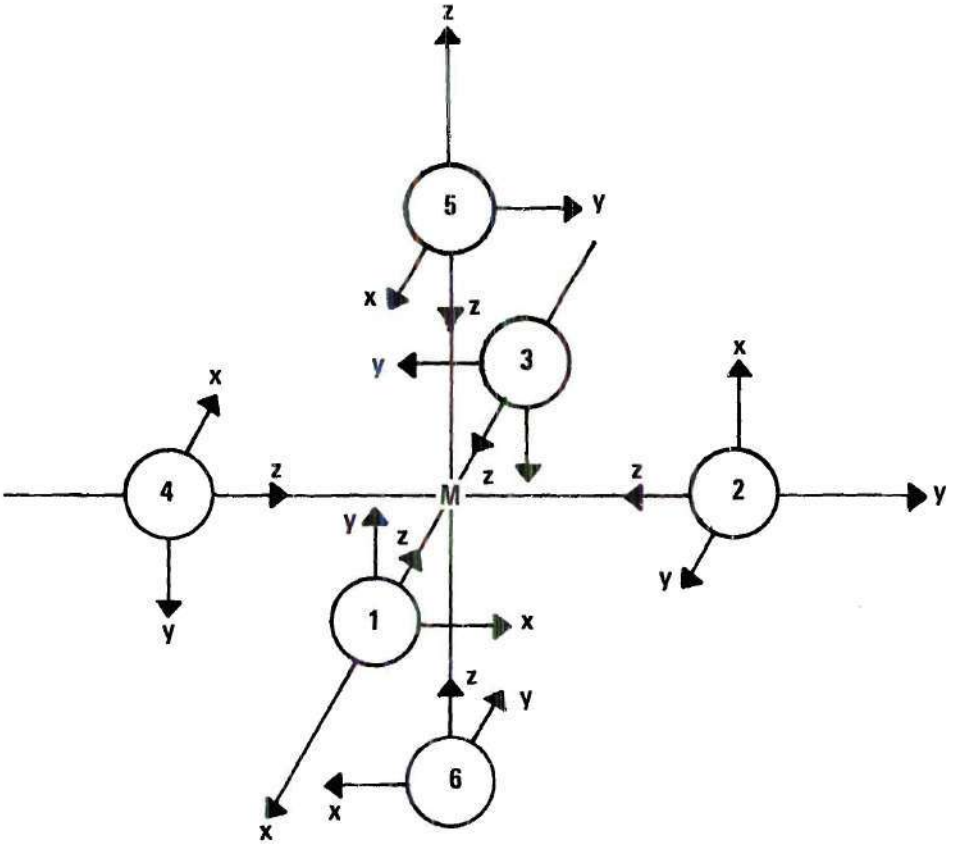

Figure 15. Coordinate System for an Octahedral Complex

and so it must be associated with a one-dimensional IR. Because it is spherically symmetric and at the center of the molecule any symmetry transformation will leave it unaltered. Thus

$$O_R \psi_{Ms} = \psi_{Ms}$$

for all O_R of the point group. The symbology ψ_{Ms} means the orbital s wave function of the metal atom. The character of the representation of each operator is one, hence the metal s orbital must be associated with the a_{1g} IR. (See Table 6 for the character table of O_h). The 4p orbitals are also relatively easy to classify. Since there are three identical orbitals (in the sense of octahedral symmetry) they must be associated with a three dimensional IR, i.e., t_{1g}, t_{1u}, t_{2g}, or t_{2u} (see Table 6). To determine the appropriate symmetry, the transformation properties under the point group operators must be evaluated. With p_x, p_y and p_z as a basis set it is easily seen that with respect to the operation C_2 the transformation takes the form

$$C_2 \begin{bmatrix} p_x \\ p_y \\ p_z \end{bmatrix} = \begin{bmatrix} -1 & 0 & 0 \\ 0 & -1 & 0 \\ 0 & 0 & 1 \end{bmatrix} \begin{bmatrix} p_x \\ p_y \\ p_z \end{bmatrix}$$

Hence $\chi_{C_2} = -1$ which by comparison with the character Table 6,

implies an association with either t_{1g} or t_{1u}. Applying the inversion operator i we have

$$i \begin{bmatrix} p_x \\ p_y \\ p_z \end{bmatrix} = \begin{bmatrix} -1 & 0 & 0 \\ 0 & -1 & 0 \\ 0 & 0 & -1 \end{bmatrix} \begin{bmatrix} p_x \\ p_y \\ p_z \end{bmatrix}$$

with a character of $\chi_i = -3$. This implies that the atomic p orbitals of the metal atom are associated with the t_{1u} IR. Evaluation of the transformation matrices under all point group operators in this manner will confirm that the characters are identical with those of the t_{1u} IR. A similar type analysis using the 3d orbitals shows that the three degenerate functions d_{xz}, d_{yz}, and d_{xy} have symmetry properties of the three dimensional t_{2g} IR and the functions d_{z^2} and $d_{x^2-y^2}$ have the symmetry of e_g. The character tables already indicate the association just described by the entry under column $f^{(j)}$. Here the basic symmetry of the IR's is described in terms of the transformation of unit direction vectors.

Identification of the appropriate ligand orbital combinations is a more difficult task. Formal procedures for their identification are available,[30] however, inspection generally requires less time. The first step is to use sets of ligand functions as bases for the point group representations and from the resulting characters to try to

determine the symmetry properties included in the set. For example, consider the transformation matrices using the six $2p\sigma$ type ligand functions as a basis. Figure 16 shows the geometry of the system. Application of the operator $O_R = C_4$ about the z axis gives

$$C_4 \begin{bmatrix} p_{z1} \\ p_{z2} \\ p_{z3} \\ p_{z4} \\ p_{z5} \\ p_{z6} \end{bmatrix} = \begin{bmatrix} 0 & 1 & 0 & 0 & 0 & 0 \\ 0 & 0 & 1 & 0 & 0 & 0 \\ 0 & 0 & 0 & 1 & 0 & 0 \\ 0 & 0 & 0 & 0 & 1 & 0 \\ 0 & 0 & 0 & 0 & 1 & 0 \\ 0 & 0 & 0 & 0 & 0 & 1 \end{bmatrix} \begin{bmatrix} p_{z1} \\ p_{z2} \\ p_{z3} \\ p_{z4} \\ p_{z5} \\ p_{z6} \end{bmatrix}$$

hence $\chi_{C_4} = 2$. Evaluating the characters of all transformation matrices results in the following character table using the six $2p\sigma$ functions as basis

Operator	E	C_3	C_2	C_4	C_2'	i	S_4	S_6	σ_h	σ_d
Character	6	0	0	2	2	0	0	0	4	2

By Theorem III it is known that the characters belonging to a given IR are unique. Hence in comparing these characters with those of the O_h character table it is found that the six σ ligand orbitals contain symmetry properties of several IR's. In fact the characters of IR's add directly as indicated by eq. (37). Hence by systematically searching the character

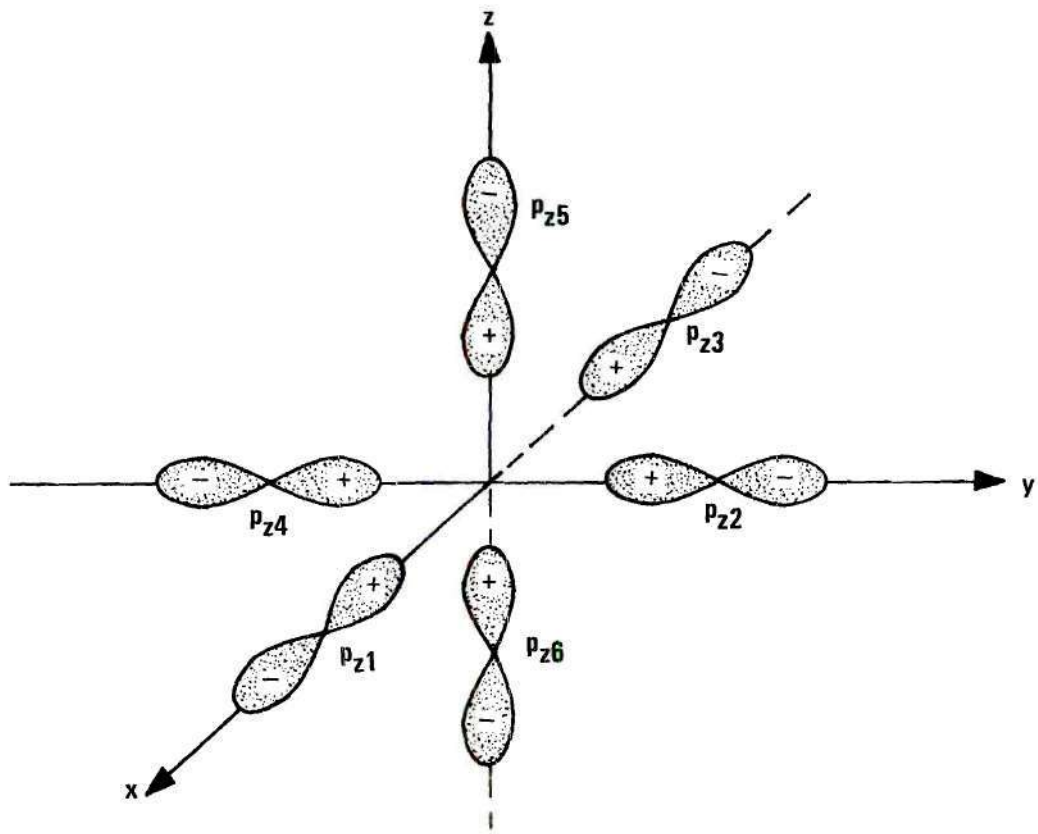

Figure 16. Diagram of the Six 2pσ Ligand Atomic Orbitals of Octahedral Site

table it is found that the above characters are a sum of those from a_{1g}, e_g, and t_{1u}. It is therefore necessary to look for subsets of p_{z1} through p_{z6} with symmetry of these three types. For example consider the t_{1u} IR. Recall that the metal functions p_x, p_y and p_z also had the symmetry of t_{1u}. Referring back to Figure 16 it is easily seen that the function

$$\Psi_1 = (p_{z1}-p_{z3})$$

will transform like the metal atomic function p_x. Likewise $\Psi_2 = (p_{z2}-p_{z4})$ is similar to p_y and $\Psi_3 = (p_{z5}-p_{z6})$ is similar to p_z. Verification of this selection can be made by using Ψ_1, Ψ_2 and Ψ_3 as a basis set and evaluating the characters of the transformation matrices under the point group operators. It is indeed found that the resulting characters are identical with those of the t_{1u} IR. Next combinations of these σ orbitals must be found which transform as a_{1g} and e_{1g}. Finally the symmetry properties of combinations of the π type orbitals are found in an analogous fashion. The process is time consuming but relatively straightforward, the final result being a set of symmetrized functions possessing the basic symmetry of the molecular site. A tabulation of these functions for the octahedral point group is presented in Table 8. Each row corresponds to a molecular orbital, and the symmetry properties of the molecular site have permitted a significant reduction in the number of atomic terms

Table 8. Metal and Ligand Symmetrized Orbitals for an Octahedral Site

Irreducible Representation	Row	Metal Orbital	Ligand Orbitals
a_{1g}	1	4s	$\frac{1}{\sqrt{6}}(p_{z1}+p_{z2}+p_{z3}+p_{z4}+p_{z5}+p_{z6})$
e_g	1	$3d_{x^2-y^2}$	$\frac{1}{2}(p_{z1}-p_{z2}+p_{z3}-p_{z4})$
	2	$3d_{z^2}$	$\frac{1}{2\sqrt{3}}(p_{z5}+p_{z6}-p_{z1}-p_{z2}-p_{z3}-p_{z4})$
t_{1u}	1	$4p_x$	$\frac{1}{\sqrt{2}}(p_{z1}-p_{z3})$, $1/2(p_{y2}+p_{x5}-p_{x4}-p_{y6})$
	2	$4p_y$	$\frac{1}{\sqrt{2}}(p_{z2}-p_{z4})$, $1/2(p_{x1}+p_{y5}-p_{y3}-p_{x6})$
	3	$4p_z$	$\frac{1}{\sqrt{2}}(p_{z5}-p_{z6})$, $1/2(p_{y1}+p_{x2}-p_{x3}-p_{y4})$
t_{2g}	1	$3d_{xz}$	$1/2(p_{y1}+p_{x5}+p_{x3}+p_{y6})$
	2	$3d_{yz}$	$1/2(p_{x2}+p_{y5}+p_{y4}+p_{x6})$
	3	$3d_{xy}$	$1/2(p_{x1}+p_{y2}+p_{y3}+p_{x4})$

Table 8. (Continued)

Irreducible Representation	Row	Metal Orbital	Ligand Orbitals
t_{1g}	1		$1/2(p_{y_1}-p_{x_5}+p_{x_3}-p_{y_6})$
	2		$1/2(p_{x_2}-p_{y_5}+p_{y_4}-p_{x_6})$
	3		$1/2(p_{x_1}-p_{y_2}+p_{y_3}-p_{x_4})$
t_{2u}	1		$1/2(p_{y_2}-p_{x_5}-p_{x_4}+p_{y_6})$
	2		$1/2(p_{x_1}-p_{y_5}-p_{y_3}+p_{x_6})$
	3		$1/2(p_{y_1}-p_{x_2}-p_{x_3}+p_{y_4})$

Note: Only p type functions are explicitly shown for σ ligand symmetrized orbitals. Symmetrized orbitals of s type functions have an identical form.

necessary to consider. In this particular case the t_{1u} orbital, i.e., the molecular orbital with symmetry of the t_{1u} IR, has three terms and it is the largest of all. Note that the coefficient with each symmetrized atomic orbital is chosen to provide a normalized function assuming orthogonality of the individual component terms. This is desirable to provide a general formulation of the symmetry orbitals, however it will be necessary to account for ligand orbital overlap before actual calculations can be completed. Finally note that for molecular orbitals t_{1g} and t_{2u} there is no metal atomic orbital with the t_{1g} or t_{2u} symmetry, yet certain combinations of ligand π orbitals do transform according to these IR's. Orbitals of this type are called "nonbonding" because electrons in them are not mutually coupled to the metal and ligand atoms.

In the garnet system studied during this research we are analyzing the energy level structure of iron atoms in both octahedral and tetrahedral sites of the crystal structure. Figure 17 is a diagram of the geometry of the tetrahedral site, again showing the conventions used for specifying orbital functions. Table 9 is a compilation of the symmetry adapted atomic functions for the tetrahedral case, i.e., T_d symmetry. Because of the lower symmetry of this site, there are in general more atomic terms per molecular orbital. For example the t_2 molecular orbital is composed of five terms in the tetrahedral case. The highest number

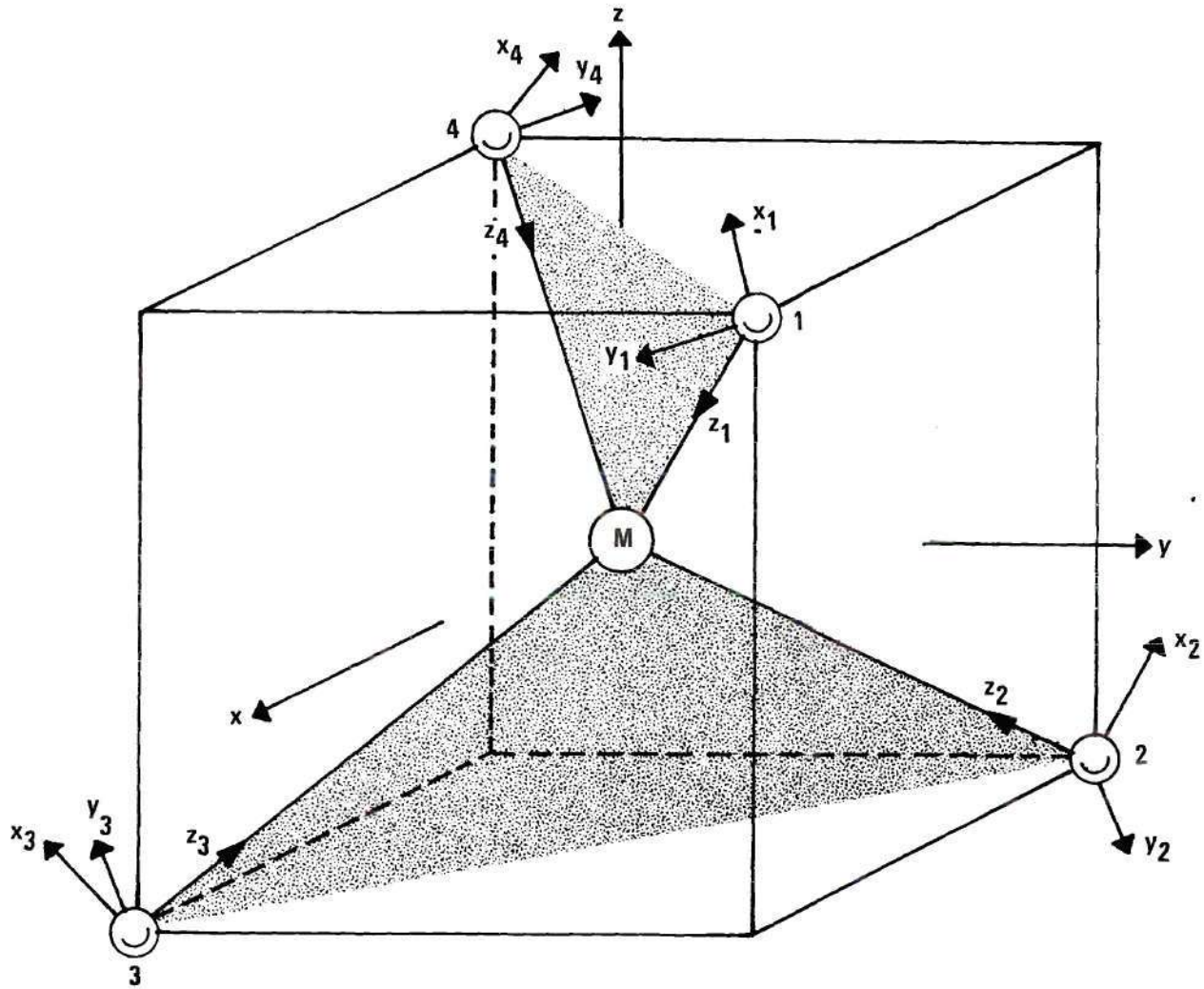

Figure 17. Coordinate System for a Tetrahedral Complex

Table 9. Metal and Ligand Symmetrized Orbitals for a Tetrahedral Site

Irreducible Representation	Row	Metal Orbitals	Ligand Orbitals
A_1	1	s	$1/2(s_1+s_2+s_3+s_4), 1/2(p_{x1}+p_{z2}+p_{z3}+p_{z4})$
E	1	d_{z^2}	$1/2(p_{x1}-p_{x2}-p_{x3}+p_{x4})$
	2	$d_{x^2-y^2}$	$1/2(p_{y1}-p_{y2}-p_{y3}+p_{y4})$
T_2	1	p_x, d_{yz}	$1/2(p_{z1}-p_{z2}+p_{z3}-p_{z4}), 1/2(s_1-s_2+s_3-s_4),$ $1/4[p_{x1}+p_{x2}-p_{x3}-p_{x4}+\sqrt{3}(-p_{y1}-p_{y2}+p_{y3}+p_{y4})]$
	2	p_y, d_{xz}	$1/2(p_{z1}+p_{z2}-p_{z3}-p_{z4}), 1/2(s_1+s_2-s_3-s_4),$ $1/4[p_{x1}-p_{x2}+p_{x3}-p_{x4}+\sqrt{3}(p_{y1}-p_{y2}+p_{y3}-p_{y4})]$
	3	p_z, d_{xy}	$1/2(p_{z1}-p_{z2}-p_{z3}+p_{z4}), 1/2(s_1-s_2-s_3+s_4),$ $-1/2(p_{x1}+p_{x2}+p_{x3}+p_{x4})$
T_1	1		$1/4[\sqrt{3}(p_{x1}+p_{x2}-p_{x3}-p_{x4})+p_{y1}+p_{y2}-p_{y3}-p_{y4}]$
	2		$1/4[\sqrt{3}(p_{x1}-p_{x2}+p_{x3}-p_{x4})-p_{y1}+p_{y2}-p_{y3}+p_{y4}]$
	3		$1/2(p_{y1}+p_{y2}+p_{y3}+p_{y4})$

of terms needed by any orbital in the octahedral case was three. In either case the number is relatively small compared to that necessary if all individual atomic terms were included.

Reduced Secular Equation

Using these symmetry adapted functions, the secular equation can be reformulated to consist of the solution of several small determinants rather than the single large one of eq. (25). First note that it is not necessary to include in the basis set all of the symmetry adapted functions. Because of the degeneracy of orbitals represented by a given IR, the coefficients associated with each term of the linear combination within that IR will be identical. We thus construct a basis from one set of symmetry adapted atomic orbitals from each IR. With this basis the secular eq. (25) is a determinant of dimension 11 x 11 for both the octahedral and tetrahedral cases (see Tables 8 and 9). The general form of the secular equation is

$$|H_{ij} - E_n G_{ij}| = 0$$

where

$$H_{ij} = \langle \Psi_i | H_{op} | \Psi_j \rangle$$

and

$$G_{ij} = \langle \Psi_i | \Psi_j \rangle \ .$$

The functions are the symmetry adapted atomic orbitals just described. The overlap integral G_{ij} is called the "group overlap" because it is made up of terms taken over all the atomic orbitals of the symmetry adapted functions.

However, many of the off diagonal matrix elements can now unambiguously be identified as 0. This is demonstrated by using the octahedral case as an example. Assume the basis is assembled with the first two functions being the atomic components of a_{1g}, the next two being those of e_g, the next three being those of t_{1u}, etc. through t_{2u}. Each of these subsets are solutions of the Hamiltonian for different eigenvalues, i.e., they correspond to different molecular orbitals. But eigenfunctions of a Hermetian operator with different eigenvalues are orthogonal. It therefore follows that

$$(H_{ij} - E_n G_{ij}) = 0 \qquad (51)$$

for i and j corresponding to functions from different IR's. The secular equation thus takes on a block diagonal form which for the octahedral case described is shown in Figure 18. The secular determinantal equation is satisfied by requiring each subdeterminant be equal to zero. If the complete set atomic valence orbitals were used for this problem the secular determinant would be 27 x 27. Because of degeneracy deduced by symmetry this can be reduced to 11 x 11. Finally by taking advantage of symmetry groupings, and having proven that

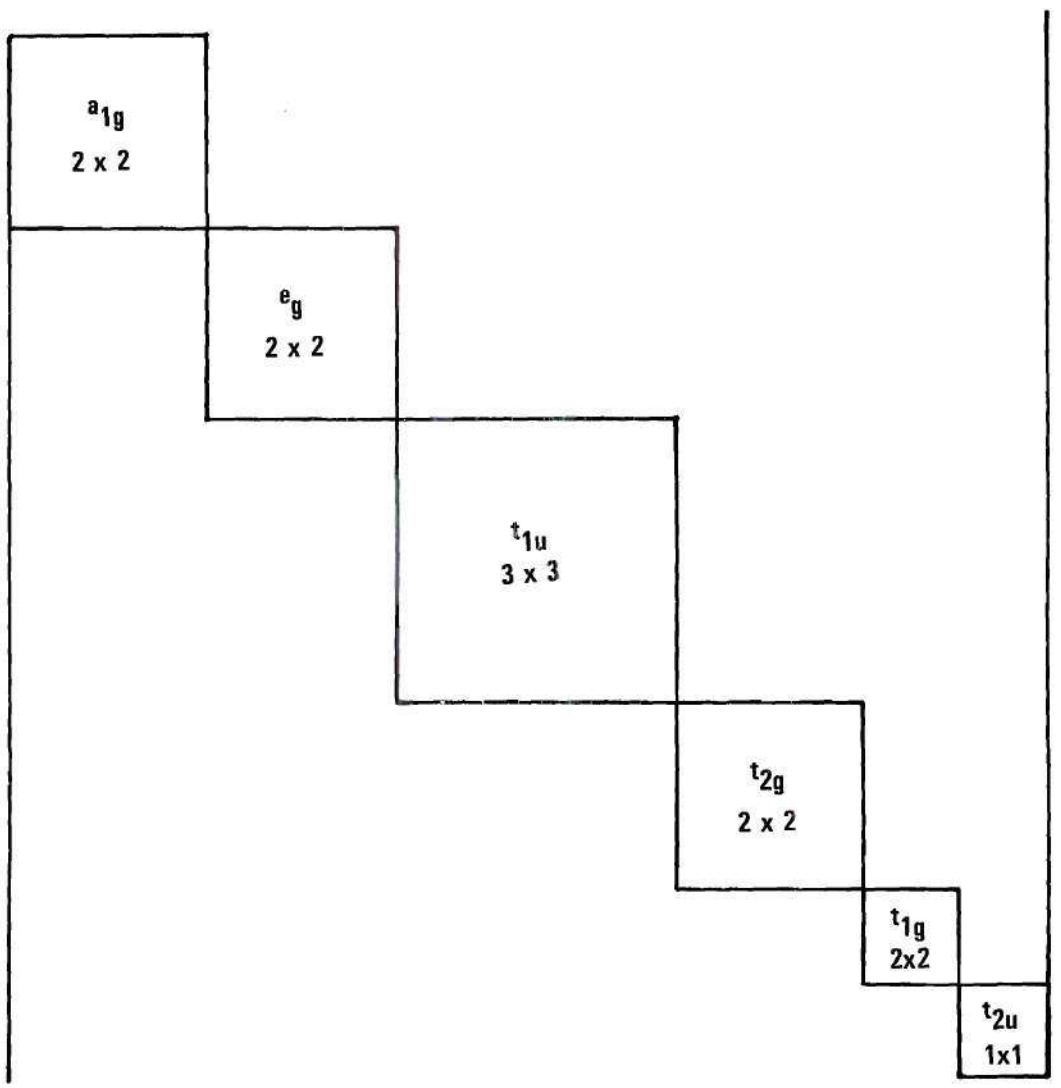

Figure 18. Block Diagonal Form of Octahedral Site Secular Equation

each symmetry set corresponds to a separate eigenvalue, the solution can be reduced to solving one 3 x 3 and three 2 x 2 determinants. The following sections outline the details necessary to actually carry out the required calculations.

Wolfsberg-Helmholz Approximations

Evaluation of the matrix elements, i.e., terms of the form

$$H_{ij} = \langle \Psi_i | H_{op} | \Psi_j \rangle \tag{52}$$

have not been solved in closed form to date because of the many body nature of the problem. Thus, simplifying assumptions must be made if practical results are to be obtained. One such approximation which has been shown to yield quite reasonable results when applied to transition metal complexes was proposed by Wolfsberg-Helmholz.[21] In this approximation terms of the form

$$H_{ii} = \langle \Psi_i | H_{op} | \Psi_j \rangle \tag{53}$$

are solved by invoking Koopman's theorem. This theorem[16] states that the energy parameter E_i in the self-consistent field Hamiltonian equation

$$H_{op} \Psi_i = \varepsilon_i \Psi_i \tag{54}$$

is the negative of the energy required to remove the electron in the state Ψ_i from the solid. Thus we have

$$\varepsilon_i = \langle\psi_i|H_{op}|\psi_i\rangle = H_{ii} = -\text{I.P.} \tag{55}$$

where I.P. is the ionization potential of the i^{th} state. The assumption is made that the molecular ionization potential for the electron does not differ appreciably from that of the atomic orbital. This is apparently a good approximation if the atomic ionization potential is determined for an orbital electron distribution determined by the molecular constraints.

Consider a matrix element of the form eq. (53) evaluated for

$$\Psi = \psi_M(3d_{z^2})$$

i.e., the $3d_{z^2}$ atomic function of the central metal atom. First, all molecular wave functions are searched to determine the effective number of electrons associated with each atomic orbital of the metal atom. Then using this distribution the ionization potential of the $3d_{z^2}$ orbital is determined from atomic energy level data available in the literature. The negative of this value is assigned to the matrix element

$$H_{ii} = \langle\psi_{3d_{z^2}}|H_{op}|\psi_{3d_{z^2}}\rangle \tag{56}$$

Implicit in this discussion is the concept of the self-consistent charge, i.e., SCC technique of the solution. In this process a distribution of electrons among the available atomic orbitals is initially assumed. Using this initial distribution, matrix elements are assigned values as just described. With these matrix elements the secular equations are solved and wave functions determined. From the resulting wave functions the actual distribution of electrons among the atomic orbitals is determined. If this distribution is different from the original, a new distribution is assumed and the process repeated. The optimum solution is considered to be when the final and initial electron distributions are identical.

So far we have discussed only matrix elements of the form H_{ii}. Obviously solution of the secular equation requires values for matrix elements H_{ij} and overlap integrals S_{ij}. The overlap integrals can be computed rigorously from the atomic orbitals and will be described later.

The evaluation of the off-diagonal matrix elements

$$H_{ij} = \langle \Psi_i | H_{op} | \Psi_j \rangle \tag{57}$$

must again be handled in an approximate way. Wolfsberg and Helmholz proposed that this "interaction energy" should be proportional to the overlap between the Ψ_i and Ψ_j functions as well as the self-energy of each orbital. Thus they

proposed the approximation

$$H_{ij} = F\, G_{ij}\, \frac{(H_{ii} + H_{jj})}{2} \,. \tag{58}$$

Here F is a proportionality constant arbitrarily chosen to yield optimum results. In all calculations performed a value of $F \approx 2$ has found to give good results. H_{ii} and H_{jj} are the diagonal matrix elements previously described, having values equal to the negative of the ionization potential of the i^{th} and j^{th} atomic orbitals. In some more recent work using this same general approach, Ballhausen and Gray[32] suggested the use of a geometric rather than arithmetic mean for the self-energy term. Thus they proposed

$$H_{ij} = -F\, S_{ij} \sqrt{H_{ii}\, H_{jj}} \,. \tag{59}$$

Again a value of $F \simeq 2$ has shown experimentally to yield good agreement with experimental measurements. During this research both approximations have been tried with very little difference being observed in the end result. However since eq. (59) leads to a more simplified form of the overlap correction coefficient of ligand symmetrized orbitals it will be used in all further developments. Thus, with this approximation determination of the diagonal matrix elements permits direct computation of the off-diagonal terms as well.

There have been various criticisms leveled at these seemingly crude approximations. However, in a recent article[33] Dahl and Ballhausen show that no improvement can be obtained by any modifications proposed to date. Even elaborate approaches attempting to approximate the matrix elements by more rigorous analytical evaluation provide only questionable improvement.

It seems likely that the SCC technique using the Wolfsberg-Helmholz approximations is not accurate enough to provide an unequivocal determination of the molecular orbitals of a complex system. When used in conjunction with experimental results, however, it appears capable of explaining the energy level structure with a high degree of certainty.

Overlap Integrals

A key factor in achieving acceptable solutions to the secular equation is the evaluation of the group overlap integral terms. Overlap integral calculations are also necessary to provide correct normalization of the ligand symmetry adapted functions. A general approach to the computation of overlap integrals was provided by Mulliken et al in a classic paper in 1949.[34] In this work, tables of two function overlap integrals are published for a variety of atomic orbital combinations. The tabulations however are only for pairs of Slater type orbitals and do not include all possible s and p type functions or any d functions. Later papers[35,36] extended the tables to include d function overlaps.

Previous LCAO molecular orbital calculations have used these tabular values to compute overlap integrals. The problem with this approach is that wave functions must be approximated by one or two Slater type orbitals to make computation of the overall integral feasible. In this present work it was decided to employ the best self-consistent field atomic functions available. This meant that the use of Mulliken type tables had to be abandoned since functions of up to ten Slater type orbital terms are required to adequately describe some atomic orbitals. The approach taken then has been to develop a generalized numerical integration procedure to permit direct computer calculation of any desired atomic orbital pair. This section first develops the appropriate equations for computation of two orbital overlap and then shows how group overlaps are found in terms of linear sums of these terms.

Two Orbital Overlaps

The atomic orbital functions are, as previously discussed, taken in the form

$$\psi_{n,\ell,m} = R_{n,\ell}(r)\ Y_{\ell,m}(\theta,\phi).$$

The wave functions are assumed normalized so that

$$\int \psi^* \psi d\tau = \int |R_{n,\ell}|^2\ |Y_{\ell,m}|^2 r^2\ \sin\theta dr d\theta d\phi = 1$$

or

$$\int |R_{n,\ell}(r)|^2 \, r^2 \, dr = 1 \tag{60}$$

and

$$\int\int |Y_{\ell,m}^{(\theta,\phi)}|^2 \sin\theta d\theta d\phi = 1. \tag{61}$$

The radial functions $R_{n,\ell}(r)$ are taken from the most recent literature available. They are nearly always expressed analytically in the form of a series of terms as:

$$R_{n,\ell} = \sum_{k=+1}^{n} \chi_{k\ell} \, C_{k\ell,n}$$

where

$$\chi_{k\ell} = [(2\xi)^{2k+1}/(2k)!]^{1/2} \, r^{k-1} \exp(-\xi_{k\ell} r).$$

Values of $C_{k\ell,n}$ and $\xi_{k\ell}$ are published for each term of each orbital. The resulting radial functions are normalized as in eq. (60) above. The angular functions have previously been given explicitly in Table 5.

Consider now the evaluation of an overlap integral resulting from orbitals located on different atoms separated a distance R. The coordinate system used to functionally describe the individual orbitals is shown in Figure 19.

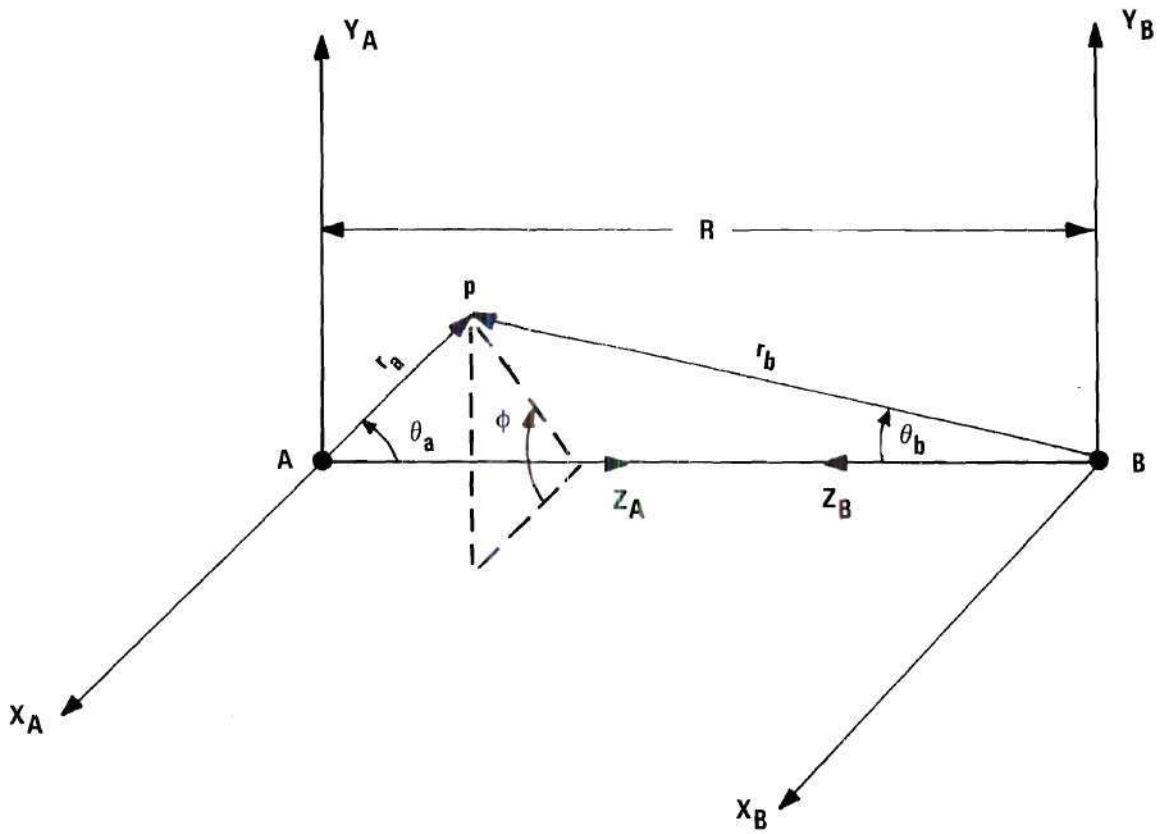

Figure 19. Coordinate System Used for Evaluation of Two Orbital Overlap Integrals

The coordinate system of each orbital is directed so the z-axes point along the interatom line. Any point p in the general three dimensional space can be expressed in terms of r_a, θ_a and ϕ_A or r_b, θ_b and ϕ_B. According to the coordinate system chosen $\phi_A = \phi_B$ as is easily seen. It is convenient with such a geometry to use spheroidal coordinates ζ, η, ϕ where

$$\zeta = r_a + r_b$$

$$\eta = r_a - r_b$$

and $$\phi = \phi_A = \phi_B.$$

The wave functions are now described in terms of ζ, η, and ϕ as follows. The angular part of the wave functions can be rewritten from Table 5 as

$$Y(s) = 1/\sqrt{4\pi}$$

$$Y(p_z) = \sqrt{3/4\pi}\ \cos\theta$$

$$Y(p_x) = \sqrt{3/4\pi}\ \sin\theta\ \cos\phi$$

$$Y(p_y) = \sqrt{3/4\pi}\ \sin\theta\ \sin\phi$$

$$Y(d_{z^2}) = \sqrt{5/16\pi}\ (3\cos^2\theta - 1)$$

$$Y(d_{xz}) = \sqrt{15/4\pi}\ \sin\theta\ \cos\theta\ \cos\phi$$

$$Y(d_{yz}) = \sqrt{15/4\pi}\ \sin\theta\ \cos\theta\ \cos\phi$$

This set of atomic functions is sufficient to describe all σ and π type overlaps. This is all that is needed in most

situations, however, extensions to so called δ overlaps involving functions of the type $d_{x^2-y^2}$ and d_{xz} can easily be added.

Thus an orbital on atom A expressed in terms of r_a, $\cos\theta_a$, $\sin\theta_a$ and ϕ_A would be written in the spheroidal coordinates according to the transformations

$$r_a = \frac{R}{2}(\zeta+\eta)$$

$$\cos\theta_a = \frac{(1+\eta\zeta)}{\zeta+\eta}$$

$$\sin\theta_a = \frac{[(\zeta^2-1)(1-\eta^2)]^{1/2}}{\zeta+\eta}$$

and $$\phi_A = \phi$$

Similarly, a function on atom B is described according to the transformations

$$r_b = \frac{R}{2}(\zeta-\eta)$$

$$\cos\theta_b = \frac{(1-\eta\zeta)}{\zeta-\eta}$$

$$\sin\theta_b = \frac{[(\zeta^2-1)(1-\eta^2)]^{1/2}}{\zeta-\eta}$$

and $$\phi_B = \phi$$

The elemental volume element $d\tau$ in terms of the new variables is

$$d\tau = \frac{(R)^2}{2}(\zeta^2-\eta^2)\ d\eta\ d\zeta\ d\theta\ .$$

Two atom overlap integrals will be described in terms of the type of orbitals and their symmetry. Thus if ψ_a is an s type wave function (σ symmetry) and ψ_b is a p_z type wave function (σ symmetry) then the overlap is described by the symbol $S_{s\sigma,p\sigma}$. If ψ_a is a p_x type wave function (π symmetry) and ψ_b is d_{xz} (π type symmetry), the overlap is denoted by $S_{p\pi,d\pi}$. In all cases the first subscript denotes the orbital on atomic site A and the second on atomic site B.

To illustrate the derivations of the general equations for these two orbital overlap integrals consider the case $S_{s\sigma,p\sigma}$. Thus

$$\psi_a = R_a(r_a)\ \sqrt{1/4\pi}$$

and

$$\psi_b = R_b(r_b)\ \sqrt{3/4\pi}\ \cos\theta_b$$

where $R_a(r_a)$ and $R_b(r_b)$ are the radial functions appropriate to the particular orbitals in question. We thus have

$$S_{s\sigma,p\sigma} = \int_{\zeta\eta\phi}\int\int \psi_a(\zeta,\eta,\phi)\psi_b(\zeta,\eta,\phi)d\tau$$

which gives

$$S_{s\sigma,p\sigma} = (R/2)^3\frac{\sqrt{3}}{4\pi}\int_{\zeta\eta\phi}\int\int R_a\left[\frac{R}{2}(\zeta+\eta)\right]\ R_b\left[\frac{R}{2}(\zeta-\eta)\right]$$

$$\times\ \frac{(1-\zeta\eta)(\zeta^2-\eta^2)}{(\zeta-\eta)}\ d\eta\ d\zeta\ d\phi$$

The range of the spheroidal variables is $0 \leq \phi \leq 2\pi$, $-1 \leq \eta \leq 1$, and $1 \leq \zeta \leq \infty$. The integration of ϕ is trivial and when carried out leaves

$$S_{s\sigma,p\sigma} = (R/2)^3 \frac{\sqrt{3}}{2} \int_1^{\infty} \int_{-1}^{+1} R_a[\tfrac{R}{2}(\zeta+\eta)]\ R_b[\tfrac{R}{2}(\zeta-\eta)] \qquad (62)$$

$$\times \frac{(1-\zeta\eta)(\zeta^2-\eta^2)}{(\zeta-\eta)}\, d\eta\, d\zeta$$

All two orbital overlaps can be reduced in this same manner to a two-dimensional integral in η and ζ.

A computer program has been written to numerically compute integrals of this type. A copy of the program is listed in Appendix D of this thesis. This program accepts radial functions of the form

$$R = \sum_i C_i r^{x_i} \exp(-A_i r)$$

where i may be any integer. After making the change of variable from r_a to $\frac{R}{2}(\zeta+\eta)$ and r_b to $\frac{R}{2}(\zeta-\eta)$ it integrates the appropriate function, for example eq. (62), after receiving inputs specifying the step size for ζ and η and an upper limit of integration for ζ. The algorithm used is based on Weddel's rule of integration. In this algorithm the function to be integrated is approximated by a sixth order polynomial. Hence for the well behaved atomic radial functions the results are quite accurate. By comparison with selected

cases from Mulliken's work it appears the overlaps are accurate to at least three decimal places. This computer program provides a unique improvement over other molecular orbital calculations performed to date in that it permits accurate overlap calculations of the best atomic orbital functions available.

Table 10 is a collection of the integral equations needed to compute two orbital overlaps. These are the equations solved by the computer program described.

Group Overlaps

The group overlap integrals, i.e., integrals of the form

$$G = \langle \Psi_1 | \Psi_2 \rangle$$

where

$$\Psi_1 = \sum_i a_i \psi_M$$

$$\Psi_2 = \sum_i b_i \psi_L$$

can be computed by adding together appropriate two orbital overlaps. This is illustrated by the example of the group overlap associated with the t_{2g} IR of the octahedral group. Referring to Table 8 it is seen the integral becomes

Table 10. Integral Equations for Two Atom Overlaps

$$S_{s\sigma,s\sigma} = (R/2)^3 \frac{1}{2} \int_1^\infty \int_{-1}^1 R_a[\tfrac{R}{2}(\zeta+\eta)]\, R_b[\tfrac{R}{2}(\zeta-\eta)]\, d\eta\, d\zeta$$

$$S_{s\sigma,p\sigma} = (R/2)^3 \frac{\sqrt{3}}{2} \int_1^\infty \int_{-1}^1 R_a[\tfrac{R}{2}(\zeta+\eta)]\, R_b[\tfrac{R}{2}(\zeta-\eta)]\, \frac{(1-\zeta\eta)(\zeta^2-\eta^2)}{(\zeta-\eta)}\, d\eta\, d\zeta$$

$$S_{p\sigma,s\sigma} = (R/2)^3 \frac{\sqrt{3}}{2} \int_1^\infty \int_{-1}^1 R_a[\tfrac{R}{2}(\zeta+\eta)]\, R_b[\tfrac{R}{2}(\zeta-\eta)]\, \frac{(1+\zeta\eta)(\zeta^2-\eta^2)}{(\zeta+\eta)}\, d\eta\, d\zeta$$

$$S_{p\sigma,p\sigma} = (R/2)^3 \frac{3}{2} \int_1^\infty \int_{-1}^1 R_a[\tfrac{R}{2}(\zeta+\eta)]\, R_b[\tfrac{R}{2}(\zeta-\eta)]\, (1-\zeta^2\eta^2)\, d\eta\, d\zeta$$

$$S_{p\pi,p\pi} = (R/2)^3 \frac{3}{4} \int_1^\infty \int_{-1}^1 R_a[\tfrac{R}{2}(\zeta+\eta)]\, R_b[\tfrac{R}{2}(\zeta-\eta)]\, (\zeta^2-1)(1-\eta^2)\, d\eta\, d\zeta$$

Table 10. (Continued)

$$S_{d\sigma,s\sigma} = (R/2)^3 \frac{\sqrt{5}}{4} \int_1^\infty \int_{-1}^1 R_a[\tfrac{R}{2}(\zeta+\eta)]\, R_b[\tfrac{R}{2}(\zeta-\eta)]\, (3\cos^2\theta_a - 1)(\zeta^2-\eta^2)\, d\eta\, d\zeta$$

$$\text{where } \cos\theta_a = \frac{1+\zeta\eta}{\zeta+\eta}$$

$$S_{d\sigma,p\sigma} = (R/2)^3 \frac{\sqrt{15}}{4} \int_1^\infty \int_{-1}^1 R_a[\tfrac{R}{2}(\zeta+\eta)]\, R_b[\tfrac{R}{2}(\zeta-\eta)]\, (3\cos^2\theta_a - 1)(\cos\theta_b)(\zeta^2-\eta^2)\, d\eta\, d\zeta$$

$$\text{where } \cos\theta_a = \frac{1+\zeta\eta}{\zeta+\eta} \quad \text{and} \quad \cos\theta_b = \frac{1-\eta\zeta}{\zeta-\eta}$$

$$S_{d\pi,p\pi} = (R/2)^3 \sqrt{45/16} \int_1^\infty \int_{-1}^1 R_a[\tfrac{R}{2}(\zeta+\eta)]\, R_b[\tfrac{R}{2}(\zeta-\eta)]\, (\zeta^2-1)(1-\eta^2)\cos\theta_a\, d\eta\, d\zeta$$

$$\text{where } \theta_a = \frac{1+\zeta\eta}{\zeta+\eta}$$

$$G_{t_{2g}}(d\pi,p\pi) = \langle d_{xz} | \tfrac{1}{2}(p_{y_1}+p_{x_5}+p_{x_3}+p_{y_6}) \rangle \tag{63}$$

$$= \tfrac{1}{2} [\langle d_{xz} | p_{y_1} \rangle + \langle d_{xz} | p_{x_5} \rangle$$

$$+ \langle d_{xz} | p_{x_3} \rangle + \langle d_{xz} | p_{y_6} \rangle]$$

It is therefore found that the group overlap reduces to the evaluation of a number of two orbital overlap integrals of the type previously discussed. Further reduction is possible however when the symmetry of the metal orbital and ligand terms is considered. The individual atomic orbitals are diagrammed in Figure 20. It is apparent from the figure that each of the two term integrals are of the form $S(d\pi,p\pi)$ and are numerically equal. Thus eq. (63) can be reduced simply to

$$G_{t_{2g}}(d\pi,p\pi) = 2\ S(d\pi,p\pi). \tag{64}$$

This has assumed no overlap between the ligand terms themselves. The effect of ligand-ligand overlap will be discussed in a succeeding section. There it will be shown that the effect of such overlap is to modify the coefficient of the symmetry adapted ligand function. Thus the only modification required is that the coefficient 1/2 in eq. (63) will be somewhat smaller and hence the coefficient of eq. (64) will be slightly less than two.

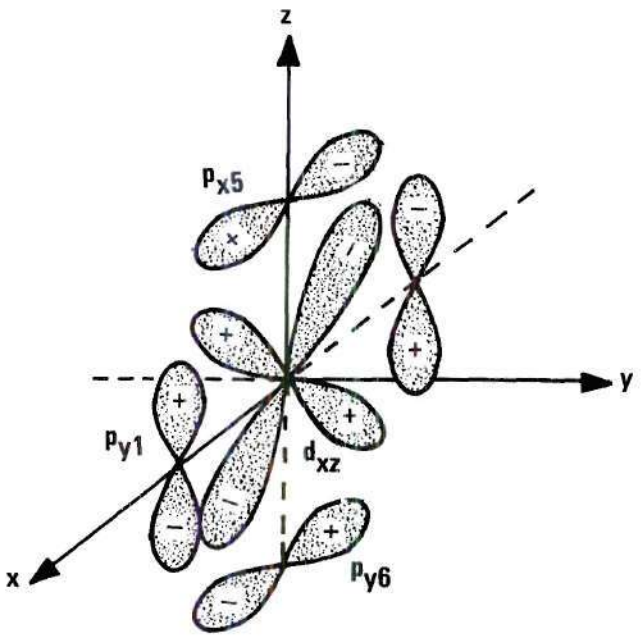

Figure 20. Diagram of Symmetry Adapted Atomic Orbitals for the t_{2g} IR of the Oh Group

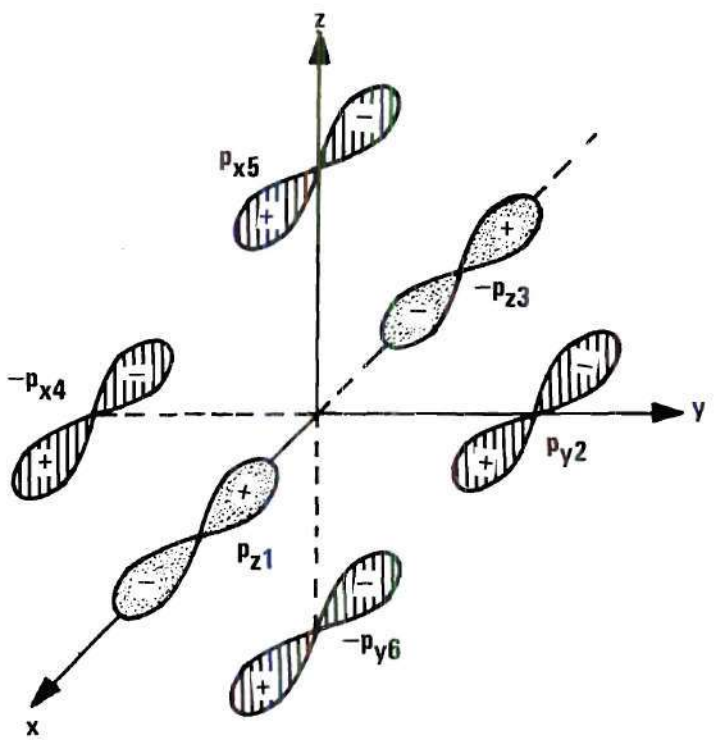

Figure 21. Symmetry Adapted Orbitals Associated with Ligand-Ligand Group Overlap of t_{1u} Symmetry

In addition to the metal-ligand group overlaps it is also necessary to consider those associated with two symmetry adapted ligand orbitals. As an example of this type consider the case of the t_{1u} IR of Table 8. The secular equation for this IR involves the basis functions

$$\Psi_1 = p_x, \quad \Psi_2 = \frac{1}{\sqrt{2}}(p_{z1}-p_{z3})$$

and

$$\Psi_3 = \frac{1}{2}(p_{y2}+p_{x5}-p_{x4}-p_{y6}).$$

Hence we will have the overlaps $\langle\Psi_1|\Psi_2\rangle$, $\langle\Psi_1|\Psi_3\rangle$, and $\langle\Psi_2|\Psi_3\rangle$. The first two are of the same general type as just discussed. The last is a ligand-ligand group overlap and is evaluated explicitly here as an example.

The orbitals associated with Ψ_2 and Ψ_3 are shown diagrammatically in Figure 21. The expression for the group overlap is

$$G_{t_{1u}}(p\sigma,p\pi) = \langle\frac{1}{\sqrt{2}}(p_{z1}-p_{z3})|\frac{1}{2}(p_{y2}+p_{x5}-p_{x4}-p_{y6})\rangle \tag{65}$$

$$= \frac{1}{2\sqrt{2}}[\langle p_{z1}|p_{y2}\rangle+\langle p_{z1}|p_{x5}\rangle+\langle p_{z1}|-p_{x4}\rangle+\langle p_{z1}|-p_{y6}\rangle$$

$$+\langle -p_{z3}|p_{y2}\rangle+\langle -p_{z3}|p_{x5}\rangle+\langle -p_{z3}|-p_{x4}\rangle+\langle -p_{z3}|-p_{y6}\rangle].$$

Again by referring to Figure 21 it is seen that because of the symmetry of the orbital arrangement each of the terms of

eq. (65) have equal magnitude. Equation (65) can thus be written as

$$G_{t_{1u}}(p\sigma, p\pi) = \frac{4}{\sqrt{2}}\langle p_{z1} | p_{y2} \rangle. \tag{66}$$

The problem now is to describe $\langle p_{z1} | p_{y2} \rangle$ in terms of σ and π two-orbital overlaps. This can be done by describing p_{z1} and p_{y2} in terms of components which have σ and π symmetry with respect to their interatomic axis. These two orbitals are sketched in Figure 22. This figure shows the relative position of p_{z1} and p_{y2} from Figure 21 but includes the coordinate system by which each orbital is described. Each function can be described in terms of σ and π by transforming the function to a new set of coordinates rotated 45° with respect to the ones shown.

Consider first p_{z1}. A new set of coordinates x', y', z' may be formed by a rotation of 45°, according to a left hand screw rule, around the y-axis. Then any point described by x, y, z in the original system may be described in x', y', z via the transformation

$$\begin{bmatrix} x' \\ y' \\ z' \end{bmatrix} = \begin{bmatrix} \cos 45° & 0 & -\sin 45° \\ 0 & 1 & 0 \\ \sin 45° & 0 & \cos 45° \end{bmatrix} \begin{bmatrix} x \\ y \\ z \end{bmatrix}.$$

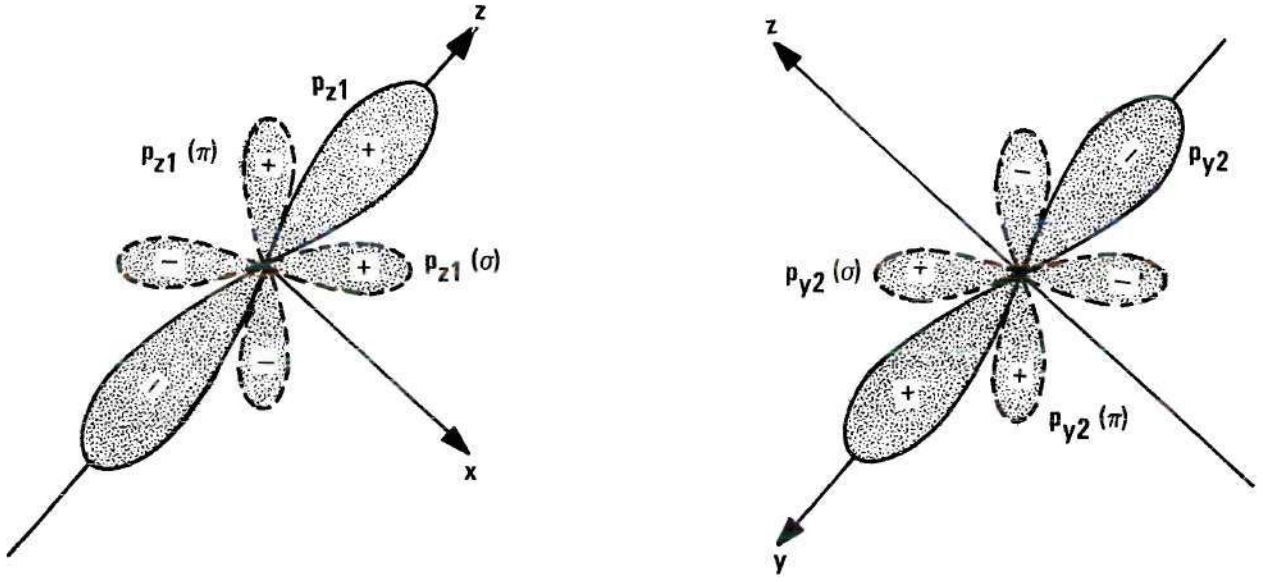

Figure 22. Diagram of p_{z_1} and p_{y_2} Atomic Orbitals of Octahedral Site and Their σ and π Components

Premultiplying both sides by the inverse of the transformation matrix gives

$$\begin{bmatrix} x \\ y \\ z \end{bmatrix} = \begin{bmatrix} 1/\sqrt{2} & 0 & 1/\sqrt{2} \\ 0 & 1 & 0 \\ -1/\sqrt{2} & 0 & 1/\sqrt{2} \end{bmatrix} \begin{bmatrix} x' \\ y' \\ z' \end{bmatrix} \tag{67}$$

so $p_{z1} = \sqrt{3/4\pi}\ \frac{z}{r}$ can now be written as

$$p_{z1} = \frac{1}{\sqrt{2}} \left[-\sqrt{3/4\pi}\ \left(\frac{x'}{r}\right) + \sqrt{3/4\pi}\ \left(\frac{z'}{r}\right) \right] . \tag{68}$$

These two terms are drawn diagrammatically in dotted lines in Figure 22, the first term as $p_{z1}(\pi)$, the second as $p_{z1}(\sigma)$.

The function p_{y2} can be similarly transformed; in this case we employ a counter clockwise rotation of the axes around the x axis. The resulting transformation, this time with respect to the coordinate system of p_{y2}, is

$$\begin{bmatrix} x \\ y \\ z \end{bmatrix} = \begin{bmatrix} 1 & 0 & 0 \\ 0 & 1/\sqrt{2} & 1/\sqrt{2} \\ 0 & -1/\sqrt{2} & 1/\sqrt{2} \end{bmatrix} \begin{bmatrix} x' \\ y' \\ z' \end{bmatrix} . \tag{69}$$

Thus $p_{y_2} = \sqrt{2/4\pi}\,\frac{y}{r}$ now becomes

$$p_{y_2} = \frac{1}{\sqrt{2}}\left[\sqrt{3/4\pi}\,\frac{y'}{r} + \sqrt{2/4\pi}\,\frac{z'}{r}\right] . \qquad (70)$$

Again the first term has π symmetry the second σ symmetry.

It has thus been shown how two orbitals can be decomposed into σ and π components. We write

$$p_{z_1} = \frac{1}{\sqrt{2}}\,p_\sigma - \frac{1}{\sqrt{2}}\,p_\pi$$

and

$$p_{y_2} = \frac{1}{\sqrt{2}}\,p_\sigma + \frac{1}{\sqrt{2}}\,p_\pi$$

therefore the overlap term becomes

$$\langle p_{z_1} | p_{y_2} \rangle = \frac{1}{2}\langle p_\sigma | p_\sigma \rangle + \frac{1}{2}\langle p_\sigma | p_\pi \rangle$$

$$- \frac{1}{2}\langle p_\pi | p_\sigma \rangle - \frac{1}{2}\langle p_\pi | p_\pi \rangle .$$

The two middle terms cancel, and substituting back into eq. (66) results in the final expression for the group overlap as

$$G_{t_{1u}}(p_\sigma, p_\pi) = \sqrt{2}\,\left[S(p\sigma, p\sigma; \sqrt{2}R) - S(p\pi, p\pi; \sqrt{2}R)\right] \qquad (71)$$

The additional term in the argument of the overlap symbol S indicates that the separation between the atoms is equal to $\sqrt{2}$ R where R is the metal to ligand atom distance of the octahedrally coordinated site. Here again the result given assumes no overlap among the orbitals making up Ψ_2 and Ψ_3. Correstions for this effect will slightly lower the coefficient $\sqrt{2}$.

Tables 11 and 12 form a complete compilation of the group overlap expressions for octahedrally and tetrahedrally coordinated sites. Each equation is divided by a factor K or product of such factors. These are the correction factors to account for interorbital overlap of the terms making up the symmetrized ligand orbitals. These factors are derived in the next section and explicitly listed in Tables 13 and 14.

Normalization of Symmetry Adapted Ligand Atomic Functions

In carrying out the actual solutions of the secular equations it is necessary to take care that all constituent functions are properly normalized, i.e., that

$$\langle \Psi | \Psi \rangle = 1.$$

The functions under consideration are those tabulated in Tables 8 and 9. The metal atom functions are chosen to be normalized and so present no problem. The individual ligand atomic functions are also normalized. However the symmetry

Table 11. Group Overlap Integrals-Octahedral Site

$$G_{a_{1g}}(s_{\sigma M}, p_{\sigma L}) = \frac{\sqrt{6}\ S(s_{\sigma M}, p_{\sigma L})}{K_{\sigma}(a_{1g})}$$

$$G_{e_g}(d_{\sigma M}, p_{\sigma L}) = \frac{\sqrt{3}\ S(d_{\sigma M}, p_{\sigma L})}{K_{\sigma}(e_g)}$$

$$G_{t_{1u}}(p_{\sigma M}, p_{\sigma L}) = \frac{\sqrt{2}\ S(p_{\sigma M}, p_{\sigma L})}{K_{\sigma}(t_{1u})}$$

$$G_{t_{1u}}(p_{\pi M}, p_{\pi L}) = \frac{2\ S(p_{\pi M}, p_{\pi L})}{K_{\pi}(t_{1u})}$$

$$G_{t_{1u}}(p_{\sigma L}, p_{\pi L}) = \frac{\sqrt{2}\ [S(p_{\sigma L}, p_{\sigma L};\ \sqrt{2}\ R) - S(p_{\pi L}, p_{\pi L};\ \sqrt{2}\ R)]}{K_{\sigma}(t_{1u})\ K_{\pi}(t_{1u})}$$

$$G_{t_{2g}}(d_{\pi M}, p_{\pi L}) = \frac{2\ S(d_{\pi M}, p_{\pi L})}{K_{\pi}(t_{2g})}$$

Table 12. Group Overlap Integrals-Tetrahedral Symmetry

$$G_{a_1}(s_M, s_{\sigma L}) = \frac{2\, S(s_{\sigma M}, s_{\sigma L})}{K_{s\sigma}(a_1)}$$

$$G_{a_1}(s_M, p_{\sigma L}) = \frac{-2\, S(s_{\sigma M}, p_{\sigma L})}{K_{p\sigma}(a_1)}$$

$$G_{a_1}(s_{\sigma L}, p_{\sigma L}) = \frac{-\sqrt{6}\, S(s_{\sigma L}, p_{\sigma L})}{K_{s\sigma}(a_1)\, K_{p\sigma}(a_1)}$$

$$G_{e}(d_M, p_{\pi L}) = \frac{(2\sqrt{6}/3)\, S(d_{\pi M}, p_{\pi L})}{K_{p\pi}(e)}$$

$$G_{t_2}(p_M, p_{\sigma L}) = \frac{-(2\sqrt{3}/3)\, S(p_{\sigma M}, p_{\sigma L})}{K_{p\sigma}(t_2)}$$

$$G_{t_2}(p_M, s_{\sigma L}) = \frac{(2\sqrt{3}/3)\, S(p_{\sigma M}, s_{\sigma L})}{K_{s\sigma}(t_2)}$$

$$G_{t_2}(p_M, p_{\pi L}) = \frac{-(2\sqrt{6}/3)\, S(p_{\pi M}, p_{\pi L})}{K_{p\pi}(t_2)}$$

$$G_{t_2}(d_M, p_{\sigma L}) = \frac{-(2\sqrt{3}/3)\, S(d_{\sigma M}, p_{\sigma L})}{K_{p\sigma}(t_2)}$$

Table 12. (Continued)

$$G_{t_2}(d_M, s_{\sigma L}) = \frac{(2\sqrt{3}/3)\ S(d_{\sigma M}, s_{\sigma L})}{K_{s\sigma}(t_2)}$$

$$G_{t_2}(d_M, p_{\pi L}) = \frac{(2\sqrt{2}/3)\ S(d_{\pi M}, p_{\pi L})}{K_{p\pi}(t_2)}$$

$$G_{t_2}(p_M, d_M) = 0$$

$$G_{t_2}(p_{\sigma L}, s_{\sigma L}) = \frac{(\sqrt{6}/3)\ S(p_{\sigma L}, s_{\sigma L})}{K_{p\sigma}(t_2)\ K_{s\sigma}(t_2)}$$

$$G_{t_2}(p_{\sigma L}, p_{\pi L}) = \frac{(2\sqrt{2}/3)\ [S(p_{\sigma L}, p_{\sigma L}) - S(p_{\pi L}, p_{\pi L})]}{K_{p\sigma}(t_2)\ K_{p\pi}(t_2)}$$

$$G_{t_2}(s_{\sigma L}, p_{\pi L}) = \frac{-(2\sqrt{3}/3)\ S(s_{\sigma L}, p_{\sigma L})}{K_{s\sigma}(t_2)\ K_{p\sigma}(t_2)}$$

adapted sum of ligand orbitals is only normalized, as shown in the tables, if there is no overlap between functions. In this section the appropriate overlap correction factors are introduced.

The molecular orbital uses combinations of atomic ligand orbitals as illustrated in the function

$$\Phi_{molec} = C_1\psi_M + C_2[N_2 \sum_i a_i \psi_i(LA)] + C_3[N_3 \sum_j a_j \psi_j(LB)]. \quad (72)$$

Here N_2 is the normalization factor for the symmetry adapted function composed of type A ligand atomic orbitals, and N_3 normalizes the function composed of type B ligand atomic orbitals. The coefficients C_1, C_2, and C_3 are determined from the solution of the secular problem.

Consider now one of the symmetry adapted ligand functions, for example the one composed of type A atomic orbitals. Assume, first of all, that there is no overlap between individual components. In this case

$$\langle a_i\psi_i(LA) | a_j\psi_j(LA)\rangle = \begin{cases} 1 \text{ if } i=j \\ 0 \text{ if } i\neq j \end{cases} \quad (73)$$

and the normalization integral of the complete function becomes

$$\langle N_2 \sum_i a_i \psi(LA) | N_2 \sum_i a_i \psi(LA)\rangle = N_2^2 \sum_i a_i^2 \quad (74)$$

Thus normalization requires

$$N_2 = (1/\Sigma_i a_i^2)^{1/2} \tag{75}$$

which is the factor accompanying the symmetrized orbitals in Tables 8 and 9.

It is also important to note the value of the one electron energy of the complete symmetry adapted orbital. In the case of no overlap between components the diagonal matrix element becomes

$$H_{aa} = \langle [(1/\Sigma_i a_i^2)] \ \Sigma_i a_i \psi(LA) | H_{op} | [(1/\Sigma_i a_i^2)] \ \Sigma_i a_i \psi(LA) \rangle \tag{76}$$

$$= \frac{1}{\Sigma_i a_i^2} \ [\Sigma_i a_i^2 \ \langle \psi(LA) | H_{op} | \psi(LA) \rangle]$$

$$= \langle \psi(LA) | H_{op} | \psi(LA) \rangle \ .$$

Thus the diagonal matrix element of a composite orbital is equal to the one electron energy of a single atomic constituent orbital. This assumes all constituent orbitals are of the same type and there is no overlap.

This simple result no longer holds in the atomic wave function overlap. In this case the normalization constant N must take on a more complicated form. In addition the matrix element is no longer simply that of a single atomic orbital.

When overlap is taken into account, the normalizing expression

$$\langle N\Sigma_i a_i \psi_i | N\Sigma_i a_i \psi_i \rangle = 1$$

when expanded in array form becomes

$$N^2 \left\{ \begin{array}{l} a_1 a_1 \langle \psi_1 | \psi_1 \rangle + a_1 a_2 \langle \psi_1 | \psi_2 \rangle + \cdots + a_1 a_n \langle \psi_1 | \psi_n \rangle \\ + a_2 a_1 \langle \psi_2 | \psi_1 \rangle + a_2 a_2 \langle \psi_2 | \psi_2 \rangle + \cdots + a_2 a_n \langle \psi_2 | \psi_n \rangle \\ + \\ . \\ . \\ . \\ + a_n a_1 \langle \psi_n | \psi_1 \rangle + \cdots\cdots\cdots + a_n a_n \langle \psi_n | \psi_n \rangle \end{array} \right\} = 1 \qquad (77)$$

Since $\langle \psi_i | \psi_i \rangle = 1$ this reduces to

$$N = \frac{1}{[\Sigma_i a_i^2 + \Sigma_{\substack{i\,j \\ i \neq j}} a_i a_j \langle \psi_i | \psi_j \rangle]^{1/2}} . \qquad (78)$$

Defining

$$k = \Sigma_{\substack{i\,j \\ i \neq j}} a_i a_j \langle \psi_i | \psi_j \rangle , \qquad (79)$$

then the normalization factor can be written as

$$N = \frac{1}{(\sum_i a_i^2)^{1/2}\left[1+\frac{k}{\sum_i a_i^2}\right]^{1/2}} = \frac{1}{(\sum_i a_i^2)^{1/2} K} . \qquad (80)$$

The square bracketed term, i.e., K, involving the overlap term k may be considered as a correction factor to the non-overlap value. For a given set of interatomic distances the overlap terms can be computed for each symmetrized ligand orbital and K calculated. Before this is illustrated it is appropriate to consider the effect of ligand overlap on the expression for the diagonal matrix element of a symmetrized ligand orbital.

Consider the energy of a composite wave function given as

$$H_{ii} = \langle N\sum_i a_i\psi_i | H_{op} | N\sum_i a_i\psi_i \rangle . \qquad (81)$$

Expanded as before this diagonal matrix element is a summation of terms as

$$H_{ii} = N^2 \left\langle \begin{array}{l} a_1a_1\langle\psi_1|H|\psi_1\rangle + a_1a_2\langle\psi_1|H|\psi_2\rangle + \cdots + a_1a_n\langle\psi_1|H|\psi_n\rangle \\ +a_2a_1\langle\psi_2|H|\psi_1\rangle + a_2a_2\langle\psi_2|H|\psi_2\rangle + \cdots \\ \quad\vdots \\ +a_na_1\langle\psi_n|H|\psi_1\rangle + \cdots\cdots\cdots\cdots + a_na_n\langle\psi_n|H|\psi_n\rangle \end{array} \right\rangle \qquad (82)$$

Since all of the component atomic functions ψ_1 through ψ_n belong to the same row of the appropriate IR they are degenerate with respect to the molecular Hamiltonian and

$$\langle\psi_1|H|\psi_1\rangle = \langle\psi_2|H|\psi_2\rangle = \cdots \langle\psi_n|H|\psi_n\rangle \triangleq \langle\psi(LA)|H|\psi(LA)\rangle \qquad (83)$$

where the notation $\psi(LA)$ simply means the orbital energy of a type A ligand orbital as in eq. (76). Using eq. (83), the sum of terms eq. (82) can be written as

$$H_{ii} = N^2\left[\left(\sum_i a_i^2\right)\langle\psi(LA)|H|\psi(LA)\rangle + \sum_{\substack{i\ j\\ i\neq j}} a_i a_j \langle\psi_i|H|\psi_j\rangle\right] . \qquad (84)$$

Using the approximation for an off-diagonal matrix element as given by eq. (52) we can write

$$\langle\psi_i|H|\psi_j\rangle = -F \langle\psi_i|\psi_j\rangle \left[\langle\psi_i|H|\psi_i\rangle \langle\psi_j|H|\psi_j\rangle\right]^{1/2} \qquad (85)$$

$$= -F \langle\psi_i|\psi_j\rangle \langle\psi(LA)|H|\psi(LA)\rangle .$$

Using eq. (85) and (80), eq. (84) can be written as

$$H_{ii} = \langle\psi(LA)|H_{op}|\psi(LA)\rangle \frac{\left[1+F\cdot\left(k/\sum a_i^2\right)\right]}{\left[1+\left(k/\sum a_i^2\right)\right]} . \qquad (86)$$

Thus the diagonal matrix element, when accounting for ligand

overlap, is simply the energy of a single atomic orbital modified by the factor

$$\frac{[1+F\cdot(k/\Sigma a_i^2)]}{[1+(k/\Sigma a_i^2)]}$$

As an example of ligand wave function normalization, consider the molecular orbital associated with the e_g irreducible representation for an octahedral site. The wave function is

$$(e_g) = C_1\psi(d_{x^2-y^2}) + C_2N[\psi_1(\sigma L)-\psi_2(\sigma L)+\psi_3(\sigma L)-\psi_4(\sigma L)] \quad (87)$$

Here $(d_{x^2-y^2})$ is a symbolic expression for the metal $3d_{x^2-y^2}$ atomic orbital, and $\psi_1(\sigma L)$ represents the expression for the ligand 2p atomic wave function. To find N we must evaluate the sum

$$k = \sum_{\substack{i \\ i\neq j}} \sum_{j} a_i a_j \langle \psi_i | \psi_j \rangle \ . \quad (88)$$

Note from eq. (87) that all $a_i = 1$. Recalling the notation previously chosen for the octahedral case, it is noted that the four ligand functions are centered on co-planar atomic sites as shown in Figure 23. It is apparent that there are essentially three types of overlap which can occur. First

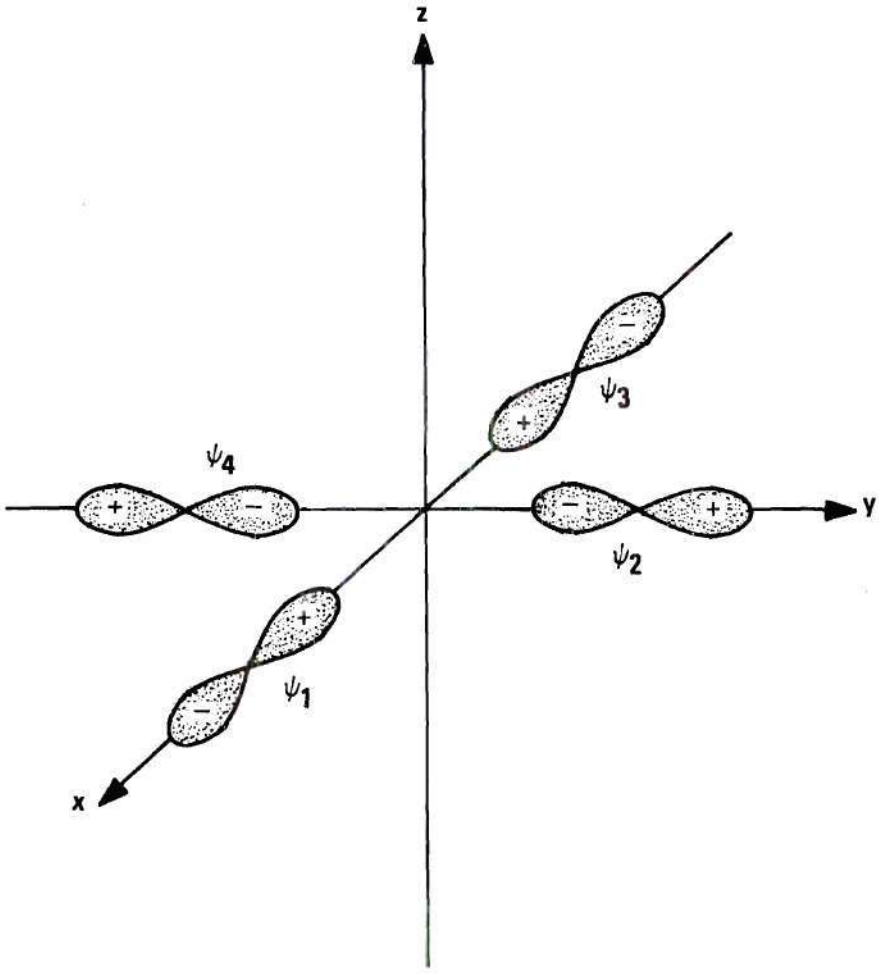

Figure 23. Ligand Orbital Arrangement for Octahedral e_g Molecular Orbital

the simple case $\langle\psi_i|\psi_i\rangle$ which is equal to 1, since the atomic functions being used are individually normalized. Secondly there is an overlap of the type $\langle\psi_1|\psi_3\rangle$, i.e., a $(p\sigma,p\sigma;2R)$ two atoms overlap where the atoms are separated by 2R, R being the metal-ligand distance. Finally there is the more complicated term of the type $\langle\psi_1|\psi_2\rangle$. Here the orbitals are directed at 45° to the interatom axis. In order to carry out the evaluation of this type of term the atomic orbital equation must be described in terms of components which are of σ and π symmetry with respect to the interatom axis as was done previously in the group overlap calculation. Carrying out the appropriate axis transformations for the two orbitals permits the overlap term to be expressed as

$$\langle\psi_1|\psi_2\rangle = \langle(\psi_{p\sigma}/\sqrt{2}) - (\psi_{p\pi}/\sqrt{2})|(-\psi_{p\sigma}/\sqrt{2}) + (\psi_{p\pi}/\sqrt{2})\rangle$$

$$= -1/2\langle\psi_{p\sigma}|\psi_{p\sigma}\rangle - 1/2\langle\psi_{p\pi}|\psi_{p\pi}\rangle .$$

Expressed in the symbology of the two orbital overlaps this becomes

$$\langle\psi_1|\psi_2\rangle = -1/2\ S(p\sigma,p\sigma;\sqrt{2}R) - 1/2\ S(p\pi,p\pi;\sqrt{2}R) .$$

We now have collected everything necessary to completely evaluate the ligand overlap factor as formally expressed in eq. (88).

$$\langle\psi_1|\psi_2\rangle = -1/2\ S(p\sigma,p\sigma;\sqrt{2}R)\ -1/2\ S(p\pi,p\pi;\sqrt{2}R)$$
$$\langle\psi_1|\psi_3\rangle = S(p\sigma,p\sigma;\ 2R)$$
$$\langle\psi_1|\psi_4\rangle = -1/2\ S(p\sigma,p\sigma;\sqrt{2}R)\ -1/2\ S(p\pi,p\pi;\sqrt{2}R)$$

$$\langle\psi_2|\psi_1\rangle = -1/2\ S(p\sigma,p\sigma;\sqrt{2}R)\ -1/2\ S(p\pi,p\pi;\sqrt{2}R)$$
$$\langle\psi_2|\psi_3\rangle = -1/2\ S(p\sigma,p\sigma;\sqrt{2}R)\ -1/2\ S(p\pi,p\pi;\sqrt{2}R)$$
$$\langle\psi_2|\psi_4\rangle = S(p\sigma,p\sigma;\ 2R).$$

It is obvious that this pattern repeats for the remaining terms of the series. The result can therefore be written as

$$k = \sum_{\substack{i\ j\\ i\neq j}} a_i a_j \langle\psi_i(\sigma L)|\psi_j(\sigma L)\rangle = 4\ S(p\sigma,p\sigma;\ 2R)$$
$$- 4\ S(p\sigma,p\sigma;\sqrt{2}R)\ -\ 4\ S(p\pi,p\pi;\sqrt{2}R).$$

Hence according to eq. (80) we see the normalizing coefficient for the ligand term in $\psi(e_g)$ is

$$N = 1/\sqrt{4}\,[1+S(p\sigma,p\sigma;2R)-S(p\sigma,p\sigma;\sqrt{2}R)-S(p\pi,p\pi;\sqrt{2}R)]^{1/2}\ .$$

A similar process must be carried out for each symmetry adapted orbital of octahedral and tetrahedral symmetry. The results are tabulated in Tables 13 and 14. From these it is easy to derive the correction terms for the diagonal matrix elements of the ligand symmetrized orbitals as given in eq. (86).

Table 13. Ligand-Ligand Normalization Overlap Correction Factors-Octahedral Symmetry

IR	Basis Function	Correction Factor
a_{1g}	p_σ	$K_\sigma(a_{1g}) = [1+S(p_{\sigma L},p_{\sigma L};2R)+2S(p_{\sigma L},p_{\sigma L};\sqrt{2}R)+2S(p_{\pi L},p_{\pi L};\sqrt{2}R)]^{1/2}$
e_g	p_σ	$K_\sigma(e_g) = [1+S(p_{\sigma L},p_{\sigma L};2R)-S(p_{\sigma L},p_{\sigma L};\sqrt{2}R)-S(p_{\pi L},p_{\pi L};\sqrt{2}R)]^{1/2}$
t_{1g}	p_π	$K_\pi(t_{1g}) = [1-S(p_{\sigma L},p_{\sigma L};2R)-S(p_{\sigma L},p_{\sigma L};\sqrt{2}R)-S(p_{\pi L},p_{\pi L};\sqrt{2}R)]^{1/2}$
t_{2g}	p_π	$K_\pi(t_{2g}) = [1-S(p_{\pi L},p_{\pi L};2R)+S(p_{\sigma L},p_{\sigma L};\sqrt{2}R)+S(p_{\pi L},p_{\pi L};\sqrt{2}R)]^{1/2}$
t_{1u}	p_σ	$K_\sigma(t_{1u}) = [1-S(p_{\sigma L},p_{\sigma L};\sqrt{2}R)]^{1/2}$
t_{1u}	p_π	$K_\pi(t_{1u}) = [1+S(p_{\pi L},p_{\pi L};2R)+2S(p_{\pi L},p_{\pi L};\sqrt{2}R)]^{1/2}$
t_{2u}	p_π	$K_\pi(t_{2u}) = [1+S(p_{\pi L},p_{\pi L};2R)-2S(p_{\pi L},p_{\pi L};\sqrt{2}R)]^{1/2}$

Table 14. Ligand-Ligand Normalization Overlap Correction Factors-Tetrahedral Symmetry

IR	Basis Function	Correction Factor
a_1	s_σ	$K_{s\sigma}(s_1) = [1+3S(s_{\sigma L}, s_{\sigma L})]^{1/2}$
a_1	p_σ	$K_{p\sigma}(s_1) = [1+2S(p_{\sigma L}, p_{\sigma L})+S(p_{\pi L}, p_{\pi L})]^{1/2}$
e	p_π	$K_{p\pi}(e) = [1+1/2S(p_{\sigma L}, p_{\sigma L})-1/2S(p_{\pi L}, p_{\pi L})]^{1/2}$
t_2	p_σ	$K_{p\sigma}(t_2) = [1-2/3S(p_{\sigma L}, p_{\sigma L})-1/3S(p_{\pi L}, p_{\pi L})]^{1/2}$
t_2	s_σ	$K_{s\sigma}(t_2) = [1-S(s_{\sigma L}, s_{\sigma L})]^{1/2}$
t_2	p_π	$K_{p\pi}(t_2) = [1+1/6S(p_{\sigma L}, p_{\sigma L})+11/6S(p_{\pi L}, p_{\pi L})]^{1/2}$
t_1	p_π	$K_{p\pi}(t_1) = [1-1/2S(p_{\sigma L}, p_{\sigma L})-3/2S(p_{\pi L}, p_{\pi L})]^{1/2}$

Note: All two atom overlaps are calculated at a separation 2 a where a is the cell dimension of the tetrahedral site.

Evaluation of Atomic Ionization Potentials

The use of Koopman's theorem to evaluate the diagonal matrix elements makes it necessary to obtain the best possible estimate of atomic ionization potentials. This is all the more true when one considers that in the Wolfsberg-Helmholz approximation the off-diagonal matrix elements are calculated in terms of the diagonal element values.

In their original paper Wolfsberg and Helmholz did not perform calculations in a self-consistent manner. They simply chose atomic ionization potentials to be associated with atomic charge configurations typical of that expected in the molecule. The first paper to explicitly include self-consistency was that by Ballhausen and Gray[32] in 1962. The basic concept they proposed has been employed in the research herein reported, however, the implementation has been somewhat modified.

Data of ionization potential as a function of charge distribution have been gathered from several sources. One rather complete compilation has been made by Viste and Basch and tabulated by Ballhausen and Gray.[22] Other sources of this type information are papers on SCF atomic wave function calculations. Specifically, data from Clementi[27] and Richardson[38] have been used. Data for the same orbital but from separate references are generally somewhat different. When multiple data sets for the same orbital ionization potential could be found, an average of all data was generally used for actual calculations.

Examples of the data available are shown graphically in Figures 24, 25, and 26 for Fe. These graphs show ionization potential as a function of the number of 3d electrons. Different curves are for various population configurations of the 4s and 4p orbitals. Figure 24 shows data for ionization of a 3d electron, Figure 25 for a 4s electron and Figure 26 for a 4p electron. Data points are of course available only for discrete numbers of electrons. In a molecular type problem however the concept of fractional charge must be introduced since electrons in molecular orbitals essentially share several atomic orbitals.

The lines connecting the discrete electron data points of Figures 24, 25, and 26 are meant only to indicate the general trend of ionization potentials at fractional charge. However they are used as trends to estimate points not available in the literature. For example the points from n = 5 of the configurations $3d^n4p^1$ and $3d^n4s^1$ were estimated by following the trend indicated in Clementi's data for the case $3d^n4s^04p^0$. The same approach was used in Figure 26 to estimate the ionization potential of the 4p orbital with the configuration $3d^n4s^14p^1$. Here the trend from Richardson's data for d^np^2 was followed.

To estimate the ionization potential for a fractional charge configuration $3d^a\ 4s^b\ 4p^c$ where a, b and c are not integers, a linear interpolation algorithm was used. A computer program was written to carry out the actual computations.

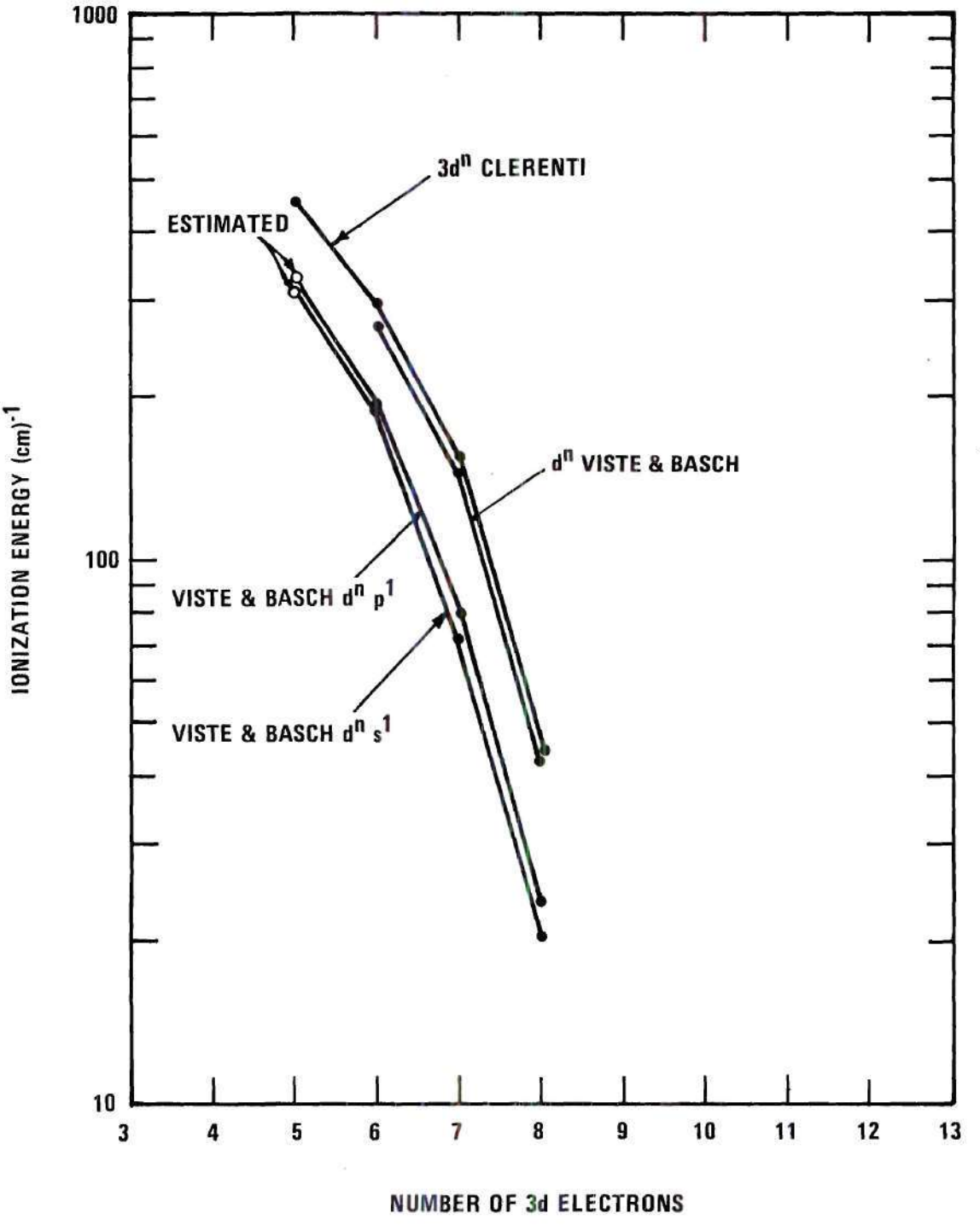

Figure 24. 3d Ionization Potentials for Fe

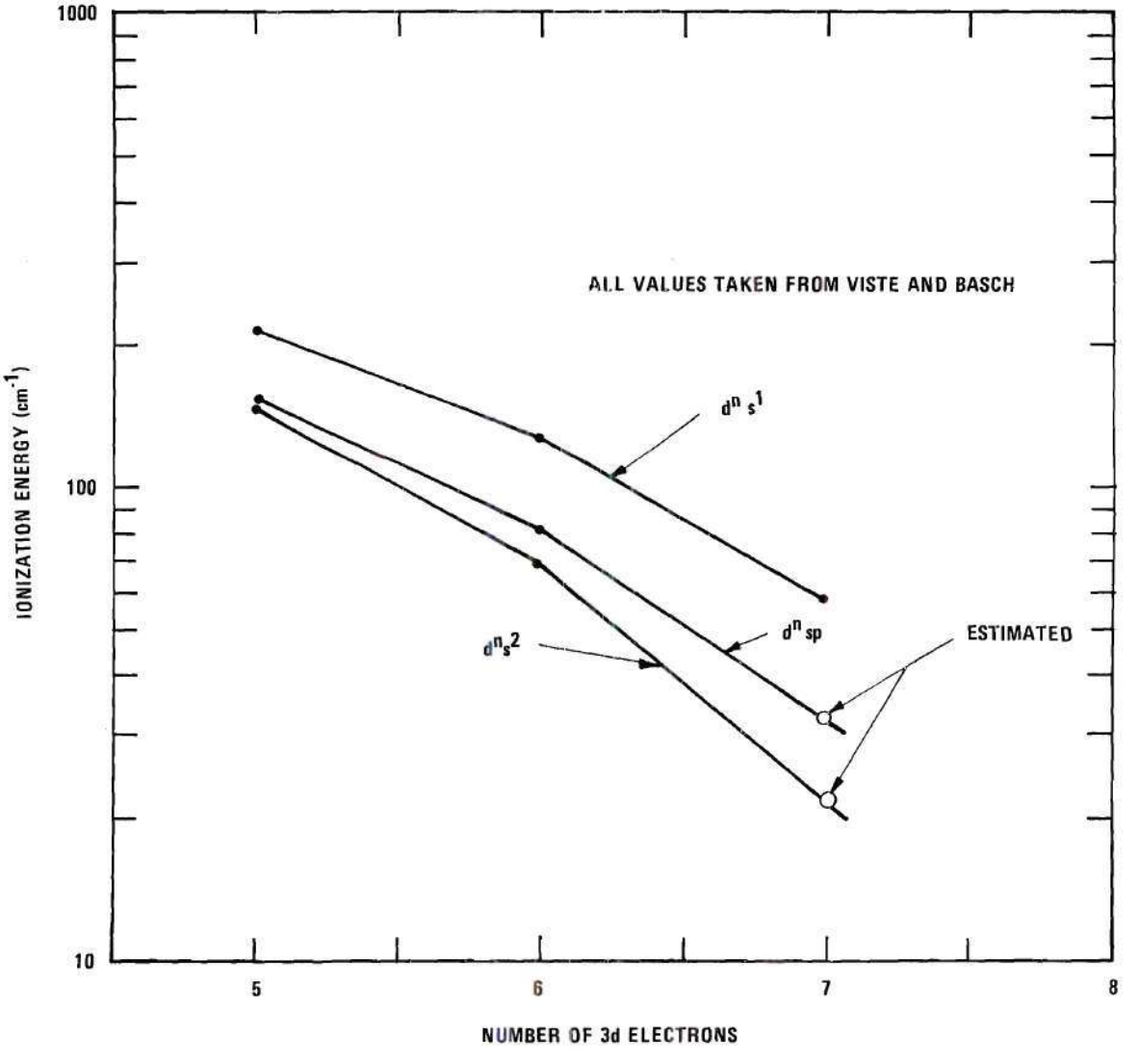

Figure 25. 4s Ionization Potentials for Fe

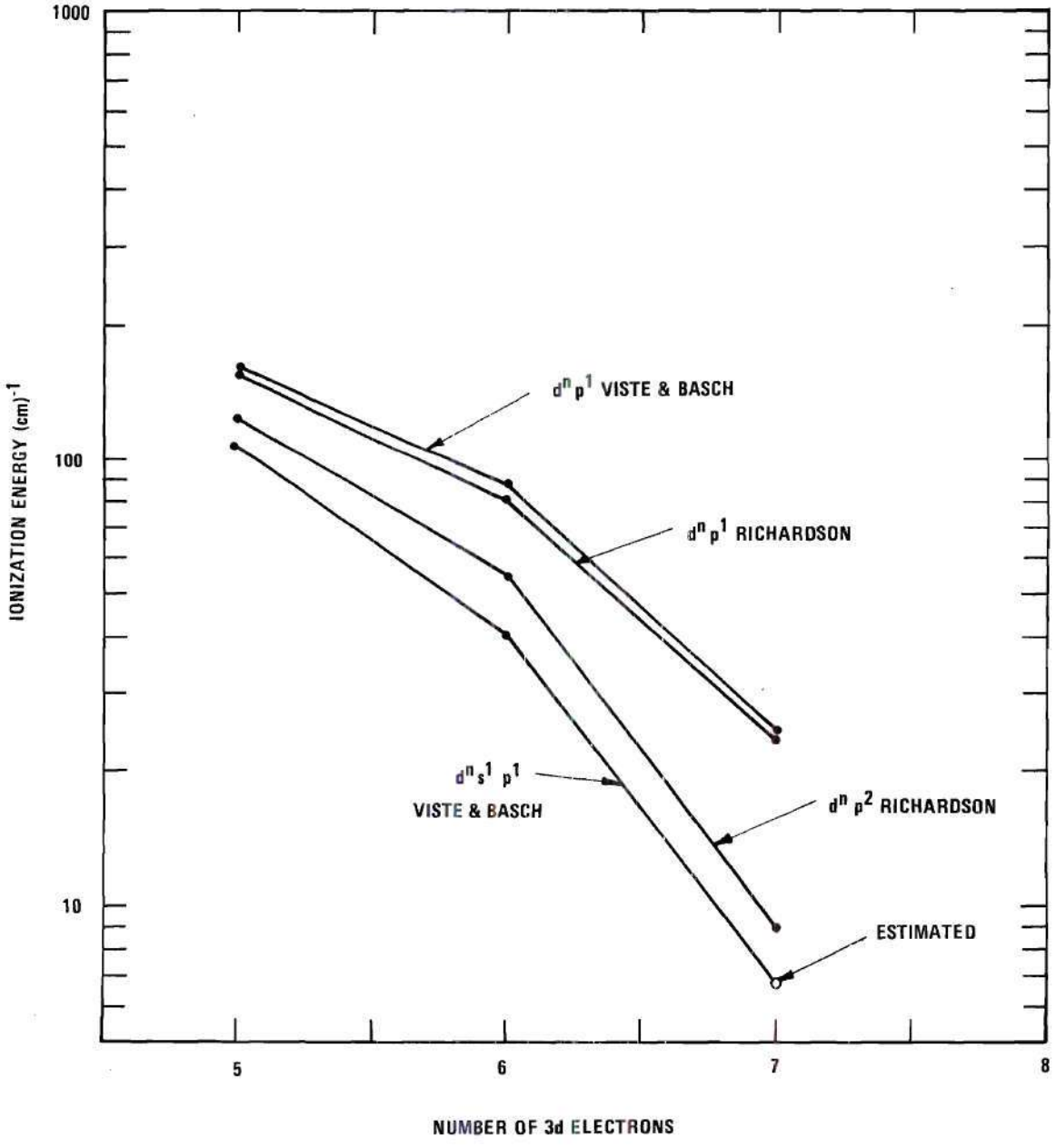

Figure 26. 4p Ionization Potentials for Fe

It is assumed that the ionization potential can be expressed functionally as

$$I.P. = f(a,b,c).$$

Very little is known about the function except its value at several combinations of integral values of the arguments. It is probable that a linear interpolation based on these few points is a rather crude approximation, however, in light of the information presently available any other approximation would be just as arbitrary.

The interpolation algorithm is slightly different for evaluation of s, p, and d I.P.'s. This is because the "known" ionization potentials are given for different argument values in each case. Figure 27 shows the points in a, b, c space for which a value of the IP exists for the s, p, and d orbitals of the Fe atom. Fortunately all calculations performed to date by this author, and those reported in the literature, produce electronic orbital populations within the region where data points are available. Population of 4s and 4p orbitals is generally less than one. From Figure 27 it then appears that approximation of 4s IP is probably the least accurate since the only data points available are for b and c equal to one or two. On the other hand evaluation of 3d IP's is probably most accurate.

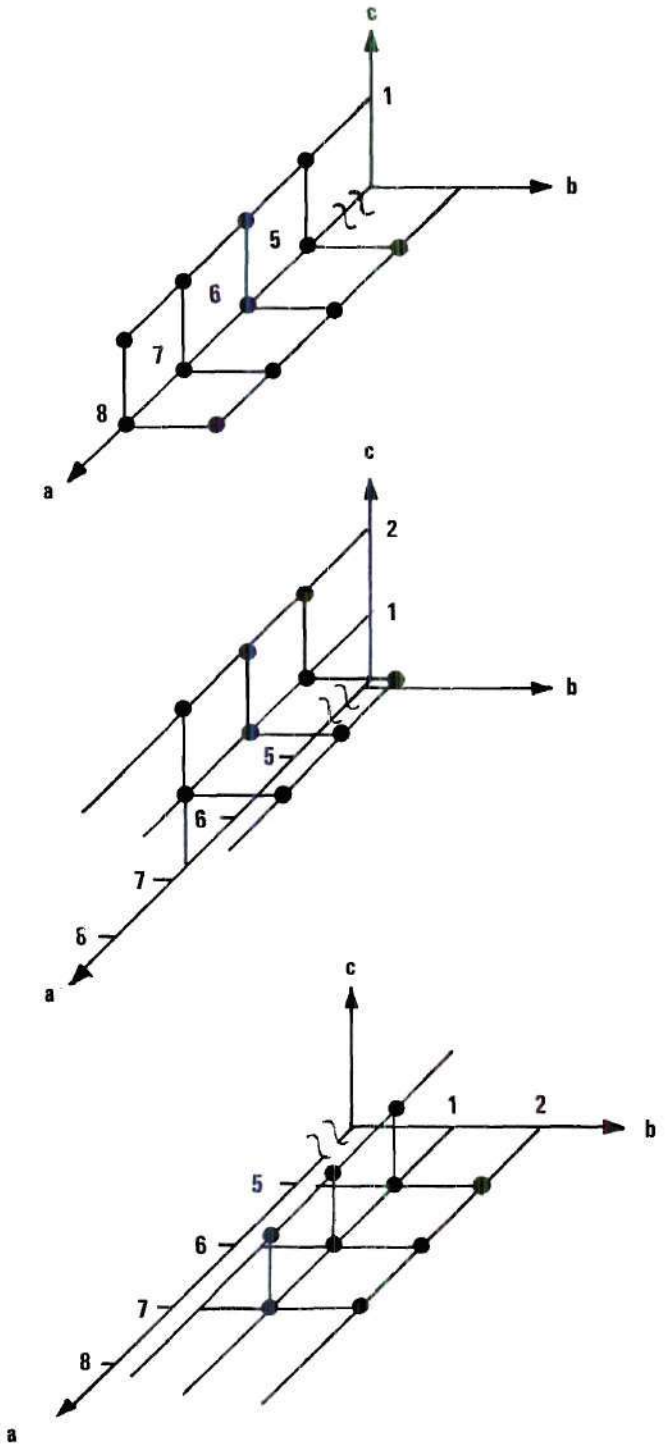

Figure 27. Points for Which Tabulated I.P. Exists for Fe (Atomic Charge Configuration for Atom is $3d^a\ 4s^b\ 4p^c$)

The algorithm to evaluate the IP of the Fe 4p orbital is given here. The other two cases are handled in a similar, but not identical fashion.

Assume we are to find the ionization potential $IP(a_1,b_1,c_1)$ where a, b, and c are non-integers. The general approach is to interpolate along the a axis to the point a_1. At this point evaluate the slopes $\Delta(IP)/\Delta b$ and $\Delta(IP)/\Delta c$. The IP is then approximated using these slopes. Specifically, define

Ta_1 = Smallest integer larger than a_1

La_1 = Largest integer smaller than a_1

then

$$\frac{\Delta IP}{\Delta a}\Big]_{a_1,0,1} \triangleq IP(Ta_1,0,1) - IP(La_1,0,1) \; . \tag{89}$$

The linear slopes $\Delta IP/\Delta b$ and $\Delta IP/\Delta c$ are calculated at $(a_1,0,1)$ as

$$\frac{\Delta IP}{\Delta b} = \{[IP(Ta_1,1,1) - IP(Ta_1,0,1)] \tag{90}$$

$$- [IP(La_1,1,1) - IP(La_1,0,1)]\} \; (a_1,-La_1)$$

$$+[IP(La_1,1,1) - IP(La_1,0,1)]$$

$$\frac{\Delta IP}{\Delta c} = \{[IP(Ta_1,0,2) - IP(Ta_1,0,1)] \qquad (91)$$

$$- [IP(La_1,0,2) - IP(La_1,0,1)]\}(a_1-La_1)$$

$$+ [IP(La_1,0,2) - IP(La_1,0,1)] .$$

These difference equations are first order approximations to the equations

$$\frac{d(IP)}{d\,b}\Big]_{a_1,0,1} = \frac{d(IP)}{d\,b}\Big]_{La_1,0,1}$$

$$+ (a_1-La_1)\{\frac{d(IP)}{d\,b}\Big]_{Ta_1,0,1} - \frac{d(IP)}{d\,b}\Big]_{La_1,0,1}\},$$

and

$$\frac{d(IP)}{d\,c}\Big]_{a_1,0,1} = \frac{d(IP)}{d\,c}\Big]_{La_1,0,1}$$

$$+ (a_1-La_1)\{\frac{d(IP)}{d\,c}\Big]_{Ta_1,0,1} - \frac{d(IP)}{d\,c}\Big]_{La_1,0,1}\} .$$

From the slopes calculated as in equations (89), (90), and (91) the ionization potential at (a_1, b_1, c_1) is determined as

$$IP(a_1,b_1,c_1) = IP(La_1,0,1)+\frac{\Delta IP}{\Delta a}(a_1-La_1)+\frac{\Delta IP}{\Delta b}(b_1)+ \frac{\Delta IP}{\Delta c}(c_1-1).$$

The only variation of this procedure for calculation of ionization potential in the case of 3d and 4s orbitals is the point at which the slopes are calculated. For 3d orbitals the slopes are computed at $(a_1,0,0)$; for 4s orbitals at $(a_1,1,0)$. This is necessary because of the known data points as illustrated in Figure 27.

These interpolation routines are written as procedures and incorporated in the complete molecular orbital program. They are given the procedural names $H_{ii}(n)$, $H_{ii}(p)$ and $H_{ii}(s)$ for the cases of 3d, 4p and 4s orbital IP's respectively.

CHAPTER IV

MOLECULAR ORBITAL CALCULATIONS

This chapter will present results of the actual calculations performed according to the theoretical description of Chapter III. Because of the complexity of the crystal structure of the rare earth iron garnets it seemed advisable to first study the results obtained on a simpler material. Recent optical spectra taken on the rare earth orthoferrites, $REFeO_3$, provided such an opportunity. These materials crystallize into a perovskite structure with the iron atoms all existing in identical octahedrally coordinated sites. Thus a comparison of the optical spectra with an octahedral LCAO molecular orbital calculation should indicate if a reasonable transition identification can be made. It has been found that the agreement between experimental and predicted transition energies is indeed quite reasonable; well within the error one might expect on the basis of the assumptions made by the LCAO theory presented.

Rare Earth Orthoferrites

The rare earth orthoferrites are of great technical interest primarily because of recent work at Bell Telephone Laboratories demonstrating their applicability in domain wall logic and storage systems.[39] The crystal structure of these

materials was evaluated in 1956 by Geller.[40] He showed that although the actual crystal structure is distorted from the ideal perovskite unit, the Fe atoms exist in a nearly symmetrical octahedrally coordinated site. Actual measured distances between Fe and the surrounding oxygen atoms were:

4 Oxygen at 1.9Å

2 Oxygen at 2.0Å.

For the LCAO calculations reported here, the average value of 1.93 angstroms was chosen for the Fe-O interatomic distance.

The neutral iron atom has an atomic structure of Argon Core + $3d^6$ + $4s^2$ and oxygen has $1s^2$ + $2s^2$ + $2p^4$. The basis set of atomic functions was therefore chosen as the iron 3d, 4s and 4p orbitals and the oxygen 2p orbitals. The iron 4p orbital is included because it is fairly close in energy to the 4s orbital. One would therefore expect it might contribute to some of the low level molecular orbitals and definitely to the higher level excited states. The 3s oxygen orbital is at a much higher energy than the 2p orbitals and since the net charge on the oxygen in the molecule is very small it seems reasonable to assume that no significant population of orbitals higher than 2p will occur.

The question of whether or not to include the 2s orbitals must also be considered. It seems likely that the $1s^2$ and $2s^2$ filled orbitals act as a closed core. Hence electrons in these orbitals would be completely localized and not contribute to the molecular orbital population. This is supported

by the fact that the orbital ionization energy for 2p orbital is approximately 128,000 cm^{-1} while that of the 2s orbital is approximately 261,000 cm^{-1}. Finally it was shown by Ballhausen and Gray[22] in LCAO calculations of CrF_6^{---} that neglect of the 2s fluorine orbitals actually improved correlation with their experimental results. Based on these considerations the oxygen 2s orbital was not included in the molecular orbital basis set.

There are therefore 32 electrons, eight from the iron atom and 24 from the six oxygen atoms, which will go into molecular orbitals. The fundamental basis set, from which the symmetry adapted orbitals are derived, consists of 27 atomic orbitals. These are the five 3d, one 4s, and three 4p orbitals of the iron atom and the 18 2p orbitals of the six oxygen atoms.

Atomic Radial Functions

The radial function for the oxygen 2p orbital was taken from Clementi.[27] The function for the neutral atom was chosen as this is very nearly the configuration finally existing in the molecular structure. Appendix F provides a derivation of the complete function from the tabulated data of the reference. The final result is:

$$R_{2p}(r) = 0.270198\ r\ e^{-(1.1536)r} + 2.875131\ r\ e^{-(1.7960)r} \quad (92)$$

$$+ 8.44977\ r\ e^{-(3.4379)r} + 3.034869\ r\ e^{-(7.9070)r}.$$

Data for the iron 3d radial function was obtained from Watson.[41] This radial function is for the charge configuration $3d^6 4s^2$. In the actual molecular case it will be shown that the stable charge distribution on the iron atom is about $3d^{6 \cdot 5} 4s^{0 \cdot 4} 4p^{0 \cdot 4}$. In his paper Watson points out that the d orbital functions are very nearly independent of population in 4s and 4p orbitals. Thus the free atom function given for six 3d electrons should be a reasonable approximation.

Derivation of this function as well as the 4s radial function from tabulated data is given in Appendix G. The result for the Fe 3d orbital is:

$$R_{3d}(r) = 2.69843\ r^2\ e^{-(2.1208)r} + 32.82718\ r^2\ e^{-(4.1580)r} \quad (93)$$

$$+ 85.39640\ r^2\ e^{-(7.8223)r} + 19.18024\ r^2 e^{-(13.9775)r}$$

The iron 4s orbital is the most complicated of all in that it requires ten terms for an adequate description according to Watson. Again the function for a configuration $3d^6 4s^2$ was chosen. The selection was not an arbitrary matter of choice however, in that this was the closest configuration available in the literature. It is anticipated that the free atom 4s orbital determined on the basis of full population is somewhat less extended than would exist for a population typical of the molecular case. As a result the computed overlaps will be a little smaller than that actually existing in the

solid. The affect of this reduced overlap is to somewhat reduce the splitting of the molecular orbitals derived from the 4s atomic basis function. In actual practice it is found that no change would be observed in the optical spectra, however, because transitions from or to molecular orbitals with 4s components occur at energies far above the ultraviolet limit of these experiments. Written out explicitly the 4s radial function for Fe is

$$R_{4S}(r) = -6.18280\, e^{-(27.1431)r} - 40.98153\, r\, e^{-(23.7801)r} \quad (94)$$

$$+ 34.16641\, r\, e^{-(12.0977)r} + 142.72488\, r^2\, e^{-(11.1832)r}$$

$$-13.56644\, r^2\, e^{-(6.5137)r} - 20.45643\, r^2\, e^{-(4.0556)r}$$

$$+ 12.73629\, r^3\, e^{-(4.4235)r} + 1.17226\, r^3\, e^{-(2.0972)r}$$

$$+ 0.18872\, r^3\, e^{-(1.2576)r} + .00766\, r^3\, e^{-(0.8370)r}.$$

The 4p radial function was obtained from Richardson et al.[42] Watson does not include the 4p orbitals in his paper, and it appears that Richardson's work is the most recent and complete. He presents radial functions for a variety of population configurations from $3d^7 4p^2$ to $3d^5 4p$. For the molecular orbital calculations of the orthoferrite the configuration $3d^6 4p^1$ has been chosen as most representative. Appendix H shows the derivation of the actual function. Repeated here

then we have for the 4p radial function of Fe,

$$R_{4p} = 17.28079\ r\ e^{-(10.60)r} - 8.96790\ r^2\ e^{-(4.17)r} + 0.31046\ r^3\ e^{-(1.25)r}. \quad (95)$$

Because of the possibility of making undetected errors in computing the appropriate wave function coefficients, a technique is desirable to provide a check on the results. To that end a computer program was written which integrates the function $F(r) = r^2\ R^2(r)$ over a wide interval of r. The result, of course, should be unity. In addition the program provides an on line plot of F(r) which can be used in comparison with published data of similar functions to indicate any obvious errors. For each of the orbitals listed the value of the integral

$$\int_0^{6\text{Å}} r^2\ R^2(r)\ dr$$

was found to be:

O 2p	1.0000
Fe 3d	1.0002
Fe 4s	1.0001
Fe 4p	0.9999

This provides a high degree of confidence that the functions used are reasonably accurate.

Copies of the on line plots of F(r) for these four functions are shown in Figures 28, 29, 30, and 31. A copy of the program is given in Appendix E.

Two Atom Overlap Integrals

Using the wave functions described in the last section, along with the Fe-O interion distance of 1.93 Å, the necessary two atom overlaps were calculated. The values are given in Table 15.

From these two atom overlaps group overlaps of the symmetry adapted orbitals can be computed as described in Chapter III. To evaluate the group overlaps it is first necessary to calculate the correction factors for ligand function normalization. The expressions for these factors for octahedral symmetry were given previously in Table 13. The actual numerical values as obtained for the orthoferrite case are listed in Table 16. The expressions for the octahedral group overlap integrals were given previously in Table 11. Values as computed for the orthoferrite, using the two atom overlap integrals and appropriate normalization correction factors, are also tabulated in Table 16.

The final information needed from the overlap values is the one electron orbital energy correction for the ligand symmetrized orbitals. This correction was derived as eq. (86) where it was shown that the diagonal matrix element

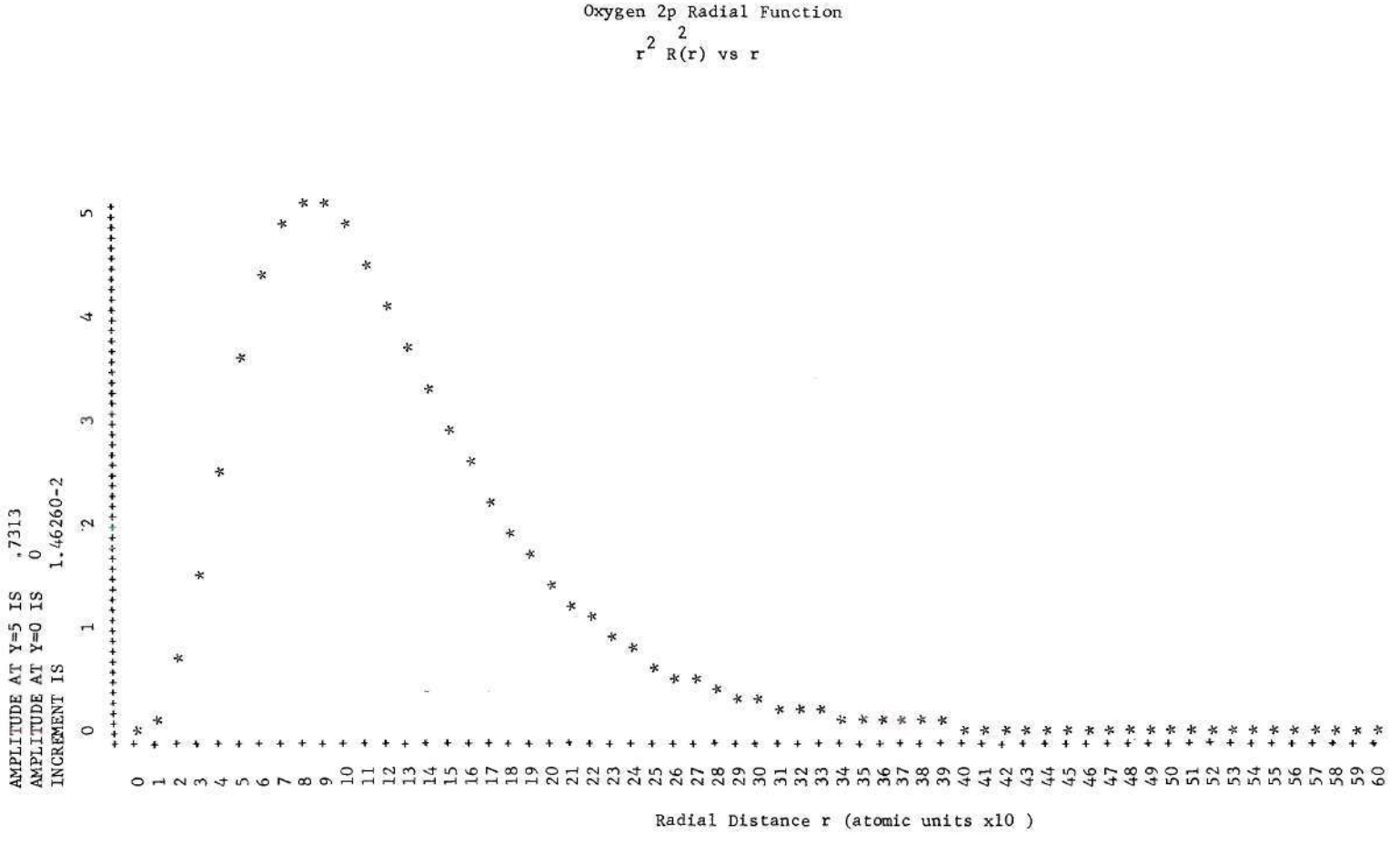

Figure 28. Oxygen 2p Radial Function

Figure 29. Fe 3d Radial Distribution

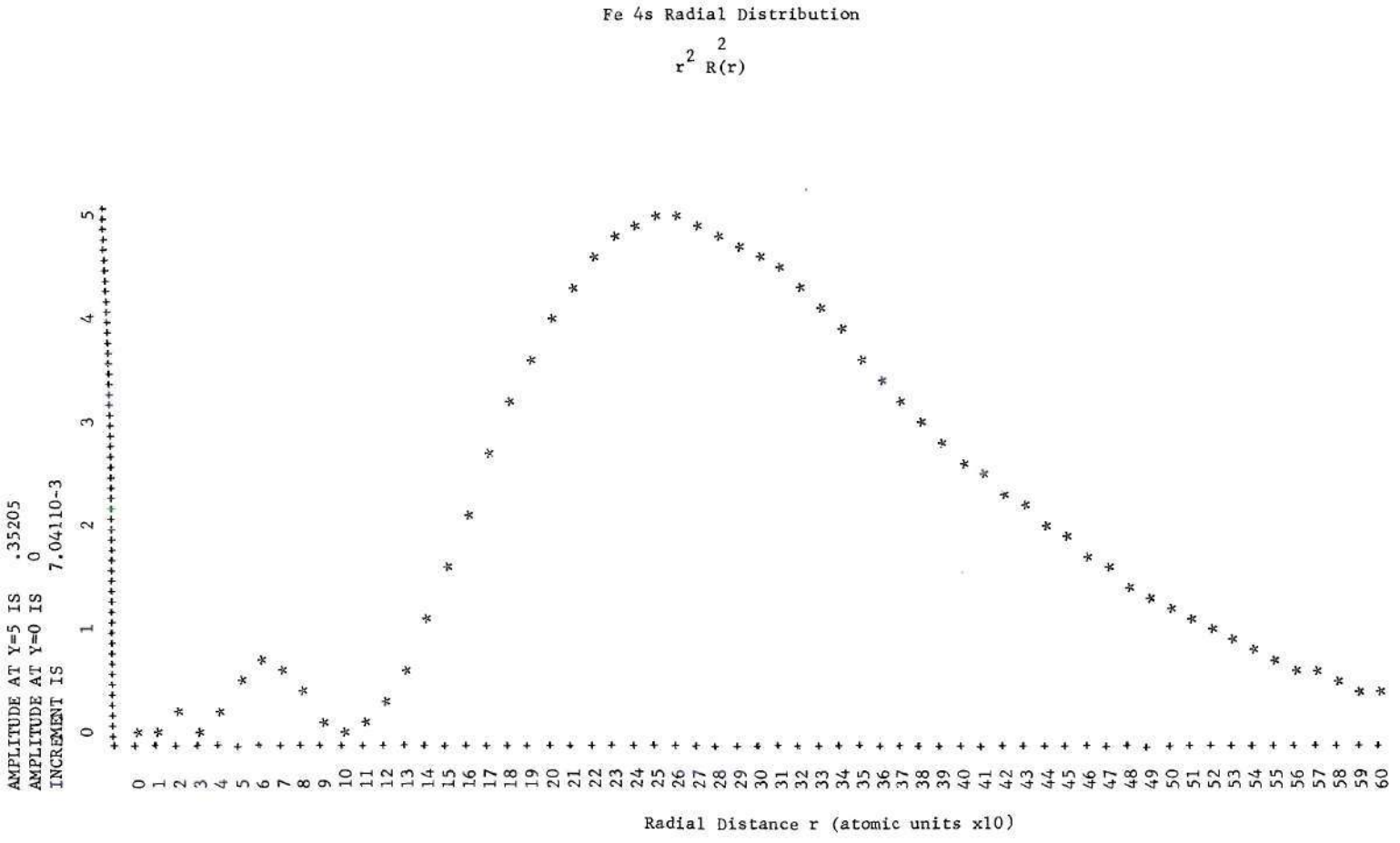

Figure 30. Fe 4s Radial Distribution

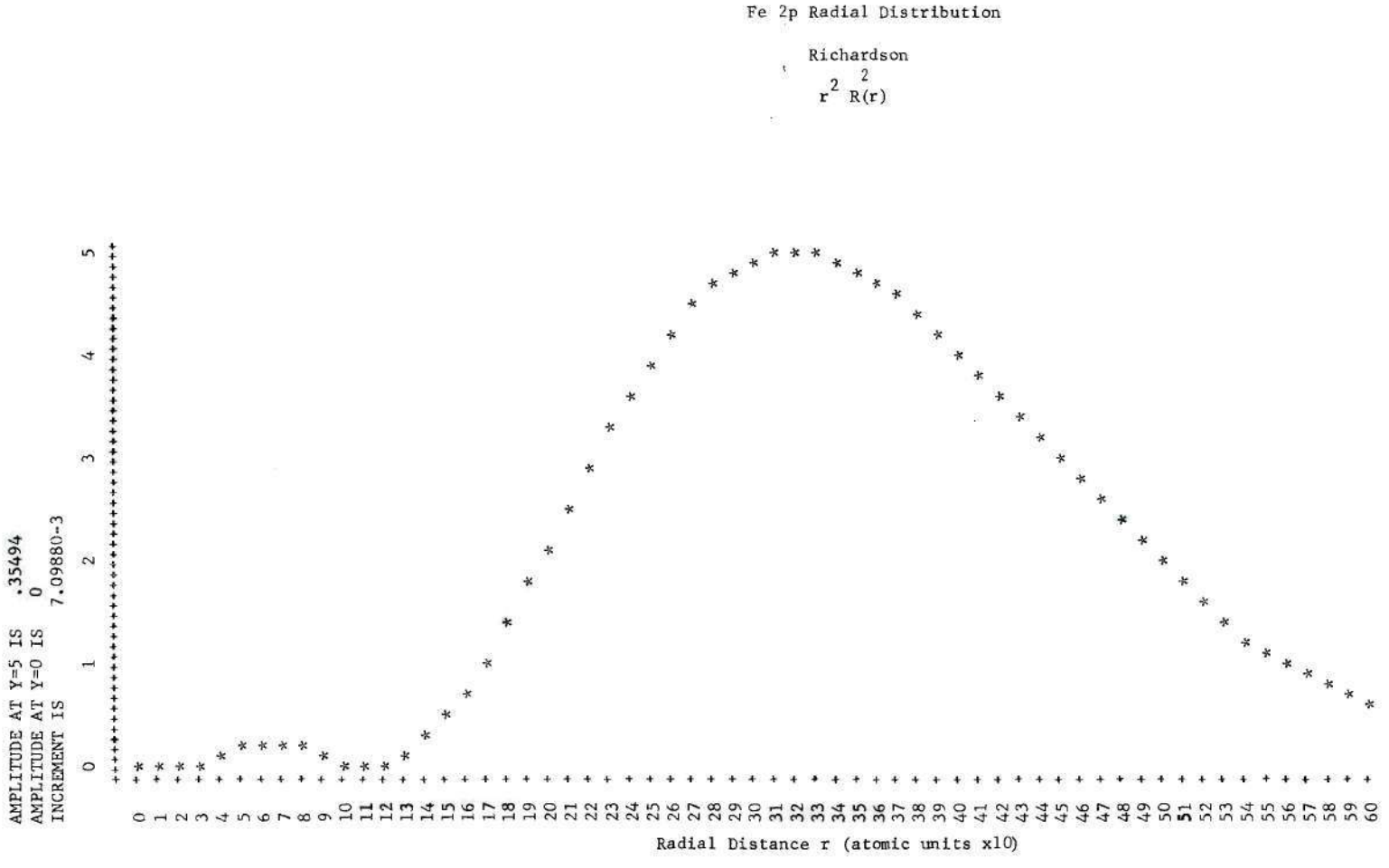

Figure 31. Fe 2p Radial Distribution

Table 15. Two Atom Overlaps for $GdFeO_3$ Orthoferrite. Metal-Ligand Separation R = 1.93 Å = 3.655 Atomic Units.

Metal-Ligand Overlaps

Type	Value
$S(4s_{\sigma M}, 2p_{\sigma L}; R)$	0.16277
$S(3d_{\sigma M}, 2p_{\sigma L}; R)$	0.09139
$S(3d_{\pi M}, 2p_{\pi L}; R)$	0.05407
$S(4p_{\sigma M}, 2p_{\sigma L}; R)$	0.14270
$S(4p_{\pi M}, 2p_{\pi L}; R)$	0.18400

Ligand-Ligand Overlaps

Type	Value
$S(2p_{\sigma L}, 2p_{\sigma L}; 2R)$	0.009214
$S(2p_{\sigma L}, 2p_{\sigma L}; \sqrt{2}R)$	0.055100
$S(2p_{\pi L}, 2p_{\pi L}; 2R)$	0.001432
$S(2p_{\pi L}, 2p_{\pi L}; \sqrt{2}R)$	0.012870

Table 16. Normalization Correction Factors, Group Overlap Integrals and Ligand Energy Correction Factors for Orthoferrite.

IR Orbital	K_{IR}	G_{IR}	N_{IR}
a_{1g}	1.07	0.373	1.127
e_g	0.97	0.163	0.938
$t_{1u}(\sigma_M\sigma_L)$	1.00	0.202	0.992
$t_{1u}(\pi_M\pi_L)$	1.01	0.365	1.014
$t_{1u}(\sigma_L\pi_L)$	-	0.0478	-
t_{2g}	1.03	0.105	1.062
t_{1g}	0.96	-	0.916
t_{2u}	0.99	-	0.975

of a symmetrized ligand orbital is given as

$$H_{ii} = \langle \psi(LA) | H_{op} | \psi(LA) \rangle \frac{[1+F(k/\Sigma a_i^2)]}{[1+(k/\Sigma a_i^2)]} .$$

Thus the energy of the symmetrized ligand orbital is equal to the energy associated with any one of its basis orbitals times the factor shown. The denominator of the correction factor, i.e., $1+(k/\Sigma a_i^2)$ is simply the square of the correction factor K_{IR} for normalization of the symmetrized orbital. The energy correction factor N_{IR} can thus be expressed then as:

$$N_{IR} = \frac{[1+F(k/\Sigma a_i^2)]}{[1+(k/\Sigma a_i^2)]} = \frac{1+F(K_{IR}^2-1)}{K_{IR}^2} . \qquad (96)$$

Experience with the overall program has shown that the value of the phenomenological proportionality constant F is very nearly two in all cases. It is therefore convenient to let F = 2 exactly for the calculation of the N_{IR} terms and treat them as constants for the rest of the calculations. The results of this computation for the orthoferrite case are given in the last column of Table 16.

With this data computed, the complete molecular orbital calculation can proceed for the octahedral Fe site in the orthoferrite. Before considering the actual results it is appropriate to outline the mechanics of the complete solution

and discuss the computer program which carries out the computation.

Complete Solution Sequence

In the application of the LCAO model to the study of magnetic oxides, such as the garnets and orthoferrites, the assumption is made that specific atomic sites can be treated as independent entities. This is obviously not true, any more than is the crystal field theory approximation that a single ion can be treated as a separate entity, perturbed only by the charge of nearest neighbor ligand ions. On the other hand, it provides a solution to a higher order of accuracy than the crystal field model, because it explicitly takes into account mixing of ligand orbitals into the total wave functions. Ultimate justification of the approximation can only be provided on the basis of agreement of results with experimental evidence.

The solution thus assumes an array of atoms, originally completely neutral, possessing a specific symmetry. In the orthoferrite we are dealing with an Fe atom surrounded by six oxygen atoms octahedrally coordinated. From the symmetry group properties of octahedral symmetry as discussed in Chapter III we know there exist the possibility of ten types of molecular orbitals, i.e., O_h possesses ten different irreducible representations. This was shown in Table 6. By evaluating the symmetry properties of the atomic orbitals to form molecular orbitals, i.e., Fe 3d, 4s, 4p and O 2p, it is

found that only six of the possible ten can actually exist. These are a_{1g}, e_g, t_{1u}, t_{2g}, t_{1g}, and t_{2u} as shown in Table 8.

Secular Equations. It has been shown that the secular equation for the entire molecular arrangement can be reduced to the solution of a set of low order secular equations involving individual IR's. Each small secular equation is of the from

$$|H_{ij} - G_{ij}E| = 0$$

where $$H_{ij} = \langle \Psi_i | H_{op} | \Psi_j \rangle$$

and $$G_{ij} = \langle \Psi_i | \Psi_j \rangle .$$

The order of each of these determinants is equal to the number of symmetry adapted atomic functions having the appropriate symmetry. Referring to Table 8 it is seen that the a_{1g} determinant will be second order as will that for e_g and t_{2g}. The t_{1u} determinant will be of order three and the orbitals t_{1g} and t_{2u} are only one dimensional. Note that in general there is degeneracy associated with each IR. For example e_g is doubly degenerate, and t_{1u}, t_{2g}, t_{1g}, and t_{2u} are triply degenerate. It is, of course, unnecessary to include a separate secular equation for each orbital of a given IR.

As an example of one secular equation consider the t_{1u} IR. Let

$$\Psi_{4p} = \psi_{4p_x} = \text{metal } 4p_x \text{ orbital} \tag{97}$$

$$\Psi_{2p\sigma} = \frac{1}{\sqrt{2}K_{\sigma}(t_{1u})}(\psi_{2p_{z_1}} - \psi_{2p_{z_2}}) = \sigma \text{ Ligand Symmetrized Orbital}$$

$$\Psi_{2p\pi} = \frac{1}{2K_{\pi}(t_{1u})}(\psi_{2p_{y_2}} + \psi_{2p_{x_5}} - \psi_{2p_{x_4}} - \psi_{2p_{y_6}}) = \pi \text{ Ligand Symmetrized Orbital.}$$

The t_{1u} secular equation then becomes

$$\begin{vmatrix} [H_{4p,4p} - E_{t_{1u}}][H_{4p,2p\sigma} - E_{t_{1u}} G_{t_{1u}}(4p,2p\sigma)][H_{4p,2p\pi} - E_{t_{1u}} G_{t_{1u}}(4p,2p\pi)] \\ [H_{2p\sigma,4p} - E_{t_{1u}} G_{t_{1u}}(2p\sigma,4p)][H_{2p\sigma,2p\sigma} - E_{t_{1u}}][H_{2p\sigma,2p\pi} - E_{t_{1u}} G_{t_{1u}}(2p\sigma,2p\pi)] \\ [H_{2p\pi,4p} - E_{t_{1u}} G_{t_{1u}}(2p\pi,4p)][H_{2p\pi,2p\sigma} - E_{t_{1u}} G_{t_{1u}}(2p\pi,2p\sigma)][H_{2p\pi,2p\pi} - E_{t_{1u}}] \end{vmatrix} = 0. \tag{98}$$

There are determinants of this general form for each symmetry, i.e., for each type of molecular orbital.

The values of the group overlap integrals can be calculated exactly as previously discussed. For $GdFeO_3$ the numerical values have been tabulated in Table 16. By symmetry $G(\Psi_i,\Psi_j) = G(\Psi_j,\Psi_i)$. The matrix elements H_{ii} and H_{ij} are assigned values based on atomic orbital ionization potential according to Koopman's theorem and the Wolfsberg-Helmholz approximation respectively.

The first iteration of the total self-consistent solution uses matrix element values based on an assumed electron distribution among the Fe orbitals. The distribution on the ligand orbitals changes very little from the free atom value because any charge redistribution from the metal atom is shared over six oxygen orbitals equally. For this reason the ionization potential of the oxygen atomic orbitals is assumed constant throughout the solution. It has, however, been found appropriate to increase the absolute value of the oxygen ionization potential about 15 per cent above the free atom value for best agreement with experimental results.

Making an initial electron distribution assumption, the ionization potentials may be estimated using the interpolation scheme discussed in Chapter III.

The matrix elements in the secular equation determinants are then assigned values

$$H_{ii} = -IP(\Psi_i) \tag{99}$$

$$H_{ij} = -F\ G(\Psi_i\Psi_j)\sqrt{H_{ii}\ H_{jj}}$$

where F is a phenomenological proportionality constant. With all terms in the determinants known the secular equation for each IR may be solved yielding a set of eigenvalues E. The t_{1u} secular equation produces three energy eigenvalues $E^1_{t_{1u}} < E^2_{t_{1u}} < E^3_{t_{1u}}$ where the superscript simply represents the relative energy with respect to the other eigenvalues corresponding to the same symmetry.

Each of the resulting eigenvalues, E^1, E^2, etc., can then be substituted back into the set of equations from which the secular equation was derived. From these equations the coefficients of the molecular orbital are determined. The set of equations of this type was given in equation (23). For the case of the octahedral t_{1u} orbital they become simply

$$C^n_1(H_{11}) + C^n_2(H_{12}-E^nG(1,2)) + C^n_3(H_{13}-E^nG(1,3)) = 0 \qquad (100)$$

$$C^n_1(H_{21}-E^nG(2,1)) + C^n_2(H_{22}) + C^n_3(H_{23}-E^nG(2,3)) = 0$$

$$C^n_1(H_{31}-E^nG(3,1)) + C^n_2(H_{32}-E^nG(3,2)) + C^n_3(H_{33}) = 0$$

where $H_{11} = H_{4p,4p}$, $H_{12} = H_{4p,2p\sigma}$, $G(1,2) = G(4p,2p\sigma)$ etc. in correspondence with equation (98).

As discussed in Chapter III only two of the three equations are independent, hence all three coefficients cannot be uniquely determined. It is possible however to determine the ratio of all coefficients with respect to any one

single coefficient. Assuming $C_1^n \neq 0$ all terms can be divided by C_1^n and using any two of the three equations, for example the first two,

$$\begin{bmatrix} H_{11} \\ H_{21}-E^nG(2,1) \end{bmatrix} = \begin{bmatrix} (H_{12}-E^nG(1,2)) & (H_{13}-E^nG(1,3)) \\ H_{22} & (H_{23}-E^nG(2,3)) \end{bmatrix} \begin{bmatrix} C_2^n/C_1^n \\ C_3^n/C_1^n \end{bmatrix}. \quad (101)$$

Orbitals having determinants higher than order three are handled by obvious extension of this three dimensional example.

At this point in the solution the complete orbital eigenfunction, for each eigenvalue of each IR is known within a multiplicative constant C_1^k. This last constant is found by invoking the normalization criteria. For example, in the case of a t_{1u} orbital with eigenvalue $E^k_{t_{1u}}$ the molecular orbital function is

$$^k\Phi_{t_{1u}} = C_1^k[\Psi_{4p}+(C_2^k/C_1^k)\Psi_{2p\sigma}+(C_3^k/C_1^k)\Psi_{2p\pi}]; \quad 1\leq k\leq 3 \quad (102)$$

where the basis functions were defined in equation (97) and the coefficients (C_j^k/C_1^k) are given from the solution of equation (101). Normalization demands $\langle {}^k\Phi_{t_{1u}} | {}^k\Phi_{t_{1u}} \rangle = 1$. Applying the normalization criteria to eq. (102) gives

$$(C_1^k)^2[\langle\Psi_{4p}|\Psi_{4p}\rangle + 2(C_2^k/C_1^k)\langle\Psi_{4p}|\Psi_{2p\sigma}\rangle + 2(C_3^k/C_1^k)\langle\Psi_{4p}|\Psi_{2p\pi}\rangle \quad (103)$$

$$+ (C_2^k/C_1^k)^2\langle\Psi_{2p\sigma}|\Psi_{2p\sigma}\rangle + 2(C_2^k/C_1^k)(C_3^k/C_1^k)\langle\Psi_{2p\sigma}|\Psi_{2p\pi}\rangle$$

$$+ (C_3^k/C_1^k)^2\langle\Psi_{2p\pi}|\Psi_{2p\pi}\rangle] = 1 \ .$$

Since all symmetry adapted functions are initially normalized, $\langle\Psi_i|\Psi_i\rangle = 1$. The other terms are group overlap integrals which have been previously calculated. Thus equation (103) can be written as

$$C_1^k = [1+2(C_2^k/C_1^k)G_{t_{1u}}(4p_M, 2p_{\sigma L}) + 2(C_3^k/C_1^k)G_{t_{1u}}(4p_M, 2p_{\pi L}) \quad (104)$$

$$+ 2(C_2^k/C_1^k)(C_3^k/C_1^k)G_{t_{1u}}(2p_{\sigma L}, 2p_{\pi L}) + (C_2^k/C_1^k)^2 + (C_3^k/C_1^k)^2]^{-1/2}$$

The general form for the normalization coefficient C_1^k for any molecular orbital IR having a secular determinant of order M can be written as a generalization of eq. (104) as:

$$C_1^k = [1 + \sum_{i=2}^{m}(C_i^k/C_1^k) + 2\sum_{i=1}^{m-1}\sum_{j=i-1}^{m}(C_i^k/C_1^k)(C_j^k/C_1^k)G_{IR}(\Psi_i,\Psi_j)]. \quad (105)$$

Solution of equation (105) for each Φ_{IR} permits complete definition of the set of all molecular orbitals.

Population Analysis. To check the validity of the originally assumed population of metal atom atomic orbitals on which the solution is based, it is necessary to analyze how the molecular orbitals distribute the electrons. The technique applied here is based on the concepts originally proposed by Mulliken.[43,44] In this model the charge assigned to a given iron orbital is that associated directly with its molecular orbital coefficient plus one half of the charge shared via overlap with all ligand orbitals.

Assume for example a molecular orbital is given as

$$\Phi_{IR} = C_1 \Psi_M + C_2 \Psi_L$$

where Ψ_M corresponds to a given metal atom orbital and Ψ_L is a symmetry adapted ligand term. Since $\langle \Phi_{IR} | \Phi_{IR} \rangle = 1$, then for N electrons occupying the orbital we can interpret the equation

$$N \Phi_{IR}^2 = NC_1^2 + 2NC_1 C_2 G(\Psi_M, \Psi_L) + NC_2^2$$

as describing the distribution of total charge between metal ligand and overlap contributions.

For the sake of carrying out the molecular orbital calculations herein described the criteria has been adopted that half of the overlap charge will be assigned to the metal

orbital and half to the symmetrized ligand orbital. Thus, in this example, the number of electrons occupying Ψ_M because of the Φ_{IR} molecular orbital is

$$n = N(C_1^2 + C_1 C_2 G(\Psi_M, \Psi_L)) \quad . \tag{106}$$

This can be generalized to a molecular orbital of the general form

$$\Phi_{IR} = C_1\Psi_{M1} + C_2\Psi_{L2} + C_3\Psi_{L3} + \cdots C_m\Psi_{Lm} \tag{107}$$

to be

$$n_{M1} = N\left[C_1^2 + \sum_{j=2}^{m} C_1 C_j G(\Psi_M, \Psi_{Lj})\right] \quad . \tag{108}$$

Evaluation of the orbital occupation constant N is carried out by first ordering the eigenfunctions according to the relative magnitude of their respective eigenvalues. Thus all the eigenfunctions resulting from the secular equations of the IR's are ordered according to energy. The total number of valence electrons are then assigned to these orbitals starting at the bottom. Each orbital can of course hold two electrons and for a specific IR the eigenfunction calculated must be remembered as only one of a degenerate set. The

degeneracy depending on the IR. For example in the case of the t_{1u} orbital, three eigenfunctions were found $1t_{1u}$, $2t_{1u}$ and $3t_{1u}$. Referring back to Table 8 it is recalled that the t_{1u} IR is triply degenerate. Hence each of the t_{1u} orbitals may be considered to hold six electrons.

After all electrons are assigned to molecular orbitals a population analysis is carried out applying equation (108) to each orbital. The total charge associated with a given atomic orbital is determined and compared with the initially assumed population. If they are different, a new original assumption is made and the process repeated.

Computer Program. The computer program for the octahedral site LCAO self-consistent charge calculation is duplicated in Appendix I. A brief description of its basic parts is in order here to facilitate its use and extensions by future investigators.

In the octahedral case, there are no secular equations higher than third order. As a consequence it is relatively easy to expand the determinants in general form by hand and simply design the solution algorithms to carry out the required arithmetic computations. This is what has been done in the octahedral program because it is most economical in terms of computer time.

For higher order secular equations, direct expansion is not possible. A completely numerical solution has been designed and written for solutions of such higher order secular

equations. It can handle up to a 20 x 20 determinant and is written as a procedure so as to be incorporable in any ALGOL program. This procedure is listed in Appendix J.

We now return to the details of the octahedral site LCAO program. The first 15 lines are simply definition statements. Then from line 16 through line 120 are listed the procedures used by the program proper which starts at line 122.

The first procedure, lines 16 through 65, carries out the solution for a third order secular equation. A molecular wave function of the type

$$\Phi = C_1\Psi_{M1} + C_2\Psi_{L2} + C_3\Psi_{L3} \qquad (109)$$

is assumed where Ψ_{M1} is a central atom atomic function. Ψ_{L2} and Ψ_{L3} are symmetry adapted ligand functions

$$\Psi_{L2} = \sum_i a_i \psi_{i,L2}$$

$$\Psi_{L3} = \sum_i a_i \psi_{i,L3}$$

each composed of combinations of particular type ligand orbitals ψ_{L2} and ψ_{L3} respectively. Thus the formal parameter list associated with the procedure statement is interpreted as follows:

H11 = $\langle\psi_M|H_{op}|\psi_M\rangle \triangleq -IP(\psi_M)$

H22 = $\langle\psi_{L2}|H_{op}|\psi_{L2}\rangle \triangleq -IP(\psi_{L2})$

N2 = Energy Correction Factor for Ψ_{L2}; Equation (96)

H33 = $\langle\psi_{L3}|H_{op}|\psi_{L3}\rangle \triangleq -IP(\psi_{L3})$

N3 = Energy Correction Factor for Ψ_{L3}; Equation (96)

S12 = Group Overlap $\langle\Psi_{M1}|\Psi_{L2}\rangle = G_{IR}(\Psi_{M1},\Psi_{L2})$

S13 = Group Overlap $\langle\Psi_{M1}|\Psi_{L3}\rangle = G_{IR}(\Psi_{M1},\Psi_{L3})$

S23 = Group Overlap $\langle\Psi_{L2}|\Psi_{L3}\rangle = G_{IR}(\Psi_{L2},\Psi_{L3})$

E = An output array for the temporary storage of the three eigenvalues E^1, E^2, E^3.

C = A two dimensional array for the storage of eigenfunction coefficients C_j^i where i corresponds to i^{th} eigenvalue and j = 1,2,3 for the appropriate term of eq.(109).

Thus, supplying this procedure with the appropriate atomic orbital energies, i.e., diagonal matrix elements, plus overlap terms, it computes the eigenvalues and corresponding eigenfunction based on the approximations previously discussed in this chapter.

A second procedure called WAVFN2 starts at line 66 and ends at line 81. It performs an identical computation to

WAVFN3 just discussed but for a generalized second order secular equation.

A series of three procedures called HIIN, HIIP, and HIIS start at line 88 and end at line 120. These are the interpolation procedures to evaluate the atomic ionization potentials for any specified charge distribution N, P, S where

N = number of electrons in 3d orbital

P = number of electrons in 4p orbital

S = number of electrons in 4s orbital.

These three procedures calculate the 3d, 4p and 4s orbital ionization potentials respectively. The technique was described in Chapter III.

From line 122 to line 153 the program inputs data. The order is as follows:

Negative Ionization Potential of Ligand 2pσ Orbital

Negative Ionization Potential of Ligand 2pπ Orbital

List of Energy Correction Coefficients N_{IR} for Ligand Symmetry Adapted Orbitals

Complete Set of Group Overlap Integrals

Value of the Phenomenological Proportionality Constant for off Diagonal Matrix Elements (F eq. (99))

Total Number of Valence Electrons to be Distributed in Molecular Orbitals

The program offers two modes of operation one of which must be specified at line 155. In mode one the operator specifies particular values for the metal atom ionization potentials. In mode two the operator specifies a charge distribution among

atomic orbitals and the computer uses the HIIN, HIIP and HIIS procedures to compute ionization potentials. Mode two is used for self-consistent charge calculations but mode one is sometimes valuable to investigate the effects by slight arbitrary modifications of the atomic energy levels independent of the charge distribution.

If mode two is selected, the program then requires input of ionization potentials at specific integral values of 3d, 4s and 4p orbital occupation. The data points requested are exactly those previously listed in Figure 27. The commands for this operation take place from line 162 to line 186.

Line 188 inputs from the operator the proposed charge distribution and lines 189 through 193 call the appropriate interpolation procedures into action and prints out the computed diagonal matrix element values.

Lines 195 through 199 call out the secular equation procedures specifying the appropriate diagonal matrix elements for each IR. The resulting eigenvalues and eigenfunction coefficients are stored in temporary small individual arrays.

The commands from line 203 to 231 collect all the eigenvalue and eigenfunction coefficient data into one large data array. In addition the group overlap values required for population analysis (equation (108)) are also included. In actuality these commands form two arrays. The first array ORB[J] is a 1 x 11 alpha array storing the name of the IR for

a particular row. The second array DAT [J,I] is the actual data array where the computed information is stored. Data are dumped into these arrays in the order originally computed. Table 17 shows the content of these arrays as they are filled by the statements from line 203 to 231.

After all data are loaded as shown in Table 17 they are rearranged so the rows are in ascending order according to orbital energy. This is done by the statements from line 232 to 242. Following this, electrons are assigned on the basis of orbital capacity (column 13 of the DAT array) starting with the lowest energy orbital until all valence electrons are used up. This information is stored in the last column of the DAT array Table 17. Hence this last column holds the factor N of equation (108), necessary to compute atomic orbital population.

The commands from line 246 to 260 carry out the population analysis for the metal 3d, 4s and 4p orbitals and print out the result.

If the operator is satisfied that the final charge distribution is sufficiently close to the initial charge distribution, he then types a zero. This causes the program to print out an array of orbital energies and eigenfunction coefficients taken from the ORB and DAT arrays. In addition the transition energy in electron volts between each pair of orbitals is printed out.

Table 17. Initial Data Distribution in ORB[J] and DAT[J,I] Arrays

ORB		DAT													
Orbital Symmetry	Energy	Orbital Coefficients								Overlap Integral Values				Orbital Electron Capacity	Orbital Occupancy
		$3d_M$	$4s_M$	$4p_M$	$2p_{\sigma L}$	$2p_{\pi L}$	G(1,4)	G(1,5)	G(2,4)	G(2,5)	G(3,4)	G(3,5)	G(4,5)		
A1G	$E^1(a_{1g})$		$C^1(a_{1g})$		$C^1_2(a_{1g})$				$G_{a_{1g}}(s_{\sigma M}, p_{\sigma L})$					2	
EG	$E^1(e_g)$	$C^1_1(e_g)$			$C^1_2(e_g)$		$G_{e_g}(d_{\sigma M}, p_{\sigma L})$							4	
T2G	$E^1(t_{2g})$	$C^1_1(t_{2g})$				$C^1_2(t_{2g})$		$G_{t_{2g}}(d_{\pi M}, p_{\pi L})$						6	
A1G	$E^2(a_{1g})$		$C^2_1(a_{1g})$		$C^2_2(a_{1g})$				$G_{a_{1g}}(s_{\sigma M}, p_{\sigma L})$					2	
EG	$E^2(e_g)$	$C^2_1(e_g)$			$C^2_2(e_g)$		$G_{e_g}(d_{\sigma M}, p_{\sigma L})$							4	
T2G	$E^2(t_{2g})$	$C^2_1(t_{2g})$				$C^2_2(t_{2g})$		$G_{t_{2g}}(d_{\pi M}, p_{\pi L})$						6	
T1U	$E^1(t_{1u})$			$C^1_1(t_{1u})$	$C^1_2(t_{1u})$	$C^1_3(t_{1u})$					$G_{t_{1u}}(p_{\sigma M}, p_{\sigma L})$	$G_{t_{1u}}(p_{\pi M}, p_{\pi L})$	$G_{t_{1u}}(p_{\sigma L}, p_{\sigma L})$	6	
T1U	$E^2(t_{1u})$			$C^2_1(t_{1u})$	$C^2_2(t_{1u})$	$C^2_3(t_{1u})$					$G_{t_{1u}}(p_{\sigma M}, p_{\sigma L})$	$G_{t_{1u}}(p_{\pi M}, p_{\pi L})$	$G_{t_{1u}}(p_{\sigma L}, p_{\sigma L})$	6	
T1U	$E^3(t_{1u})$			$C^3_1(t_{1u})$	$C^3_2(t_{1u})$	$C^3_3(t_{1u})$					$G_{t_{1u}}(p_{\sigma M}, p_{\sigma L})$	$G_{t_{1u}}(p_{\pi M}, p_{\pi L})$	$G_{t_{1u}}(p_{\sigma L}, p_{\sigma L})$	6	
T1G	$N_{t_{1g}} H_{2p\pi}$					1.00								6	
T2U	$N_{t_{2u}} H_{2p\pi}$				1.00									6	

If the final population distribution was not consistent with the initial assumption, a one is entered causing the program to ask for new assumed atomic orbital occupancies. When these are entered, the cycle repeats, starting at the computation of new diagonal matrix elements (line 187).

Final Orthoferrite Results

In this section the results of the LCAO analysis of the Fe site in the rare earth orthoferrites are presented. They are the direct result of inserting the overlap terms and ionization potentials previously tabulated into the computer program discussed in the last section.

The program has three parameters which may be adjusted to modify the resultant energy level structure. These are the phenomenological constant F and the self-energy, i.e., diagonal matrix element magnitudes, $H_{2p\sigma}$ and $H_{2p\pi}$, of the ligand 2p orbitals. Initially F is assigned a value of two and the ligand orbital energies a value about equal to the free atom oxygen ionization potential. This latter value is approximately -130,000 cm^{-1}. Using these parameters a self-consistent charge solution is obtained. From the resulting energy level structure transition energies are determined and these are then compared with experimental absorption spectra as a test.

Optical absorption data on europium orthoferrite was reported recently by Kahn and Pershan.[45] Their data, obtained by a Kramers-Kronig analysis from low angle of incidence

reflectivity data, is reproduced as Figure 32. This data shows only major broad structure. However, additional data reported in their paper obtained from complex Kerr rotation measurements indicates fine structure peaks to exist at the approximate energies indicated by the short vertical lines. These lines appear to be consistent with general features of the Kramers-Kronig analysis. The fine structure data does not provide much information beyond about 4.5 eV; undoubtedly this is due to the difficulty of obtaining good measurements in the 5 eV region. The amplitude of the Kramers-Kronig loss curve however indicates absorption lines exist well beyond 4.5 eV.

This experimental data is used as a basis of comparison for the results of the calculated energy level structure. Runs were made for values of F from 1.8 to 2.3 and oxygen 2p matrix elements from -110,000 cm^{-1} to -160,000 cm^{-1}. The solution selected as most nearly agreeing with the experimental data used F = 2.1, $H_{2p\pi}$ = -140,000 cm^{-1} and $H_{2p\sigma}$ = -150,000 cm^{-1}. The use of excess ligand sigma orbital stability was first instituted by Wolfsberg and Helmholz. Subsequent work by Ballhausen and Gray also found it necessary. In the various trial runs during this research a variety of values were tried. It was always found that excess stability of the $2p\sigma$ orbital provided results in closest agreement with experimental data. The physical reason for this effect is that the sigma ligand orbitals are directed in towards the metal atom. Hence the overlap associated with the sigma orbitals is relatively large. This overlap is of course associated with the

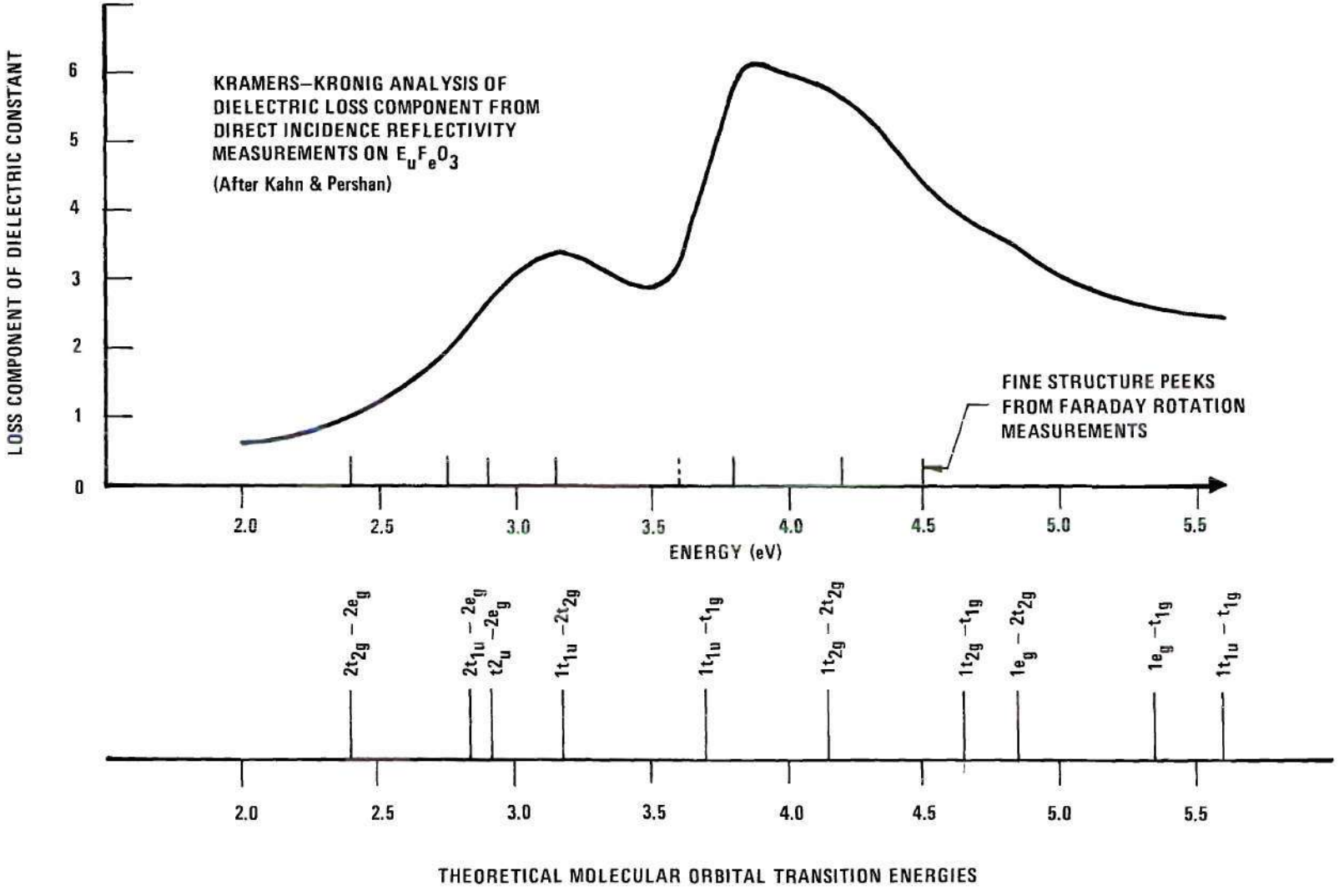

Figure 32. Experimental Orthoferrite Data (upper figure) and LCAO Theoretical Molecular Orbital Eigenvalues (lower figure)

binding energy of the molecular site and hence one would then expect the extra stability of the sigma orbital. The actual splitting, i.e., 10,000 cm^{-1} is less than eight per cent of the 2p orbital energy of about -140,000 cm^{-1}.

The energy level structure as calculated by the computer program is shown in Figure 33. Table 18 is a copy of the actual printout showing the charge distribution and eigenfunction coefficients.

A good indication of the general validity of the computed eigenvalues is the relative position of the second t_{2g} and e_g orbitals. Note that the second t_{2g} orbital is the last populated orbital in the ground state, having two electrons. This orbital has a large Fe 3d atomic component. The second e_g orbital also has a large 3d atomic component, but is empty in the ground state. The energy difference between those two orbitals is 2.4 eV and corresponds to a low level inter-d band type transition. This energy difference is related to the quantity 10 Dq of crystal field theory, which generally has a magnitude of about 2 eV.

Included in Figure 33 are arrows representing transition energies for electrons being excited from ground state to higher level excited states. These energies should correspond approximately to absorption peaks observed in experimental data. This is of course only approximately true, since the total wave function for a given electron configuration must consist of an antisymmetric product of orbital and spin

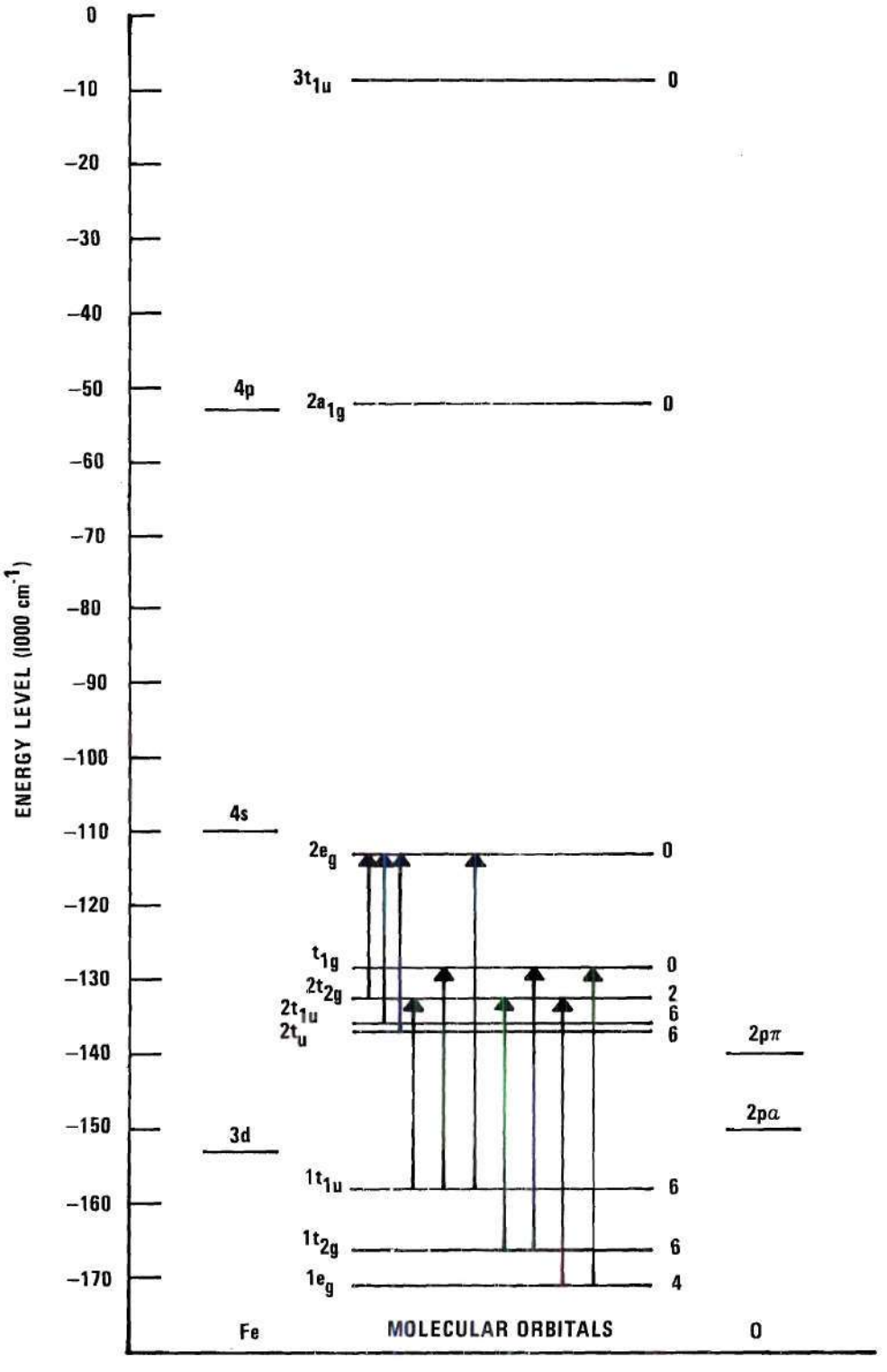

Figure 33. Energy Level Structure for Orthoferrite Iron Site

Table 18. LCAO Molecular Orbital Eigenfunctions for Fe Octahedral Site in Orthoferrite

FINAL CHARGE DISTRIBUTION

Q3D = 6.4969

Q4S = .3699

Q4P = .42138

			ORBITAL DATA				
ORBL	OCU	ENERGY	3D-METAL	4S-METAL	4P-METAL	2P-SIG	2P-PI
T1U	0	-8.2828	0	0	1.0786	-.25148	-.54187
A1G	0	-51.85	0	1.0154	0	-.71399	0
EG	0	-112.9	.69679	0	0	-.83979	0
T1G	0	-128.24	0	0	0	0	1
T2G	2	-132.41	.69931	0	0	0	-.79201
T1U	6	-135.86	0	0	9.2299@-2	-.68614	.74593
T2U	6	-136.5	0	0	0	0	1
T1U	6	-158.08	0	0	.16466	.71332	.55131
T2G	6	-166.06	.72257	0	0	0	.61957
EG	4	-171.72	.73605	0	0	.5675	0
A1G	2	-183.89	0	.36131	0	.80736	0

wave functions. By assuming the total wave function energy equal to the molecular orbital energy we are neglecting inter-electronic repulsion terms. These terms cause a splitting of the molecular orbital energy, providing different transition energies for excited states of different spin multiplicity. There is no way to get an actual calculation of the splitting energies associated with the different electronic states. Thus it has been assumed that the energy of the molecular orbital is essentially at the center of gravity of the distribution. Because of spin and symmetry selection rules transitions can not take place to all states originating from a given excited orbital level. Hence the experimentally observed transitions could be shifted above or below the inter-molecular orbital energies by an amount equal to the inter-electron repulsion energies.

Some of the transitions, indicated by arrows on Figure 33, would normally be considered as parity forbidden. An example is the 2 t_{2g}--2 e_g transition both of which are even functions. As previously discussed this would be considered an inter-d orbital transition in a crystal field model and is known to be experimentally observable in most transition metal compounds. The major structure shown in Figure 32 however is accounted for by transitions which are electric dipole allowed.

Consider for example the position of these transition energies in comparison with the experimental data of Figure 32.

The LCAO predicted interorbital energies are drawn on an energy scale identical with the experimental data. The peak around 3 eV is predicted as a result of transitions 2 $t_{1u} \rightarrow 2\ e_g$, $t_{2u} \rightarrow 2\ e_g$ and 1 $t_{1u} \rightarrow 2\ t_{2g}$. These are all parity allowed transitions. The large peak at about 3.8 eV is predicted as being due to the parity allowed 1 t_{1u}--t_{1g} transition. In general a close correspondence between interorbital energies and experimental absorption peaks has been obtained. The dotted line shown on the data by Kahn and Pershan is a small peak indicated by their fine structure data. There seems to be little evidence of such a transition in the dielectric loss component data shown graphically. The LCAO analysis does not indicate a line there assuming that the allowed 1 $t_{1u} \rightarrow t_{1g}$ transition is properly associated with the large absorption at 3.8 eV. This is the most logical assignment. A comparison of the LCAO transition energies with the experimentally observed peaks between 2 eV and 4.5 eV is shown in Table 19. Based on this assignment the average energy difference between LCAO theory and observation is 0.06 eV.

This relatively good correlation provides support for the belief that the LCAO model is essentially correct. In addition the optimum parameters found here for F, $H_{2p\sigma}$, and $H_{2p\pi}$ provide a very good initial estimate for the octahedral solution of the more complicated garnet structure.

Table 19. Comparison of LCAO-MO Computed Transition Energies Compared with Kahn and Pershan's Dielectric Loss Data on $EuFeO_3$

LCAO Theory		Kahn & Pershan Observed
$2\ t_{2g}\text{-}2\ e_g$	2.41	2.4
$2\ t_{1u}\text{-}2\ e_g$	2.83	2.8
$t_{2u}\text{-}2\ e_g$	2.91	2.9
$1\ t_{1u}\text{-}2\ t_{2g}$	3.17	3.14
		3.6
$1\ t_{1u}\text{-}t_{1g}$	3.68	3.8
$1\ t_{2g}\text{-}2\ t_{2g}$	4.15	4.2
$1\ t_{2g}\text{-}t_{1g}$	4.67	4.5

Garnets

We turn finally to the analysis of the energy level structure of the rare earth iron garnets. The details of the LCAO solution follow those discussed for the orthoferrite case. We are still dealing with Fe atoms coordinated by oxygen ligands. Thus the atomic radial functions can be applied to the garnet also. The ionization potential data from which diagonal matrix elements are calculated is also good for the garnet case. In fact for the octahedral site all that is necessary is to recalculate the overlap integrals, because of difference in interatomic spacing, and obtain the self-consistent charge solution with the computer program. The tetrahedral site will be handled somewhat differently and discussed separately.

Octahedral Site

The Fe-O interatomic distance is R = 2.00 Å or 3.78 atomic units as reported by Geller and Gilleo.[3] Table 20 lists the values of the two atom overlap integrals calculated using the program of Appendix D. From these values the group overlap integrals and ligand overlap correction terms were computed. These values are listed in Table 21.

These latter values are used as input data for the self-consistent charge LCAO computer program (Appendix I). The adjustable parameters F, $H_{2p\sigma}$ and $H_{2p\pi}$ are assigned values of 2.1, -150,000 cm^{-1} and -140,000 cm^{-1} respectively based on the orthoferrite case. The resulting charge distribution

Table 20. Two Atom Overlaps for Rare Earth Iron Garnet Octahedral Site. Metal Ligand Separation R = 2.00 A = 3.78 Atomic Units

Metal-Ligand Overlaps

Type	Value
$S(4s_{\sigma M}, 2p_{\sigma L}; R)$	0.1616
$S(3d_{\sigma M}, 2p_{\sigma L}; R)$	0.0846
$S(3d_{\pi M}, 2p_{\pi L}; R)$	0.0472
$S(4p_{\sigma M}, 2p_{\sigma L}; R)$	0.1548
$S(4p_{\pi M}, 2p_{\pi L}; R)$	0.1731

Ligand-Ligand Overlaps

Type	Value
$S(2p_{\sigma L}, 2p_{\sigma L}, 2R)$	0.00743
$S(2p_{\sigma L}, 2p_{\sigma L}, \sqrt{2}R)$	0.04960
$S(2p_{\pi L}, 2p_{\pi L}, 2R)$	0.00111
$S(2p_{\pi L}, 2p_{\pi L}, \sqrt{2}R)$	0.01120

Table 21. Normalization Correction Factors, Group Overlap Integrals and Ligand Energy Correction Factors for Rare Earth Iron Garnet Octahedral Site

IR ORBITAL	K_{IR}	G_{IR}	N_{IR}
a_{1g}	1.063	0.372	1.114
e_g	0.973	0.151	0.944
$t_{1u}(\sigma_M\sigma_L)$	0.996	0.220	0.993
$t_{1u}(\pi_M\pi_L)$	1.012	0.342	1.023
$t_{1u}(\sigma_L\pi_L)$	-----	0.054	-----
t_{2g}	1.029	0.092	1.056
t_{1g}	0.965	-----	0.927
t_{2u}	0.989	-----	0.978

and eigenfunction data, including orbital energy, is shown in Table 22.

Figure 34 shows the molecular orbital eigenvalues with respect to the atomic orbital energy levels forming the basis. Arrows drawn between molecular orbital levels correspond to transitions which are parity allowed. These are shown along the right side of the figure as transition lines in electron volts. As in the orthoferrite case the numbers listed to the right of the molecular orbital lines are the ground state electron occupation. All orbitals are completely filled up to the second t_{2g} level which has only two electrons. Evaluation of the validity of these results rests on their agreement with the optical absorption data reported in Chapter II.

In Chapter II the absorption spectra as evaluated from reflectivity data analysis indicated the following garnet lines: 2.2 eV, 2.45 eV, 2.73 eV, 2.8 eV, 3.02 eV, 3.32 eV, 3.63 eV, 3.9 eV, 4.03 eV, 4.9 eV, and 5.3 eV. Measurements above 5 eV are very difficult to obtain and are unreliable. In addition there is a line at 4.35 eV which is tentatively believed to be due to an impurity. As discussed in Chapter II this is substantiated by recent transmission data on a GdIG sputtered thin film which does not show the line present.

The intermolecular orbital transition energies from Figure 34 are

Table 22. LCAO Molecular Orbital Eigenfunctions for Fe Octahedral Site in Gadolinium Iron Garnet

FINAL CHARGE DISTRIBUTION

Q3D = 6.5568

Q4S = .37827

Q4P = .3821

			ORBITAL DATA				
ORBL	OCU	ENERGY	3D-METAL	4S-METAL	4P-METAL	2P-SIG	2P-PI
T1U	0	-10.665	0	0	1.075	-.28934	-.49818
A1G	0	-50.848	0	1.0131	0	-.71706	0
EG	0	-116.22	.69382	0	0	-.8325	0
T1G	0	-129.78	0	0	0	0	1
T2G	2	-134.17	.68271	0	0	0	-.79619
T2U	6	-136.92	0	0	0	0	1
T1U	6	-137.15	0	0	6.768@-2	-.67782	.75934
T1U	6	-157.92	0	0	.16407	.71296	.5552
T2G	6	-163.74	.7365	0	0	0	.61206
EG	4	-170.17	.73617	0	0	.5747	0
A1G	2	-182.32	0	.36651	0	.80401	0

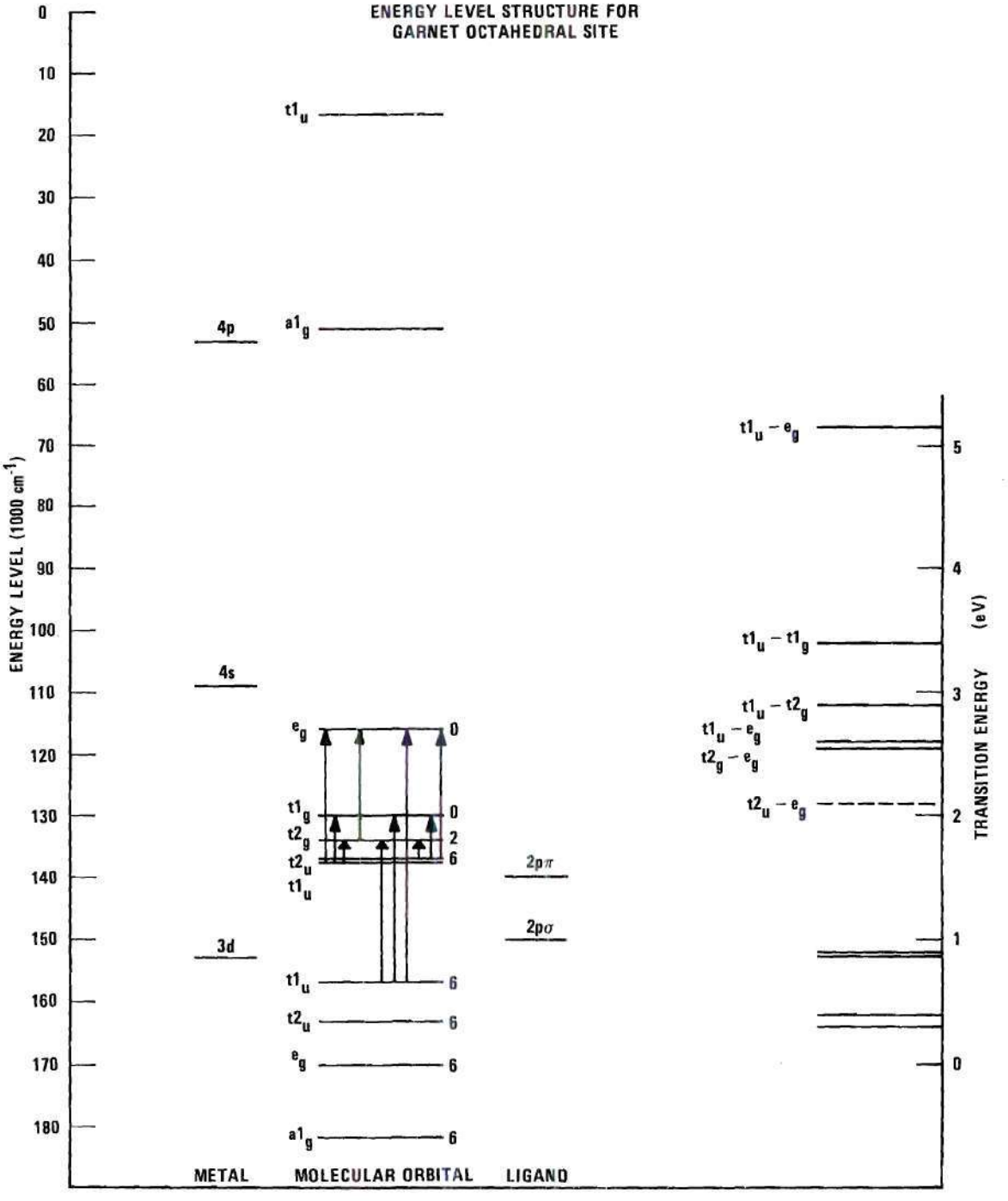

Figure 34. Energy Levels of Octahedral Fe Site in Rare Earth Iron Garnet

$t_{2g} \rightarrow 2\ e_g$ = 2.22 eV

$t_{2u} \rightarrow 2\ e_g$ = 2.55 eV

$2\ t_{1u} \rightarrow 2\ e_g$ = 2.58 eV

$1\ t_{1u} \rightarrow 2\ t_{2g}$ = 2.93 eV

$1\ t_{1u} \rightarrow t_{1g}$ = 3.47 eV

$1\ t_{1u} \rightarrow 2\ e_g$ = 5.15 eV

There is quite close agreement between these theoretical transitions and the experimentally observed lines. The 2.22 eV $t_{2g} \rightarrow 2\ e_g$ line matches very closely with the 2.2 eV experimental line. The 2.45 eV experimental line seems to lie near the theoretical $t_{2u} \rightarrow 2\ e_g$ transition at 2.55 eV, however, there appears to be a closer resemblance between the close pairing of the 2.73 and 2.8 eV lines and the theoretical $t_{2u} \rightarrow 2\ e_g$ and $2\ t_{1u} \rightarrow 2\ e_g$ at 2.55 and 2.58 eV respectively. It seems likely that relative line position is more meaningful than absolute values. Therefore the most natural assignment would be to associate the experimental 2.73 eV line with $t_{2u} \rightarrow 2\ e_g$ and that at 2.8 eV with $2\ t_{1u} \rightarrow 2\ e_g$. The experimental 3.02 eV line then falls nicely with the theoretical $1\ t_{1u} \rightarrow 2\ t_{2g}$ at 2.93 eV. The $1\ t_{1u} \rightarrow t_{1g}$ orbital transition energy at 3.47 eV falls between the experimental 3.32 and 3.63 eV lines. Based on the apparent trend of the theoretical lines to be somewhat lower than the experimental lines the most consistent

assignment appears to be to associate the 3.63 eV line with $1\ t_{1u} \rightarrow t_{1g}$. Finally the $1\ t_{1u} \rightarrow 2\ e_g$ orbital transition at 5.15 eV is associated with the 5.3 eV experimental transition. Based on this assignment the average difference between theoretical and experimental lines is $\Delta E(avg) = 0.13$ eV with a best estimate of standard deviation of $\sigma = 0.07$ eV. Thus the theoretical transition energies are not only very close to experimental values but the relative position, as indicated by the small standard deviation, matches quite well. These results seem especially reasonable when it is noted that data peaks of actual experimental measurements often shows differences of 0.1 to 0.2 eV for the same type of material but different authors.

Tetrahedral Site

The energy level structure associated with the tetrahedral garnet site has been estimated by slightly adjusting the results of Viste and Gray's[46] LCAO solution for MnO_4^-. MnO_4^- is isoelectronic with the FeO_4 tetrahedral site complex of the garnet. Also since Mn and Fe are neighbors in the transition metal series their radial wave functions are quite similar. This implies that for identical interatomic separations the overlap integrals are nearly equal. Similarly, the ionization potentials of Mn are nearly equal to Fe, being only about five per cent lower based on the data of Arlen and Viste. It is therefore reasonable to assume the interorbital transition energies of the two systems would be approximately equal.

The molecular orbital treatment of MnO_4^- by Viste and Gray is recognized in the literature[33] as being one of the most reliable calculations presently available. To apply the results to the tetrahedral site of the garnet it is however necessary to modify their values to account for the different interatomic spacing. To do this we observe the effect of the overlap integral on molecular orbital energy.

Consider a molecular orbital obtained from a two dimensional secular equation. Thus

$$\Phi_{MO} = C_1 \Psi_M + C_2 \sum_i a_i \psi_{iL} \ .$$

Now using the LCAO approximations previously discussed

$$H_{11} \triangleq -IP\ (\Psi_M)$$

$$H_{22} \triangleq -IP\ (\Psi_L)$$

$$H_{12} = H_{21} \triangleq -F\ G_{12} \sqrt{H_{11}\ H_{22}} \ .$$

The secular equation defining the molecular orbital eigenvalues E is

$$\begin{vmatrix} (H_{11}-E) & (H_{12}-G_{12}E) \\ (H_{21}-G_{12}E) & (H_{22}-E) \end{vmatrix} = 0 \ .$$

Expanding the secular equation formally and solving for E^1 and E^2 gives

$$E^1 = \frac{H_{11}+H_{22}}{2} + 1/2\sqrt{(H_{11}-H_{22})^2 + F^2G_{12}^2 H_{11}H_{22}} \qquad (110a)$$

$$E^2 = \frac{H_{11}+H_{22}}{2} - 1/2\sqrt{(H_{11}-H_{22})^2 + F^2G_{12}^2 H_{11}H_{22}} , \qquad (110b)$$

where we have assumed

$$(1-G_{12}^2) \simeq 1$$

$$\text{and } (H_{11}+H_{22}) >> 2G_{12}^2 \sqrt{H_{11}H_{22}} .$$

If $H_{11} \approx H_{22}$, a condition usually met in practice, then we have

$$E^{1,2} \simeq \frac{H_{11}+H_{22}}{2} \pm G_{12}\frac{F\sqrt{H_{11}H_{22}}}{2} = \frac{H_{11}+H_{22}}{2} \pm E_s , \qquad (111)$$

where E_s is defined as the splitting energy.

This simply demonstrates that the off-diagonal matrix element is the source of the interaction which causes one molecular eigenvalue to be above and one below the mean of the atomic basis orbitals. The key point to note, however, is that the splitting energy, i.e., the energy by which the molecular eigenvalue is shifted from the mean energy of the

atomic basis functions, is directly proportional to the overlap integral, G_{12}.

Thus suppose that Φ_{IR} is a molecular orbital resulting from a given atomic basis pair having orbital energies H_{11} and H_{22}. For a given interatomic spacing, A, the group overlap might be called $G_{12}(A)$. At a new interatomic spacing, B, the diagonal matrix elements will remain unchanged,but the group overlap will become $G_{12}(B)$. (This neglects the very small modification of the ligand diagonal matrix element due to ligand-ligand overlap change.)

As a result we find that the ratio of splitting energies for the dimensionally different sites is to the first order equal to the ratio of group overlap integral values, i.e.,

$$\frac{E_S(A)}{E_S(B)} = \frac{G_{12}(A)}{G_{12}(B)} \qquad (112)$$

The actual molecular eigenvalues are given as

$$E^{1,2}(A) = (H_{11}+H_{22})/2 \pm E_S(A) \qquad (113a)$$

$$\text{and } E^{1,2}(B) = (H_{11}+H_{22})/2 \pm E_S(B) \; . \qquad (113b)$$

It is reasonable to approximate the overlap integral by a reciprocal distance function, since $G_{12} \to 0$ as the interatomic

separation increases to large values. Thus if we include the additional relationship

$$G_{ij} \propto 1/R \ ,$$

where R is the interatomic distance, then equation (112) becomes

$$\frac{E_s(A)}{E_s(B)} = \frac{R(B)}{R(A)} \ . \qquad (114)$$

Equations (114) and (113) have been used to estimate the GdIG tetrahedral atomic structure from the MnO_4^- data of Viste and Gray. From the tabulated eigenfunction coefficients for MnO_4^-, the two predominant atomic basis functions were determined. Since the energy of the atomic basis functions, and the molecular eigenvalue is known, the splitting energy is calculated according to equation (113a). Then the splitting energy for the same orbital but in the GdIG tetrahedral site is estimated using equation (114). Thus having previously calculated $E_s(A)$, A representing MnO_4^-, $E_s(B)$ is computed as

$$E_s(B) = \frac{E_s(A)\ R(A)}{R(B)} \qquad (115)$$

where $E_s(B)$ is the splitting energy of GdIG, R(A) is the

interatomic distance of MnO_4^- and R(B) the interatomic distance at the GdIG tetrahedral site. Finally, the eigenvalue of the orbital in GdIG is computed by equation (113b). As an example of this computation consider the molecular orbital 2e. Viste and Gray computed an eigenvalue of E = -72,980 cm^{-1} for this orbital and found the eigenfunction to be

$$\Phi_{2e} = -0.72\ \psi_{3dM} + 0.90\ \Sigma\ \psi_{2p\pi}\ .$$

The diagonal matrix elements yielding the self-consistent charge solution were

$$H_{3d} = -121,280\ cm^{-1}\ ,$$

$$\text{and } H_{2p\pi} = -101,700\ cm^{-1}\ .$$

The splitting energy according to eq. (113a) becomes

$$E_S(MnO_4^-) = -72,980 + (121,280 + 101,700)/2\ cm^{-1}$$

$$= 38,510\ cm^{-1}\ .$$

In MnO_4^- the interatomic distance is 1.6 Å as reported by Viste and Gray. In the garnets the x-ray analysis by Geller and Gileo shows the tetrahedral Fe-0 interatom distance to be

1.88 Å. According to equation (115) we therefore estimate 2e MO splitting in the garents as

$$E_s(\text{REIG}) = (38,510)(1.6/1.88)\ \text{cm}^{-1} = 32,450\ \text{cm}^{-1}$$

Finally the eigenvalue of the 2e orbital in the garnet is found by equation (113b) to be

$$E_{2e}^2 = -(121,280 + 101,700)/2 + 32,450\ \text{cm}^{-1}$$

$$E_{2e}^2 = -79,040\ \text{cm}^{-1}\ .$$

Table 23 shows the results of this type calculation carried out for all molecular orbital energy levels of interest in terms of optical transitions. Based on these results, the energy level structure and observable interorbital transitions are shown in Figure 35. The only transitions occurring in the 2 to 5 eV energy range are $t_1 \rightarrow 2e$ = 2.3 eV, 3 $t_2 \rightarrow 2e$ = 3.2 eV, 2 $a_1 \rightarrow 2e$ = 3.9 eV and $t_2 \rightarrow 4\ t_2$ = 4.6 eV.

Discussion of LCAO-MO Results

Figure 36 shows a comparison of the experimentally determined absorption lines from Chapter II and the LCAO octahedral and tetrahedral lines predicted theoretically. It is observed that the lines for the tetrahedral site fit nicely with the previously made assignments from the octahedral calculation. The "natural" fit adds to the confidence of the

Table 23. Tabulated Results of Molecular Orbital Eigenvalue Shift Resulting from Dimensional Change of 1.6 Å for MnO_4^- to 1.88 Å for REIG (All Energies in cm^{-1})

IR Orbital	MnO_4^- Eigenvalue	Basis Orbitals	MnO_4^- Splitting Energy	REIG Splitting Energy	REIG Eigenvalue
$5t_2$	-18,830	$4p_M, 2p_{\pi L}$	61,300	51,800	-28,300
$4t_2$	-49,290	$3d_M, 2p_{\sigma L}$	62,200	52,500	-59,000
$3t_2$	-105,620	$3d_M, 2p_{\sigma L}$	-4,000	-3,370	-105,100
t_1	-96,400	$2p_{\pi L}$	5,300	4,460	-97,200
2e	-72,980	$3d_M, 2p_{\pi}$	38,510	32,540	-79,040
$2a_1$	-112,100	$2p_{\pi\sigma}$	-10,400	-8,760	-110,500

Self-consistent charge diagonal matrix element values from Vists and Gray reported as $H_{3dM} = 121,280\ cm^{-1}$, $H_{4sM} = 93,410\ cm^{-1}$, $H_{4pM} = -58,400\ cm^{-1}$ and $H_{2pL} = 101,700\ cm^{-1}$

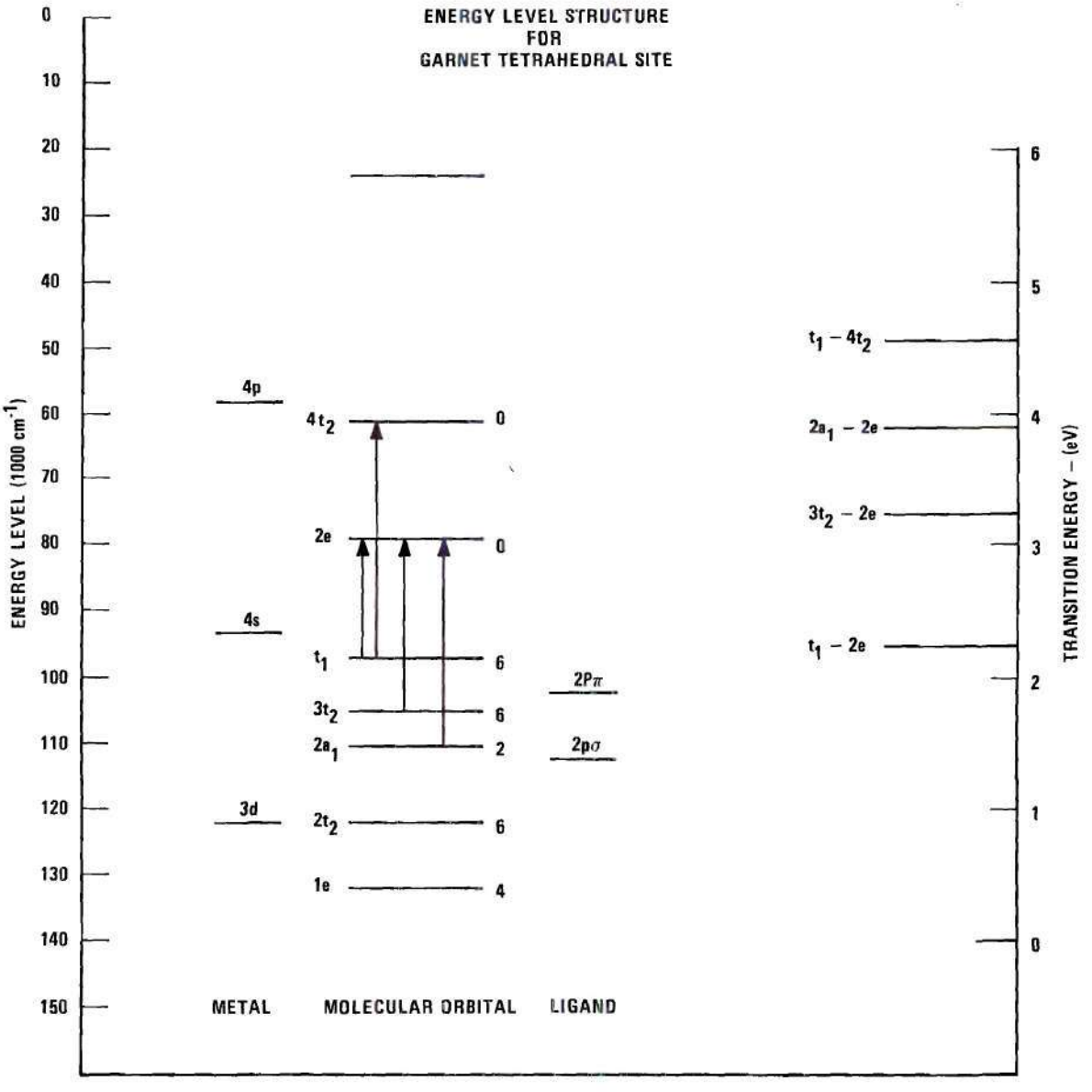

Figure 35. Energy Levels of Tetrahedral Fe Site in Rare Earth Iron Garnet

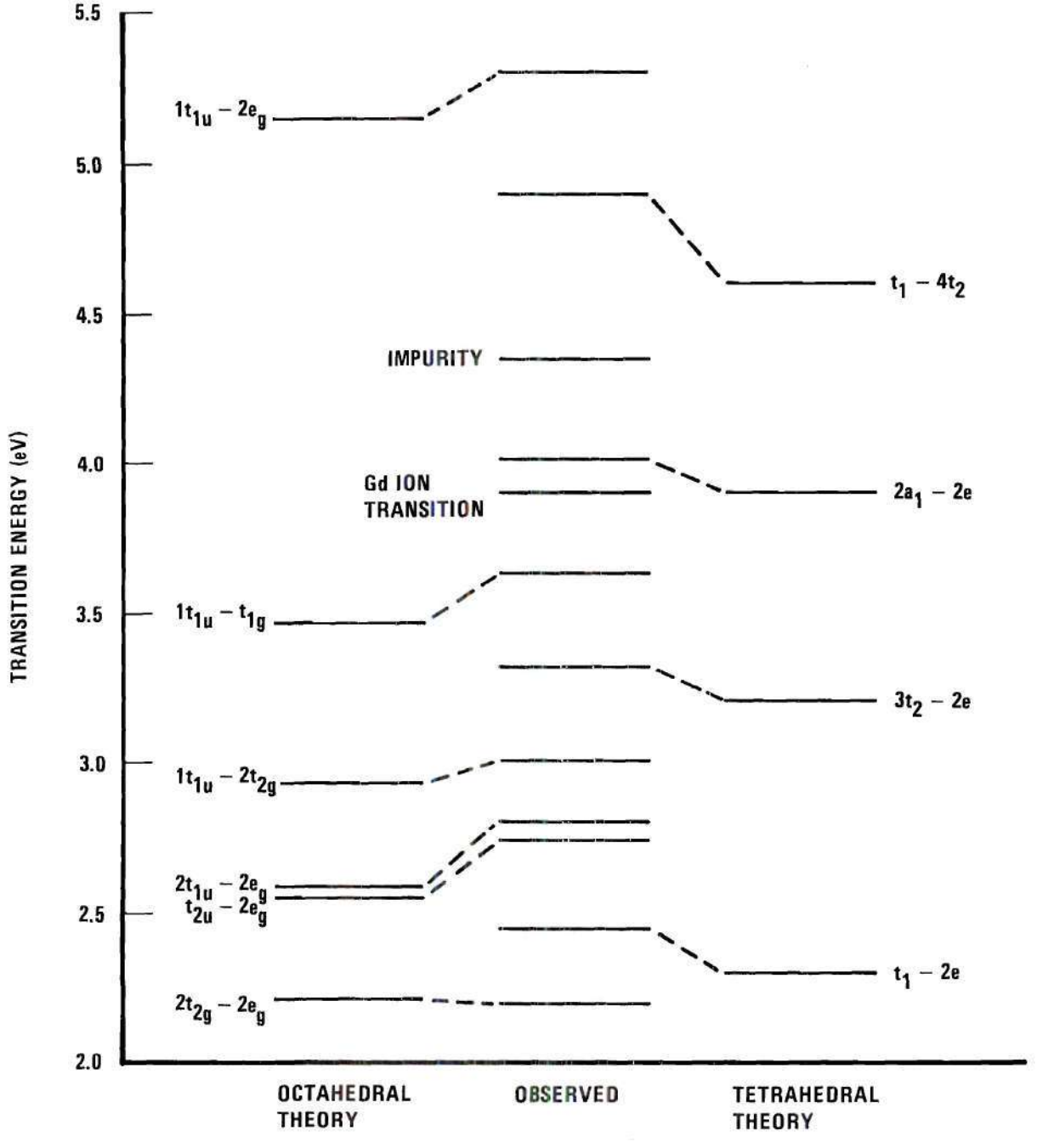

Figure 36. Comparison of Complete LCAO Eigenvalue Set with Experimentally Observed Lines

general validity of the results. The general trend appears to be that the theoretical results are low by about 0.1 to 0.15 eV. As previously discussed however more weight is placed on the interline relationship than the absolute magnitude. The assignment of the $2\ a_1 \rightarrow 2e$ tetrahedral line was based on two factors. First, it is most consistent with the general trend of having the theoretical lines somewhat lower than the experimental one. Secondly, the experimental results showed the 4 eV line to be much stronger than the one at 3.9. There is a spin forbidden gadolinium ion transition at 3.9 eV which should be very small. It is natural therefore to assign the $2\ a_1 \rightarrow 2e$ molecular orbital transition to the strong 4 eV line, and the weak 3.9 eV line to a gadolinium transition.

As discussed in the octahedral section the experimentally observed line at 4.35 eV is attributed to an impurity in the crystals, probably due to lead atoms. There are no molecular orbital transitions which can naturally account for it. This line is absent on thin garnet films prepared by R.F. sputtering. One would expect such films to be less contaminated than the bulk crystals studied here grown from a lead fluoride flux melt.

As a result of these calculations it has been possible, for the first time, to give a theoretical molecular orbital assignment of the optical spectra in the rare earth iron garnets. Transitions which could not be accounted for by crystal field theory are now assigned to specific interorbital

excitations in a natural way, and the nature of the transitions previously referred to simply as "charge transfer transitions" is now explicitly provided.

Consider, for example, the t_{1u} orbital of the octahedral site. The eigenfunction as determined by the calculations is given as

$$\Phi_{(1t_{1u})} = 0.16\ \Psi_{4p} + .71\ \Sigma\ \Psi_{2p}(\sigma) + .56\ \Sigma\ \Psi_{2p}(\pi)$$

where the symbol Ψ_{4p} simply represents the complete function for an iron atom 4p wave function, and the symbols $\Sigma\ \Psi_{2p}(\sigma)$ and $\Sigma\ \Psi_{2p}(\pi)$ stand for normalized combinations of oxygen $2p(\sigma)$ and $2p(\pi)$ orbitals belonging to the same irreducible representation of the octahedral point group. Note that $(0.16)^2 + (.71)^2 + (.56)^2 \neq 1$. This is because the individual components are not orthogonal to each other, and correct normalization must include the overlap terms. As previously discussed this has been carried out in the computer solution, and the total wave function $\Phi(t_{1u})$ is in fact normalized. Now consider the transition $1\ t_{1u} \rightarrow e_g$. The wave function for e_g is

$$\Phi_{(e_g)} = .69\ \Psi_{3d} - .83\ \Sigma\ \Psi_{2p}(\sigma)\ .$$

This orbital contains a significant fraction of iron 3d atomic characteristic. Therefore the $1\ t_{1u} \rightarrow e_g$ transition has often

been referred to as a charge transfer transition since $\Phi_{(t_{1u})}$ is predominantly oxygen in nature, and $\Phi_{(e_g)}$ is significantly metal in nature. The same is true for the transition $t_{2u} \rightarrow e_g$.

Another type of transition characterized explicitly by this analysis is of the interoxygen orbital transition. This is illustrated by the transition 2 $t_{1u} \rightarrow t_{1g}$. The t_{1u} orbital is predominantly oxygen in nature as shown before. The t_{1g} orbital is completely made up of oxygen atomic function. This is called a non-bonding level since it cannot mix with the metal wave functions. The t_{1g} orbital is given as

$$\Phi_{(t_{1g})} = \Sigma \Psi_{2p\pi} .$$

The transition $t_{1u} \rightarrow t_{1g}$ is therefore predominantly an oxygen-oxygen transition, or, more accurately stated, it is a transition between molecular orbitals of predominantly oxygen atomic characteristics.

Finally it is noted that the explicit description of the molecular orbital eigenfunctions should make it possible to calculate the optical rotary effects associated with the molecular orbital transitions. This involves evaluation of matrix elements of the form

$$H = \langle \Phi_1 | x \pm jy | \Phi_2 \rangle ,$$

which describes the interaction between left and right hand

circularly polarized radiation and the energy level structure. Evaluation of these matrix elements is not a simple task, however, with the orbital functions now available it is definitely possible. The results would be of significant value in evaluating the magneto optic characteristics of not only the rare earth iron garnets but also other materials of a similar nature. The LCAO molecular orbital analysis technique therefore appears capable of providing valuable basic information in our continuing efforts to relate practical device application to atomic properties of materials.

CHAPTER V

FEASIBILITY OF A RARE EARTH IRON GARNET OPTICALLY PUMPED MEMORY

From the results of Chapter IV we conclude that the majority of the optical absorption spectra is due to iron site transitions. The optically pumped memory concept, depends on selectively exciting the rare earth atoms. It has been concluded that the low level line at 3.9 eV in GdIG is a gadolinium transition. The terbium absorption which occurs at about 2.5 eV in terbium substituted yttrium gallium garnet, is apparently masked here by the strong tetrahedral iron transition at 2.45 eV.

Because the line does show up in Tb gallium garnet at 2.5 eV it is quite likely that the transition energy in TbIG is nearly the same. Also, to a first order approximation, the line width might be assumed to be the same as that of the gadolinium line.

In this chapter approximations of this nature will be made in order to estimate order of magnitude effects related to optical pumping. An analysis of the pumping process itself is developed in some detail and estimates of pumping power required for a practical situation are made.

Theory of Optical Pumping Process

The magnetic moment of the rare earth ions is a result of the orbital and spin angular momentum of a partially filled 4f shell. These electrons are shielded by completely filled 5s and 5p shells and thus the magnetic properties of these ions are not greatly affected by bonding and crystalline field perturbations.

Terbium for example has eight 4f electrons and has a ground state of $^7F_6$. The spin degeneracy 2S + 1 having a value seven corresponds to a net spin moment of $u_s = 6u_B$ where u_B is the Bohr magneton. The first excited state for terbium is given as $^5D_4$ corresponding to $u_s(\text{excited}) = 4u_B$. Hence when the terbium ion is raised to its first excited state the spin contribution to the total moment has decreased 33 per cent.

The first excited state, $^5D_4$, corresponds to a spin flip transition and as such is not normally allowed. Actually this selection rule generally does not hold rigorously in solids, especially when coupling can occur to allowed transitions having approximately the same transition energy. However to keep the pumping expression completely general we consider a three level system. In this scheme an incoming photon excites an ion in the ground state, state one, to a short-lived intermediate state, state three, via an allowed transition. The ion is then assumed to relax, via an electron phonon interaction, to the spin flip state two.

The rate equations for this pumping scheme are then given as:

$$\dot{n}_1 = -w_{13} n_1 + b_{21} n_2 + b_{31} n_3$$

$$\dot{n}_2 = - b_{21} n_2 + b_{32} n_3$$

$$\dot{n}_3 = w_{13} n_1 - b_{32} n_3$$

where n_1, n_2, n_3, = number of ions per cm^3 in states one, two, three, respectively,

w_{13} = transition rate for ions going from state one to state three,

b's = relaxation rates.

These transitions are shown diagrammatically in Figure 37. There is in addition the constraint given by

$$n_1 + n_2 + n_3 = N_T$$

where N_T = total ions in the system. In the steady state, $\dot{n}_1 = \dot{n}_2 = \dot{n}_3 = 0$, and the second rate equation in conjunction with the constraint yields a steady state population of the second level of

$$n_{2F} = \frac{b_{32} (N_T - n_{1F})}{b_{32} - b_{21}} . \qquad (116)$$

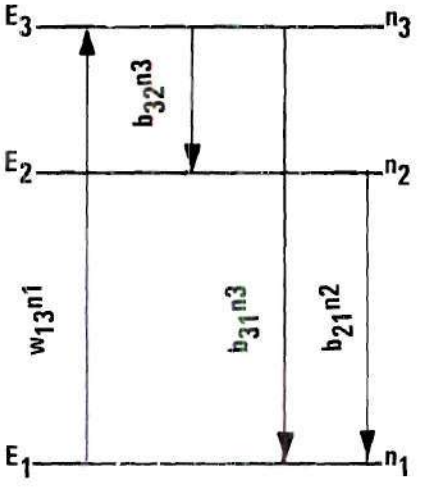

Figure 37. Diagram of the Transitions Involved in the Transition Rate Equations of the Assumed Optical Pumping Process

The subscript F represents the final or steady state value. The assumption that state three is very short-lived with respect to state two, implies $b_{32} >> b_{21}$. Under this condition equation (116) becomes $n_{2F} \simeq N_T - n_{1F}$, i.e., state three is essentially unpopulated. Under the conditions where n_3 remains unpopulated $\dot{n}_3 = 0$ or $w_{13} n_1 = b_{32} n_3$. The second rate equation with this substituion then becomes a two level approximation for n_2 and is given as

$$\dot{n}_2 = w_{13} n_1 - b_{21} n_2 \ . \tag{117}$$

Since $N_T = n_1 + n_2$ in this approximation we find the steady state solution equation (117) to be

$$n_{2F} = \frac{(w_{13}/b_{21})N_T}{(1 + w_{13}/b_{21})} = \frac{N_T}{(1 + \frac{b_{21}}{w_{13}})} \ , \tag{118}$$

and is reached in a time constant of

$$\tau = \frac{1}{(b_{21} + w_{13})} \ . \tag{119}$$

Equations (118) and (119) describe the steady state population of level two and the time constant required to reach it in terms of transition and relaxation probabilities.

At first sight it might be assumed that the coefficient w and b are simply the Einstein A and B coefficients so often discussed in laser theory. This is, however, not the case. The Einstein rate equations are based on the premise that the radiation inducing transitions between states can be described in terms of a radiation density $I(\nu)$, and that the spectral distribution is very broad with respect to the line width of the absorption. In the case to be considered in this research the absorption line will be excited with a monochromatic laser source. Hence the radiation line width is small with respect to that of the absorption line.

In Appendix B the quantum mechanical expression for the transition probability for absorption in the monochromatic case has been derived. In this case one must consider excitation not to a single higher state but a distribution of higher states described by a density of states $N(\omega)$ states/unit frequency/cm^3. The result is given as

$$w = \frac{4\pi^2}{c\hbar^2} N(\omega)\ I|M_{km}|^2 \ \frac{\text{transitions/sec}}{cm^3} \qquad (120)$$

where M_{km} = electric dipole moment matrix element associated with the ground state k and a state m in the upper density of states,

I = incident monochromatic radiation intensity.

The spontaneous emission from an excited state $N(\omega_k)d\omega$ can be shown to be given as[24]

$$db = \frac{4\omega_{km}^3}{\hbar c^3} |M_{km}|^2 N(\omega_k)d\omega \ . \qquad (121)$$

Integrating over the range of excited density of states for the given line, the total spontaneous transition rate to ground becomes

$$b = \frac{4\omega_{km}^3 N}{\hbar c^3} |M_{km}|^2 \ , \qquad (122)$$

where $\int N(\omega)d\omega = N$ the number of atoms/cm^3. This assumes one excited state per atom.

Now the ratio of b/w may be found as from equations (120) and (122) as

$$\frac{b}{w} = \frac{8\pi E^3 \Delta E}{h^3 c^2 I} \ , \qquad (123)$$

where ΔE = the energy half width of the absorption line,

E = transition energy

I = incident light intensity.

Here we have assumed that the density of states is constant over the line half width so $N(\omega) = (1/h)N(E) = (1/h)N/\Delta E$ where

as before N is the number of atoms per cm^3. It is observed from equation (118) that the b/w ratio is the only factor determining the population of the excited state. Thus the population of excited atoms is now expressible in terms of the material absorption line parameters E and ΔE, the line transition energy and half width respectively and the pumping light intensity.

Pumping Power Estimate

Hanton[47] has presented experimental data showing the relationship of coercive force versus temperature for the rare earth iron garnets near their compensation temperature. In general it is found that a 2°C swing from the compensation temperature will cause a reduction in H_c by a factor of two. The iron sublattice magnetization remains nearly constant over such a small temperature differential at the compensation point. As discussed in Chapter I the effective field constant coupling rare earth ions is nearly zero. Thus the rare earth ions behave paramagnetically, experiencing a local field due to the iron sublattice through the effective field constant n_{cd}. Assuming the iron sublattice magnetization remains approximately constant over the temperature range of interest the rare earth magnetization will then obey a Curie type law

$$M_{RE}(T) = \frac{H_{eff}\ C}{T} .$$

In the vicinity of the compensation temperature the percentage change of rare earth can then be approximated as

$$\Delta M = 1 - \frac{T_C}{(T_C + \Delta T)} \ . \qquad (124)$$

We can estimate the required number of excited rare earth atoms to achieve this change in M by using the high temperature approximation of the Brillouin function to describe the moment of the paramagnetic sublattice. Thus assuming the orbital angular momentum is completely quenched

$$M \approx H_{mol}\, Ng^2\, [S(S+1)]\, u_B{}^2/3kT = K[N \cdot S(S+1)] \ . \qquad (125)$$

where H_{mol} = Weiss molecular field,

K is simply a constant of the system.

If there are N_T total rare earth ions per cm^3, and n_{2F} are excited so as to have a different spin quantum number, the total sublattice magnetization is

$$M = K[n_{2F}\, S_e(S_3+1) + (N_T - n_{2F})\, S_g(S_g+1)] \qquad (126)$$

where S_g = spin quantum number in the ground state,

S_e = spin quantum number in the excited state.

The percent change in magnetization can then be written as

$$\Delta M = \frac{n_{2F}}{N_T} \left[1 - \frac{S_e(S_e+1)}{S_g(S_g+1)} \right] . \qquad (127)$$

Thus the population of optically excited atoms necessary to achieve a change in M equivalent to a temperature excursion ΔT from compensation is

$$\frac{n_{2F}}{N_T} = \frac{\left[1 - \frac{T_c}{T_c + \Delta T} \right]}{\left[1 - \frac{S_e(S_e+1)}{S_g(S_g+1)} \right]} . \qquad (128)$$

Since $S_e = 4$, $S_g = 6$ and $T_c = 246°K$ for TbIG the population requirement of the equivalence of $\Delta T = 2°K$ is

$$\frac{n_{2F}}{N_T} = 0.0135 \quad \text{or} \quad 1.35 \text{ per cent.}$$

Knowing the desired excited state population, it is now possible to calculate the radiation intensity required. From equations (118) and (123) we obtain, for the case $n_{2F} << N_T$,

$$I = \frac{8\pi E^3 \Delta E}{h^3 c^2 I} \cdot \frac{n_{2F}}{N_T} \quad \frac{\text{erg}}{\text{sec} \cdot \text{cm}^2} . \qquad (129)$$

If we assume the terbium line is at 2.5 eV and has a line width of about 0.5 eV (similar to Gd^{3+} at 3.9 eV), the required pumping power can be computed. For an excited state population of 0.02 N_T the result is found to be

$$I = 9.5 \times 10^{10} \frac{\text{erg}}{\text{sec} \cdot \text{cm}^2} = 9.5 \times 10^7 \text{ watts/m}^2 .$$

Even though this is a high power density in terms of conventional radiation sources, it is easily achieved with a focused laser. The output beam of a laser is nearly completely parallel, divergence being of the order of several milliradians. Thus high intensities can be achieved simply by focusing the beam to a small diameter spot. For memory operation it would be desirable to have storage regions no larger than ten microns in diameter. Actual size would be limited by the requirement of having a stable magnetic domain wall around the spot. Experimental results[48] indicate 8μ is readily obtainable. To achieve a power density of approximately 4×10^7 watts/m^2 over a 10μ spot requires a total power of only

$$P \approx 4 \text{ milliwatts.}$$

This is of course an easily achievable power with a small gas laser. It indicates that in terms of the parameters associated with pumping, a practical memory should be feasible.

CHAPTER VI

CONCLUSIONS

This work has been directed towards evaluation of the optical spectra and energy level structure of the rare earth iron garnets. Specifically gadolinium and terbium iron garnets have been evaluated. Original motivation for the study was based on the need of such information to evaluate the feasibility of an optically pumped digital memory concept.

The experimental phase has resulted in the determination of the complex refractive index components (n,k) over the 2 eV to 5 eV energy range. This appears to be the only measurement of these important fundamental parameters on the rare earth garnets. In addition this is the first reported measurement of absorption coefficients for single crystal bulk samples above 2.5 eV.

Individual absorption line characteristics have been evaluated by fitting the complete spectra with a series of Lorentzian shaped transitions. As a result the transition energy oscillator strength and line width for the transitions have been determined. In general it was found that oscillator strengths were in the range $10^{-2} \leq f \leq 10^{-1}$ and line widths were between 0.1 and 0.5 electron volts. These parameters are consistent with what would be expected for allowed electric

dipole transitions in solids. Tables of these parameters were given in Chapter II (Tables 2 and 3).

A detailed application of molecular orbital theory in the form of the LCAO approach was employed to obtain a theoretical basis for the observed structure. The technique involved the solution of the LCAO secular equation applying the Wolfsberg-Helmholz approximations. The library of computer programs to compute overlap integrals and molecular orbital eigenvalues and eigenfunction coefficients are included as appendices for future additional research using this approach.

It was found that, in contrast to the failure of previous crystal field calculations, the molecular orbital theory provides a very satisfactory explanation of the complete measured absorption spectra. In general the theoretically predicted transition energies were within 0.2 eV of the experimental values. Also the relative interline spacing was in consistent agreement with the observed structure.

On the basis of the molecular orbital eigenvalue analysis it was concluded that the 3.9 eV line observed in the GdIG structure is a Gd^{3+} ion transition. No other transitions due to rare earth ions were distinctly identifiable. It was however noted that the terbium ion line which should appear around 2.5 eV is probably masked by the large t_1 - 2e tetrahedral iron transition at 2.45 eV.

These calculations provide the first explicit theoretical derivation of the "charge transfer" nature of the significant rare earth iron garnet absorption structure. Metal-ligand, ligand-metal, and interligand transitions are all contained in the spectra and identified. The set of molecular orbital eigenfunction computed open the way for future theoretical evaluation of the Faraday rotation characteristics of these materials.

Finally, the proposed optically pumped memory process was evaluated in detail. Based on estimates of transition parameters from the experimental data, the optical pumping intensity required to create a significant change in coercive force was calculated. It was estimated that required pumping powers of less than ten milliwatts should be required.

The ability of the molecular orbital theory approach to describe the experimental data is a finding of significant importance. This research has indicated that this relatively simple theoretical technique overcomes many of the shortcomings of the crystal field approach used in the past. It appears that it is applicable for the study of a variety of solid materials, especially the oxides. It is envisioned that this approach will provide a versatile tool for the evaluation of mechanical and thermal as well as conduction and magnetic properties of materials in the future.

APPENDIX A

PROGRAM FOR COMPUTATION OF COMPLEX REFRACTIVE INDEX BY DOUBLE ANGLE REFLECTIVITY METHOD

The program is written to be interactive through a remote terminal. Because of the relative sizes of n and k found to be typical of the garnets all data analyzed used 20° and 70° angles of incidence. The program is completely general and will accept data at any two angles, the researcher simply gives the appropriate radian values for THETA 1 and THETA 2. In print out communications, however, the program will write 20° and 70°. These print statements can be modified by any one using the program. Reference to Hunter's paper will show optimum angles to take data based on the approximate magnitudes of n and k.

```
 100:BEGIN
 200:ALPHA FILE IN F1 14(1,5);
 300:ALPHA FILE OUT F2 14(1,5);
 400:STRING STR1(200), STR2(72);
 500:ARRAY PHI[0:2],RP[0:2], E[0:2,0:2];
 600:REAL DELTA,N,NO,K,KO,SIPHI,CSPHI,AA,AB,A,B,
 700:RSA,RSB,RPA,RPB,R20,R70,ALFA,LAMDA;
 800:INTEGER X,Y,I,XMIN,YMIN;
 900:LABEL AGN,ABSP,OVR,OCT;
1000:REAL PROCEDURE READATA;
1100:BEGIN REAL R;  LABEL RD;
1200:RD:  R:=READCON(FALSE);
1300:IF R=2 THEN READATA:=INREAL ELSE BEGIN
1400:PRINT #$#;  GO TO RD; END;
1500:END READATA;
1600:INPUT(F1,STR1);  OUTPUT F2,STR2);
1700:PRINT #INITIAL VALUES OF N AND K#;
1800:NO:=READATA;  KO:=READATA;
```

```
1900:PRINT#THETA1  AND THETA2#;
2000:PHI[0] :=READATA; PHI[1] :=READATA;
2100:PRINT#DELTA#; DELTA:=READATA;
2200: OVR: PRINT#LAMBDA   R20    R70 #;
2300:LAMDA:=READATA;
2400:IF LAMDA=0 THEN GO TO OOT;
2500:R20:=READATA;   R70:=READATA;
2600:PRINT#N=#NO#  K=#KO#  R20=#R20#  R70=#R70;
2700:AGN:  FOR X:=0 STEP 1 UNTIL 2 DO BEGIN
2800:N:=NO+(X-1)/DELTA;
2900:FOR Y:=0 STEP 1 UNTIL 2 DO BEGIN
3000:K:=KO+(Y-1)/DELTA;
3100:FOR 1:=0 STEP 1 UNTIL 1 DO BEGIN
3200:SIPHI:=SIN(PHI[I]); CSPHI:=COS(PHI[I])  ;
3300:AA:=SQRT((N*2-(K*2)-(SIPHI*2))*2 + 4/(N*2)/(K*2));
3400:AB:=N*2-K*2-SIPHI*2;
3500:A:=SQRT(0.5/(AA+AB));
3600:B:=SQRT(0.5/(AA-AB));
3700:RSA:=(A-CSPHI)*2 + B*2;
3800:RSB:=(A+CSPHI)*2 + B*2;
3900:RPA:=(A-(SIPHI*2/CSPHI))*2 + B*2;
4000:RPB:=(A+(SIPHI*2/CSPHI))*2 + B*2;
4100:RP[I] :=(RSA/RSB)/(RPA))/RPB; END;
4200:E[X,Y] :=((R20-RP[0])/R20)*2 +((R70-RP[1])/R70)*2;
4300:
4400:END;  END;
4500:XMIN:=0;  YMIN:=0;
4600:FOR X:=2  STEP -1 UNTIL 0 DO
4700:FOR Y:=2  STEP -1 UNTIL 0 DO
4800:IF E [XMIN,YMIN]  GTR E[X,Y] THEN
4900:BEGIN  XMIN:=X; YMIN:=Y; END;
5000:IF XMIN=1 AND YMIN=1 THEN GO TO ABSP;
5100:NO:=NO+(XMIN-1)/DELTA; KO:=KO+(YMIN-1)/DELTA;
5200:GO TO AGN;
5300:ABSP:  ALFA:=(12.5664/KO/1@+07)/LAMDA;
5400:PRINT #NO=#NO#   KO=#KO#   ALPHA=#ALFA ;
5500:PRINT #E[#XMIN#,#YMIN#]=#E[XMIN,YMIN];
5600:GO TO OVR;
5700:OOI: END.
```

APPENDIX B

DERIVATION OF PUMPING TRANSITION PROBABILITY

The transition probability for the transfer of an atom to an energy state above ground level is calculated by first order perturbation theory. We assume the radiation interaction is small and that the Hamiltonian of the atom can be expressed as

$H = H_o + H_I$ where

$H_o \Phi_n = E_n \Phi_n$, Φ_n being eigenfunctions of stable states of the atom

In general the perturbation is time varient, i.e., the radiation is not only periodic but is applied at t = 0, and hence the solution for the perturbed states must satisfy the time varient Schröedinger equation, i.e.,

$$H\Psi = jh \frac{d\Psi}{dt}$$

We know the general solution for Ψ is separable into the product of spacially dependent and time dependent parts, or

$$\Psi(\bar{r},t) = \mu(\bar{r}) e^{\frac{-jEt}{\hbar}} .$$

Since the unperturbed wave functions

$$\Phi_n = \mu_n(\bar{r})e^{\frac{-jE_nt}{\hbar}}$$

form a complete orthonormal set, the perturbed wave functions can be written as an expansion in them so we get

$$\Psi(\bar{r},t) = \Sigma_n C_n \mu_n(\bar{r})e^{\frac{-jE_nt}{\hbar}} .$$

Now

$$\frac{d\Psi}{dt} = \sum_{n-1}^{n} - \frac{jE_nt}{\hbar} C_n\mu_n(\bar{r})e^{\frac{-jE_nt}{\hbar}} + \mu_n(\bar{r})e^{\frac{-jE_nt}{\hbar}} \dot{C}_n$$

so Schröedinger's equation becomes

$$H \Sigma C_n\mu_r(\bar{r})e^{\frac{-jE_nt}{\hbar}} = \Sigma[E_nC_n\mu_n(\bar{r})e^{\frac{-jE_nt}{\hbar}} + jhC_nU_n(\bar{r})e^{\frac{-jE_nt}{\hbar}}]$$

or

$$\Sigma\, C_n(H_o+H_I)(U_n(r)e^{\frac{-jE_nt}{\hbar}}) = \Sigma[C_nE_n\mu_n(\bar{r})e^{\frac{-jE_nt}{\hbar}} + \Sigma j\dot{C}_n hU_n(\bar{r})e^{\frac{-jE_nt}{\hbar}}]$$

Since $H_o\mu_n = E_n\mu_n$ we can write,

$$\Sigma\, C_nE_n\mu_n e^{\frac{-jE_nt}{\hbar}} + \Sigma\, C_nH_I\mu_n e^{\frac{-jE_nt}{\hbar}} = \Sigma\, C_nE_n\mu_n e^{\frac{-jE_nt}{\hbar}} + \Sigma j\dot{C}_n h\mu_n e^{\frac{-jE_nt}{\hbar}}$$

The technique of solving for the C's is to multiply through both sides of $\overset{*}{\mu}_k$ and integrate over all space, thus

$$\Sigma\, C\, \overset{*}{\mu}_k H_I\mu_n e^{\frac{-jE_nt}{\hbar}} = \Sigma j\dot{C}_n\overset{*}{\mu}_k\mu_n e^{\frac{-jE_nt}{\hbar}},$$

and integrating over all space, recalling that $\int\overset{*}{\mu}_k\mu_n d\tau = \delta_{kn}$ we obtain

$$\sum_o^\infty C_n[\int\overset{*}{\mu}_k H_I\mu_n d\tau]\, e^{\frac{-jE_nt}{\hbar}} = j\dot{C}_k\hbar e^{\frac{-jE_kt}{\hbar}}$$

or

$$(j\hbar)^{-1} \sum_{n=0}^{\infty} C_n [\int \mu_k^* H_I \mu_n d\tau] e^{\frac{-j(E_n - E_k)t}{\hbar}} = \dot{C}_k .$$

The various approximations associated with first second -- etc. order of perturbation are found by describing H_I as $H_I(o) + \lambda H_I$ and expanding the C's as a power series in λ. Thus

$$(j\hbar)^{-1} \sum_{n=0}^{\infty} (C_n^{(0)} + \lambda C_n^{(1)} + \lambda^2 C_n^{(2)}) \lambda H_I e^{+j\omega_{kn}t} = \dot{C}_k^{(0)} + \lambda \dot{C}_k^{(1)} + \lambda^2 \dot{C}_k^{(2)}$$

$$\text{where } \lambda H_I = \lambda \int \mu_k^* H_I \mu_n d\tau$$

and the approximation has been carried to the second order. Equating like coefficients of λ we get

$$0 = \dot{C}_k^{(0)}$$

$$(j\hbar)^{-1} \Sigma\, C_n^{(0)}\, H_I e^{j\omega_{kn}t} = \dot{C}_k^{(1)}$$

$$(j\hbar)^{-1} \Sigma\, C_n^{(1)}\, H_I e^{j\omega_{kn}t} = \dot{C}_k^{(2)}$$

We are thus able to derive the first order perturbation coefficients from the zeroth order coefficients which we know are independent of time by the first equation. Since the system is assumed to be in the ground state at t = 0 then the unperturbed C's must all be zero except $C_m^{(0)}$ which is to be 1, i.e., m is ground state. Therefore we have,

$$(j\hbar)^{-1} H_I e^{j\omega_{km}t} = \dot{C}_k^{(1)}$$

and integrating both sides with respect to time gives

$$C_k^{(1)} = (j\hbar)^{-1} \int H_I e^{j\omega_{km}t} \, dt.$$

If the interaction is independent of time then

$$C_k^{(1)} = - \frac{H_I}{\hbar} \frac{e^{j\omega_{km}t} - 1}{\omega_{km}}$$

$$\text{where } H_I = \int \bar{\mu}_k H_I \mu_m d\tau.$$

The probability of finding the system in state k at time t after the perturbation was turned on is

$$C_k \bar{C}_k = \frac{4|H_I|^2}{\hbar} \frac{\sin^2 1/2\omega_{km}t}{\omega_{km}^2}$$

Now assume H_I, the interaction Hamiltonian operator, is given as

$$H_I = 0 \quad ; \quad t < 0$$

$$H_I = H_I(o) \sin \omega t \quad ; \quad t \geq 0.$$

Then for $t > 0$

$$C_k^{(1)} = (j\hbar)^{-1} H_I(o) \int \sin \omega t e^{j\omega_{km}} dt$$

or carrying out the integration

$$C_k^{(1)} = (j\hbar)^{-1} H_I(o) \left[\frac{e^{j(\omega_{km}+\omega)t} - 1}{\omega_{km} + \omega} - \frac{e^{j(\omega_{km}-\omega)t} - 1}{\omega_{km} - \omega}\right]$$

and the probability of finding the system in state, i.e., $C_k\overline{C}_k$ is

$$C_k\overline{C}_k = \frac{|H_I(o)|^2}{\hbar^2} \frac{1 - 2\cos(\omega_{km}-\omega)t}{(\omega_{km}-\omega)^2}$$

or

$$C_k\overline{C}_k = \frac{4|H_I(o)|^2}{\hbar^2} \frac{\sin^2 1/2(\omega_{km}-\omega)t}{(\omega_{km} - \omega)^2}$$

where only the transition to the higher level state has been considered.

If state k is represented as an energy level in a continuous density of states of an excited band then describing the band by

$$N(\omega) \quad \frac{\text{states}}{\text{cm}^3\text{erg}}$$

the probability of finding the system in any state between E_k and $E_k + dE$ is

$$C_k \overline{C}_k = \frac{4|H_I o|^2}{2} \frac{\sin^2 {}_1/_2(\omega_{km}-\omega)t}{(\omega_{km} - \omega)^2} N(\omega)\, d\omega.$$

The interaction Hamiltonian for radiation of vector potential A is

$$H_I = \frac{je\hbar}{mc} \int \mu_k^* (e^{jk\cdot r})\, A_o \cdot \nabla \mu_m \, d\tau$$

so

$$|H_I{}^o|^2 = \frac{e^2 \hbar^2 A^o}{m^2 c^2} \left| \int \mu_k^* \, e^{jk\cdot r} \, \nabla \mu_m \, d\tau \right|^2$$

The Poynting vector $\frac{c}{4\pi}$ E x H can be calculated from A since

$$E = -\frac{1}{c}\frac{dA}{dt} \qquad \text{and } H = \nabla \times A$$

The result is $P_D = \frac{\omega^2}{2\pi c}|A_o|^2 \frac{\text{erg}}{\text{sec cm}^2} = I$ (Intensity of Radiation)

Making this substitution into H_I^o and noting that if (dimensions of atom), $e^{jk\cdot r} \approx 1$,

$$|H_I^o|^2 = \frac{e^2 \hbar^2}{m^2 c^2}\frac{2\pi I}{\omega^2} \qquad |\int \mu_k^* \nabla \mu_n d\tau|^2$$

and

$$C_k \overline{C}_k = \frac{8\pi I N(\omega) e^2}{m^2 c \omega^2} \quad |\int \mu_k^* \nabla \mu_n d\tau|^2 \frac{\sin^2 1/2(\omega_{kn}-\omega)t}{(\omega_{kn}-\omega)^2} \, d\omega$$

The integral $\int \mu_k^* \nabla \mu_n d\tau = \frac{m}{\hbar}\omega_{km}\int \mu_k^* r_A \mu_m d\tau$ i.e., the expected interaction displacement so

$$C_k \overline{C}_k = \frac{8\pi I N(\omega)}{m^2 c \omega^2} \frac{m^2 \omega_{km}^2}{\hbar^2} |M|^2 \frac{\sin^2 1/2(\omega_{km}-\omega)t}{(\omega_{km}-\omega)^2} \, d\omega \; .$$

Integrating over ω in order to find the probability of finding the system in the upper band - making the usual approximation

$$\int \frac{\sin^2 1/2(\omega_{km}-\omega)t \, d\omega}{\omega_{km}-\omega^2} = 1/2 \, \pi t$$

so

$$p = \frac{4\pi^2 I}{c\hbar^2} N(\omega) |M|^2 t$$

The transition rate then to the upper level is

$$w = \frac{4\pi^2}{c\hbar^2} I N(\omega) |M|^2 \quad \frac{\text{transition}}{\text{sec cm}^3} .$$

APPENDIX C

REPRESENTATION OF A SYMMETRY OPERATOR

The symbol

$$O_R \overline{P} = \overline{P}' \tag{130}$$

means that the vector $\overline{P}$ operated on by O_R yields a new vector $\overline{P}'$. Assume $\overline{P}$ is described in terms of an orthogonal basis set and we add the restriction that the length of $\overline{P}$ is unchanged by the operation. A linear transformation of this type is called an orthogonal transformation and corresponds to a simple rotation or reflection or inversion of the vector.

The problem is to formalize the operation symbolized by equation (130), i.e., to represent the operation with an explicit description of $\overline{P}'$ This is simply done as follows. Assume $\overline{P}$ is written in terms of the basis vectors, $\overline{e}_1$, $\overline{e}_2$, $\cdots$ $\overline{e}_n$ as

$$\overline{P} = [\overline{e}_1 \ \overline{e}_2 \cdots \overline{e}_n] \begin{bmatrix} x_1 \\ x_2 \\ \vdots \\ x_n \end{bmatrix} \tag{131}$$

then we want to describe $\overline{P}'$ as

$$\overline{P}' = [\overline{e}_1 \ \overline{e}_2 \cdots \overline{e}_n] \begin{bmatrix} y_1 \\ y_2 \\ \cdot \\ \cdot \\ \cdot \\ y_n \end{bmatrix} \tag{132}$$

where

$$\begin{bmatrix} y_1 \\ y_2 \\ \cdot \\ \cdot \\ \cdot \\ y_n \end{bmatrix} = \begin{bmatrix} \\ \quad T_R \quad \\ \\ \end{bmatrix} \begin{bmatrix} x_1 \\ x_2 \\ \cdot \\ \cdot \\ \cdot \\ x_n \end{bmatrix} . \tag{133}$$

The matrix T_R is called the representation of the operator O_R with respect to basis $\overline{e}_1, \overline{e}_2 \cdots \overline{e}_n$. It is a linear operator which transorms the coefficients of $\overline{P}$ into those of $\overline{P}'$. The transformation is chosen to leave the magnitude of the vector unchanged. Given some vector $\overline{P}$ then $O_R\overline{P} = \overline{P}'$ is a new vector, identical in length to $\overline{P}$ but pointing to a different direction. Now assume that we perform the identical transformation to the original set of basis vectors creating a new basis set $[\overline{a}_1, \overline{a}_2 \cdots \overline{a}_n]$. The operation is

$$[O_R\overline{e_1} \ \ O_R\overline{e_2} \cdots O_R\overline{e_n}] = [\overline{a_1} \ \overline{a_2} \cdots \overline{a_n}].$$

Since the same transformation was applied to the vector and its basis, the relative position between the two is identical to the original vector $\overline{P}$ and the original basis. We can therefore write

$$\overline{P}' = [\overline{a_1}\ \overline{a_2} \cdots \overline{a_n}] \begin{bmatrix} x_1 \\ x_2 \\ \cdot \\ \cdot \\ \cdot \\ x_n \end{bmatrix} . \tag{134}$$

We now need only to describe the basis vectors $\overline{a_i}$ in terms of the $\overline{e_i}$'s. Thus if we have a transformation matrix T_B such that

$$\begin{bmatrix} \overline{a_1} \\ \overline{a_2} \\ \cdot \\ \cdot \\ \cdot \\ \overline{a_n} \end{bmatrix} = \begin{bmatrix} \\ \\ T_B \\ \\ \\ \end{bmatrix} \begin{bmatrix} \overline{e_1} \\ \overline{e_2} \\ \cdot \\ \cdot \\ \cdot \\ \overline{e_n} \end{bmatrix} , \tag{135}$$

then by the rules of matrix algebra

$$\overline{a_1}\ \overline{a_2} \cdots \overline{a_n} = \overline{e_1}\ \overline{e_2} \cdots \overline{e_n} \quad \left[T_B \right]^t , \tag{136}$$

where the superscript t means the transpose. Equation (135) is the key definition of the desired transformation for now

combining equations (135) and (134) we get

$$\overline{P}' = [\overline{e_1}\ \overline{e_2} \cdots \overline{e_n}] \left[T_B \right]^t \begin{bmatrix} x_1 \\ x_2 \\ \cdot \\ \cdot \\ \cdot \\ x_n \end{bmatrix} . \qquad (137)$$

This equation then becomes identical to eq. (133) i.e.,

$$\overline{P}' = [\overline{e_1}\ \overline{e_2} \cdots \overline{e_n}] \begin{bmatrix} & T_R & \end{bmatrix} \begin{bmatrix} x_1 \\ x_2 \\ \cdot \\ \cdot \\ \cdot \\ x_n \end{bmatrix} , \qquad (138)$$

where $\left[T_R \right] = \left[T_B \right]^t$.

The operator can thus be represented by an n x n matrix T_R . T_R is found by taking the transpose of the matrix which describes a set of transformed basis vectors in terms of the original basis set according to equation (135).

Note that as $\overline{e_1}$, $\overline{e_2} \cdots \overline{e_n}$ form the basis of an n dimensional vector space then a linear operator O_R applied to any vector in this space will produce another vector in the space. Thus if $\overline{P}$ is a general vector in a space spanned by the $\overline{e}$'s, it may be written as

$$\overline{P} = x_1\overline{e_1} + x_2\overline{e_2} + \cdots x_n e_n = \sum_{k=1}^{n} x_k\overline{e_k} . \qquad (139)$$

Then

$$O_R P = T(R)_1 \overline{e_1} + T(R)_2 \overline{e_2} + \cdots + T(R)_n \overline{e_n} = \sum_{j=1}^{n} T(R)_j \overline{e_j} \quad (140)$$

where

$$T(R)_j = \sum_{k=1}^{n} r_{jk} x_k ,$$

r_{jk} being the element at the j^{th} row, k^{th} column of $[T_R]$ in equation (138).

A case of special interest is where an operator is applied directly to a basis vector. In this case

$$P = \overline{e_j} \qquad \text{i.e.,} \qquad x_k = \begin{matrix} 0 \text{ for } k \neq j \\ 1 \text{ for } k = j \end{matrix} .$$

In this case

$$O_R \overline{e_j} = [\overline{e_1}\ \overline{e_2} \cdots \overline{e_n}] \begin{bmatrix} r_{11} r_{12} & \cdots & \\ \vdots & & \\ r_{j1} r_{j2} & \cdots & \\ \vdots & & \end{bmatrix} \begin{bmatrix} 0 \\ \vdots \\ 0 \\ 1 \\ 0 \\ \vdots \end{bmatrix} , \quad (141)$$

and

$$O_R\overline{e_j} = [\overline{e_1}\ \overline{e_2} \cdots \overline{e_n}] \begin{bmatrix} r_{1j} \\ r_{2j} \\ . \\ . \\ . \\ r_{nj} \end{bmatrix} = \Sigma(i) r_{ij} \overline{e_i} \ . \qquad (142)$$

If O_R is applied to the column vector of basis functions then

$$O_R \begin{bmatrix} \overline{e_1} \\ \overline{e_2} \\ . \\ . \\ \overline{e_n} \end{bmatrix} = \begin{bmatrix} r_{11} r_{12} & \cdots & r_{n1} \\ r_{12} r_{22} & \cdots & r_{n2} \\ . & & \\ . & & \\ r_{1n} & \cdots & r_{nn} \end{bmatrix} \begin{bmatrix} \overline{e_1} \\ \overline{e_2} \\ . \\ . \\ \overline{e_n} \end{bmatrix} \qquad (143)$$

the result becomes that the appropriate transformation matrix is the transpose of the representation in eq. (138). It is essentially a restatement of equation (135), but is illustrated explicitly because of the frequency with which the transformation of eq. (143) is employed in molecular orbital theory. It can be shown that if the operators of the symmetry point groups are represented by matrices as described above, then operator multiplication is described by matrix multiplication of the representations. Similarly the inverse of an operator is represented by the inverse matrix of the operator representation. As a result the matrix representations themselves form

a group. This representation group has the same number of elements and classes of conjugate elements as the point group of operators.

APPENDIX D

PROGRAM TO CALCULATE TWO ATOM OVERLAP INTEGRALS

```
 100:BEGIN COMMENT
 200:PROGRAM TO CALCULATE  TWO ATOM OVERLAP INTEGRALS;
 300:COMMENT ACCEPTS WAVE FUNCTIONS
 400:COMPOSED OF STO NORMALIZED SO;
 500:COMMENT  THAT INTEGRAL(R*2/F(R)*2)=1;
 600:FILE REMOTE;
 700:REAL SEP,D,ZMAX,COSA,COSB,INT,Z,E,NM,NL,S;
 800:INTEGER I,NZ,NE,J,K,L,AGN;
 900:ARRAY C[1:10],X[1:10],A[1:10],CL[1:6],XL[1:6],AL[1:6];
1000:ARRAY FX[0:500],FY[0:240];
1100:LABEL SSSIGMA,SPSIGMA,PSSIGMA,
1200:PPSIGMA,PPPI,DPSIGMA,DSSIGMA,DPPI;
1300:LABEL CONT,DONE,AGAIN;
1400:SWITCH  SEL:=SSSIGMA,SPSIGMA,
1500:PSSIGMA,PPSIGMA,PPPI,DPSIGMA,DSSIGMA,DPPI;
1600:REAL PROCEDURE RADM(R); VALUE R; REAL R;
1700:RADM:=C[1]/R*X[1]/EXP(-A[1]/R)
1800:+C[2]/R*X[2]/EXP(-A[2]/R)
1900:+C[3]/R*X[3]/EXP(-A[3]/R)
2000:+C[4]/R*X[4]/EXP(-A[4]/R)
2100:+C[5]/R*X[5]/EXP(-A[5]/R)
2200:+C[6]/R*X[6]/EXP(-A[6]/R)
2300:+C[7]/R*X[7]/EXP(-A[7]/R)
2400:+C[8]/R*X[8]/EXP(-A[8]/R)
2500:+C[9]/R*X[9]/EXP(-A[9]/R)
2600:+C[10]/R*X[10]/EXP(-A[10]/R);
2700:REAL PROCEDURE RADL(R); VALUE R; REAL R;
2800:RADL:=CL[1]/R*XL[1]/EXP(-AL[1]/R)
2900:+CL[2]/R*XL[2]/EXP(-AL[2]/R)
3000:+CL[3]/R*XL[3]/EXP(-AL[3]/R)
3100:+CL[4]/R*XL[4]/EXP(-AL[4]/R)
3200:+CL[5]/R*XL[5]/EXP(-AL[5]/R)
3300:+CL[6]/R*XL[6]/EXP(-AL[6]/R);
3400:PROCEDURE INTEGRATE(F,INC,LIM);
3500:COMMENT BE SURE AND DECLARE
3600:THE VARIABLE"INT" GLOBALLY IN THE PROGRAM;
3700:VALUE INC,LIM; REAL INC,LIM; ARRAY F[0];
3800:BEGIN REAL SUB; INTEGER N;
3900:SUB:=0;
4000:FOR N:=0 STEP 6 UNTIL LIM-6 DO
4100:SUB:=SUB+F[N]+5/F[N+1]+F[N+2]+6/F[N+3]
```

```
4200:  +F[N+4]+5/F[N+5]+F[N+6];
4300:INT:=3/INC/SUB/10;
4400:END INTEGRATE;
4500:FOR I:=1 STEP1 UNTIL 10 DO BEGIN
4600:C[I]:=0; X[I]:=0; A[I]:=0; END;
4700:FOR I:=1 STEP 1 UNTIL 6 DO BEGIN
4800:CL[I]:=0; XL[I]:=0; AL[I]:=0; END;
4900:PRINT SPACE; PRINT SPACE;
5000:PRINT #NUMBER OF METAL BASIS FUNCTIONS#;
5100:NM:=READN(TWX);
5200:PRINT #NUMBER OF LIGAND BASIS FUNCTIONS#;
5300:NL:=READN(TWX);
5400:PRINT SPACE; PRINT SPACE;
5500:PRINT #BASIS ELEMENTS OF FORM R=(C)(R*X)EXP(-R/A)#;
5600:PRINT SPACE:
5700:FOR I:=1 STEP L UNTIL NM DO BEGIN
5800:PRINT #C[#I#],X[#I#],A[#I#]#;
5900:C[I]:=READN(TWX); X[I]:=READN(TWX); A[I]:=READN(TWX);
6000:END; PRINT SPACE;
6100:PRINT SPACE;
6200:FOR I:=1 STEP 1 UNTIL NL DO
6300:BEGIN
6400:PRINT #CL[#I#],XL[#I#],AL[#I#]#;
6500:CL[I]:=READN(TWX); XL[I]:=READN(TWX); AL[I]:=READN(TWX);
6600:END; PRINT SPACE;
6700:PRINT SPACE;
6800:PRINT #ION SEPARATION IN ATOMIC UNITS
6900:---0.529 ANGSTROMS/AU#;
7000:SEP:=READN(TWX);  D:=SEP/2;
7100:AGAIN: PRINT SPACE; PRINT SPACE;
7200:PRINT #TYPE OF OVERLAP TO BE COMPUTED#;
7300:PRINT #1=SSSIGMA#;
7400:PRINT #2=SPSIGMA#;
7500:PRINT #3=PSSIGMA#;
7600:PRINT #4=PPSIGMA#;
7700:PRINT #5=PPPI#;
7800:PRINT #6=DPSIGMA#;
7900:PRINT #7=DSSIGMA#;
8000:PRINT #8=DPPI#;
8100:L:=READN(TWX); PRINT SPACE;
8200:PRINT #NUMBER OF ZETA INCREMENTS AND UPPER ZETA LIMIT#;
8300:NZ:=READN(TWX);  ZMAX:=READN(TWX);
8400:PRINT #NUMBER OF ETTA INCREMENTS#;
8500:NE:=READN(TWX);
8600:GO TO SEL[L];
8700:CONT: PRINT SPACE; PRINT SPACE; PRINT SPACE;
8800:PRINT #METAL WAVE FUNCTION#;
8900:FOR I:=1 STEP 1 UNTIL NM DO
9000:PRINT SPACE(10),C[I],SPACE(4),X[I],SPACE(4),A[I];
9100:PRINT SPACE;
9200:PRINT #LIGAND WAVE FUNCTION#;
```

```
 9300:FOR I:-1 STEP L UNTIL NL DO
 9400:PRINT SPACE(10),CL[I],SPACE(4),XL[I],SPACE(4),AL[I];
 9500:PRINT SPACE; PRINT SPACE;
 9600:PRINT #OVERLAP INTEGRAL=#S; PRINT SPACE; PRINT SPACE;
 9700:PRINT #TYPE 1 TO GO AGAIN 0 TO STOP#;
 9800:AGN:=READN(TWX);
 9900:IF AGN=1 THEN GO TO AGAIN ELSE GO TO DONE;
10000:SSSIGMA: Z:=1;
10100:FOR  J:=0 STEP 1 UNTIL NZ DO
10200:BEGIN E:=-1;
10300:FOR K:=0 STEP 1 UNTIL NE DO
10400:BEGIN
10500:FX[K]:=RADM(D/(Z+E))/RADL(D/(Z_E))/(Z*2-E*2);
10600:E:=E+2/NE;
10700:END;
10800:INTEGRATE(FX,2/NE,NE); FY[J]:=INT;
10900:Z:=Z+ZMAX/NZ;
11000:END;
11100:INTEGRATE(FY,ZMAX/NZ,NZ);
11200:S:=(1/2)/D*3/INT;
11300:PRINT SPACE(10)#SSSIGMA OVERLAP#;
11400:GO TO CONT;
11500:SPSIGMA: Z:=1;
11600:FOR J:=0 STEP 1 UNTIL NZ DO
11700:BEGIN E:=-1;
11800:FOR K:=0 STEP 1 UNTIL NE DO
11900:BEGIN
12000:COSB:=IF (Z-E)=0 THEN 1 ELSE (1-Z/E)/(Z-E);
12100:FX[K]:=RADM(D/(Z+E))/RADL(D/(Z-E))/COSB/(Z*2-E*2);
12200:E:=E+2/NE;
12300:END;
12400:INTEGRATE(FX,2/NE,NE);  FY[J]:=INT;
12500:Z:=Z+ZMAX/NZ;
12600:END;
12700:INTEGRATE(FY,ZMAX/NZ,NZ);
12800:S:=(SQRT(3)/2)/D*3/INT;
12900:PRINT SPACE(10)#SPSIGMA OVERLAP#;
13000:GO TO CONT;
13100:PSSIGMA:  Z:=1;
13200:FOR J:=0 STEP 1 UNTIL NZ DO
13300:BEGIN E:=-1;
13400:FOR K:=0 STEP 1 UNTIL NE DO
13500:BEGIN
13600:COSA:=IF (Z+E)=0 THEN 1 ELSE (1+Z/E)/(Z+E);
13700:FX[K]:=RADM(D/(Z+E))/RADL(D/(Z-E))/COSA/(Z*2-E*2);
13800:E:=E+2/NE;
13900:END;
14000:INTEGRATE(FX,2/NE,NE); FY[J]:=INT;
14100:Z:=Z+ZMAX/NZ;
14200:END;
14300:INTEGRATE(FY,ZMAX/NZ,NZ);
```

```
14400:S:(SQRT(3)/2)/D*3/INT;
14500:PRINT SPACE(10)#PSSIGMA OVERLAP#;
14600:GO TO CONT;
14700:PPSIGMA: Z:=1;
14800:FOR J:=0 STEP 1 UNTIL NZ DO
14900:BEGIN E:=-1;
15000:FOR K:=0 STEP 1 UNTIL NE DO
15100:BEGIN
15200:FX[K]:=RADM(D/(Z+E))/RADL(D/(Z-E))/(1-(Z*2/E*2));
15300:E:=E+2/NE;
15400:END;
15500:INTEGRATE(FX,2/NE,NE); FY[J]:=INT;
15600:Z:=Z+ZMAX/NZ;
15700:END;
15800:INTEGRATE(FY,ZMAX/NZ,NZ);
15900:S:=(3/2)/D*3/INT;
16000:PRINT SPACE(10)#PPSIGMA OVERLAP#;
16100:GO TO CONT;
16200:PPPI:  Z:=1;
16300:FOR J:=0 STEP 1 UNTIL NZ DO
16400:BEGIN E:=-1;
16500:FOR K:=0 STEP 1 UNTIL NE DO
16600:BEGIN
16700:FX[K]:=RADM(D/(Z+E))/RADL(D/(Z-E))/(Z*2-1)/(1-E*2);
16800:E:=E+2/NE;
16900:END;
17000:INTEGRATE(FX,2/NE,NE);  FY[J]:=INT;
17100:Z:=Z+ZMAX/NZ;
17200:END;
17300:INTEGRATE(FY,ZMAX/NZ,NZ);
17400:S:=(3/4)/D*3/INT;
17500:PRINT SPACE(10)#PPPI OVERLAP#;
17600:GO TO CONT;
17700:DPSIGMA:  Z:=1;
17800:FOR J:=0 STEP 1 UNTIL NZ DO
17900:BEGIN E:=-1;
18000:FOR K:=0 STEP 1 UNTIL NE DO
18100:BEGIN
18200:COSA:=IF (Z+E)=0 THEN 1 ELSE (1+Z/E)/(Z+E);
18300:COSB:=IF (Z-E)=0 THEN 1 ELSE (1-Z/E)/(Z-E);
18400:FX[K]:=RADM(D/(Z+E))/RADL(D/(Z-E))/((3/COSA*2)-1);
18500:COSB/(Z*2=E*2);
18600:E:=E+2/NE;
18700:END;
18800:INTEGRATE(FX,2/NE,NE);  FY[J]:=INT;
18900:Z:=Z+ZMAX/NZ;
19000:END;
19100:INTEGRATE(FY,ZMAX/NZ,NZ);
19200:S:=(SQRT(15)/4)/D*3/INT;
19300:PRINT SPACE:  PRINT SPACE(10)#DPSIGMA OVERLAP#;
19400:GO TO CONT;
19500:DSSIGMA:  Z:=1;
```

```
19600:FOR J:=0 STEP 1 UNTIL NZ DO
19700:BEGIN E:=-1;
19800:FOR K:=0 STEP 1 UNTIL NE DO
19900:BEGIN
20000:COSA:=IF (Z+E)=0 THEN 1 ELSE (1+Z/E)/(Z+E);
20100:FX[K]:=RADM(D/(Z+E))/
20200:RADL(D/(Z-E))/((3/COSA*2)-1)/(Z*2-E*2);
20300:E:=E+2/NE;
20400:END;
20500:INTEGRATE(FX,2/NE,NE);  FY[J]:=INT;
20600:Z:=Z+ZMAX/NZ;
20700:END;
20800:INTEGRATE(FY,ZMAX/NZ,NZ);
20900:S:=SQRT(5/16)/D*3/INT;
21000:PRINT SPACE; PRINT SPACE(10)#DSSIGMA OVERLAP#;
21100:GO TO CONT;
21200:DPPI:  Z:=1;
21300:FOR J:=0 STEP 1 UNTIL NZ DO
21400:BEGIN E:=-1;
21500:FOR K:=0 STEP 1 UNTIL NE DO
21600:BEGIN
21700:COSA:=IF (Z+E)=0 THEN 1 ELSE (1+Z/E)/(Z+E);
21800:FX[K]:=RADM(D/(Z+E))/RADL(D/(Z-E))/(Z*2-1)/(1-E*2)/COSA;
21900:E:=E+2/NE;
22000:END;
22100:INTEGRATE(FX,2/NE,NE);  FY[J]:=INT;
22200:Z:=Z+ZMAX/NZ;
22300:END;
22400:INTEGRATE(FY,ZMAX/NZ,NZ);
22500:S:=SQRT(45/16)/D*3/INT;
22600:PRINT SPACE; PRINT SPACE(10)#DPPI OVERLAP#;
22700:GO TO CONT;
22800:DONE: END.
22900:
```

APPENDIX E

ONE DIMENSIONAL INTEGRAL OF RADIAL FUNCTIONS

This program will perform

$$\int_0^{r_{max}} R(r)dr \quad \text{or} \quad \int_0^{r_{max}} R(\hat{r}^2)dr \quad \text{of} \quad \int_0^{r_{max}} r^2R(\hat{r}^2)dr$$

where

$$R(r) = C_1 r^{x_1} e^{-A_1 r} + C_2 r^{x_2} e^{-A_2 r} + \cdots C_6 r^{x_6} e^{-A_6 r}$$

```
 100:BEGIN
 200:FILE REMOTE;
 300:REAL R,DX,X2,INT;
 400:ARRAY FX[0:1000],C[1:6],X[1:6],A[1:6];
 500:INTEGER I,QRY,NR,GR,RMU;
 600:LABEL AGN,OOT,CONT,R0,R1,R2;
 700:SWITCH RMULT:= R0,R1,R2;
 800:PROCEDURE GRAPH(X,IMAX);
 900:ARRAY X[0]; INTEGER IMAX;
1000:BEGIN INTEGER I; REAL XMAX, XMIN,G;
1100:FOR I:=0 STEP 1 UNTIL IMAX DO
1200:XMAX:=IF XMAX LSS X[I] THEN X[I] ELSE XMAX;
1300:FOR I:=0 STEP 1 UNTIL IMAX DO
1400:XMIN:=IF XMIN GTR X[I] THEN X[I] ELSE XMIN;
1500:PRINT SPACE(4)#0#SPACE(9)#1#SPACE(9)#2#
1600:SPACE(9)#3#SPACE(9)#4#SPACE(9)#5#;
1700:PRINT SPACE(3)#++++++++++++++++++++++++++
1800:++++++++++++++++++++++#;
1900:FOR I:=0 STEP 1 UNTIL IMAX DO BEGIN
2000:G:=((X[I]-XMIN)/(XMAX-XMIN))/50;
2100:PRINT I;
2200:PRINT SKIP(3)#+#SPACE(G)#*#;
```

```
2300:END;
2400:PRINT SPACE;
2500:PRINT #AMPLITUDE AT Y=5 IS#SPACE(2)XMAX;
2600:PRINT #AMPLITUDE AT Y=0 IS#SPACE(2)XMIN;
2700:PRINT #INCREMENT IS#SPACE(7),(XMAX-XMIN)/50;
2800:END GRAPH;
2900:PROCEDURE INTEGRATE (F,INC,LIM);
3000:REAL LIM,INC;  ARRAY F[0];
3100:BEGIN REAL SUB;  INTEGER N;
3200:SUB:=0;  FOR N:=0 STEP 6 UNTIL LIM-6 DO
3300:SUB:=SUB+F[N]+5/F[N+1]+F[N+2]+6/F[N+3]
3400:+F[N+4]+5/F[N+5]+F[N+6];
3500:INT:=(3/INC/10)/SUB;
3600:END INTEGRATE;
3700:REAL PROCEDURE FNCT(R);   REAL R;
3800:BEGIN
3900:FNCT:=C[1]/(R*X[1])/EXP(-A[1]/R)
4000:+C[2]/(R*X[2])/EXP(-A[2]/R)
4100:+C[3]/(R*X[3])/EXP(-A[3]/R)
4200:+C[4]/(R*X[4])/EXP(-A[4]/R)
4300:+C[5]/(R*X[5])/EXP(-A[5]/R)
4400:+C[6]/(R*X[6])/EXP(-A[6]/R);
4500:END FNCT;
4600:PRINT #BASIS FNCTS OF FORM C[I]/R*X[I]/EXP(-A[I]/R)#;
4700:FOR I:=1 STEP 1 UNTIL 6 DO BEGIN
4800:PRINT #C[#I#], X[#I#], A[#I#]#;
4900:C[I]:=READN(TWX); X[I]:=READN(TWX); A[I]:=READN(TWX);
5000:END;
5100:PRINT #TYPE 0 FOR INTEGRAL F(R)#;
5200:PRINT #TYPE 1 FOR INTEGRAL F(R)**2#;
5300:PRINT #TYPE 2 FOR INTEGRAL FR**2/F(R)**2#;
5400:RMU:=READN(TWX);
5500:AGN: PRINT #NUMBER OF RADIAL STEPS#;
5600:NR:=READN(TWX);
5700:PRINT #UPPER LIMIT OF RADIAL INTEGRATION#;
5800:X2:=READN(TWX);
5900:DX:=X2/NR;
6000:R:=0;
6100:FOR I:=0 STEP 1 UNTIL NR DO BEGIN
6200:GO TO RMULT[RMU+1];
6300:CONT: R:=R+DX; END;
6400:INTEGRATE(FX,DX,NR);
6500:PRINT SPACE; PRINT SPACE;
6600:PRINT #INTEGRAL=#INT;
6700:PRINT SPACE; PRINT SPACE;
6800:PRINT #TYPE 1 FOR GRAPH 0 OTHERWISE#;
6900:GR:=READN(TWX);
7000: IF GR = 1 THEN GRAPH(FX,NR);
7100:PRINT #TYPE 1 TO CONTINUE 0 TO STOP#;
7200:QRY:=READN(TWX);
```

```
7300:IF QRY EQL 1 THEN GO TO AGN ELSE GO TO OOT;
7400:RO: FX[I]:=FNCT(R); GO TO CONT;
7500:R1: FX[I]:=FNCT(R)*2; GO TO CONT;
7600:R2: FX[I]:=(R*2)/(FNCT(R)*2); GO TO CONT;
7700:OOT:END.
7800:
```

APPENDIX F

OXYGEN RADIAL WAVE FUNCTIONS

From Clementi's paper[27] we have for oxygen ^3P

Expansion Coefficients C_{nji}

1s

$C_{1,1} = 0.93835$

$C_{1,2} = 0.03825$

$C_{1,3} = -0.00097$

$C_{1,4} = 0.00439$

$C_{1,5} = -0.00829$

$C_{1,6} = 0.04171$

2s

$C_{2,1} = -0.21979$

$C_{2,2} = -0.00573$

$C_{2,3} = 0.42123$

$C_{2,4} = 0.54368$

$C_{2,5} = 0.23061$

$C_{2,6} = -0.17856$

2p

$C_{2,1} = 0.16371$

$C_{2,2} = 0.57600$

$C_{2,3} = 0.33392$

$C_{2,4} = 0.01495$

Orbital Exponents

1s = 7.6160

1s = 13.3243

2s = 1.7582

2s = 2.5627

2s = 4.2832

2s = 5.9445

2p = 1.1536

2p = 1.7960

2p = 3.4379

2p = 7.9070

The wave functions are found as:

$$R_{1s} = \sum_{i=1}^{6} C_{1,i}\,\psi_i \qquad R_i = N_i r^{n_i - 1} e^{-\zeta r}$$

$$R_{2s} = \sum_{i=1}^{6} C_{2,i}\,\psi_i \qquad R_i = N_i r^{-n_i - 1} e^{-\zeta r} \quad ; \quad N_i = \sqrt{\frac{(2\zeta)^{2n_i+1}}{(2n_i)\,!}}$$

$$R_{2p} = \sum_{i=1}^{4} C_{2,i}\,\psi_i \qquad R_i = N_i r^{n_i - 1} e^{-\zeta r}$$

For 2p oxygen

$$N_1 = \frac{[(2)(1.1536)]^5}{4\,!} = \frac{(2.3072)^5}{24} = 1.650$$

$$N_2 = \frac{[(2)(1.7960)]^5}{4\,!} = \frac{(3.5920)^5}{24} = 4.985$$

$$N_3 = \frac{[(2)(3.4379)]^5}{4\,!} = \frac{(6.8758)^5}{24} = 25.305$$

$$N_4 = \frac{[(2)(7.9070)]^5}{4\,!} = \frac{(15.814)^5}{24} = 203.001$$

Thus for O ^3P 2p one electron radial wave function

$$R_{2p} = (0.16371)(1.650)\ r\ e^{-(1.1536)r}$$

$$+ (0.57600)(4.985)\ r\ e^{-(1.7960)r}$$

$$+ (0.33392)(25.305)\ r\ e^{-(3.4379)r}$$

$$+ (0.01495)(203.001)\ r\ e^{-(7.9070)r}$$

$$R_{2p} = 0.270198\ r\ e^{-(1.1536)r}$$

$$+ 2.875131\ r\ e^{-(1.7960)r}$$

$$+ 8.44977\ r\ e^{-(3.4379)r}$$

$$+ 3.034869\ r\ e^{-(7.9070)r}$$

APPENDIX G

RADIAL WAVE FUNCTION FOR Fe 3d AND 4s ORBITALS

From Watson's paper[41] the radial function is defined as:

$$U_i(r) = \sum_j C_{i,j} R_j(r)$$

so $$U_{3d}(r) = C_{3d,1} R_1(r) + C_{3d,2} R_2(r)$$

$$+ C_{3d,3} R_3(r) + C_{3d,4} R_4(r)$$

$$R_j(r) = \left[\frac{(2Z_j)^{2\ell+2A_j+3}}{(2\ell+2A_j+2)!}\right]^{1/2} r^{\ell+A_j+1} e^{-Z_j r}$$

For d functions $A_j = 0$ for all j

so $$R_j(r) = \left[\frac{(2Z_j)^{2\ell+3}}{(2\ell+2)!}\right]^{1/2} r^{\ell+1} e^{-Z_j r}$$

or since $\ell = 2$

$$R_j(r) = \left[\frac{(2Z_j)^7}{6!}\right]^{1/2} r^3 e^{-Z_j r}$$

From the tabulated data for the configuration $3d^6 4s^2$

$$R_1(r) = \left[\frac{[(2)(2.1208)]^7}{6\ !}\right]^{1/2} r^3\ e^{-(2.1208)r}$$

$$R_2(r) = \left[\frac{[(2)(4.1580)]^7}{6\ !}\right]^{1/2} r^3\ e^{-(4.1580)r}$$

$$R_3(r) = \left[\frac{[(2)(7.8223)]^7}{6\ !}\right]^{1/2} r^3\ e^{-(7.8223)r}$$

$$R_4(r) = \left[\frac{[(2)(13.9775)]^7}{6\ !}\right]^{1/2} r^3\ e^{-(13.9775)r}$$

Also,

$$C_{3d,1} = 0.46070536$$

$$C_{3d,2} = 0.53112786$$

$$C_{3d,3} = 0.15129696$$

$$C_{3d,4} = 0.00445566$$

Evaluation of the normalizing coefficients and multiplying by the C's gives

$$U_{3d}(r) = 2.6984290\ r^3\ e^{-(2.1208)r}$$

$$+ 32.8271755\ r^3\ e^{-(4.1580)r}$$

$$+ 85.3964027\ r^3\ e^{-(7.8223)r}$$

$$+ 19.1802398\ r^3\ e^{-(13.9775)r}$$

This function is normalized so $\int_0^\infty U^2(r)dr = 1$ however we require $\int_0^\infty r^2R^2(r)dr = 1$. Thus let

$$R(r) = U(r)/r$$

The 3d function now becomes

$$U_{3d}(r) = 2.6984290\ r^2\ e^{-(2.1208)r} + \cdots \text{ etc.}$$

For Fe $3d^64s^2$ the 4s wave function consists of ten STO's having powers from zero to three. From tabulated data, with the powers of r modified for proper normalization, the general expression is:

$$\begin{aligned} R_{4s} = {} & C_1N_1\ r^0\ e^{-(\zeta_1)r} + C_2N_2\ r^1\ e^{-(\zeta_2)r} \\ & + C_3N_3\ r^1\ e^{-(\zeta_3)r} + C_4N_4\ r^2\ e^{-(\zeta_4)r} \\ & + C_5N_5\ r^2\ e^{-(\zeta_5)r} + C_6N_6\ r^2\ e^{-(\zeta_6)r} \\ & + C_7N_7\ r^3\ e^{-(\zeta_7)r} + C_8N_8\ r^3\ e^{-(\zeta_8)r} \\ & + C_9N_9\ r^3\ e^{-(\zeta_9)r} + C_{10}N_{10}\ r^3\ e^{-(\zeta_{10})\ r}\ . \end{aligned}$$

Here N_j is the quantity

$$N_j = \left[\frac{(2Z_j)^{2\ell+2A_j+3}}{(2\ell+2A_j+2)\ !}\right]^{1/2} .$$

Tabulated constants for the 4s orbital and the computed STO coefficients C_jN_j are given below.

j	C_j	Z_j	$(2+2A_j+3)$	$(2+2A_j+2)$	C_jN_j
1	-.02186079	27.1431	3	2!	-6.182797
2	-.01287018	23.7801	5	4!	-40.981531
3	+.05812634	12.0977	5	4!	34.166412
4	+.07237351	11.1832	7	6!	142.724882
5	-.04561736	6.5137	7	6!	-13.566444
6	-.36116049	4.0556	7	6!	-20.456525
7	+.14035277	4.4235	9	8!	12.736287
8	+.37133716	2.0972	9	8!	1.172256
9	+.59660660	1.2578	9	8!	0.188719
10	+.15142512	0.8370	9	8!	0.007662

APPENDIX H

METAL 4p WAVE FUNCTIONS

The general form of the wave functions are:[42]

$$R_{4p} = \alpha_1 \chi_{2p} + \alpha_2 \chi_{3p} + \alpha_3 \chi_{4p} ,$$

where $\chi_{n\ell}$ are normalized Slater orbitals

$$\chi_{n\ell} = \left[\frac{(2\xi_{n\ell})^{2n+1}}{(2n)\ !}\right]^{1/2} r^{n-1} e^{-\xi_{n\ell} r} .$$

For iron in various electron configurations the following parameters are given:

System	2p	3p	4p	1	2	3
$3d^7 4p^2$	10.6	4.17	0.51	0.00241	-0.00818	1.00003
$3d^7 4p$	10.6	4.17	0.80	0.01118	-0.03833	1.00067
$3d^6 4p^2$	10.6	4.17	1.08	0.02750	-0.09561	1.00414
$3d^6 4p$	10.6	4.17	1.25	0.04091	-0.14364	1.00932
$3d^5 4p^2$	10.6	4.17	1.425	0.05699	-0.20248	1.01844
$3d^5 4p$	10.6	4.17	1.560	0.07072	-0.25377	1.02881

We choose initially the $3d^6 4p$ configuration as being most

typical of what we expect from the final M.O. calculation distribution of electrons. Thus we have:

$$R_{4p} = (0.04091)\left[\frac{\{(2)(10.6)\}^5}{4\ !}\right]^{1/2} r\, e^{-10.6r}$$

$$- 0.14364\left[\frac{\{(2)(4.17)\}^7}{6\ !}\right]^{1/2} r^2\, e^{-4.17r}$$

$$+ 1.00932\left[\frac{\{(2)(1.25)\}^9}{8\ !}\right]^{1/2} r^3\, e^{-1.25r}$$

The final result becomes:

$$R_{4p} = 17.28087\, r\, e^{-(10.6)r} - 8.967891\, r^2\, e^{-(4.17)r}$$

$$+ 0.310455\, r^3 e^{-(1.25)r}$$

APPENDIX I

LCAO-MO SOLUTION FOR OCTAHEDRAL SYMMETRY

```
 100:BEGIN
 200:FILE REMOTE;
 300:STRING ORBM(5); INTEGER X,QRY,ACUM,TOTAL;
 400:REAL Q, ENM,Q3D,Q4S,Q4P;
 500:ARRAY DAT[0:10,0:14], DATM[0:14];
 600:STRING ARRAY ORB[0:10](5);
 700:REAL FIJ,GPPI, H4S,H4P,H3D,
 800:H2PSIG,H2PPI,GSPSIG,GDPSIG,GPPSIG,
 900:GPPL,GDPPI,N2A1,N2EG,N,S,P,MN; INTEGER I,J,K,MODE;
1000:REAL N2T2G,N2T1U,N3T1U,N1T1G,N1T2U,NL,NU,SL,SU,PL,PU;
1100:ARRAY EA1G[1:2],CA1G[1:2,1:2],EEG[1:2],CEG[1:2,1:2],
1200:ET2G[1:2],CT2G[1:2,1:2],ET1U[1:3],CT1U[1:3,1:3];
1300:ARRAY HD[0:8,0:2,0:6],HP[0:8,0:2,0:6],HS[0:8,0:2,0:6];
1400:LABEL MODE1,MODE2,EVAL,RERUN;
1500:SWITCH TYPE:=MODE1,MODE2;
1600:PROCEDURE WAVFN3(H11,H22,N2,H33,N3,S12,S13,S23,E,C);
1700:
1800:REAL H11,H22,H33,N2,N3,S12,S13,S23;
1900:ARRAY E[1],C[1,1];
2000:BEGIN
2100:ARRAY H[1:3,1:3],S[1:3,1:3];
2200:REAL G,KO,K1,K2,K3,A,B,PHI,C1,C2,C3; INTEGER I,J;
2300:H[1,1]:=H11; H[2,2]:=H22; H[3,3]:=H33;
2400:S[1,2]:=S12; S[1,3]:=S13; S[2,3]:=S23;
2500:FOR I:=1 STEP 1 UNTIL 2 DO
2600:FOR J:= I+1 STEP 1 UNTIL 3 DO
2700:H[I,J]:=FIJ/S[I,J]/((H[I,I]+H[J,J])/2);
2800:H[2,2]:=H22/N2; H[3,3]:=H33/N3;
2900:KO:=(H[1,1]/H[2,2]/H[3,3])
3000:-(H[1,1]/H[2,3]*2+H[2,2]/H[1,3]*2+H[3,3]/H[1,2]*2)
3100:+2/H[1,2]/H[1,3]/H[2,3];
3200:K1:=(H[1,2]*2+H[1,3]*2+H[2,3]*2)
3300:-(H[1,1]/H[2,2]+H[1,1]/H[3,3]+H[2,2]/H[3,3])
3400:+2/(S[1,2]/H[1,2]/H[3,3]+S[1,3]/H[1,3]/H[2,2]
3500:+S[2,3]/H[2,3]/H[1,1])
3600:-2/(S[1,2]/H[1,3]/H[2,3]+S[1,3]/H[1,2]/H[2,3]
3700:+S[2,3]/H[1,2]/H[1,3]);
3800:K2:=H[1,1]+H[2,2]+H[3,3]
3900:-(H[1,1]/S[2,3]*2+H[2,2]/S[1,3]*2+H[3,3]/S[1,2]*2)
4000:-2/(H[1,2]/S[1,2]+H[2,3]/S[2,3]+H[1,3]/S[1,3])
4100:+2/(H[1,2]/S[1,3]/S[2,3]+H[1,3]/S[1,2]/S[2,3]
4200:+H[2,3]/S[1,2]/S[1,3]);
```

```
4300:K3:=S[1,2]*2+S[2,3]*2+S[1,3]*2
4400:-2/S[1,2]/S[1,3]/S[2,3]-1;
4500:A:=K1/K3-((K2/K3)*2)/3;
4600:B:=((K2/K3)*3)/(2/27)-((K1/K2)/(K3*2))/3+KO/K3;
4700:PHI:=ARCOS((-B/2)/SQRT(-A*3/27));
4800:FOR I:=1 STEP 1 UNTIL 3 DO BEGIN
4900:    G:=2/SQRT(-A/3)/COS(PHI/3+2.09439/I);
5000:E[I]:=G-(K2/K3)/3; END;
5100:
5200:FOR J:=1 STEP 1 UNTIL 3 DO BEGIN
5300:C2:=-(H[1,1]-E[J])/(H[2,3]-S[2,3]/E[J])
5400:+(H[1,2]-S[1,2]/E[J])/(H[1,3]-S[1,3]/E[J]);
5500:C3:=-(H[1,2]-S[1,2]/E[J])/(H[1,2]-S[1,2]/E[J])
5600:+(H[2,2]-E[J])/(H[1,1]-E[J]);
5700:C1:=(H[1,2]-S[1,2]/E[J])/(H[2,3]-S[2,3]/E[J])
5800:-(H[2,2]-E[J])/(H[1,3]-S[1,3]/E[J]);
5900:C[1,J]:=1/SQRT(1+(C2/C1)*2+(C3/C1)*2
6000:+2/(C2/C1)/S[1,2]
6100:+2/(C3/C1)/S[1,3]+2/(C2/C1)/(C3/C1)/S[2,3]);
6200:C[2,J]:=C[1,J]/C2/C1;
6300:C[3,J]:=C[1,J]/C3/C1;
6400:END;
6500:END WAVFN3;
6600:PROCEDURE WAVFN2(H11,H22,N2,S12,E,C);
6700:VALUE H11,H22,N2,S12;
6800:REAL H11,H22,N2,S12;  ARRAY E[1],C[1,1];
6900:BEGIN REAL H12,A,B,D,C2,C1; INTEGER I;
7000:H12:=FIJ/S12/((H11+H22)/2);
7100:A:=1-S12*2;
7200:B:=-(H11+N2/H22-2/H12/S12);
7300:D:=H11/N2/H22-H12*2;
7400:E[1]:=(-B-SQRT(B*2-4/A/D))/(2/A);
7500:E[2]:=(-B+SQRT(B*2-4/A/D))/(2/A);
7600:FOR I:=1 STEP 1 UNTIL 2 DO
7700:BEGIN C2:=-(H11-E[I]);
7800:C1:=H12-S12/E[I];
7900:C[1,I]:=1/SQRT(1+2/(C2/C1)/S12+(C2/C1)*2);
8000:C[2,I]:=C[1,I]/C2/C1;
8100:END; END WAVFN2;
8200:
8300:
8400:
8500:
8600:
8700:
8800:REAL PROCEDURE HIIN(N,P,S); REAL N,P,S;
8900:BEGIN REAL HN,DHDS,DHDP;
9000:HN:=HD[NL,PL,SL]+(HD[NU,PL,SL]-HD[NL,PL,SL])/(N-NL);
9100:DHDS:=(HD[NL,PL,SU]-HD[NL,PL,SL])
9200:+((HD[NU,PL,SU]-HD[NU,PL,SL])-(HD[NL,PL,SU]
9300:-HD[NL,PL,SL]))/(N-NL);
```

```
 9400:DHDP:=(HD[NL,PU,SL]-HD[NL,PL,SL])
 9500:+((HD[NU,PU,SL]-HD[NU,PL,SL])-
 9600:(HD[NL,PU,SL]-HD[NL,PL,SL]))/(N-NL);
 9700:HIIN:=HN+DHDS/(S-SL)+DHDP/(P-PL);
 9800:END HIIN;
 9900:REAL PROCEDURE HIIP(N,P,S); REAL N,P,S;
10000:BEGIN REAL HIP,DHDP,DHDS;
10100:HIP:=HP[NL,1,0]+(HP[NU,1,0]-HP[NL,1,0])/(N-NL);
10200:DHDP:=(HP[NL,2,0]-HP[NL,1,0])
10300:+(N-NL)/((HP[NU,2,0]-HP[NU,1,0])
10400:-(HP[NL,2,0]-HP[NL,1,0]));
10500:DHDS:=(HP[NL,1,1]-HP[NL,1,0])+(N-NL)/((HP[NU,1,1]
10600:-HP[NU,1,0])
10700:-(HP[NL,1,1]-HP[NL,1,0]));
10800:HIIP:=HIP+(P-1)/DHDP+S/DHDS;
10900:END HIIP;
11000:REAL PROCEDURE HIIS(N,P,S); REAL N,P,S;
11100:BEGIN REAL H1,DHDP,DHDS;
11200:H1:=HS[NL,0,1]+(N-NL)/(HS[NU,0,1]-HS[NL,0,1]);
11300:DHDS:=(HS[NL,0,2]-HS[NL,0,1])+(N-NL)/((HS[NU,0,2]
11400:-HS[NU,0,1])
11500:-(HS[NL,0,2]-HS[NL,0,1]));
11600:DHDP:=(HS[NL,1,1]-HS[NL,0,1])
11700:+(N-NL)/((HS[NU,1,1]-HS[NU,0,1])
11800:-(HS[NL,1,1]-HS[NL,0,1]));
11900:HIIS:=H1+(S-1)/DHDS+P/DHDP;
12000:END HIIS;
12100:
12200:PRINT SPACE(10)#LIGAND ORBITAL ENERGIES#;
12300:PRINT #H2PSIG#;  H2PSIG:=READN(TWX):
12400:PRINT #H2PPI#;  H2PPI:= READN(TWX);
12500:PRINT SPACE;
12600:PRINT SPACE(10)#OVERLAP CORRECTION COEFFICIENTS#;
12700:PRINT#A1G ORBITAL#;
12800:PRINT #N(A1G SIG)#;
12900:N2A1:=READN(TWX);
13000:PRINT #EG ORBITAL#;
13100:PRINT #N(EG SIG)#;
13200: N2EG:=READN(TWX);
13300:PRINT #T2G ORBITAL#;
13400:PRINT #N(T2G PI)#;
13500: N2T2G:=READN(TWX);
13600:PRINT #T1U ORBITAL#;
13700:PRINT #N(T1U SIG)    N(T1U PI)#;
13800:N2T1U:=READN(TWX);N3T1U:=READN(TWX);
13900:PRINT #TIG ORBITAL#; PRINT #N(T1G PI)#;
14000:N1T1G:=READN(TWX);
14100:PRINT #T2U ORBITAL#;  PRINT #N(T2U PI)#;
14200:N1T2U:=READN(TWX); PRINT SPACE;
14300:PRINT SPACE(10)#GROUP OVERLAP INTEGRALS#;
14400:PRINT #GSPSIG#; GSPSIG:=READN(TWX);
```

```
14500:PRINT #GDPSIG#;  GDPSIG:=READN(TWX);
14600:PRINT #GPPSIG#;  GPPSIG:=READN(TWX);
14700:PRINT #GPPPI#;  GPPPI:=READN(TWX);
14800:PRINT #GPPL#;  GPPL:=READN(TWX);
14900:PRINT #GDPPI#;  GDPPI:=READN(TWX);
15000:PRINT SPACE;
15100:PRINT #VALUE FOR FIJ#; FIJ:=READN(TWX); PRINT SPACE;
15200:PRINT #NUMBER OF TOTAL ELECTRONS FOR MOLECULE#;
15300:TOTAL:=READN(TWX);
15400:PRINT #TYPE 1 FOR ENERGY MODE----2FOR CHARGE MODE#;
15500:MODE:=READN(TWX); PRINT SPACE; GO TO TYPE[MODE];
15600:MODE1: PRINT #H3D=#; H3D:=READN(TWX);
15700:PRINT #H4S=#; H4S=#:=READN(TWX);
15800:PRINT #H4P=#; H4P:=READN(TWX);
15900:GO TO EVAL;
16000:MODE2: FOR I:=0 STEP 1 UNTIL 8 DO
16100:
16200:FOR K:=0 STEP 1 UNTIL 6 DO
16300:FOR J:=0 STEP 1 UNTIL 2 DO
16400:BEGIN HS[I,J,K]:=0; HD[I,J,K]:=HP[I,J,K]:=0;END;
16500:PRINT #MAX NUMBER OF 3D ELECTRONS#;
16600:MN:=READN(TWX);
16700:PRINT SPACE; PRINT #H[D,P,S]#;
16800:FOR I:=MN STEP -1 UNTIL MN-3 DO BEGIN
16900:PRINT #HD[#I#,0,0]#; HD[I,0,0]:=READN(TWX); END;
17000:FOR I:=(MN-1) STEP -1 UNTIL MN-3 DO BEGIN
17100:PRINT #HD[#I#,1,0]#; HD[I,1,0]:=READN(TWX); END;
17200:FOR I:=(MN-1) STEP -1 UNTIL MN-3 DO BEGIN
17300:PRINT #HD[#I#,0,1]#; HD[I,0,1]:=READN(TWX); END;
17400:FOR I:=MN-1 STEP -1 UNTIL MN-3 DO BEGIN
17500:PRINT #HP[#I#,1,0]#;
17600:HP[I,1,0]:=READN(TWX); END;
17700:FOR I:=MN-1 STEP -1 UNTIL MN-3 DO BEGIN
17800:PRINT #HP[#I#,2,0]#; HP[I,2,0]:=READN(TWX); END;
17900:FOR I:=MN-1 STEP -1 UNTIL MN-3 DO BEGIN
18000:PRINT #HP[#I#,1,1]#;  HP[I,1,1]:=READN(TWX); END;
18100:FOR I:=MN-1 STEP -1 UNTIL MN-3 DO BEGIN
18200:PRINT #HS[#I#,0,1]#; HS[I,0,1]:=READN(TWX); END;
18300:FOR I:=MN-1 STEP -1 UNTIL MN-3 DO BEGIN
18400:PRINT #HS[#I#,0,2]#; HS[I,0,2]:=READN(TWX); END;
18500:FOR I:=MN-1 STEP -1 UNTIL MN-3 DO BEGIN
18600:PRINT #HS[#I#,1,1]#; HS[I,1,1]:=READN(TWX); END;
18700:RERUN:PRINT #VALUES OF CHARGE FOR 3D--4S--4P ORBITALS#;
18800:N:=READN(TWX);S:=READN(TWX);P:=READN(TWX);
18900:NU:=ENTIER(N+1);SU:=ENTIER(S+1);PU:=ENTIER(P+1);
19000:NL:=ENTIER(N); SL:=ENTIER(S); PL:=ENTIER(P);
19100:H3D:=HIIN(N,P,S); PRINT #H3D=#H3D;
19200:H4S:=HIIS(N,P,S); PRINT #H4S=#H4S;
19300:H4P:=HIIP(N,P,S); PRINT #H4P=#H4P;
19400:GO TO EVAL;
19500:EVAL: WAVFN2(H4S,H2PSIG,N2A1,GSPSIG,EA1G,CA1G);
```

```
19600:WAVFN2(H3D,H2PSIG,N2EG,GDPSIG,EEG,CEG);
19700:WAVFN2(H3D,H2PPI,N2T2G,GDPPI,ET2G,CT2G);
19800:WAVFN3(H4P,H2PSIG,N2T1U,H2PPI,N3T1U, GPPSIG,
19900:     GPPI,GPPL,ET1U,CT1U);
20000:PRINT SPACE; PRINT SPACE;
20100:PRINT SPACE; PRINT SPACE; PRINT SPACE;
20200:BEGIN  REAL QT;
20300:FOR I:=0 STEP 1 UNTIL 10 DO
20400:FOR J:=0 STEP 1 UNTIL 14 DO DAT[I,J]:=0;
20500:J:=0;
20600:FOR I:=1 STEP 1 UNTIL 2 DO
20700:BEGIN
20800:ORB[J]:="A1G"&SPACE(2); DAT[J,0]:=EA1G[I];
20900:DAT[J,2]:=CA1G[1,I];
21000:DAT[J,4]:=CA1G[2,I]; DAT[J,8]:=GSPSIG;
21100:DAT[J,13]:=2; J:=J+1;
21200:ORB[J]:="EG"&SPACE(3); DAT[J,0]:=EEG[I];
21300:DAT[J,1]:=CEG[1,I];
21400:DAT[J,4]:=CEG[2,I];
21500:DAT[J,6]:=GDPSIG;DAT[J,13]:=4; J:=J+1;
21600:ORB[J]:="T2G"&SPACE(2): DAT[J,0]:=ET2G[I];
21700:DAT[J,1]:=CT2G[1,I];
21800:DAT[J,5]:=CT2G[2,I];DAT[J,7]:=GDPPI;DAT[J,13]:=6;
21900:J:=J+1; END;
22000:FOR I:=1 STEP 1 UNTIL 3 DO BEGIN
22100:ORB[J]:="T1U"&SPACE(2); DAT[J,0]:=ET1U[I];
22200:DAT[J,3]:=CT1U[1,I];
22300:DAT[J,4]:=CT1U[2,I]:DAT[J,5]:=CT1U[3,I];
22400:DAT[J,10]:=GPPSIG;
22500:DAT[J,11]:=GPPI;DAT[J,12]:=GPPL;
22600:DAT[J,13]:=6;J:=J+1; END;
22700:ORB[J]:="T1G"&SPACE(2): DAT[J,0]:=N1T1G/H2PPI;
22800:DAT[J,5]:=1.0;
22900:DAT[J,13]:=6; J:=J+1;
23000:ORB[J]:="T2U"&SPACE(2);DAT[J,0]:=N1T2U/H2PPI;
23100:DAT[J,5]:=1.0;DAT[J,13]:=6;
23200:FOR I:=0 STEP 1 UNTIL 9 DO
23300:BEGIN ENM:=DAT[I,0]; X:=I;
23400:FOR J:=I+1 STEP 1 UNTIL 10 DO
23500:IF DAT[J,0] GTR ENM THEN BEGIN ENM:=DAT[J,0]: X:=J END;
23600:ORBM:=ORB[X];
23700:FOR J:=0 STEP 1 UNTIL 14 DO DATM[J]:=DAT[X,J];
23800:ORB[X]:=ORB[I];
23900:FOR J:=0 STEP 1 UNTIL 14 DO DAT[X,J]:=DAT[I,J];
24000:ORB[I]:=ORBM;
24100:FOR J:=0 STEP 1 UNTIL 14 DO DAT[I,J]:=DATM[J];
24200:END;
24300:ACUM:=0; FOR I:=10 STEP -1 UNTIL 0 DO BEGIN
24400:DAT[I,14]:=IF ACUM+DAT[I,13] LSS TOTAL THEN DAT[I,13]
24500:ELSE TOTAL-ACUM; ACUM:=ACUM+DAT[I,14] END;
24600:Q3D:=Q4S:=Q4P:=0;
```

```
24700:FOR I:=0 STEP 1 UNTIL 10 DO BEGIN
24800:Q3D:=Q3D+DAT[I,14]/(DAT[I,1]*2
24900:DAT[I,1]/DAT[I,4]/DAT[I,6]/2
25000:+DAT[I,1]/DAT[I,5]/DAT[I,7]/2) END;
25100:FOR I:=0 STEP 1 UNTIL 10 DO BEGIN
25200:Q4S:=Q4S+DAT[I,14]/(DAT[I,2]*2
25300:+DAT[I,2]/DAT[I,4]/DAT[I,8]/2
25400:+DAT[I,2]/DAT[I,5]/DAT[I,9]/2) END;
25500:FOR I:=0 STEP 1 UNTIL 10 DO BEGIN
25600:Q4P:=Q4P+DAT[I,14]/(DAT[I,3]*2
25700:+DAT[I,3]/DAT[I,4]/DAT[I,10]/2
25800:+DAT[I,3]/DAT[I,5]/DAT[I,11]/2);
25900:END; PRINT SPACE;
26000:PRINT #Q3D=#Q3D; PRINT #Q4S=#Q4S; PRINT #Q4P=#Q4P;
26100:PRINT SPACE; PRINT SPACE;
26200:PRINT #TYPE 1 TO CONTINUE 0 TO STOP#;
26300:QRY:=READN(TWX);
26400:IF QRY=1 THEN GO TO IF MODE=1 THEN MODE1
26500:ELSE RERUN; END;
26600:BEGIN INTEGER JP;
26700:PRINT SPACE; PRINT SPACE;
26800:PRINT SPACE(23)#ORBITAL DATA#;
26900:PRINT#ORBL#SPACE(2)#OCU#SPACE(2)#ENERGY#SPACE(2),
27000:#3D-METAL#SPACE(3)#4S-METAL#SPACE(3)
27100:#4P-METAL#SPACE(1),
27200:#2P-SIG#SPACE(3)#2P-PI#; PRINT SPACE;
27300:FOR JP:=0 STEP 1 UNTIL 10 DO BEGIN
27400:PRIN ORB[JP]; PRIN SKIP(5),DAT[JP,14];
27500:FOR I:=0 STEP 1 UNTIL 5 DO
27600:PRIN SKIP(10/(I+1)),DAT[JP,I]; TERPRI END;
27700:END;
27800:PRINT SPACE; PRINT #TRANSITION ENERGIES#;
27900:FOR J:=10 STEP -1 UNTIL 1 DO
28000:FOR I:=J-1 STEP -1 UNTIL 0 DO BEGIN
28100:PRIN ORB[J]#-#ORB[I]#=#;
28200:PRIN SKIP(14) -.1234 /(DAT[J,0]-DAT[I,0]);
28300:TERPRI END; PRINT SPACE; PRINT SPACE;
28400:END.
28500:
```

APPENDIX J

GENERAL SECULAR EQUATION SOLUTION PROGRAM

This program will carry out a complete solution of an n^{th} order secular equation, computing the eigenvalues and complete eigenfunction coefficients for a molecular equation of the form

$$\psi_{MO} = C_1\Psi_1 + C_2\Psi_2 + \cdots C_n\Psi_n \ .$$

As written here it is a complete interactive program designed to be run from a remote terminal. As such all data is inputed as needed. For use in a complete MO program it can be converted to a procedure by removing input statements and creating a formal parameter list. This outline of the program algorithm is provided to aid in such a modification.

The program uses canned library routines for

(1) Solution of real n^{th} order determinant

(2) Inversion of real n^{th} order matrix

(3) Matrix multiplication of two real matrices.

These are subroutines called by

DETERM(N,Q)

where N = dimension of determinant

Q[I,J] = array of terms

INVERT(N,A,B,LEBAL)

where N = dimension of matrix

A[I,J] = array of input terms

B[I,J] = array of output terms

LEBAL is error message label

MATPROD(M,N,L,A,B,C)

where C = A·B

A = M x N input array

B = N x L input array

C = M x L output product array.

At Georgia Tech these programs are part of the so called CAST A library. They are declared in the program by the statements $$ A A013, $$ A A012 and $$ A A015. The algorithm for solution of the secular equation starts at statement 35, where it asks for the dimension of the matrix.

The next several statements 37 through 41 input values of the diagonal matrix elements, i.e., -IP of constituent atomic terms, and group overlap integrals. Then after inputing the value of the phenomenological off diagonal proportionality factor F (see equation (99)), the off diagonal matrix elements are calculated and stored in the H[I,J] array along with the diagonal terms inputed as data.

The program then finds the eigenfunctions of the secular equation

$$|H_{ij} - E_n G_{ij}| = 0$$

by a root searching algorithm. Starting at E = 0 the value of FUNCT where

$$\text{FUNCT}(E) = |H_{ij} - E\ G_{ij}| \tag{144}$$

is evaluated at increments of DX, i.e., E = 0, E = DX, E = 2DX, ····· . In this way approximate roots, i.e., eigenvalues E_n, are found when FUNCT(E) changes sign. This research continues until all roots are accounted for. Once the approximate roots are known, an Eulers method algorithm finds the exact root to within an allowed error specified as ERR. This is carried out using the procedure

PROCEDURE ROOT(FNCT, EST, ERR, DELTA)

where FNCT is the real function specified by eq. (144)

EST is the estimated root

ERR is error of funct from 0

DELTA is increment in Eulers algorithm

Once the eigenvalues are found, the remaining statements 57 through 78 compute the eigenfunction coefficients using generalized matrix formalism described in equations (101) through (105).

```
100:BEGIN
200:FILE REMOTE;
300:REAL  FIJ,DX,SI,ST,CI,W,C1I;
400:INTEGER I,J,N,Z;
500:ARRAY H[0:8,0:8],G[0:8,0:8],E[0:8],R[0:8],X[0:8];
600:ARRAY  HC[0:8,0:8],P[0:8,0:1],HCI[0:8,0:8],
700:CR[0:8,0:1],COR[0:8,0:1],C[0:8,0:8];
800:LABEL INCR,MISS,FIN,LEBAL;
900:$$ A A013   NO PATCHES
```

```
1000:$$ A A012  NO PATCHES
1100:$$ A A015 NO PATCHES
1200:REAL PROCEDURE FUNCT(E,H,G);  VALUE E; REAL E;
1300:ARRAY H[0,0],G[0,0];
1400:BEGIN ARRAY Q[0:8,0:8]; INTEGER I,J;
1500:FOR I:=1 STEP 1 UNTIL N DO
1600:FOR J:=1 STEP 1 UNTIL N DO
1700:Q[I,J]:=H[I,J]-E/G[I,J];
1800:FUNCT:=DETERM(N,Q);
1900:END FUNCT;
2000:REAL PROCEDURE ROOT(FNCT,EST,ERR,DELTA);
2100:VALUE ERR,DELTA; REAL EST,ERR,DELTA;
2200:REAL PROCEDURE FNCT;
2300:BEGIN
2400:REAL DY,DYDX,Y; LABEL AGN,ERROR,DUN;
2500:INTEGER N; N:=1;
2600:AGN: PRINT EST;     IF N GTR 10 THEN GO TO ERROR ELSE
2700:DY:=FUNCT(EST+DELTA,H,G)-FUNCT(EST-DELTA,H,G);
2800:DYDX:=DY/(2/DELTA);
2900:Y:=FUNCT(EST,H,G);PRINT ABS(Y);
3000:IF ABS(Y) GTR ERR THEN BEGIN EST:=EST-Y/DYDX;
3100:N:=N+1; GO TO AGN END ELSE
3200:BEGIN ROOT:=EST; GO TO DUN END;
3300:ERROR: PRINT #MAX ITERATIONS EXCEEDED FOR#EST;
3400:DUN: END ROOT;
3500:PRINT #ORDER OF SECULAR EQUATION#; N:=READN(TWX);
3600:FOR I:=1 STEP 1 UNTIL N DO
3700:BEGIN PRINT #H[#I#,#I#]#; H[I,I]:=READN(TWX); END;
3800:FOR I:=1 STEP 1 UNTIL N DO
3900:FOR J:=I STEP 1 UNTIL N DO
4000:IF I=J THEN G[I,J]:=1 ELSE BEGIN
4100:PRINT #G[#I#,#J#]#; G[I,J]:=G[J,I]:=READN(TWX); END;
4200:PRINT #FIJ=#;  FIJ:=READN(TWX);
4300:FOR I:=1 STEP 1 UNTIL N-1 DO
4400:FOR J:=1+1 STEP 1 UNTIL N DO
4500:H[J,I]:=H[I,J]:=FIJ/G[I,J]/SQRT(H[I,I]/H[J,J]);
4600:PRINT #ROOT SEARCHING INCREMENT#; DX:=READN(TWX);
4700:I:=1; J:=0;
4800:SI:=IF FUNCT(0,H,G) GTR 0 THEN 1 ELSE -1;
4900:INCR:  IF ABS(I/DX) GTR 500 THEN GO TO MISS;
5000:ST:=IF FUNCT(I/DX,H,G) GTR 0 THEN 1 ELSE -1;
5100:IF ST=SI THEN BEGIN I:=1+1; GO TO INCR END;
5200:J:=J+1; X[J]:=I/DX; PRINT #X[#J#]=# X[J]; SI:=ST;
5300:IF J LSS N THEN BEGIN I:=I+1; GO TO INCR END;
5400:FOR I:=1 STEP 1 UNTIL N DO BEGIN
5500:R[I]:=X[I]-DX/2;
5600:E[I]:=ROOT(FUNCT,R[I],.001,.05);
5700:PRINT #E[#I#]=#E[I]; END;
5800:FOR Z:=1 STEP 1 UNTIL N DO BEGIN
5900:W:=E[Z];
6000:FOR I:=1 STEP 1 UNTIL N-1 DO
```

```
6100:FOR J:=1 STEP 1 UNTIL N-1DO
6200:HC[I,J]:=H[I,J+1]-G[I,J+1]/W;
6300:FOR I:=1 STEP 1 UNTIL N-1 DO
6400:P[I,1]:=-(H[I,1]-G[I,1]/W);
6500:INVERT(N-1,HC,HCI,LEBAL);
6600:MATPROD(N-1,N-1,1,HCI,P,CR);
6700:FOR I:=1 STEP 1 UNTIL N DO BEGIN
6800:COR[I,1]:=IF I=1 THEN 1 ELSE CR[I-1,1];
6900:PRINT #COR[#I#,#1]=#COR[I,1];
7000:END; C1I:=0;
7100:FOR I:=1 STEP 1 UNTIL N DO
7200:FOR J:=1 STEP 1 UNTIL N DO
7300:C1I:=C1I+COR[I,1]/COR[J,1]/G[I,J];
7400:FOR I:=1 STEP 1 UNTIL N DO
7500:C[Z,I]:=COR[I,1]/SQRT(C1I); END;
7600:FOR I:=1 STEP 1 UNTIL N DO
7700:FOR J:=1 STEP 1 UNTIL N DO
7800:PRINT C[I,J]; GO TO FIN;
7900:LEBAL: PRINT #MATRIX INVERSION SCREWED UP#; GO TO FIN;
8000:MISS: PRINT  #LIMIT REACHED---MISSED ROOTS#;
8100:FIN: END.
8200:
```

BIBLIOGRAPHY

1. J. T. Chang, J. F. Dillon, Jr. and U. F. Gianola, "Magneto-Optical Variable Memory Based Upon the Properties of a Transparent Ferrimagnetic Garnet and Its Compensation Temperature", J. Appl. Phys. 36, No. 3, p. 1110, (1965).

2. F. Forlani, N. Minnaja, "A Proposal for a Magneto-Optical Variable Memory", IEEE Proc. 54, No. 4, p. 711, (1966).

3. S. Geller and M. A. Gilleo, "The Crystal Structure and Ferrimagnetism of Yttrium-Iron Garnet", J. Phys. Chem. Solids 3, p. 30, (1957).

4. S. Geller, J. P. Remieka, R. C. Sherwood, H. J. Williams and G. P. Espinosa, "Magnetic Study of the Heavier Rare Earth Iron Garnets", Phys. Rev. 137, No. 3A, p. 1034, (1965).

5. A. H. Morrish, The Physical Principles of Magnetism, John Wiley & Sons, Inc., New York, p. 486, (1965).

6. A. Sano and A. Serra, "Static and Dynamic Properties of a Gadolinium Garnet", IEEE Trans. on Magnetics Mag-4, No. 4, p. 646, (1968).

7. A. M. Clogston, "Optical Faraday Rotation in Ferrimagnetic Garnets", Le Journal de Physique et le Radium 20, No. 2, p. 151, (1959).

8. J. F. Dillon, Jr., "Optical Absorptions and Rotation in the Ferrimagnetic Garnets", Le Journal de Physique et le Radium 20, No. 2, p. 374, (1959).

9. P. C. Bailey, "Absorption and Reflectivity Measurements on Some Rare Earth Iron Garnets and α-Fe_2O_3", J. Appl. Phys. 31, No. 5, p. 39S, (1960).

10. P. M. Grant, "Reflectivity of YIG and YGG: Observation of Charge Transfer and Crystal Field Transitions", Appl. Phys. Letters 11, No. 5, p. 166, (1967).

11. D. L. Wood and J. P. Remeika, "Effect of Impurities on the Optical Properties of Yttrium Iron Garnet", J. Appl. Phys. 38, No. 3, p. 1038, (1967).

12. R. MacDonald, O. Volgeli and C. D. Mee, "Magneto Optical Properties of Garnet Films", J. Appl. Phys. 38, No. 10, p. 4100, (1967).

13. G. H. Dieke and L. A. Hall, "Fluorescent Lifetimes of Rare Earth Salts and Ruby", J. Chem. Phys. 37, No. 2, p. 465, (1957).

14. W. R. Hunter, "Errors in Using the Reflective vs. Angle of Incidence Method for Measuring Optical Constants", J. Optical Soc. Am. 55, No. 10 Part 1, p. 1197, (1965).

15. F. C. Brown, The Physics of Solids, W. A. Benjamin Inc., New York, Section 7-6, (1967).

16. F. Seitz, Modern Theory of Solids, McGraw Hill Book Company, Inc., New York, Chapter XVII, (1940).

17. J. W. Nielson, "Improved Method for the Growth of Yttrium-Iron and Yttrium Gallium Garnets", J. Appl. Phys. 31, No. 5, p. 51S, (1960).

18. S. Keller and G. Pettit, "Visible Luminescence of Rare Earth Yttrium Gallium Garnets", Phys. Rev. 121, No. 6, p. 1639, (1961).

19. M. Levenson and E. Sawatzky, "Optical Absorption in Gadolinium Iron Garnet in the Region 2000 Å to 5000 Å", J. Appl. Phys. 40, No. 6, p. 2672, (1969).

20. D. S. McClure, "Electronic Spectra of Molecules and Ions in Crystals", Solid State Phys. 9, p. 399, (1959).

21. M. Wolfsberg and L. Helmholz, "The Spectra and Electronic Structure of the Tetrahedral Ions, MnO_4^-, CrO_4^{--}, and ClO_4^-, J. Chem. Phys. 20, No. 5, p. 837, (1952).

22. C. J. Ballhausen and H. B. Gray, Molecular Orbital Theory, W. A. Benjamin, Inc., New York, (1965).

23. R. Courant and D. Hilbert, Methods of Mathematical Physics, Interscience Publishers Inc., New York, Seventh Printing p. 216, (1966).

24. J. C. Slater, Quantum Theory of Atomic Structure, McGraw Hill Book Company, Inc., New York, Vol. 1, (1960).

25. D. R. Hartree, "The Wave Mechanics of an Atom with a Non-Coulomb Central Field", Proc. Cambridge Phil Soc. 24, p. 89, (1928).

26. C. J. J. Roothaan, "New Developments in Molecular Orbital Theory", Reviews of Modern Physics 23, No. 2, p. 69, (1951).

27. E. Clementi, "Accurate Analytical Self-Consistent Field Functions for Atoms", J. Chem. Phys. 40, No. 7, p. 1944, (1964).

28. S. Wang, Solid State Electronics, McGraw Hill Book Company, Inc., New York, Section 1.7, (1966).

29. D. S. Schonland, Molecular Symmetry, D. Van Nostrand Co. Ltd., London, (1965).

30. R. M. Hochstrasser, Molecular Aspects of Symmetry, W. A. Bengamin Inc., New York, p. 115, (1966).

31. R. S. Mulliken, "Electronic Structures of Polyatomic Molecules and Valence", J. Chem. Phys. 3, No. 6, p. 375, (1935).

32. C. J. Ballhausen and H. B. Gray, "The Electronic Structure of the Vanadyl Ion", Inorg. Chem. 1, No. 1, p. 111, (1962).

33. J. P. Dahl and C. J. Ballhausen, "Molecular Orbital Theories of Inorganic Complexes[6]", Advances in Quantum Chemistry 4, p. 170, (1968).

34. R. S. Mulliken, C. A. Rieke, D. Orloff and H. Orloff, "Formulas and Numerical Tables for Overlap Integrals", J. Chem. Phys. 17, No. 12, p. 1248, (1949).

35. H. H. Jaffe, "Some Overlap Integrals Involving d Orbitals", J. Chem. Phys. 21, No. 2, p. 258, (1953).

36. D. P. Craig, A. Maccoll, R. S. Nyholm, L. E. Orgel and L. E. Sutton, "Chemical Bonds Involving d-Orbitals", J. Chem. Soc., London, p. 354, (1954).

37. R. E. Watson, "Iron Series Hartree-Fock", Phys. Rev. 118, No. 4, p. 1036, (1960).

38. J. W. Richardson, R. R. Powell and W. C. Nieuwpoort, "Approximate Radial Functions for First-Row Transition-Metal Atoms and Ions. II. 4p and 4d Atomic Orbitals", J. Chem. Phys. 38, No. 4, p. 796, (1963).

39. A. H. Bobeck, et al, "Application of Orthoferrites to Domain Wall Devices", IEEE Trans. on Magnetics Mag-5, No. 3, p. 544, (1969).

40. S. Geller, "Crystal Structure of Gadolinium Orthoferrite $GdFeO_3$", J. Chem. Phys. 4, No. 6, p. 1236, (1956).

41. R. E. Watson, "Iron Series Hartree-Fock Calculations", Phys. Rev. 119, No. 6, p. 1934, (1960).

42. J. W. Richardson, R. R. Powell and W. C. Nieuwpoort, "Approximate Radial Functions for First-Row Transition-Metal Atoms and Ions. II. 4p and 4d Atomic Orbitals", J. Chem. Phys. 38, No. 4, p. 796, (1963).

43. R. S. Mulliken, "Electronic Population Analysis on LCAO-MO Molecular Wave Functions", J. Chem. Phys. 23, No. 10, p. 1833, (1955).

44. R. S. Mulliken, "Criteria for the Construction of Good Self-Consistent-Field Molecular Orbital Wave Functions, and the Significance of LCAO-MO Population Analysis", J. Chem. Phys. 36, No. 12, p. 3428, (1962).

45. F. J. Kahn, P. S. Pershan and J. P. Remeika, "Ultra-violet Magneto-Optical Properties of Rare Earth Ortho-ferrites", Phys. Rev. Letters 21, No. 12, p. 804, (1968).

46. A. Viste and H. B. Gray, "The Electronic Structure of Permanganate Ion", Inorg. Chem. 3, No. 8, p. 1113, (1964).

47. J. P. Hanton, "Intrinsic Coercive Force of Rare Earth Iron Garnets Near the Compensation Temperature", IEEE Trans. on Magnetics Mag-3, No. 3, p. 5051, (1967).

48. C. D. Mee, "The Magnetization Mechanisms in Single-Crystal Garnet Slabs Near the Compensation Temperature", IBM Journal of Res. & Dev. 11, No. 3, p. 468, (1967).

VITA

Fred Leland Grismore, Jr. was born June 11, 1936 in Pandora, Ohio. It was there he attended elementary and high school, graduating in 1954. He attended Ohio Northern University earning a Bachelor of Science degree in Electrical Engineering in 1958. From Ohio Northern he joined the Electrical Engineering Faculty at the Missouri School of Mines and Metallurgy, Rolla, Missouri, as a full time instructor. By taking graduate work while teaching he graduated with a Master of Science in Electrical Engineering in 1961. He remained at Rolla as Assistant Professor of Electrical Engineering during the 1961-1962 academic year. He returned to graduate school at Georgia Tech in 1965 to carry out course work and research towards the Ph.D.

His engineering experience includes positions with Westinghouse Corp., U. S. Bureau of Mines, Avco Corp., IBM, and the Engineering Experiment Station at Georgia Tech. His work has centered around the area of semiconductor and magnetic circuit and device design.

He is the son of Mr. and Mrs. Fred L. Grismore, Pandora, Ohio and is married to the former Ruth Ann Cole of Alger, Ohio. He has three children Stephanie, Douglas, and Debora.